The hot and dusty interstellar medium through X-ray spectroscopy

Rogantini, D.

Publication date
2020
Document Version
Final published version
License
Other

Link to publication

Citation for published version (APA):
Rogantini, D. (2020). *The hot and dusty interstellar medium through X-ray spectroscopy*. [Thesis, externally prepared, Universiteit van Amsterdam].

The hot and dusty interstellar medium

Daniele Rogantini

The hot and dusty interstellar medium
through X-ray spectroscopy

Daniele Rogantini

The hot and dusty interstellar medium through X-ray spectroscopy

ACADEMISCH PROEFSCHRIFT

ter verkrijging van de graad van doctor
aan de Universiteit van Amsterdam
op gezag van de Rector Magnificus
prof. dr. ir. K.I.J. Maex,
ten overstaan van een door het College voor Promoties
ingestelde commissie,
in het openbaar te verdedigen in de Aula der Universiteit
op vrijdag 6 maart 2020, te 13:00 uur

door

Daniele Rogantini

geboren te Bergamo

Promotiecommissie:

Promotor:	Prof. dr L.B.F.M. Waters	Universiteit van Amsterdam
Copromotor:	Dr E. Costantini	SRON Universiteit van Amsterdam
Overige leden:	Prof. dr S.B. Markoff	Universiteit van Amsterdam
	Prof. dr C. Dominik	Universiteit van Amsterdam
	Prof. dr J.W.A. den Herder	Universiteit van Amsterdam
	Dr J. Vink	Universiteit van Amsterdam
	Prof. dr R. Schneider	Sapienza, University of Rome
	Dr C. Jaeger	Friedrich Schiller University

Faculteit der Natuurwetenschappen, Wiskunde en Informatica

ISBN: 978-94-028-1957-1

The research reported in this thesis was carried out at the Netherlands Institute for Space Research (SRON) and at the Anton Pannekoek Institute for Astronomy, University of Amsterdam, The Netherlands, with support from a NWO (Nederlandse Organisatie voor Wetenschappelijk Onderzoek) VIDI Grant.

Ai miei nonni e
alla mia famiglia

and my two axolotls

Contents

"And if the dam breaks open many years too soon
And if there is no room upon the hill
And if your head explodes with dark forebodings too
I'll see you on the dark side of the moon"

Pink Floyd - Brain Damage (1973)

1

Introduction

1.1 The birth of high-resolution X-ray spectroscopy

The discovery of X-rays, on November 8, 1895, by Wilhelm Röngten, is one of the most famous serendipitous discoveries of science. Röntgen's X-rays had energies of 30–50 keV, about the same energy as X-rays used today for medical diagnostics. Most X-rays from astronomical X-ray sources are much less energetic ($0.5 - 5$ keV) and, therefore, more easily absorbed by intervening atoms and ions. This radiation cannot penetrate even the thin outer layers of the Earth's atmosphere. It is thus impossible to observe X-rays from astronomical sources with ground-based instruments. Hence, observing from above the atmosphere is essential.
In the last century, advanced technology was necessary to build an instrument that was sensitive enough to detect cosmic X-rays, and yet small enough to fit within a rocket or balloon payload. The heritage of the rocket technology from World War II and the knowledge of nuclear physicists helped the group led by Riccardo Giacconi to successfully overcome this technological barrier. The X-ray astronomy revolution started on June 18, 1962, when two X-ray Geiger counters onboard an Aerobee rocket, made the now historic first detection of a powerful cosmic X-ray source, the well known low-mass X-ray binary Sco X-1 (Giacconi et al. 1962).

In the following years, the first spectral line feature was detected in an extrasolar X-ray source: an O VIII line was detected in the Cygnus Loop with a proportional counter (Gorenstein et al. 1971; Novick 1973). This instrument acquired its name because the number of electrons produced in the avalanche after the X-ray photon interacted with the gas in the detector was proportional to the energy of that photon. Although this does yield spectral information, it is very crude, due to the limited number of electrons generated in the first step of this process.

Thanks to the rapid space technology development, many successes were achieved such as the launch of the first X-ray dedicated satellite *Uhuru* in 1970 (which led to a catalogue of 339 X-ray sources) and the manufacture of new X-ray spectrometers. The *Einstein* Observatory and EXOSAT (launched in 1978 and 1983, respectively) were the first missions with X-ray spectroscopy as their principal aim. Different spectrometers were incorporated on the satellites including the earliest grating spectrometers (Dijkstra et al. 1978; Brinkman et al. 1980). With a resolving power ($R = \lambda/\Delta\lambda$) up to 100 in the soft X-ray band, these missions opened the high-resolution X-ray spectroscopy field. Detailed X-ray spectra were taken for several bright sources, primarily supernova remnants. Absorption features due to the intervening interstellar medium were observed for the first time. In particular, the spectral resolution permitted the detection of the oxygen K-edge located in the soft band of the X-ray, E = 0.53 keV (Charles et al. 1979; Schattenburg & Canizares 1986). The absorption by the interstellar medium had been already predicted twenty years before (Strom & Strom 1961) and observations from rockets were useful to build a cross-section model based on the photoelectric absorption (Bell & Kingston 1967; Cruddace et al. 1974).

Another major progress in high-resolution X-ray spectroscopy occurred with the launch of *ASCA* in 1993. The novelty of this satellite was the two charge-coupled devices (well known, now, as CCD) whose energy resolution was roughly an order of magnitude better than what was achievable with proportional counters. These sensitive and efficient detectors can be used for both imaging and spectroscopy and allowed for the first detailed, broadband spectra of distant sources (mainly quasars) to be observed. In operation for eight years, ASCA enabled complex spectral analysis, leading to discoveries of warm gas in active galactic nuclei (AGN) and the complexity of the hot X-ray emission gas in the intracluster medium.

The year 1999 witnessed a great change in the history of high-resolution X-ray spectroscopy with the launch of the flagship missions *Chandra* and XMM-*Newton*. With more than an order of magnitude improvement in spectral and spatial resolution sensitivity, *Chandra* and XMM-*Newton* shed light on known problems, as well as opened new era of research into topics as diverse as comets and supermassive black holes. High-resolution X-ray spectroscopy with transmission and reflection gratings and advanced CCDs on *Chandra* and XMM-*Newton* enabled measurement of many spectral lines, including resolved multiplets, and in some cases, line profiles and line shifts. The measurements provided, for example, critical diagnostic of densities, temperature, flow velocities and composition of gas intrinsic to accreting sources, such as AGN and X-ray binaries, giving insight into the accretion process that powers their activity (e.g., Guainazzi & Bianchi 2007). Another field which opened up with the high resolution provided by *Chandra* and XMM-*Newton* was that of the non-equilibrium plasma in supernova remnants. X-ray spectral line ratios measured the temperature and chemical abundance for shocked material, and line profiles lead to kinematic velocities estimates (Vink 2011). Moreover, these cornerstone missions were fundamental to define the properties and the distribution of both cold and ionised interstellar medium (see Section 1.2). An example of the spectral capabilities of grating spectrometers is the detailed studied of the O K-edge. In spite of the complexity of the oxygen region due to the overlapping absorption of ionised, neutral and molecular oxygen together with dust, it has

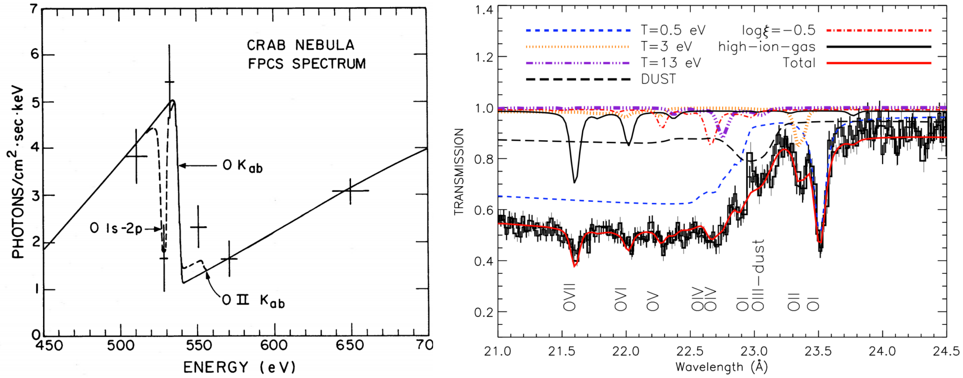

Figure 1.1: The oxygen K-edge: the comparison highlights the enormous technology development that occurred in high-resolution X-ray spectroscopy in the second half of the last century. *Left panel*: The oxygen K-edge region of the Crab Nebula due to the interstellar medium absorption observed with *Einstein*, in eV units. The dashed curve is the model prediction for the O $1s \rightarrow 2p$ absorption line (Schattenburg & Canizares 1986). *Right panel*: The oxygen K-edge region detected in the XMM-*Newton* grating spectrum of the low-mass X-ray binary 4U 1820-30. The spectrum is shown in wavelengths. The high spectral resolution of XMM-*Newton* enables the analysis of the different phase of the interstellar medium (Costantini et al. 2012).

been possible to disentangle the absorption by the different phases. In Figure 1.1, we show a comparison between the O K-edges detected with the first spectroscopy mission *Einstein* and the current XMM-*Newton*.

The importance of the X-ray absorption edges for studies of the interstellar dust was first pointed out by Fireman (1974) and Ryter et al. (1975). They emphasised the fact that X-rays are absorbed alike by atoms in the dust or the gas along the line of sight towards distant continuous X-ray sources. *Chandra* and XMM-*Newton* grating observations confirmed this idea, enabling the detection of interstellar dust footprints in the absorption edge bands of elements such as magnesium and silicon (see Chapter 3 and references therein).

Micro-calorimeter X-ray detectors represent the future for X-ray astronomy, in particular for high-resolution X-ray spectroscopy. Despite the first attempts to use this technique in space were cursed by different failures (*Astro-E*, *Suzaku* and *Hitomi*), the micro-calorimeter X-ray detectors promise a large step forward in the field. This has been confirmed by the spectacular first light that was acquired by the JAXA satellite *Hitomi*. The impressive spectral resolution of this single spectrum of the Perseus cluster motivated scientists and space agencies to plan a recovery mission now known as *XRISM*. Micro-calorimeters will be also incorporated in the ESA large class mission *Athena*. These two satellites will give a huge boost in our understanding of the hot and energetic universe, for example on how the black holes grow and shape the universe. Their impact will revolutionise many sub-fields including the X-ray spectroscopy of interstellar dust (see Section 1.3.2 and Chapter 5).

1.2 Interstellar medium

The interstellar medium (ISM), is literally the matter that exists in the space between the stellar systems in a galaxy. Although stars dominate the baryonic matter of spiral galaxies such as the Milky Way, both gas and dust play a key role in the life cycle and evolution of the Galaxy. Particularly important is the interplay between the stars and the ISM, often referred to as the "star-gas cycle". The stars constantly replenish the ISM with matter. Thermonuclear fusion in stellar interiors gradually and continuously enrich the ISM with elements like oxygen and iron through outflows from stars in the late stage of their life (giant stars and planetary nebulae). The release of elements into the surrounding medium can also happen following catastrophic events, like supernova explosions (Tielens 2005; Maciel 2013). Elements are formed via s-processes in the envelopes of red giants and supergiants, seeded by available iron nuclei (Boothroyd 2006). Rare elements with atomic number $Z > 42$ are generated by r-processes. These are produced efficiently in kilonova events which are the result of neutron star mergers (Pian et al. 2017).

The dynamics of these mass exchanges are important because they involve supersonic processes which drive shocks and produce cavities in the ISM. Eventually, the hot gas cools, forming cold, neutral hydrogen clouds and warmer, diffuse, neutral hydrogen layers. Part of the interstellar matter can form molecular clouds, where the denser regions give birth to new stars whose chemical composition differ from the previous generations (Dyson & Williams 1997).

1.2.1 Three-phases interstellar medium

The interstellar matter assumes several distinct, stable configurations of volume density, covering a range from 10^{-3} to 10^{7} cm^{-3} and temperature ranging between 10 and 10^{7} K. With this wide range of temperatures and densities, the ISM is characterised by several structures with different morphology that occupy different fractions of the Galactic volume. Specific physical processes characterise these distinct environments (for a review see Spitzer 1998).

McKee & Ostriker (1977) classified the ISM in three general phases: the cold neutral medium, the warm neutral and ionised medium, and the hot ionised medium. Because of the long cooling times, the hot phase dominates the Galactic volume, although most of the mass is concentrated in the cold phase, mostly in the Galactic disc. The hot gas is, therefore, a diffuse medium in which the other phases are embedded.

In the following we describe the main characteristics of them, referring to Tielens (2005).

Cold phase - it is a complex phase containing dense molecular clouds and cold neutral medium. The H_2 clouds have temperatures of 10-20 K and densities $n_{\mathrm{H}} \sim 10^{2-6}$ cm^{-3} (Goldsmith 1987). They comprise a significant fraction of the mass of the ISM but occupy only $\sim 0.05\%$ of its volume. Most molecular clouds are gravitationally bound and they are important because star formation takes place inside them. Instead, the cold neutral gas is distributed in sheets and filaments occupying $\sim 1-4\%$ of the ISM, with temperatures of $50-100$ K and densities $n_{\mathrm{H}} = 20-50$ cm^{-3} (Kulkarni & Heiles 1987). The main tracers are the mm-wavelength emission lines of CO and fine structure lines such as [C IV] at 157 microns together with the UV and optical absorption lines seen towards bright stars or quasars.

Warm phase - it is characterised by a blend of neutral and ionised gas with temperatures of about 10^{3-4} K. The warm neutral atomic gas occupies $\sim 30\%$ of the volume of the ISM and is located mainly in photodissociation regions on the boundary of H II regions and molecular clouds. This medium has a temperature between $6000 - 10,000$ K and density $n_H \sim 0.2 - 0.5$ cm^{-3} (Kulkarni & Heiles 1987). It is traced by H I 21 cm emission lines.
The warm ionised gas ($T \sim 8000$ K) is photoionised by the UV emission from hot O and B stars. It shows a large range of densities. In particular, dense regions, with $n_H \sim 10^4$ cm^{-3}, are found in H II regions surrounding young hot stars or in planetary nebulae, formed around stars with a large mass loss. Globally, 90% of the Galactic ionised hydrogen mass is contained in photoionised diffuse regions with a density of ~ 0.1 cm^{-3} (Reynolds 1986). The warm ionised gas is traced by low-surface brightness Hα emission and radio recombination lines.

Hot phase - it consists of highly ionised gas with a temperature higher than $10^{5.5}$ K. Gas at this temperature floats in the Galactic gravitational field and has a thermal scale-height of several kpcs. It is likely produced by supernovae explosions and stellar winds from early-type stars, heating and accelerating cold and warm H I by shocks. This gas is generally found in collisional ionisation equilibrium and it shows high-ionisation states as O VI and higher. This component is also known as coronal gas because its physical state is very similar to the one found in stellar coronae. The hot medium has very low density, $n_H < 0.007$ cm^{-3} occupying possibly $\sim 20 - 70\%$ of the interstellar space (Ferrière 2001). This hot gas is often buoyant and appears as bubbles, chimneys and fountains high above the Galactic disc. Its primary tracers are the absorption lines seen towards hot stars in the far-UV in gas with $T \approx 10^5$ K, together with diffuse soft X-ray emission and absorption from gas hotter than 10^6 K. Moreover, the distribution of the O VI absorption line in the far-UV, suggests the existence of a conductive interface between the cool and hot gas where the bulk of the O VI is originated (Bowen et al. 2008).

1.2.2 X-ray spectroscopy of the interstellar gas

In the energy range $0.1 - 10$ keV, the photoelectric effect represents the main interaction between the X-ray radiation and matter. Compton scattering starts to be important beyond 10 keV for all the elements. In Figure 1.2 we illustrate the expected cross-section per atom for a plasma using the protosolar abundances of Lodders (2010). The photoelectric effect is due to the transfer of energy from the X-ray radiation to an electron. In particular, an atom absorbs the photon and ejects an electron with kinetic energy equal to that of the photon minus the binding energy of the electron.
The photoelectric cross-section varies as a function of energy and atomic number Z of the material, $\sigma_{\mathrm{pe}} \propto E^{-3} Z^n$, where n is a number between 4 and 5 (Davisson 1965). High-Z materials show a better capability to absorb X-ray radiation. Although the probability of the photoelectric absorption of X-ray photon decreases, in general, with increasing photon

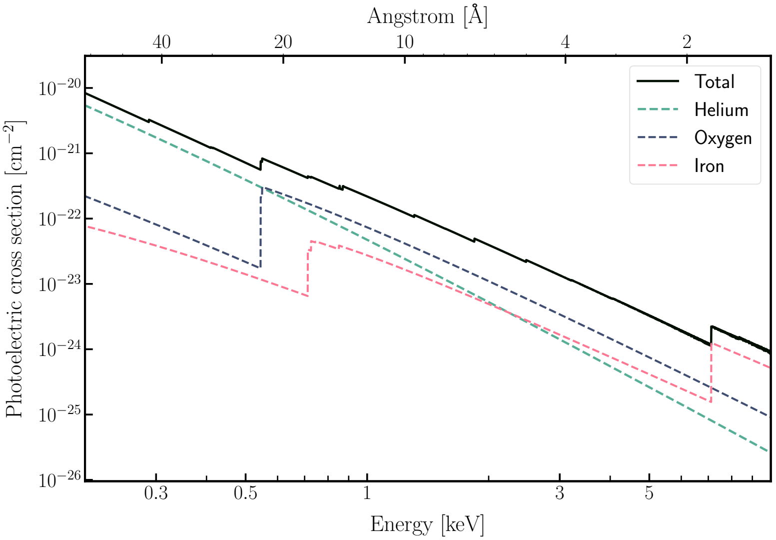

Figure 1.2: Photoionisation cross-section per H atom calculated using the Lodders (2010) abundances (black solid line). The helium (green dashed), oxygen (blue dashed) and iron (pink dashed) contributions are also indicated.

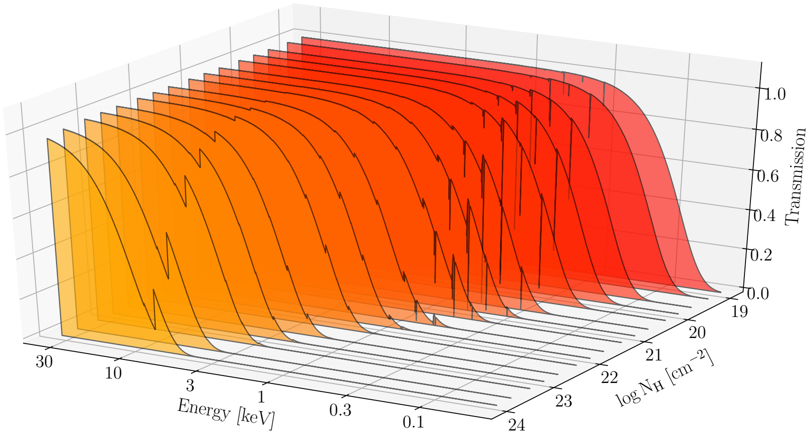

Figure 1.3: Transmission curves for different values of hydrogen column densities.

energy, there are sharp discontinuities in the cross section curve. These usually referred to as absorption edges and they correspond to the binding energies of electrons from atomic shells. The X-ray energy band contains almost all the K-edges (1st electron shell) and L-edges (2nd electron shells) transitions of the most abundant elements from carbon to nickel.

The transmission of X-rays across the ISM is defined as $T = e^{-\sigma_{\rm pe} N_{\rm H}}$, where $N_{\rm H}$ is the relative hydrogen column density of a particular line of sight. X-ray spectroscopy probes a large range of column densities. The cold interstellar absorption radically affects the shape of the background source spectrum, especially in the low-energy band. Figure 1.3 shows how the transmission varies as a function of the hydrogen column density and the energy of the incident photons. Roughly, values of $N_{\rm H} \lesssim 5 \times 10^{21}$ cm^{-2} enable the study of the spectral feature below 1 keV. Instead, a column density of $N_{\rm H} \gtrsim 5 \times 10^{21}$ cm^{-2} guarantees enough optical depth ($\tau = \sigma_{\rm pe} N_{\rm H}$) to probe the spectral feature in the absorber above 1 keV.

The XMM-*Newton* and *Chandra* satellites enabled the first dedicated studies of the ISM through X-ray absorption spectroscopy (e.g., Pinto et al. 2010). The absorption edges detected in the X-ray spectra of background sources allow the study of the abundances and depletion of the most important elements, such as oxygen, neon, iron, silicon and magnesium, present in the cold phase of the ISM (Juett et al. 2004; Pinto et al. 2013). High (low) ionisation lines, such as O VII, O VIII, and Ne IX (O II, O III, Ne II, and Ne III), permit, instead, the investigation of the gas in the hot (warm) medium (Yao & Wang 2005; Juett et al. 2006). For several sightlines, it is possible to study the multiphase structure of the ISM through high-resolution X-ray spectroscopy of the cold, warm, and hot phases (Yao & Wang 2006; Costantini et al. 2012).

1.3 Interstellar dust

Interstellar dust is coupled to gas clouds of the Milky Way. These clouds come in a vast variety of shapes, sizes, densities and temperatures. They can, however, be qualitatively classified in two wide categories: diffuse clouds and molecular clouds. Diffuse clouds are limited in density to less than about 1000 hydrogen atoms per cubic centimetre and are at a temperature of 50 – 100 K. Molecular clouds can have kinetic temperatures as low as 20 K and density higher than 1000 cm^{-3}, sufficient for the cloud to collapse and form stars. Diffuse clouds contain hydrogen in atomic form while molecular clouds are dominated by molecular hydrogen (Whittet 2002).

The evolution of dust is intimately associated with that of stars, because at almost every stage of their evolution, stars interact with dust (Jones 1997). The life cycle of interstellar dust is illustrated in Figure 1.4. Dust is thought to condensate in the atmosphere of evolved stars, in their Asymptotic Giant Branch (AGB) phase, and consequently ejected in the interstellar space. Other significant sources of interstellar dust are supernovae, both type Ia and core-collapse, young stellar objects, red supergiants, Wolf-Rayet stars and planetary nebulae (Jones 1997; Tielens 2001). The contribution of supernovae is uncertain since the fresh dust grains can be destroyed by fast shock waves generated by the supernova explosion. The destruction efficiency of this shock is still debated (Slavin et al. 2015; Micelotta et al. 2018, and references therein).

Once ejected in interstellar space, dust rapidly mixes with the ISM and will cycle many

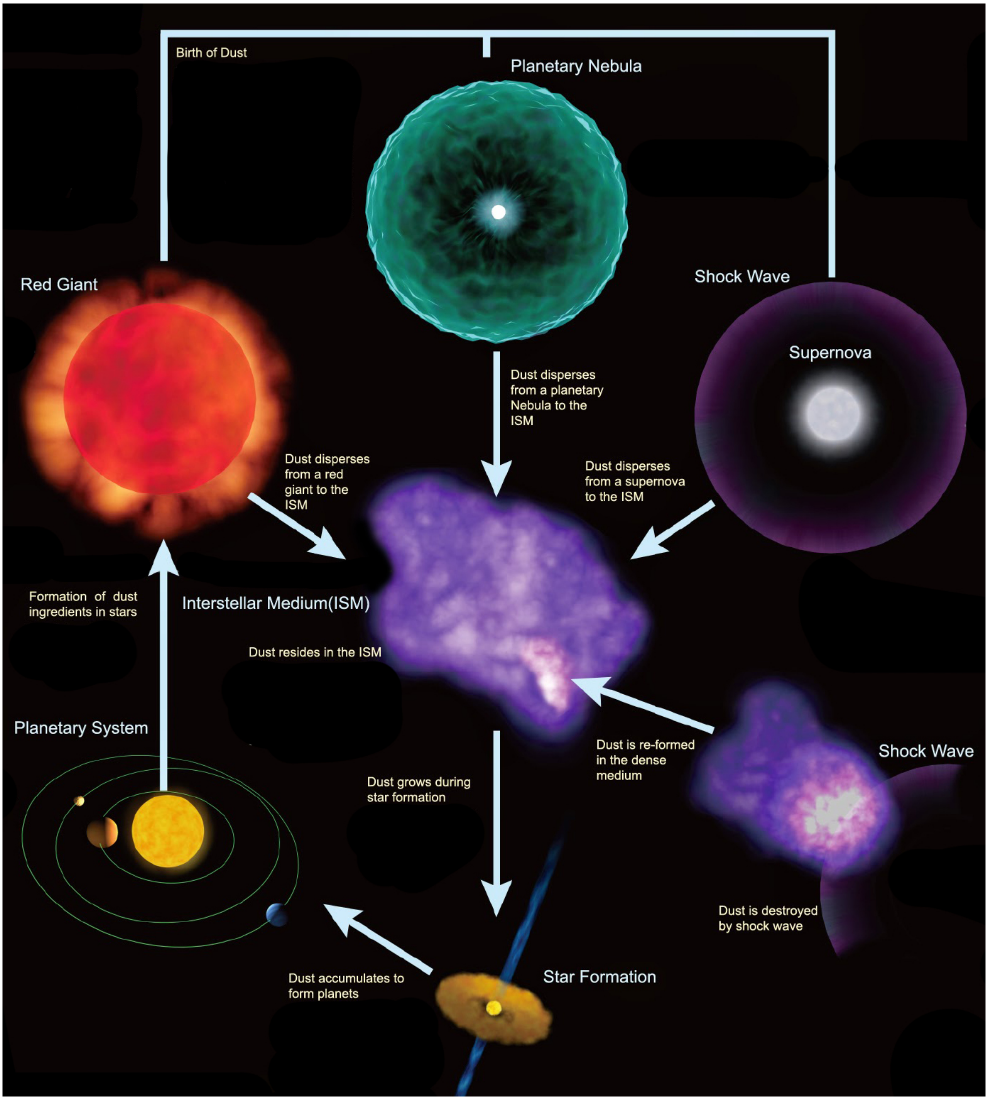

Figure 1.4: The life cycle of cosmic dust. Credits: Francisca Kemper, Hirashita Hiroyuki, ASIAA (adapted).

times between the cloud and the intercloud phase on a fast timescale ($\approx 10^7$ years, Tielens et al. 2005). In these recurrent cycles, the cosmic dust is subject to both growth and destruction processes which affect the size of the grain (Zhukovska et al. 2018). The dust size distribution is, indeed, a balance between the formation and destruction processes that operate in the ISM. Growth processes such as nucleation, condensation, accretion and coagulation are present in the diffuse medium and in denser regions such as diffuse clouds

(Draine 2009). Destructive processes such as sputtering by gas atoms, and shattering and energetic grain-grain collision, generally occur in the low-density interstellar gas (e.g., Dwek & Scalo 1980; Jones & Nuth 2011). Here, the dust is shattered by shock waves arising from supernovae and from stellar winds.

The supernovae shocks, together with stellar winds, collisions between clouds and turbulence, can also cause an instability in the cloud which may lead to compression of the cloud into a denser and colder cloud. Dust can also heat the gas through the photoelectric effect on grains, causing them to become charged. Subsequently, the cloud might become dense enough for dust grains to shield the interior of the cloud from optical and UV radiation, allowing molecules to form (van Dishoeck 2014). Dust may act as a coolant for the gas in the case where the surrounding gas has a higher temperature than the dust grain, causing the cloud to cool down further and compress (Galli et al. 2002; Li et al. 2003).

In a dense and cold cloud, large interstellar grains can form by a coagulation process in which small grains accrete onto large grains (Kim & Martin 1996). Moreover, layers of ice can form and coat the refractive grains. The mantles are composed, for the most part, of species formed by surface reactions and these reactions open up new pathways to molecule formation that are not possible in the gas phase (Whittet et al. 1997; Pontoppidan et al. 2004).

The destiny of dense clouds is gravitational collapse, forming one or multiple stars. Dust plays an important role as the building blocks in the formation of planets inside the protoplanetary discs which surround the young stars. The densities are so high in these systems that dust grains collide, sticking together, and quickly growing to the size of pebbles, rocks, or even planetesimals. When finally a newborn star has cleared its surroundings, a new planetary system emerges. Elements will be created through nucleosynthesis in the cores of stars that ultimately will end up in dust grains as soon the star ages. Thus, the whole process will start again.

Cosmic dust is omnipresent in the Universe and it can be observed everywhere: in our solar system (Altobelli et al. 2016), around young stars (Waters & Waelkens 1998), in giant clouds (Reddish 1971), in the Galaxy (Trumpler 1930), but also in distant galaxies (Hughes et al. 1998). High-redshift galaxies can contain a surprisingly large amount of dust, suggesting that dust can rapidly and effectively form in the early stage of the Universe (Watson et al. 2015). Therefore, understanding the dust formation process can give some hints regarding the evolution of the Universe (e.g., Dwek & Cherchneff 2011).

1.3.1 Dust properties

In order to develop accurate interstellar models, it is important to understand the properties of dust such as its chemical composition, size distribution, crystallinity. Here, I will describe some properties of the dust derived so far, mainly from infrared spectroscopy of dust in the Galaxy.

Composition of interstellar dust

The combination of abundances and depletions (which refers to the underabundance of a gas-phase element with respect to its standard reference abundance) in the ISM suggests that the cosmic dust consists mainly of carbon, oxygen, magnesium, silicon and iron. In addition to these elements, less abundant, but highly depleted elements, such as titanium, calcium, nickel, and aluminium can also be present in cosmic dust especially embedded in the refractory core of the grains (Jenkins 2009).

The composition of interstellar dust can be identified using more direct methods, such as identification through infrared spectroscopy of circumstellar or interstellar dust and through studies of pre-solar dust grains recovered from meteorites or interplanetary dust particles.

Cosmic dust is conventionally divided into two main groups, namely silicates and carbonaceous dust, with the addition of oxides (e.g., MgO, Fe_2O_3, SiO_2), silicon carbides (SiC) and metals (Draine 2011).

Silicates are assumed to be a major constituent of dust. This is supported by infrared spectroscopy observations, in particular through the features at ~ 10 μm and ~ 18 μm due to the Si-O bond stretching and O-Si-O bonds bending, respectively (Woolf & Ney 1969; Treffers & Cohen 1974). This is also confirmed by X-ray spectroscopy of cosmic dust (Zeegers et al. 2017, 2019, see also Section 1.3.2). Both spectroscopy techniques allow investigating which species of silicates may be present. The ratio of pyroxene, $(\mathrm{Mg,Fe})\mathrm{SiO_3}$, over olivine, $(\mathrm{Mg,Fe})_2\mathrm{SiO_4}$, is uncertain as well as the Mg to Fe ratio within a certain silicate (Chiar & Tielens 2006; Min et al. 2007).

Carbon is often mainly modelled by graphite (e.g., Draine & Lee 1984), which can undergo an amorphisation process and exist in the ISM in the form of (hydrogenated) amorphous carbon (Compiègne et al. 2011). Furthermore, smaller amounts of carbon can be locked up in nanodiamond particles (Tielens et al. 1987), polycyclic aromatic hydrocarbons (PAH, Tielens 2013) and fullerene (Ehrenfreund & Foing 2015).

Grain size distributions

The typical size of dust grains contains important information about their origin and evolution. The dust size distribution can reveal important information on the processes of dust production and destruction and on the efficiency of the dust growth in the ISM. In the literature there are several size distribution models, computed assuming different grain compositions and particle size ranges (Figure 1.5). All these size distributions seem to agree that most of the dust mass is included in large grains, while the surface area is dominated by smaller grains. The size distribution model can be constrained by studying the dust extinction at a different wavelengths. The extinction at a certain wavelength depends on the typical dust size. For instance, small grains ($a \sim 0.001$ μm) dominate the extinction in the UV, while large grains ($a \sim 0.25$ μm) are responsible for the extinction in the near-infrared. These grain models have to be able to reproduce not only the shape of the extinction curve but also the observed depletion of elements from the gas phase. In particular, the carbon budget represents a challenge (Draine 2009).

Mathis, Rumpl, & Nordsieck (1977) developed a size distribution model (MRN) for average diffuse clouds that consists of two separate dust grains components, namely bare spheri-

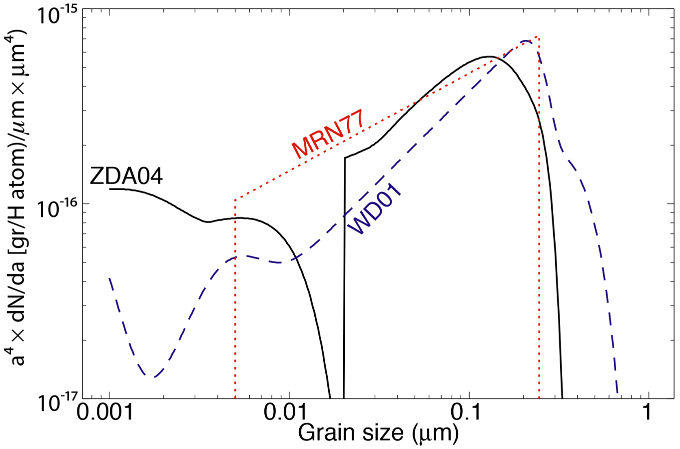

Figure 1.5: Comparison of different grain size distributions computed by Mathis, Rumpl, & Nordsieck (1977) (red dotted line), Weingartner & Draine (2001) (blue dashed line) and Zubko, Dwek, & Arendt (2004) (black solid line). Figure adapted from Smith et al. (2016a).

cal silicates and small graphite grains. The MRN size distribution is given by: $n(a)da = A \cdot a^{-3.5}\, da$, where $n(a)$ is the number of grains, and A is the normalisation constant which depends on the type of dust. Particle sizes range between 0.005 μm $< a <$ 0.25 μm. More sophisticated size distributions consider more complex grain compositions and non-spherical geometries (e.g., Weingartner & Draine 2001; Zubko et al. 2004; Draine & Li 2007; Hoffman & Draine 2016).

1.3.2 X-ray spectroscopy of interstellar dust

X-ray absorption fine structure (XAFS) represents a powerful, and relatively simple, way to determine the chemical composition of condensed matter. This dust fine structure characterises the band beyond the energy threshold of the absorption edges. When an incoming X-ray photon encounters a dust grain it can be absorbed by an atom in the dust particle. The ejected photon-electron behaves like a wave as shown in Figure 1.6. For an isolated atom, the absorption probability is a smooth function above the edge as shown in panel (a). In condensed matter, the ejected photo-electron scatters from neighbouring atoms. Due to a phase shift associated with the scattering event, the outgoing and scattered waves interfere. This interference at the absorbing atom varies with energy, causing the oscillation in the absorption probability, in particular in the post-edge region as shown in panel (b). The XAFS are usually divided into two main regimes: the X-ray absorption near-edge (XANES) which extends from about 5 to 10 eV below the edge threshold energy to about 50 eV above the edges; and the extended X-ray absorption fine structure (EXAFS), which extends from $\sim$ 50 eV above the edge energy to some hundreds eV (Newville 2004).

XAFS is suitable to study the chemistry and crystallinity of the cosmic dust. The fine

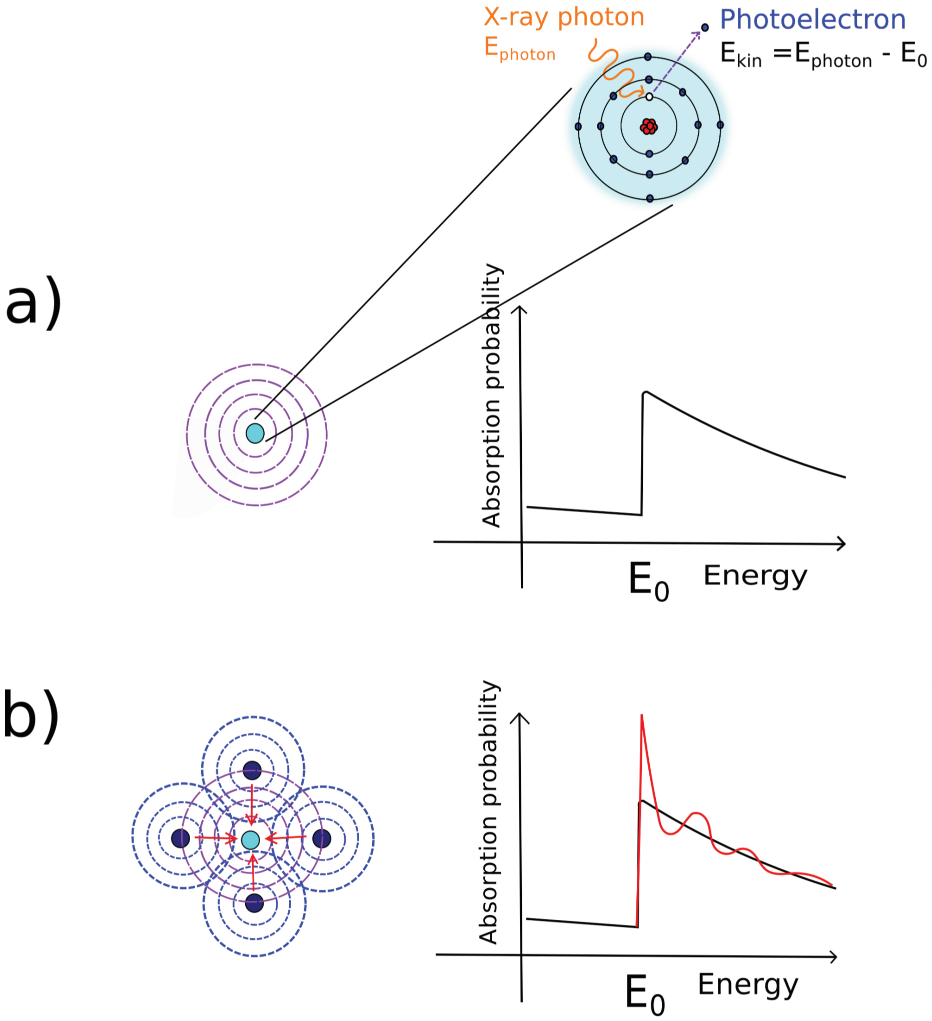

Figure 1.6: Photoelectric absorption of an X-ray photon with an emission of a core-level electron. (*a*) In case of a single absorbing atom, the absorption probability shows a smooth edge. The electron-wave produced by the photoelectric absorption is free to propagate without interruption. (*b*) On the other hand, if the absorbing atom is included in a solid, the electron-wave is back-scattered by the surrounding atoms. The interference between the energy waves modulates the post-edge of the absorption probability, imprinting the XAFS above the edge. Credits: Sascha Zeegers

structure pattern is sensitive to the nature and position of the surrounding atoms. Thus, the specific structure of the XAFS is determined by the chemical composition and level of crystallinity of the condensed matter. The small panel of Figure 1.7 shows a set of three absorption measurements of compounds with different crystalline structures and different compositions.

1.4 X-raying the Galaxy

The possibility of observing the XAFS of interstellar grains through high-resolution X-ray spectroscopy was initially discussed by Martin (1970) and Evans (1986). Thanks to the then new X-ray satellites, XMM-*Newton* and *Chandra*, Lee et al. (2002) detected for the first time dust fine structures in the X-ray spectrum of the bright microquasar GRS 1915-258. They observed residuals in the region of the absorption edge, which they concluded to be the traces of interstellar dust absorption. At that time, it was not possible to characterise them since a proper X-ray extinction model was not available. Literature data of XAFS did not include measurements tailored for astronomical purposes. The lack of available models led to the start of laboratory measurement campaigns to create an adequate database of models for characterising the XAFS observed with XMM-*Newton* and *Chandra* (Lee & Ravel 2005; Lee et al. 2009; Costantini & de Vries 2013).

In this section, I briefly describe the dust extinction models that I helped to develop in order to study the X-ray absorption of interstellar dust. Moreover, I present the technique and the statistics used to detect and to analyse the spectral features imprinted by the ISM in spectra of bright X-ray sources.

1.4.1 Laboratory extinction cross-section model

The X-ray Interstellar Dust Extinction (XRIDE) model is the first broadband model for investigating the absorption and scattering of cosmic dust. At the time of writing, the model is in the process of being finalised but it has already shown its potential in the study of the cosmic dust (see Zeegers et al. 2017, 2019, and Chapters 3 and 4). The model has been developed by our group led by Elisa Costantini at SRON, in The Netherlands. The model consists of a large collection of extinction curves for different dust analogues, mainly silicates, oxides, and sulphides.

In Figure 1.7, I illustrate the broadband extinction model with all the edges analysed so far. Different measurement techniques have been used to measure the XAFS. For edges at energies beyond 1 keV (e.g, the Mg, Si, Al, S, Fe K-edges) synchrotron radiation, both in transmission and fluorescence configuration, is widely employed. Edges located at energies below 1 keV (e.g, the Fe L- and O K-edges) are measured using an electron microscope through the electron energy loss spectroscopy (Egerton 2009).

The model is based on the refractive index obtained from the laboratory absorption measurements and the Kramers-Kronig relations (see Bohren 2010; Watts 2014, for a review). The optical constants are used to derive the extinction efficiency which is computed adopting the anomalous diffraction theory (van de Hulst 1957). Finally, to obtain the total cross sections as a function of energy, the extinction efficiency is integrated over the particle size

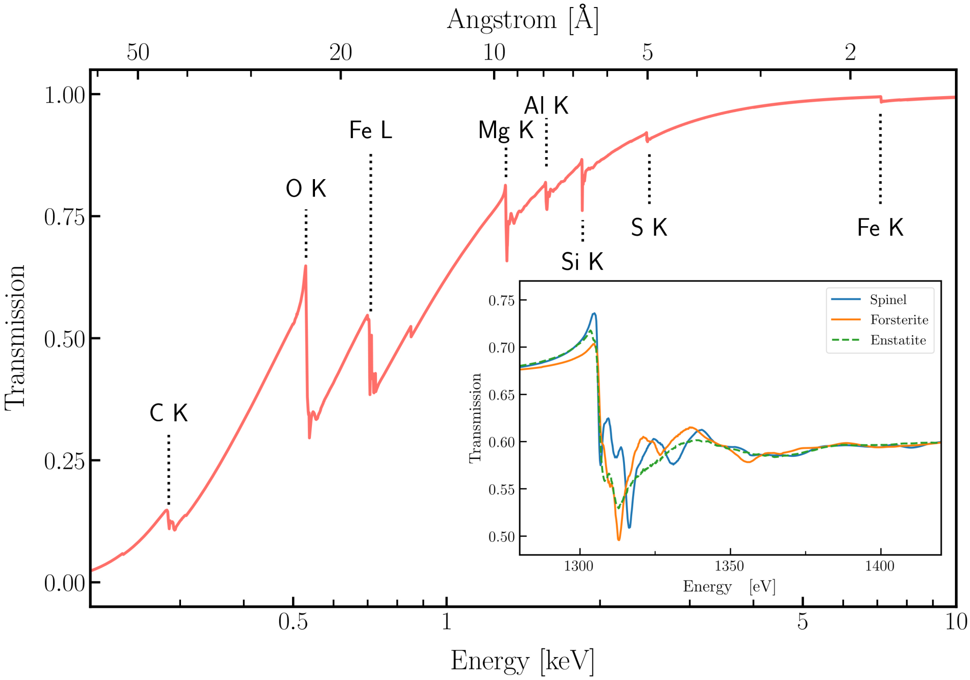

Figure 1.7: Illustrative XRIDE model in transmission for an arbitrary hydrogen column density. In the small panel is represented the zoom in of the magnesium K-edge. We compare the transmission K-edge of crystalline spinel (blue solid line), crystalline forsterite (orange solid line) and amorphous enstatite (green dashed line).

distribution. The size distribution has an important effect on the resulting extinction model, shaping the pre-edge regions differently (for details see Corrales et al. 2016; Zeegers et al. 2017). Therefore, the final extinction models are sensitive to the adopted size distribution and they can be used to investigate the dimension of the cosmic grains in different environments of the Galaxy. The models are now implemented into the SPEX X-ray fitting code (Kaastra et al. 2018).

Summarising, these new extinction models are a unique tool to probe the properties of the interstellar dust. Through the analysis of the XAFS, it is possible to probe the chemical composition and crystallinity of the dust whereas the pre-edge shape enables the study of the size distribution of the cosmic grains.

1.4.2 Observations

Low-mass X-ray binaries represent a suitable class of background sources for studying the absorption of the ISM. Typically, they are persistent bright X-ray sources and their spectra are usually not contaminated by the companion star activity. The large fluxes in the 0.1-10

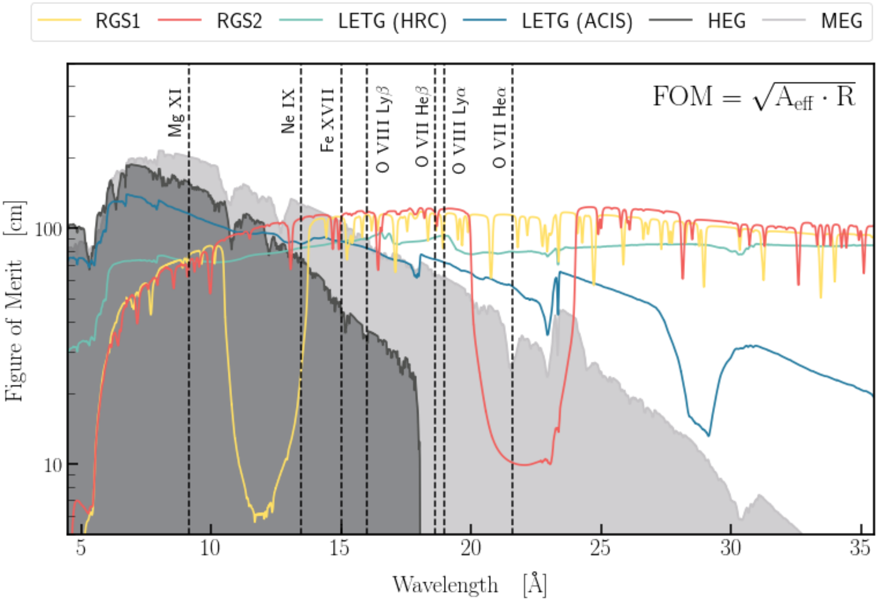

Figure 1.8: Line detection figure of merit (FoM) of RGS/XMM-*Newton*, HETGS/*Chandra* (both HEG and MEG) and LETGS/*Chandra*.

keV ensure a high signal-to-noise necessary to characterise the XAFS and the ISM absorption lines. Moreover, they are often distributed along the Galactic plane where the absorption of interstellar matter becomes significant, especially in the vicinity of the Galactic bulge. Bright X-ray binaries enable, therefore, to map the chemical and physical properties of the dust in different environments of the Galaxy. Moreover, through the study of X-ray absorption of these sources, it is possible to investigate directly the abundances and depletions of several metals in the inner part of the Galaxy and therefore to characterise the metallicity, even in the vicinity of the Galactic Centre (Zeegers et al. 2019).

The study profits from the large amount of archival data of *Chandra* and XMM-*Newton* collected in the last two decades. *Chandra* carries two high spectral resolution instruments, namely the High Energy Transmission Grating (HETG, Canizares et al. 2005) and the Low Energy Transmission Grating (LETG, Brinkman et al. 2000). The HETG consists of two grating assemblies, the high-energy grating (HEG) and the medium-energy grating (MEG). The energy resolution of the HEG, MEG and LETG are 0.012, 0.023, 0.05 Å (FWHM), respectively. On the other hand, XMM-*Newton* carries behind the multi-mirror assemblies two Reflection Grating Spectrometers (RGS, den Herder et al. 2001). The energy resolutions of the two instruments, RGS1 and RGS2, are on average 0.06 Å and 0.07 Å. In Figure 1.8 I show the capabilities of these spectrometers to detected the ISM spectral features present in the 0.1-10 keV. I indicate with a vertical dashed line the location of the main spectral features relevant for the present work.

1.4.3 Statistics for data analysis

In the last decades, the historically old Bayesian approach to statistics (Bayes 1763) has rapidly grown in popularity in several astrophysics fields such as cosmology (Trotta 2008) and exoplanets (Ruffio et al. 2018). The increased computer power enabled the feasibility of several computationally intensive statistical algorithms adopted for parameter estimations such as MultiNest and `emcee` (Feroz et al. 2009; Goodman & Weare 2010; Foreman-Mackey et al. 2013). These algorithms are very flexible and can be used to fit models over the data. The first use of the Bayesian data analysis in high-resolution X-ray spectroscopy was made by van Dyk et al. (2001). In their work, they showed how Bayesian methods can provide practical solutions for fitting low-count spectra or complex hierarchical structures inherent in the collection of high-quality spectra. Moreover, the Bayesian approach does optimisation and error estimation simultaneously using a parameter inference and error analysis. The goal in Bayesian parameter estimation is to identify sub-volumes which constitute the bulk of the probability integral over the parameter space. Finally, the Bayesian evidence provides a solid model comparison for both nested and non-nested models.

The Bayesian framework can be used to model the absorption of the ISM. In Chapter 2, I present a new tool which integrates the nested sampling algorithm MultiNest with the Spex fitting software. Similar work has been done previously by Buchner et al. (2014) for the XSpec spectral-fitting program. This approach works perfectly for the characterisation of the broadband model and the study of the absorption features present in the spectra of X-ray sources.

1.5 Future prospects

Instrumental capabilities have played a major role in the assessment of the physical properties of the gas and the dust over the past decades. Despite the great discoveries which were only made possible with the advent of *Chandra* and XMM-*Newton*, there are yet fundamental questions to be answered. Where is the iron in the interstellar medium? How much is the sulfur content in interstellar dust? What is the level of crystallisation in cosmic grains? What is the connection between the cold and hot phase, crucial for understanding the Galaxy formation and evolution? How is the hot coronal gas distributed in the Galaxy? For the next few years, X-ray astronomy will rely on the current flying observatories. Both XMM-*Newton* and *Chandra* are expected to operate for another decade, although the sensitivity of the *Chandra* Observatory is progressively degrading at energies $\lesssim 1$ keV. Deeper observations of dedicated lines of sight can improve the detection of the spectral features.

In the long term, a breakthrough in X-ray astronomy is expected with the next generation X-ray observatories. Below, I describe some of the highlights of future X-ray missions.

The X-ray Imaging and Spectroscopy Mission (*XRISM*, expected launch in 2021) is the successor of *Hitomi*. Following a successful launch in February 2016, the JAXA/NASA X-ray collaboration satellite *Hitomi* was unexpectedly lost shortly after. The two instruments onboard XRISM will be a soft X-ray calorimeter spectrometer, *Resolve*, and a soft X-ray imager, *Xtend* (Tashiro et al. 2018). *Resolve* will provide a non-dispersive 5 eV energy resolution in the 0.3-12 keV bandpass. Detailed studies of absorption edges of sulfur and iron will be possible for the first time (Chapter 5 and Costantini et al. 2019).

Athena is the flagship mission of ESA expected to launch in 2031 and will provide a giant leap on the understanding of the X-ray Universe (Nandra et al. 2013). The superb capabilities of *Athena* are based on its large effective area, while retaining a spectral resolution of 2.5 eV over a broad X-ray band ($0.3 - 10$ keV, Barret et al. 2016). From a spectral point of view, the high sensitivity over this large X-ray energy band will enable to study in details not only the edges of heavy elements such as iron but also the edges of less abundant elements, such as aluminium and calcium (Chapter 5 and Costantini et al. 2019). With *Athena* the study of the XAFS and the absorption lines will be possible also for fainter X-ray sources, enabling a finer sampling of lines of sight in the Galaxy.

Finally, there are two mission concepts currently under study. The first is *Arcus*, a high-resolution X-ray grating spectrometer mission proposed by NASA (Smith et al. 2016b). The spectrometer is expected to achieve an unprecedented resolution R=3000 over soft X-ray energy bandpass ($\sim 0.2 - 1$ keV). This would enable the study of the ISM even at low column densities, resolving high-ionisation lines of oxygen, neon and iron into all their kinematic components, similarly to what achieved nowadays with UV data. *Arcus* will also detect in great detail the XAFS of the carbon K-, iron L-, and oxygen K-edges. The second mission concept is *Lynx*, a satellite consisting of a high-definition X-ray imager, an X-ray microcalorimeter and an X-ray grating spectrometer (Gaskin et al. 2019). With the enormous capability expected for *Lynx*, it will be possible to probe the interstellar heavy elements in both gaseous and solid form over a broad range of ISM column densities (The Lynx Team 2018).

1.6 Thesis content

This thesis is focused on the study of the hot coronal gas and the properties of the interstellar dust in dense Galactic environments. The study of these components is of extreme importance to understand the physical processes present in the Galaxy. The models developed here aim to uncover the physical and chemical properties of the cosmic grains. They also set the path for future missions, which will allow these methods to be routinely used for mapping the interstellar matter in great detail. In this direction, the novel Bayesian inference tool will facilitate the analysis of the features detected in high-resolution X-ray spectra through the SPEX spectral fitting program.

In Chapter 2, I present a detailed study of the high-ionisation absorption lines observed in the spectrum of the ultra-compact binary 4U 1820-30. Previous works showed how these features can be represented by a photoionised gas associated with the atmosphere of the disc or by the foreground hot coronal gas. To define the nature of the absorber, I use two broadband models which allow constraining the ionisation state, temperature and kinematics associated with the ionisation lines. Applying the Bayesian data analysis to the extensive XMM-*Newton* and *Chandra* observations of the source, I determine the interstellar origin of the high-ionisation lines. The detected Fe XVII line can only be produced by a gas in a collisional ionisation equilibrium state, typical for the hot coronal gas.

The main part of the thesis is focused on the modelling of the absorption and scattering of dusty matter. This is done through the study of the XAFS imprinted on the spectra of background X-ray sources. Accurate extinction models of the absorption edges are fundamental to retrieve the information contained in the dust fine structures. In Chapter 3, I present the extinction models for the magnesium K-edge based on newly acquired synchrotron measurements. The sample-set consists of silicate, both pyroxene and olivine, with different magnesium and iron content and different level of crystallinity. Moreover, I calculate the extinction cross-sections for dust grains with different size distributions. Considering also the models for the silicon edge calculated by Zeegers et al. (2019), I analyse the magnesium and silicon fine structure present in the spectra of GX 3+1, a bright low-mass X-ray binary. Through the simultaneous fit of the two edges, I am able to constrain the properties of the interstellar silicates found along the line of sight.

In Chapter 4, I expand the study presented in Chapter 3 to several lines of sight of bright low-mass X-ray binaries extensively observed with *Chandra*. The goal is to map the properties of the interstellar dust along with the Galactic disc, especially close to the Galactic bulge. This is a well-processed and mixed environment of the Galaxy, which might influence the chemistry and the size of the cosmic grains. Moreover, by exploiting the capability of X-rays to go through dense regions, I am able to constrain the abundances and the depletion of magnesium and silicon in the inner part of the Galaxy. I also analyse the cosmic dust present along the line of sight towards LMC X-1, a bright X-ray source in the Large Magellanic Cloud.

Finally, in Chapter 5, I calculate the extinction models for the Fe K-edge, which is located at 7.1 keV. In this high energy band, the resolving power of current X-ray telescope dramatically degrades, making the detection of this feature impossible. The iron K-edge has a great potential for investigating the properties of interstellar dust along extremely absorbed sightlines. It is indeed the only main feature detectable in spectra with column density larger than 10^{23} cm^{-2}. In this work, I show the potential of future X-ray missions (*XRISM* and *Athena*) together with the new dust extinction models to reveal the missing iron in the ISM.

2

The hot interstellar medium towards 4U 1820-30: a Bayesian analysis

D. Rogantini, E. Costantini, M. Mehdipour, P. Ranalli, L.B.F.M. Waters

To be submitted to Astronomy & Astrophysics

Abstract

High ionisation lines in the soft X-ray band are generally associated to either interstellar hot gas along the line of sight or to photoionised gas intrinsic to the source. In the low-mass X-ray binary 4U 1820-30, the nature of these lines is not well understood. We characterised the ionised gas present along the line of sight towards the source producing the X-ray absorption lines of Mg XI, Ne IX, Fe XVII, O VII, and O VIII. We analysed all the observations available for this source in the XMM-*Newton* and *Chandra* archives, taken with the HETG, LETG, RGS spectrometers. The high-resolution grating spectra have been accurately examined through a standard X-ray analysis based on the C-statistic and through the Bayesian parameter inference. We tested two physical models which describe a plasma in either collisional ionisation or photoionisation equilibrium. We adopted the Bayesian model comparison to statistically compare the different combinations of the models used for the analysis. We found that the lines are consistent with hot gas in the interstellar medium rather than being associated to the intrinsic gas of the X-ray binary. Our best-fit model reveals the presence of a collisionally ionised plasma with a temperature of $T = 1.98 \pm 0.05 \times 10^6$ K. The photoionisation model fails to fit the Fe XVII (which is detected with a significance of 4.4σ) due to the low column density predicted by the model. Moreover, the low inclination of the binary system is likely the reason for the non-detection of ionised gas intrinsic to the source.

2.1 Introduction

In the space among the stars resides interstellar matter, a vast and heterogeneous mixture of atoms, molecules and solid dust grains. As a function of the temperature and density of the diffuse gas, the interstellar medium can be classified in three main phases (Ferrière 2001, and reference therein): *cold* phase ($T_{\rm ISM} < 100$ K and density, $n_{\rm H} = 10 - 10^6$ cm^{-3}), *warm* phase ($T_{\rm ISM} \sim 8000$ K and $n_{\rm H} = 0.2 - 0.5$ cm^{-3}, including both warm neutral and warm photoionised gases), and *hot* phase ($T_{\rm ISM} \sim 10^6$ K and $n_{\rm H} \sim 6.5 \times 10^{-3}$ cm^{-3}).

The existence of the hot interstellar medium (also known as hot coronal gas) in the Milky Way has been discovered through the detection of the soft X-ray background in the 0.1-1 keV energy range (Tanaka & Bleeker 1977) and through the UV O VI absorption lines in the spectra of OB stars (Jenkins 1978). The hot phase has been proposed to account for much of the missing baryons within the Galactic halo, and as a tracers of energetic feedback from stars and supernovae, which plays an important role in shaping the ecosystem of the Galaxy (McKee & Ostriker 1977; Miller & Bregman 2013).

In the past several years it has been demonstrated that the hot phase of the ISM can be effectively characterised through X-ray absorption line spectroscopy (e.g. Futamoto et al. 2004; Yao & Wang 2005; Wang 2010; Liao et al. 2013; Gatuzz & Churazov 2018). Through the measurements of absorption lines produced by various ions in the spectra of bright X-ray sources, primarily active galactic nuclei and X-ray binaries, it is possible to set physical constraints on ionisation process, temperature, kinematics, and chemical abundances of hot gas. It is also possible to study its distribution in both disc and halo of the Galaxy.

However, the interpretation of these high-ionisation absorption lines can be uncertain. Indeed, these features are not always clearly associated with the interstellar hot gas in a collisional ionisation equilibrium state. In some systems, they can be produced by an absorber intrinsic to the background X-ray source and photoionised by its strong radiation. The presence of multiple blueshifted and/or variable high-ionisation lines indicates a wind outflowing in our line of sight, in particular from the accretion disc of stellar mass black holes (e.g., Lee et al. 2002; Parmar et al. 2002; Ueda et al. 2004; Díaz Trigo et al. 2006). On the other hand, in dipping X-ray binaries, strong absorption lines that are local to the source are found not to be blueshifted and they are thought to be associated with the corona of the accretion disc (Sidoli et al. 2001a; Díaz Trigo et al. 2006). Therefore, for some sources, it might be difficult to discern if the presence of high-ionisation lines in the spectrum is associated with a collisionally ionised gas in interstellar space rather than with a photoionised absorber associated to the X-ray source. One example is the source that we analyse in the present work.

4U 1820-30 is a well known bright X-ray source in the Sagitarius constellation, first observed by the *Uhuru* satellite (Giacconi et al. 1972). This source is an accreting neutron star low-mass X-ray binary, residing in the globular cluster NGC 6624 at $(l, b) = (2^\circ.8, -7^\circ.9)$. The binary consists of an ultracompact system with an orbital period of ~ 11 min and size

$r = 1.3 \times 10^{10}$ cm (Stella et al. 1987). The companion has been identified with a He-white dwarf. The distance of 4U 1820-30 has been determined to be 7.6 ± 0.4 kpc (Kuulkers et al. 2003), thus it is very close to the Galactic centre. Consequently, our line of sight samples the entire inner Galactic disk radially to a height of ~ 1 kpc off the Galactic plane.

The soft X-ray band of 4U 1820-30 was demonstrated to be a useful tool to study simultaneously the different phases of the interstellar medium. In previous works, the cold phase has been studied through the oxygen, neon, and iron photoelectric edges detected in the high-resolution X-ray spectra (Juett et al. 2004, 2006; Miller et al. 2009). An accurate analysis of the oxygen K-edge and iron L-edges is performed by Costantini et al. (2012), hereafter C12, where they modelled the absorption by both cold gas and interstellar dust. The detection of low-ionisation lines[1], such as Ne II (14.608 Å), Ne III (14.508 Å), O II (23.351 Å), O III (23.028 Å) indicates the presence of a low-ionised gas towards 4U 1820-30 with a temperature of $\sim 5 \times 10^4$ K (Cackett et al. 2008; Costantini et al. 2012).

The presence of hot gas towards the source has been previously studied at length. Futamoto et al. (2004) clearly detected the O VII (21.602 Å), O VIII (18.967 Å) and Ne IX (13.447 Å) absorption lines in the spectrum of 4U 1820-30. A Gaussian fit to those lines provides estimates for the column densities through the curve of growth analysis. An important shortcoming of such method is that in the case of saturated or non-resolved lines, various possible line broadening effects influence the equivalent width of the line and hence the derived column density. To tackle this degeneracy, Yao & Wang (2005) constructed an absorption line model which includes ionisation equilibrium conditions. This model allows studying directly the physical conditions of the absorbing gas, such as temperature and ionic abundances.
Both Futamoto et al. (2004) and Yao & Wang (2005) associated these high-ionisation lines to interstellar hot gas under the assumption of a unity filling factor and that all the absorption arises from the same gas. Moreover, the absolute velocity has been found to be consistent with zero, ruling out the possibility of an outflowing gas.
Subsequently, Cackett et al. (2008) modelled the high-ionisation lines in the spectra of 4U 1820-30 using the photoionisation code XSTAR (Bautista & Kallman 2001) and they found that photo-ionisation can reproduce the observed lines well suggesting a photoionised absorber, possibly an atmosphere intrinsic to the accretion disc as a plausible explanation.

In the present work, we aim at investigating the origin of these high-ionisation absorption lines. In order to advance previous studies, we apply state-of-art plasma models of the SPEX code, with latest accurate atomic databases, to all the XMM-*Newton* and *Chandra* spectra of 4U 1820-30. We test a photoionisation model, a collisionally ionized model and combinations of them. We then analyse the X-ray spectra and compare the models through two different statistical approaches: the standard C-statistic (Cash 1979) and the Bayesian analysis (van Dyk et al. 2001; Gelman et al. 2013). The latter method carefully explores the whole parameter space inferring the most probable estimate of the model parameters.
The organisation of the paper is as follows: in Section 2.2, we describe the XMM-*Newton* and *Chandra* observations and our data reduction procedure. The broadband model of 4U 1820-

---

[1] For the wavelength of the lines we refer to Juett et al. (2006) and the SPEX atomic database Kaastra et al. (2018).

Table 2.1: Observation log of XMM-*Newton* and *Chandra* data used for our spectral modelling of 4U 1820-30.

Dataset	Obs. ID	Date	Exposure (ks)	Count Rate (cts s^{-1})	Instrument	Mode
			Chandra			
1	**98**	10/03/2000	15.0	37.7	LETG/HRC-S	-
2	**1021**	21/07/2001	9.6	84.3	HETG/ACIS	TE
	1022	12/09/2001	10.7	107.1	HETG/ACIS	TE
3	**6633**	12/08/2006	25.1	126.0	HETG/ACIS	CC
	6634	20/10/2006	25.0	174.0	HETG/ACIS	CC
	7032	05/11/2006	46.2	148.1	HETG/ACIS	CC
4	**12444**	08/03/2011	89.7	84.4	LETG/ACIS	CC
			XMM-*Newton*			
5	**008411**0201	09/10/2001	39.6	74.7	RGS	Spec. HER+SES
6	**055134**0201	02/04/2009	41.8	51.3	RGS	Spec. HER

30 is presented in Section 2.3. The ionised gas features are analysed and described in Section 2.4, where we also compare the two different models. In Section 2.5 we discuss the nature of the high-ionisation absorption lines seen in the spectra of the accreting source. The summary of the main results of this work is given in Section 2.6. All errors are measured at the 68% (1σ) confidence unless marked otherwise.

2.2 Observations and data reduction

4U 1820-30 has been observed by the grating spectrometers aboard on both *Chandra* and XMM-*Newton*. *Chandra* carries two high spectral resolution instruments, namely the High Energy Transmission Grating (HETG, Canizares et al. 2005) and the Low Energy Transmission Grating (LETG, Brinkman et al. 2000). The LETG can operate with either the Advanced CCD Imaging Spectrometer (ACIS) or the High-Resolution Camera (HRC), whereas the HETG can be coupled only with the ACIS. The HETG consists of two grating assemblies, the high-energy grating (HEG) and the medium-energy grating (MEG). The energy resolution of the HEG, MEG and LETG are 0.012, 0.023, 0.05 Å (FWHM), respectively. On the other hand, XMM-*Newton* carries behind the multi-mirror assemblies two Reflection Grating Spectrometers (RGS, den Herder et al. 2001). The energy resolutions of the two instruments, RGS1 and RGS2, are about 0.07 Å.

In the band of interest of high-ionisation lines, RGS, LETG and HETG have comparable resolving power but different instrumental characteristics. RGS and LETG present higher effective areas and a broader coverage in the softer bands (>15 Å), which are an optimal combination for detecting in one single observation the absorption lines of highly ionised atoms of multiple elements, such as, iron, oxygen, carbon and nitrogen. HETGS has better energy resolution for resolving narrow ionisation lines (e.g. Ne IX and Ne X). We model both HEG and MEG data. Our joint modelling of XMM-*Newton* and *Chandra* data enables us to better constrain all the high-resolution spectral components, and therefore better understand the nature and origin of hot gas towards 4U 1820-30. The synergy of these different grating instruments improves therefore quantitatively and qualitatively the analysis of the X-ray spectrum of 4U 1820-30.

The observations used in this work are displayed in Table 2.1. The XMM-*Newton* data reduction is performed using the Science Analysis System[2] (SAS, version 18.0.0). The earlier observation, obsID 008411, shows a flaring background, which is filtered out. This results in a cut of $\sim$ 3 ks on the total exposure time. The two RGS observations are taken in two different *spectroscopy mode* flavours: high-event-rate with single-event-reconstruction (HER+SES, for obsID 008411) and high-event-rate (HER, for obsID 055134).
We obtain the *Chandra* observations from the Transmission Grating Catalogue[3] (TGCat, Huenemoerder et al. 2011). We combine the positive and negative first-order dispersion of each observation using the Chandra's data analysis system (CIAO version 4.11, Fruscione et al. 2006). The two observations taken in 2001 in timed exposure (TE) mode, display similar fluxes and continuum parameters, therefore we stack the data, for the HEG and MEG arms using the CIAO tool `combine_grating_spectra`. Similarly, we combine the three observations taken in 2006 in continuous clocking (CC) mode. We fit with the same continuum model the HEG and MEG spectra of the same stacked data correcting them for the slightly different ($\sim$ 5%) instrumental normalization. Therefore, after the combination of the grating spectra, we obtain six different datasets as listed in the first column of Table 2.1.

During all the observations, the source is observed in high state with an average flux $F_{(2-10\ \mathrm{keV})} \sim 10^{-8}$ erg cm^{-2} s^{-1}. Because of this high flux, the observations are affected by pileup. This effect is particularly present in the *Chandra* observations taken in TE mode, changing the shape of the spectrum. We overcome this issue ignoring the region of the spectra (λ between 4 and 19 Å) most affected by pileup. At longer wavelengths ($\lambda > 20$ Å), the combined effect of high absorption and low effective area reduces significantly the observed flux. Thus, this region is unaffected by pileup and can be safely used. However, the narrow absorption features are in general minimally influenced by pileup.

2.3 Broadband spectrum

We fit the HETG, LETG and RGS data simultaneously using the SPEX X-ray spectral fitting package[4] (Version 3.05.00, Kaastra et al. 2018) with the C-statistic. Considering all the datasets, the observations cover the soft X-ray energy band between 4 and 35 Å ($0.35 - 3.10$ keV). Given that the source was observed at different epochs, the continuum shape may differ significantly. To take into account continuum variability, we assign each dataset to a specific `sector` in SPEX allowing the continuum parameters to vary freely for each sector. The broadband model with the cold and warm absorptions (described below) is fitted to the data using the C-statistic and it is displayed in Figure 2.1.

---

[2] https://www.cosmos.esa.int/web/xmm-newton/sas

[3] http://tgcat.mit.edu/

[4] http://doi.org/10.5281/zenodo.2419563

Table 2.2: Best-fit parameters of our model for the broadband spectrum of 4U 1820-30

data	`bb`	`comt`[a]		`hot` (cold) [b]	`hot` (warm)		$F_{0.5-2\ \mathrm{keV}}$	$F_{2-10\ \mathrm{keV}}$	Cstat/dof
	$k_{\mathrm{B}}T$	$k_{\mathrm{B}}T_0$	$k_{\mathrm{B}}T_1$	N_{H}	N_{H}	$k_{\mathrm{B}}T$	$[10^{-9}]$	$[10^{-9}]$	
	keV	keV	keV	10^{21} cm^{-2}	10^{19} cm^{-2}	10^{-3} keV	erg cm^{-2} s^{-1}	erg cm^{-2} s^{-1}	
RGS/XMM-*Newton*									
008411	0.164 ± 0.003	0.65 ± 0.08	24 ± 11	1.51 ± 0.03	0.9 ± 0.2	2.6 ± 0.3	2.2 ± 0.2	13 ± 2	**5642/3700**
055134	0.139 ± 0.004	0.32 ± 0.02	29 ± 9	1.56 ± 0.03	1.2 ± 0.3	2.8 ± 0.2	1.5 ± 0.3	5.4 ± 0.8	**5541/3921**
LETG/*Chandra*									
98	0.16 ± 0.01	0.40 ± 0.08	7 ± 5	0.08 ± 0.05	< 0.45	2 ± 1	1.8 ± 0.8	7 ± 1	**2070/1842**
12444	0.22 ± 0.01	1.9 ± 0.7	20 ± 9	1.4 ± 0.1	2.0 ± 0.9	4.6 ± 0.4	1.5 ± 0.7	27 ± 9	**1141/870**
HETG/*Chandra*									
2001 [c]	0.14 ± 0.04	0.20 ± 0.05	1.5 ± 0.2	1.1 ± 0.2	1.5 ± 0.9	4 ± 1	1.7 ± 0.2	4.9 ± 0.7	**7423/6628**
2006 [d]	0.07 ± 0.01	0.16 ± 0.02	9 ± 5	2.1 ± 0.1	1.2 ± 0.9	3 ± 1	2.3 ± 0.3	7.4 ± 0.9	**6304/4988**
Mean	0.15 ± 0.01	0.6 ± 0.2	15 ± 7	1.53 ± 0.08	1.4 ± 0.6	3.4 ± 0.6	1.8 ± 0.4	10 ± 2	**28123/21949**

(a) We fix the optical depth τ to its default value of 3.

(b) We fix the temperature at the lower limit 0.5 eV. In the cold phase we also consider the contribution of the dust.

(c) Combination of obsId (1021, 1022) taken in 2001.

(d) Combination of obsId (6633, 6634 and 7032) taken in 2006.

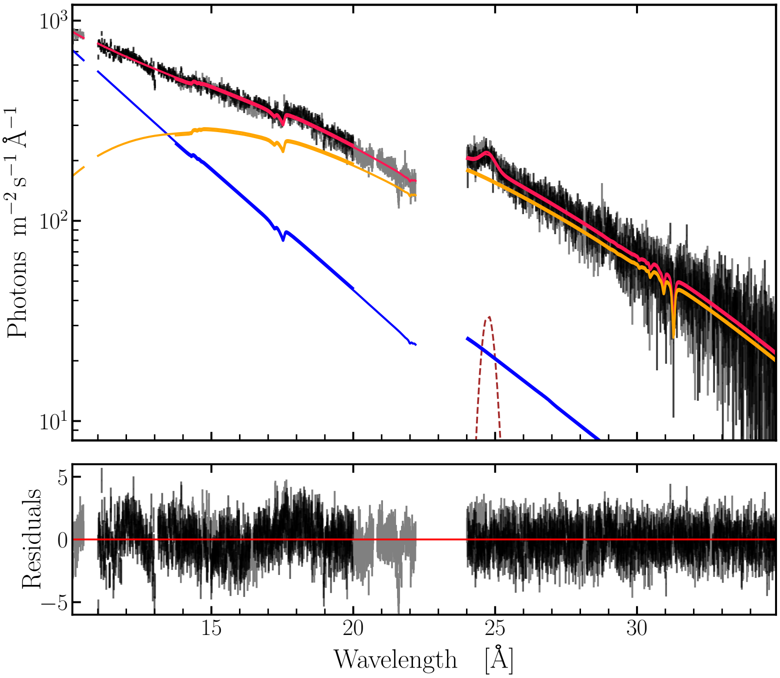

Figure 2.1: Broadband best-fit to the X-ray spectrum of 4U 1820-30 with warm and cold absorption described in Section 2.3. We display for clarity only RGS1 and RGS2 (in gray and black, respectively) of obsID 008411. We overlap the best model of the broadband spectrum (in red), which is made up of a Comptonisation model (in blue solid line) and a blackbody (in orange solid line). We also show the gaussian (in brown dashed line) added to the model in order to fit the possible instrumental bump in excess centred at 24.7 Å.

The source shows a Comptonised continuum together with soft black-body component (e.g., Sidoli et al. 2001b; Costantini et al. 2012), which we reproduce in our modelling using the `comt` and `bb` components in SPEX (Titarchuk 1994; Kirchhoff & Bunsen 1860, respectively). We first fix the absorption model by the neutral ISM gas. This is done by applying a collisionally ionised plasma model (model `hot` in SPEX, de Plaa et al. 2004; Steenbrugge et al. 2005) with a temperature frozen to $k_B T = 0.5$ eV in order to mimic the neutral gas. Continuum absorption by this neutral Galactic absorber takes into account most of the low-energy curvature of the spectrum especially for $\lambda \gtrsim 6$ Å ($E \lesssim 2$ keV). Due to the complexity of the oxygen K-edge region and to the uncertainties of its modelling we exclude from the fit the region extending between $22.2 - 24$ Å ($\sim 516 - 558$ eV). Modelling this complex edge is beyond the goal of this paper.

Two other photoabsorption edges are present in the spectrum of the source: the neon K-edge at $\lambda = 14.3$ Å (Gorczyca 2000) and the iron $L_{2,3}$-edges at $\lambda_{2,3} = 17.2,\ 17.5$ Å (Kortright & Kim 2000). While neon is expected to be only in gaseous form due to its inert nature, iron is highly depleted from the gaseous form (C12). To minimise the residual in the Fe L-edge band and to characterise the dust contribution, we add to our model the `AMOL` component (Pinto et al. 2010). In particular, we adopt the Fe L-edges of the metallic iron. Coupling the abundance of the dust among all the datasets, we find that $(92 \pm 4)\%$ of the iron is locked into interstellar dust grains.

The detection of the Ne II, Ne III lines at 14.608 Å, 14.508 Å (848.74 eV and 854.59 eV), respectively, traces the presence of low-ionised gas along this line of sight. Therefore, to describe these low-ionisation lines we add a second collisionally ionised plasma model to our broadband model.

The best fit parameters of the broadband continuum including the cold and warm absorption are shown in Table 2.2. The different fit of LETG obsID 98 might be caused by residuals at the metal edges, in particular the O K-edge, due to uncertainties in the *Chandra* response matrix Nicastro et al. (2005). Thus, the estimates of the hydrogen column densities are altered by these residuals and we do not consider them in the average computations. However, the high-ionisation absorption lines are not affected and we can reliably consider them in our analysis.

2.4 High-ionisation lines

The spectra of 4U 1820-30 display several high-ionisation lines: Mg XI (9.1688Å), Ne IX (13.447 Å), Fe XVII (15.012 Å), O VII (Heα at 21.590 Å and Heβ at 18.626 Å) and O VIII (Lyα at 18.967 Å and Lyβ at 16.005 Å). The effective area of RGS and LETG HRC should allow us to detect the absorption line of C IV located at 33.734 Å. However, since in this region the cold-gas absorption of the continuum is severe, the signal-to-noise ratio is too low to distinguish the feature.

These lines are produced by ionised plasma present along the line of sight of the source. To reveal the nature of this ionised gas we study the associated absorption features through two different physical models defined by us as *ism* and *photo* models:

ism model - To model the absorption by the hot coronal gas in the interstellar medium we use the collisionally ionised plasma model `hot` with a temperature above $10^{5.5}$ K ($E \gtrsim 0.05$ keV).

photo model - To investigate the occurrence of photoionised gas intrinsic to the binary, we adopt the `xabs` model in SPEX (Steenbrugge et al. 2003). The `xabs` model calculates the transmission through a slab of photoionised gas where all ionic column densities are linked in a physically consistent fashion through a photoionisation model. To compute the ionisation balance for the `xabs` model, we use the photoionisation model of SPEX, called `pion` (Mehdipour et al. 2016). For this calculation we adopt the spectral energy distribution (SED) of C12 and the proto-solar abundances of Lodders (2010). The `pion` calculations yield temperature and ionic column densities as a function of the ionisation parameter ξ (Tarter et al. 1969), which are used for fitting with the `xabs` model. The ionisation state of the absorber is measured through the ionisation parameter, which is defined as:

$$\xi = \frac{L_{\rm ion}}{n_{\rm H} r^2} \ ,$$

where L_{ion} is the source ionisation luminosity between 1 and 1000 Ryd, n_{H} the hydrogen density of the absorber and r its distance from the ionising source.

We fit the two models using two different approaches: the C-statistic, widely used in X-ray data analysis, and then the Bayesian parameter inference (Gregory 2005; Gelman et al. 2013). The C-statistic can have some difficulties to identify multiple, separate, adequate solutions (i.e. local probability maxima) in the parameter space. On the other hand, the Bayesian approach explores the entire parameter space identifying the sub-volumes which constitute the bulk of the probability. Moreover, it does optimisation and error estimation simultaneously, but requires large computation time depending on the number of free parameters. For each model, we evaluate the equivalent hydrogen column density (N_{H}), the flow- (v) and turbulence-velocities (σ_{v} or velocity dispersion) of the absorber together with the temperature ($k_{\mathrm{B}}T$) or the ionisation parameter (ξ), depending on the model.

2.4.1 C-statistic analysis

For each dataset, we apply separately the *ism* and *photo* models to the braodband continuum model. We constrain all the free parameters of the broadband fit to within 1σ uncertainties. We leave free to vary only the normalisations of the blackbody and Comptonisation components (see Section 2.2). Then, we fit the `hot` and `xabs` parameters separately for each dataset and we report their best values in Table 2.3 with the relative uncertainties.

For each epoch, a collisionally ionised gas with an average temperature of 0.16 ± 0.01 keV ($1.9\pm0.1\times10^{6}$ K) better represents (with a total $\Delta C-\mathrm{stat} = 407$) the high-ionisation absorption lines than a photoionised gas with an average ionisation parameter $\log\xi = 1.80 \pm 0.11$. We do not observe any significant flow velocity (v) associated to the absorber. The estimates of v are, indeed, consistent within the uncertainties with a static gas. In the LETG observation 12444, v indicates an outflow for the collisionally ionised gas and a low velocity for the fit with `xabs`. However, this is not a robust result since the flow velocity estimate is affected by the large σ_{v} of this instrument. This is also the case for RGS and LETG/HRC, where to tackle the degeneration between the fit parameters (in specific between σ_{v} and N_{H}), we fix the turbulent velocities to their default value of 100 km/s. Only with HETG, we are able to resolve the turbulent and flow velocities of the absorber. Moreover, the tabulated parameter, such as temperature and N_{H}, do not show a significant variance among the different epochs, as shown in Figure 2.2. They can be considered consistent within their uncertainties which can be large for some parameters like the flow velocity.

Furthermore, we fit the high-ionisation lines with both the *ism* and *photo* models to test the possible coexistence of photoionised and collisionally ionised gases along the line of sight. In this scenario the *ism*-model dominates the fit and the contribution of the photoionised gas is negligible for each epoch analysed. Statistically, the fit does not improve significantly to support the coexistence of the two absorbers. We find a C-stat/dof = 26865/21906 with a tiny improvement in the C-stat ($\Delta C = 6$) with respect to the *ism* model.

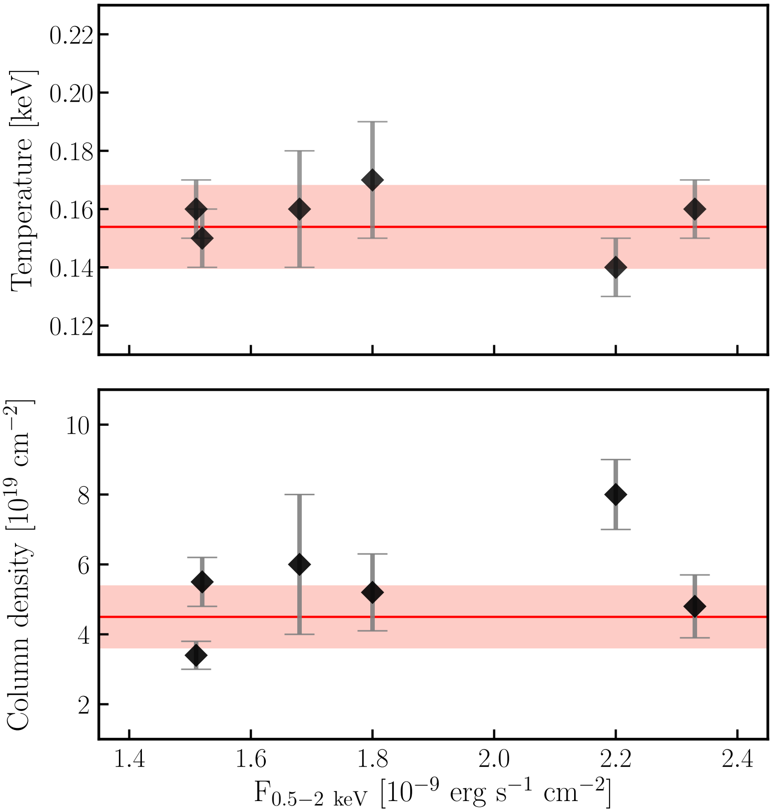

Figure 2.2: Temperature and the hydrogen column density of the *ism*-model versus the $0.5 - 2$ keV unabsorbed flux for each dataset using the C-statistic fitting model. The horizontal red line represents the inverse-variance weighted average and the coloured band indicates the 3σ confidence level. Only RGS 008411 (the observation with a flux $\sim 2.2 \times 10^{-9}$ erg cm^{-2} s^{-1}), shows a deviating column density value.

Table 2.3: Comparison of the photo-ionised and collisional-ionised best-fit models parameters obtained through the C-statistic analysis.

dataset	*ism* model (`hot`)				Cstat/dof	*photo* model (`xabs`)				Cstat/dof
	N_{H} $10^{19}\mathrm{cm}^{-2}$	$k_{\mathrm{B}}T$ keV	σ_{v} km/s	v km/s		N_{H} cm^{-2}	$\log\xi$	σ_{v} km/s	v km/s	
					RGS/XMM-*Newton*					
008411	8.0 ± 1.0	0.14 ± 0.01	100 (f)	13^{+10}_{-160}	**5214/3696**	16 ± 3	1.94 ± 0.02	100 (f)	2^{+18}_{-201}	**5354/3696**
055134	5.5 ± 0.7	0.15 ± 0.01	100 (f)	23^{+63}_{-55}	**5372/3917**	7 ± 2	1.81 ± 0.44	100 (f)	40 ± 82	**5389/3917**
					LETG/*Chandra*					
98	5.2 ± 1.1	0.17 ± 0.02	100 (f)	16 ± 67	**2004/1838**	5 ± 3	1.77 ± 0.11	100 (f)	76 ± 160	**2018/1838**
12444	3.4 ± 0.4	0.16 ± 0.01	223 ± 92	-190 ± 60	**1000/866**	4.2 ± 0.7	1.65 ± 0.09	305 ± 63	-30^{+12}_{-254}	**1048/866**
					HETG/*Chandra*					
2001	6 ± 2	0.16 ± 0.02	40^{+42}_{-29}	-60 ± 26	**7329/6624**	9 ± 3	1.82 ± 0.03	54^{+63}_{-27}	-66 ± 60	**7362/6624**
2006	4.8 ± 0.4	0.16 ± 0.01	154 ± 30	2^{+6}_{-50}	**5950/4984**	6 ± 1	1.81 ± 0.01	136 ± 36	12 ± 32	**6105/4984**
Mean	5.5 ± 0.9	0.16 ± 0.01	139^{+55}_{-50}	-32^{+40}_{-70}	**26871/21925**	8 ± 2	1.80 ± 0.11	165^{+54}_{-42}	6^{+61}_{-105}	**27278/21925**

Notes. We indicate with (f) the frozen parameters of the model.

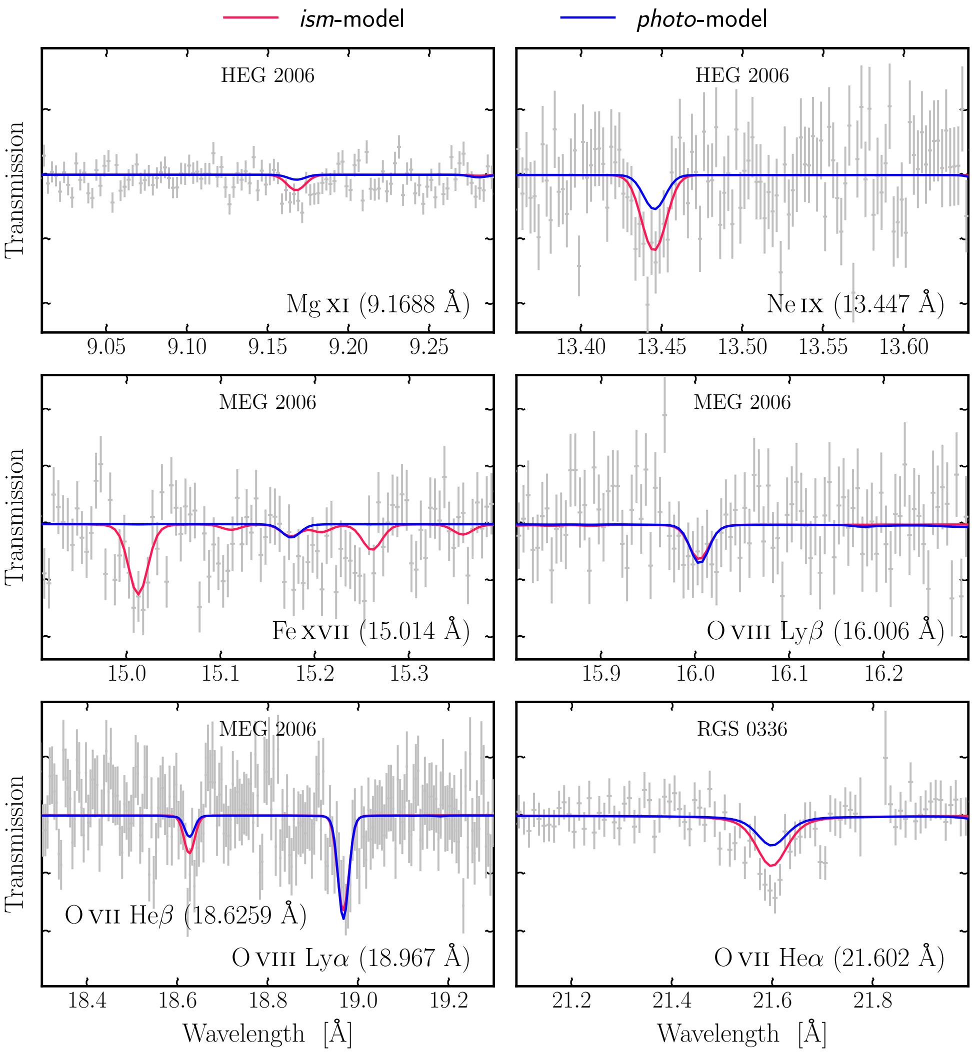

Figure 2.3: High ionisation lines detected in the spectra of 4U 1820-30. For clarity of presentation, we do not display all the datasets. We superimpose the *ism* and *photo* models (in red and blue lines, respectively) obtained with the Bayesian parameter inference.

2.4.2 Bayesian analysis

For the spectral analysis in the framework of Bayesian analysis (Bayes 1763), we use the MultiNest algorithm (version 3.10, Feroz et al. 2009, 2013). This method is applicable to low-dimensional problems of X-ray spectral modelling. Its strength is the capability to identify local maxima without difficulty computing points of equal weighting similar to a Markov

Chain. It provides values, error estimates and marginal probability distributions for each parameter.

To connect the X-ray analysis framework Spex with the Bayesian methodology we create a Python package BaySpex[5], which is a simplified and adapted version of the `PyMultiNest` and Bayesian X-ray Analysis (`BXA`) developed by Buchner et al. (2014). This script is adapted to PYSPEX, the python interface to Spex. The logic behind the script is that MultiNest suggests parameters on a unit hypercube which are translated into model parameters, readable by Spex, using the prior definitions. At this point, BaySpex computes a probability using the Spex likelihood implementation, which is passed back to the MultiNest algorithm.

Parameter inference

Similar to the C-statistic approach, we separately multiply the broadband continuum fit with the *ism* and *photo* models. To minimise the number of the free parameters in the fit, we freeze the broadband continuum shape calculated in Section 2.3. Furthermore, we impose the parameters of the *ism* (*photo*) models to be the same for all datasets. These two arrangements are justified by the previous C-statistic analysis. The `hot` and `xabs` components do not modify the shape of the broadband model and their parameters are constant along all the epochs (see Table 2.3).

In Figures 2.4 and 2.5, we display, respectively, the normalised probability distributions of the *ism* and *photo* model parameters computed through the Bayesian parameter inference. The estimate values with their errors are reported on the top of each panel. We also illustrate the two-dimensional distribution of the probability pairing the free parameters with each other. In both fits, we do not observe any strong covariance between the free parameters of the fit. Only the ionisation parameter (ξ) and the hydrogen column density of the absorber show a weak correlation visible in the $\log \xi - \log N_{\mathrm{H}}$ plot of Figure 2.5.

We also test the coexistence of collisionally ionised and photoionised gases along the line of sight fitting together the two models (*ism+photo* model). Since the Bayesian approach explores the full parameter space, it can return more solid results than the C-stat. We show the probability distribution of the parameters for these models in Figure 2.6. While the parameters of the `hot` component (the four upper distributions) are well defined, the `xabs` quantities (the four lower distributions) are not constrained. Only the relative column density shows a peaked probability distribution indicating that the fraction of the possible photoionisation gas in modelling the high-ionisation lines is very small (less than 0.002).

Moreover, we investigate if multiple temperature interstellar hot gas (*ism+ism* model) or multiple photoionised gases (*photo+photo* model) can better describe the absorption features. In both cases we find that a single gaseous component dominates the fit and the contribution of the other can be considered negligible.

To understand which candidate among the *ism*, *photo*, *ism+photo*, *ism+ism*, *photo+photo* model better fits the high-ionisation lines of 4U 1820-30, we compute the Bayesian model analysis presented in the following subsection.

---

[5] BaySpex is publicly available on `GitLabLINK` and `ZenodoLINK`.

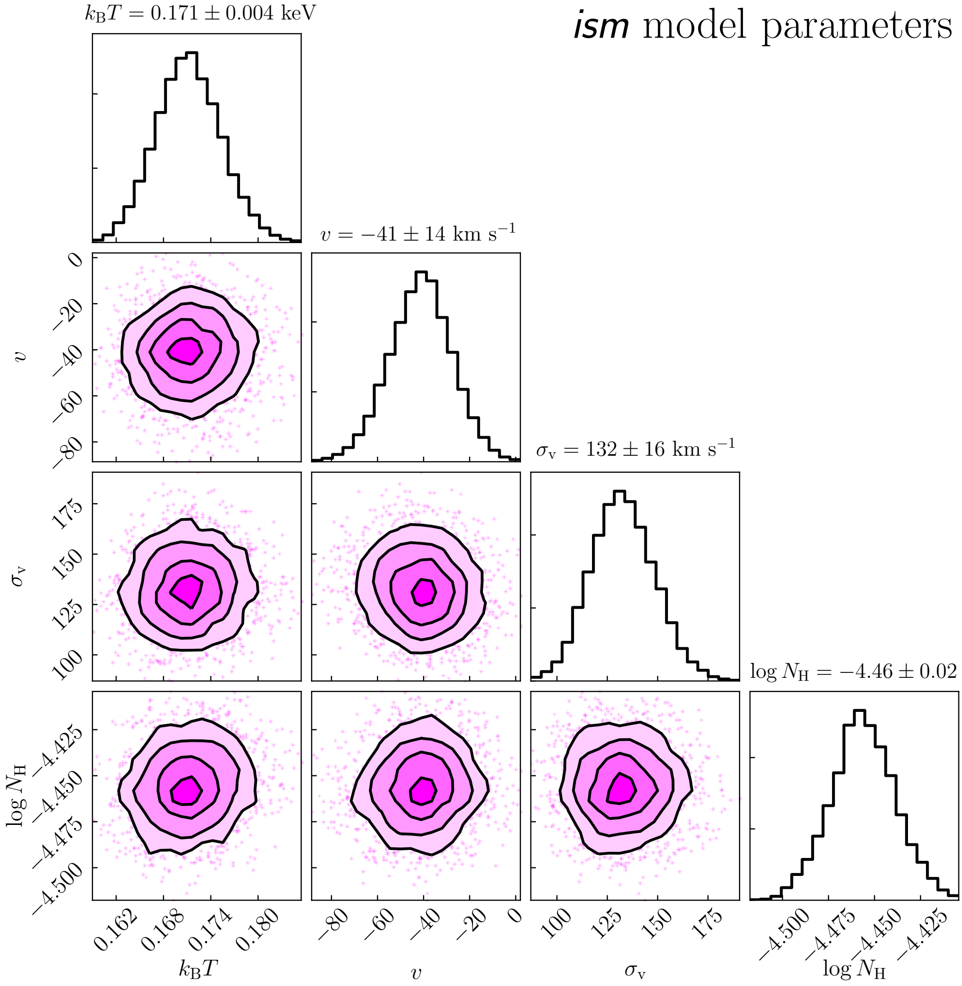

Figure 2.4: The posterior distribution from MultiNest is plotted with two-dimensional histograms comparing each pair of free parameters `hot`-model ($N_{\rm H}$, $k_{\rm B}T$, v and σ_v). The contour indicate the 1σ, 2σ, 3σ and 4σ confidence intervals in two dimensional space.

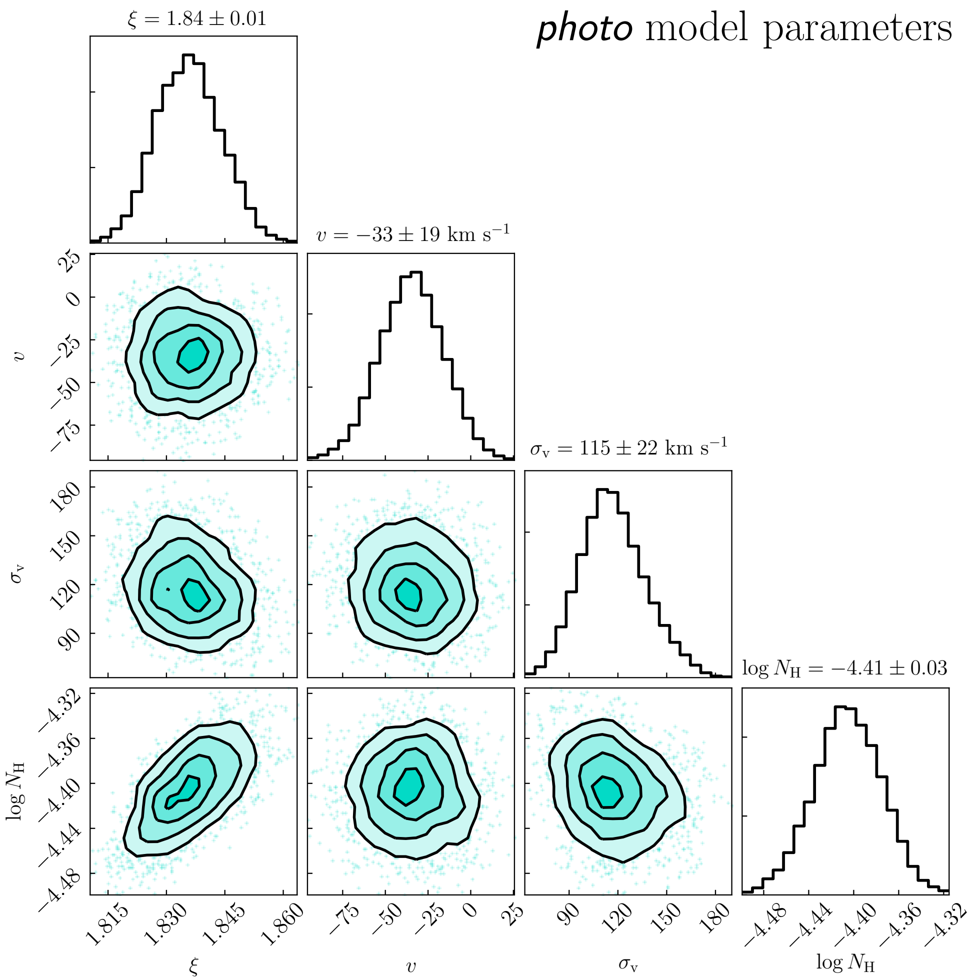

Figure 2.5: The posterior distribution from MultiNest is plotted with two-dimensional histograms comparing each pair of free parameters of the `xabs`-model ($N_{\rm H}$, ξ, v and σ_v). The contour indicate the 1σ, 2σ, 3σ and 4σ confidence intervals in two dimensional space.

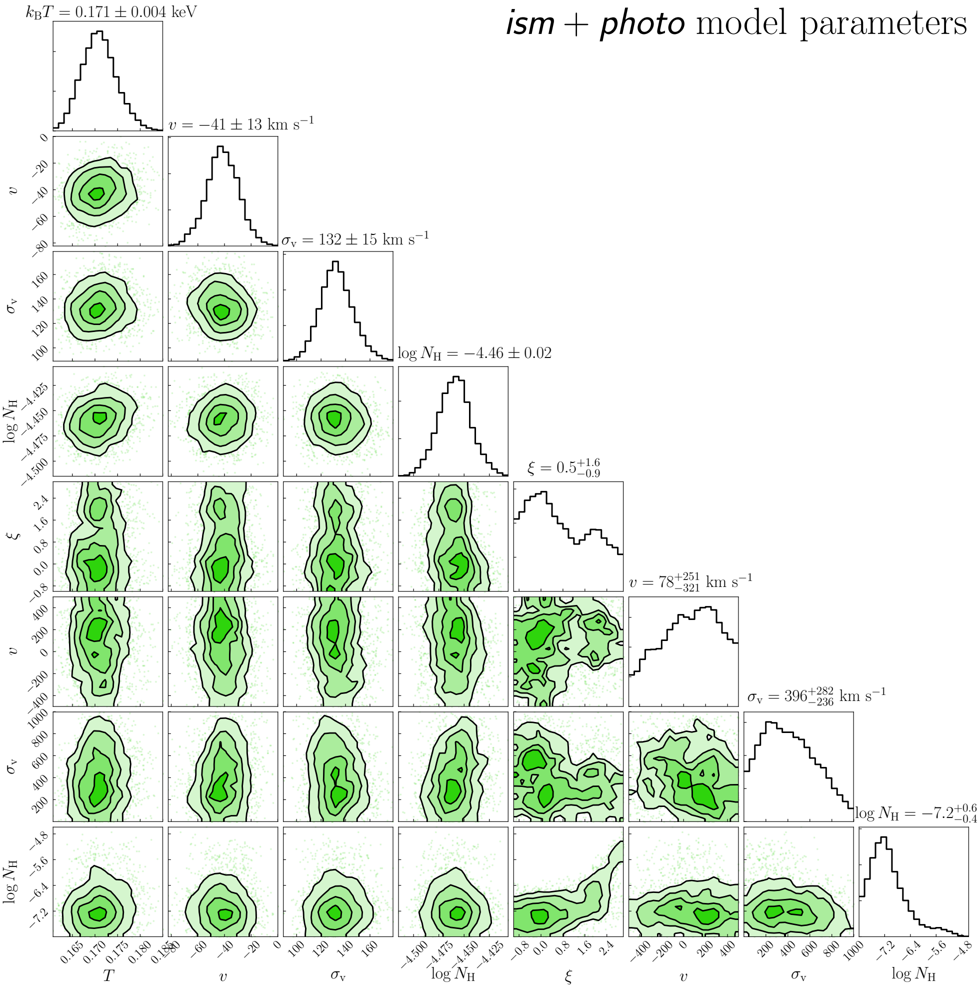

Figure 2.6: The posterior distribution from MultiNest is plotted with two-dimensional histograms comparing each pair of free parameters of the `hot`-model ($N_{\rm H}$, $k_{\rm B}T$, v and $\sigma_{\rm v}$), in the four upper distributions, together with the free parameters of the `xabs`-model ($N_{\rm H}$, ξ, v and σ_v) in the four lower distributions. The contour indicate the 1σ, 2σ, 3σ and 4σ confidence intervals in two dimensional space.

Model comparison

Bayesian model comparison is done by comparing models on the basis of the posterior probability of the model given the data, known as *Bayesian evidence*. Using Bayes's rule, the Bayesian evidence (Z) is proportional to the prior probability for the model, $p(M)$, multiplied by the likelihood of the data (y) given the model, $p(y|M)$. The choice between two models, M_1 and M_2, can be made on the basis of the ratio of their Bayesian evidences. This ratio is known as Bayes factor ($B_{1,2}$, Wasserman 2000; Liddle 2007; Trotta 2008; Knuth et al. 2014). Since we choose uniform priors for different models in our analysis, the Bayes factor is defined as:

$$B_{1,2} = \frac{Z_1}{Z_2} = \frac{p(y|M_1)}{p(y|M_2)} \ .$$

A large value of this ratio gives support for M_1 over M_2. Specifically, we adopt the scale of Jeffreys (1961) and we rule out models which show $B_{1,2} > 30$ ($\log B_{1,2} > 1.5$). A Bayes factor above 30 represents, indeed, a "very strong evidence" against M_2. The strength of this method is that it does not require models to be nested (i.e. M_2 is a special case of M_1) nor does it make assumptions about the parameter space or the data. Moreover, it automatically introduces a penalty for including too much model structure, guarding against overfitting the data (Kass & Raftery 1995).

The Bayesian statistics includes an approximation to the Bayesian evidence known as the Bayesian Information Criterion (BIC Schwarz 1978) which is defined as BIC $= -2\ln\mathcal{L} + k\ln N$, where $\mathcal{L}$ is the maximum likelihood, k the number of parameters of the model and N the number of data points used in the fit.

An alternative model comparison are the information-theoretic methods, pioneered by Akaike (1974) with his Akaike Information Criterion (AIC), which is defined as AIC $= -2\ln\mathcal{L} + 2k$. Similarly to the Bayesian model selection, AIC and BIC can be used to decide which model is more probable to have produced the data: the most probable model corresponds to the fit with the smallest AIC,BIC value, respectively. Both AIC and BIC include an over-fitting term with which the more complex model is disfavoured by the additional number of parameters. A description geared to astronomers can be found in Takeuchi (2000) and Liddle (2004), while the full statistical justification can be found in Burnham & Anderson (2002).

We compare all the models presented in Section 2.4.2 (*ism*, *photo*, *ism* + *photo*, *ism* + *ism*, and *photo* + *photo*) using the Bayesian evidence. We list the results of the model comparison in Table 2.4, where we also report the relative AIC and BIC values. An interstellar hot gas with a single temperature is the favourite scenario for describing the high-ionisation lines observed in the spectra of 4U 1820-30. The result of the Bayesian analysis is, therefore, in agreement with the outcome of the C-statistic (see Section 2.4.1).

2.5 Discussion

In order to determine the origin of the high-ionisation absorption lines observed in the spectra of 4U 1820-30, we fit them adopting both photo-ionisation and collisional-ionisation models. In Figure 2.3, we compare the fits of the two models obtained through the Bayesian parameter inference. The *ism* model reproduces all the lines better than the *photo* model, in particular the Fe XVII which is detected with a significance of 4.4σ. This line has been previously detected by Yao et al. (2006). The *photo*-model does not describe the Fe XVII line (see Figure 2.3), since the fraction of the ion according to the photo-ionised model is very low.

In Figure 2.7, we plot the ionisation fractions of the ionised atoms for which we detected the lines in the spectrum. In particular, on the left panel, we show the relative column densities

Table 2.4: Model selection results for 4U 1820-30.

Model	$\log Z$	ΔAIC	ΔBIC
ism	0.0	0	0
$ism + photo$	-1.7	+8	+57
$ism + ism$	-25.5	+156	+204
photo	-74.7	+348	+356
$photo + photo$	-88.6	+367	+407

Notes. The last three columns show the model comparison based on log-evidence, AIC and BIC. The log-evidence is normalised to the maximum value found whereas both AIC and BIC are normalised to the minimum value which indicates the preferred model. Models with $\log Z < 1.5$ or $\Delta AIC(\Delta BIC) > 10$ can be ruled out as a plausible model that generates the data (Jeffreys 1961; Burnham & Anderson 2002).

of the *ism* model whereas on the right, the respective column densities for the *photo* model. With the dashed vertical lines we indicate the best value of $k_{\rm B}T$ and ξ obtained with the Bayesian analysis. The different distributions of the column densities of the ions are crucial to select which model fit the best the spectral features. For a photoionised gas with a mild photoionisation parameter as we find $\log \xi \sim 1.8$, the iron is divided in multiple ionisation states. Consequently, the ionisation fraction of each Fe ion becomes low. Instead, for a collisionally ionised gas the column densities are distributed differently: the ionisation fraction is more peaked at the preferred ionisation state, which is determined by the temperature of the gas. Therefore, the detection of the Fe XVII line suggests an interstellar nature for the high-ionisation lines.

Moreover, the photoionisation nature is statistically ruled out (see Table 2.4). All the three model comparison criteria considered indicate the *ism* as preferred model. The evidence against the other models is particularly strong with the *BIC* criterion which severely penalises complex models. In the following, we discuss in detail the results obtained for the *ism* and *photo* models.

2.5.1 Photoionisation origin

Both Bayesian and *C*-statistic approaches show a less statistical significance for the photoionisation modelling with respect to the collision-ionisation one. The absorber is found to have a small flow-velocity which is consistent with the radial velocity of the spacecraft at different epochs. Therefore, our results together with previous works (e.g., Cackett et al. 2008) do not support the presence of a disc wind in outflow.

Moreover, the presence of a local bound ionised gas, such as a disc atmosphere, is not well supported physically by the results obtained from our photoionisation modelling. Through the ionisation parameter, we can calculate the density, $n_{\rm H}$, if one knows where the plasma is located with respect to the X-ray source. Taking an ionising luminosity of $L_{\rm ion} = 8 \times 10^{37}$ erg s^{-1} (computed using the SED of C12, for the range 1-1000 Ryd), distance $r < 1.3 \times 10^{10}$ (which correspondes to the size of the system, Stella et al. 1987) and ion-

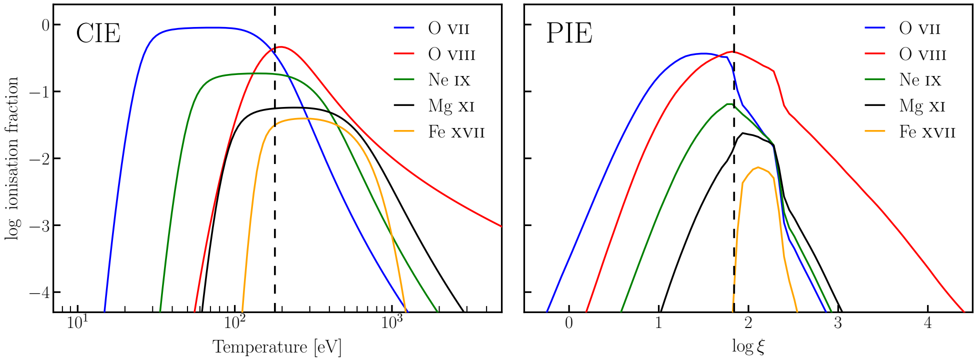

Figure 2.7: Ionisation fractions of oxygen, neon, magnesium and iron ions as a function of the electron temperature for collisional ionisation equilibrium plasma (CIE, *ism*-model on the left panel) and as a function of the ionisation parameter for a gas in photoioionisation equilibrium (PIE, *photo*-model, on the right panel). The vertical dashed lines indicate the best values for $k_{\mathrm{B}}T$ and ξ obtained through the Bayesian analysis.

isation parameters $\xi = 69.2$ erg s^{-1}cm (Section 2.4.2) the density of the plasma must be $n > 7 \times 10^{15}$ cm^{-3}, some orders of magnitude larger than the density of the typical disc atmosphere of a low-mass X-ray binary system (van Peet et al. 2009). This large density value would also imply that the filling factor, $f = N_{\mathrm{H}}/nr$, is extremely low $f < 4 \times 10^{-7}$, with $N_{\mathrm{H}} = 3.9 \times 10^{19}$ cm^{-2}. Cackett et al. (2008) argued that a proper physical solution for such small filling factor is the presence of dense structures above the disc, like high-density blobs, produced by thermal instabilities. For example, a similar clumped atmosphere was observed for the X-ray binary EXO 0748-676 (Psaradaki et al. 2018). However, the dense atmosphere of this source shows clumps with a density $n_H \sim 10^{13}$ cm^{-3}, two orders of magnitude lower than the density expected for a possible locally photoionised material.
Another argument against the photoionisation origin is the lack of variability of the lines observed among the different epochs (Figure 2.2 and Cackett et al. 2008).

The fact that the collisional-ionisation model best represents the ionised lines of the spectra does not exclude the existence of ionised gas intrinsic to the source. Thus, to test the possible presence of this photo-ionised gas beside the hot interstellar plasma we compute a fit using both models. Our analysis, in particular the C-statistic, shows a lack of a significant contribution by photo-ionised gas towards the source for the epochs covered by the observations. Furthermore the Bayesian parameter inference shows a negligible column density of the photo-ionised gas (see Figure 2.6).

A question that arises is why we do not detect any significant absorption lines from a photoionised wind/atmosphere intrinsic to 4U 1820-30. One possible explanation is that the X-ray source is not luminous enough to ionise any significant amount of gas that may be too far away. 4U 1820-30 belongs to the atoll source class which in general show lower luminosities than the Z sources (Hasinger & van der Klis 1989; Muno et al. 2002). Yet considering

the SED of the ionisation source and the small size of the system, the disc/atmosphere could be fully ionised and it will be impossible to detect any absorption lines (Stella et al. 1987; Futamoto et al. 2004).
Finally, the inclination angle of the system can also be a crucial factor for the non-detection of photoionised lines. Díaz Trigo & Boirin (2016) showed that the preferential detection of absorbing photoionised plasma is for system with a relative high ($i > 50^{\circ}$) inclination. The lower inclination of the 4U 1820-30 ($i = 43^{\circ}{}^{+8}_{-9}$, Anderson et al. 1997) system may imprint weaker absorption lines in the spectra as our line of sight would go through a thinner layer of gas.

2.5.2 Interstellar origin

A single temperature hot gas can describe the absorption lines well. In specific, we observe a gas with a temperature of $\sim 1.98 \times 10^{6}$ K, which is consistent with the values obtained by previous works (e.g., Yao et al. 2006) and with the temperature observed for several Galactic low-mass X-ray binaries (Yao & Wang 2005). Furthermore, we tested the presence of multiple temperature gas adding a supplementary `hot` component. One may expect variation in physical, and possibly chemical, properties of the hot gas along the line of sight to 4U 1820-30 which crosses several bubbles such as the Local Bubble around the Sun (with $T \sim 10^{6}$ K, Kuntz & Snowden 2000) and Loop I Bubble (with $T \sim 3.5 \times 10^{6}$ K, Miller et al. 2008). However, from our modelling we do not find multiple gases with different temperatures. The absorption of the gas contained in local bubbles is too low to be detected in the spectrum. Therefore, for the line of sight towards 4U 1820-30 we assume a single hot plasma component which is consistent with the scenario suggested by Hagihara et al. (2011). In addition, this uniform hot coronal gas is also in agreement with the presence of a hot and thick interstellar disc, as suggested by extragalactic source observations (Yao et al. 2009; Hagihara et al. 2010).
Through the Bayesian data analysis and multi-lines modelling, we are able to evaluate the velocity dispersion of the hot coronal gas, $\sigma_{\rm v} = 130 \pm 15$ km s^{-1}. Yao & Wang (2006) found a dispersion velocity[6] between 117 km s^{-1} and 262 km s^{-1} for the hot gas along the line of sight towards 4U 1820-30. Our velocity dispersion estimate is also in agreement with the dispersion velocities observed from the survey of the O VI ($\sigma_{\rm v} = 50 - 200$ km s^{-1}) with the Far UltraViolet Spectroscopic Explorer, FUSE (Otte & Dixon 2006). The O VI line is often used as tracer of gas with a peak temperature of $T \approx 3 \times 10^{5}$ K. Such intermediate-temperature gas is expected primarily at the interfaces between the cool/warm clouds and the hot coronal gas (Sembach et al. 2003).
For a collisionally ionised gas with a temperature of $T \sim 1.98 \times 10^{6}$ K, the expected thermal broadening is $\sigma_{\rm v} = 0.0321\sqrt{T} = 43.5$ km s^{-1}. This value is too low to explain our velocity dispersion. This velocity cannot be accounted for by differential Galactic rotation either. The lines are far wider than expected if the absorption came from a smoothly distributed ISM corotating with the disc of the Milky Way (Bowen et al. 2008). The observed velocity dispersion supports, instead, the picture of a turbulent hot coronal gas churned by shock-heated gas from multiple supernova explosions. The numerical simulations of de Avillez

---

[6] In their paper, Yao & Wang (2006) defined the dispersion velocity (b_v) as $b_v = \sqrt{2} \cdot \sigma_v$)

& Breitschwerdt (2005) show hot gas arises in bubbles around supernovae, which is then sheared through turbulent diffusion, destroying the bubbles and stretching the hot absorbing gas into filaments and vortices that dissipate with time. Furthermore the hot gas is involved in systematic vertical motion as it streams to the halo at a speed of $100 - 200$ km s^{-1}. This kinetic energy can be transformed into disordered, turbulent motions, resulting in higher turbulent velocities near the halo (Kalberla et al. 1998).

2.5.3 Abundances of the hot coronal gas

We further investigate the abundances of oxygen, neon, magnesium and iron for the hot phase of the interstellar medium. For this elements we detect high-ionisation lines. Using the Bayesian parameter inference we obtain abundances close to their protosolar values: $A_{\rm O} = 0.90 \pm 0.06\ A_{\odot}$, $A_{\rm Ne} = 1.16 \pm 0.08\ A_{\odot}$, $A_{\rm Mg} = 1.9 \pm 0.4\ A_{\odot}$, and $A_{\rm Fe} = 1.07 \pm 0.11\ A_{\odot}$, keeping as references the abundances tabulated in Lodders (2010).

The hot phase abundances of oxygen and neon are consistent with the characteristic depletion of these elements in the interstellar medium. Since neon is a noble element, it is very unlikely to be depleted in dust grains in all the medium phases and oxygen shows low depletion values in the interstellar medium (Jenkins 2009). Iron and magnesium are, instead, highly depleted from the gas phase in the interstellar medium (e.g. Jenkins 2009; Rogantini et al. 2018, 2019). The depletion of iron, in particular, remains high even in harsh environments (Whittet 2002). However, the observed abundances for magnesium and iron suggests that in the hot coronal gas along the line of sight towards 4U 1820-30, these two elements are mostly present in the gas phase. Thus, this support the scenario where all the interstellar dust in this very hot phase ($T \gtrsim 10^{5.5}$ K) is destroyed by frequent and/or severe shocks during the dust grain processing in the interstellar medium. This interpretation may not be unique. Reports of an overabundance of heavier elements relative to oxygen in neutral matter toward the Galactic centre would elevate the contribution of these elements in the hot phase as well. A comparison with different lines of sight especially towards sources at high latitudes, is therefore essential before drawing conclusions.

2.6 Summary

Motivated by defining the origin of the high ionisation absorption features present in the spectrum of the ultracompact system 4U 1820-30, we systematically analyse all the observations present in the *Chandra* and XMM-*Newton* archive: 5 *Chandra*/HETG spectra together with 2 *Chandra*/LETG and 2 XMM-*Newton*/Newton observations. We study the soft X-ray energy band covering the main high-ionisation absorption lines: namely, Mg XI, Ne IX, Fe XVII, O VII Heα, O VII Heβ, O VIII Lyα and O VIII Lyβ. We adopt realistic plasma models to fit simultaneously the multiple lines: in particular we use the SPEX model `xabs` and `pion` to reproduce a photo-ionised gas and `hot` for a thermal gas in collisional ionised equilibrium state. A Bayesian framework is used to model the spectral absorption features. Bayesian data analysis provides a robust approach to infer the model parameters and their uncertainties and offers a solid model comparison.

Both the C-statistic and Bayesian data analysis show the presence of hot coronal gas with a temperature of $T \sim 1.98 \times 10^6$ K ($k_B T = 0.171 \pm 0.004$ keV) along the line of sight towards 4U 1820-30. This hot interstellar gas is responsible for the high-ionisation absorption lines detected in the spectra. We summarise our main results as follows:

- The mean centroids of the absorption lines are consistent with their rest frame wavelengths. The small line of sight velocity observed is within the uncertainty due to the dynamic radial velocity of the observer. As previous works already concluded (e.g., Futamoto et al. 2004), an outflowing disc wind can be ruled out as possible ionised absorber.
- The lack of variability of the lines through the multiple observations shows also that the absorber is independent from the activity of the source suggesting a non-local origin for the gas.
- In the spectra of 4U 1820-30 we detect the Fe XVII line at 15.012 Å with a significance of 4.4σ. This line is best reproduced by a gas in collisional ionisation equilibrium. In contrast, for an absorber photoionised by the source the contribution of Fe XVII is not high enough to justify the strength of the absorption line detected.
- We constrain the turbulent velocity of the hot gas to be $\sigma_{\rm v} = 130 \pm 15$ km s^{-1} which is likely caused by shock-heated gas from multiple supernova explosions.

ACKNOWLEDGEMENTS

DR, EC, IP and MM are supported by the Netherlands Organisation for Scientific Research (NWO) through *The Innovational Research Incentives Scheme Vidi* grant 639.042.525. The Space Research Organization of the Netherlands is supported financially by NWO. This research has made use of data obtained from the Chandra Transmission Grating Catalog and archive (`http://tgcat.mit.edu`), and software provided by the *Chandra* X-ray Center in the application package CIAO. We also made used of the XMM-*Newton* Scientific Analysis System developed by a team of scientist located at ESA's XMM-*Newton* Science Operations Centre and at the XMM-*Newton* Survey Science Centre. We are grateful to M. Díaz-Trigo for a useful discussion on the photoionised atmosphere of 4U 1820-30. We thank A. Dekker and D. Lena for reading an early draft of the manuscript and for providing valuable comments and suggestions. We also thank I. Psaradaki for her input on the XMM-*Newton* data reduction.

3

Interstellar dust along the line of sight of GX 3+1

D. Rogantini, E. Costantini, S.T. Zeegers, C.P. de Vries, M. Mehdipour, F. de Groot, H. Mutschke, I. Psaradaki, L.B.F.M. Waters

Published in Astronomy & Astrophysics, Volume 630, A143 (2019)

Abstract

Studying absorption and scattering of X-ray radiation by interstellar dust grains allows us to access the physical and chemical properties of cosmic grains even in the densest regions of the Galaxy. We aim at characterising the dust silicate population which presents clear absorption features in the energy band covered by the *Chandra* X-ray Observatory. Through these absorption features, in principle, it is possible to infer the size distribution, composition, and structure of silicate in the interstellar medium. In particular, in this work we investigate magnesium and silicon K-edges. We built X-ray extinction models for 15 dust candidates using newly acquired synchrotron measurements. These models were adapted for astrophysical analysis and implemented in the SPEX spectral fitting program. We used the models to reproduce the dust absorption features observed in the spectrum of the bright low mass X-ray binary GX 3+1, which is used as a background source. With the simultaneous analysis of the two edges we test two different size distributions of dust: one corresponding to the standard Mathis-Rumpl-Nordsieck model and one considering larger grains ($n(a) \propto a_i^{-3.5}$ with $0.005\,\mu\text{m} < \text{a}_1 < 0.25\,\mu\text{m}$ and $0.05\,\mu\text{m} < \text{a}_2 < 0.5\,\mu\text{m}$, respectively, with a the grain size). These distributions may be representative of the complex Galactic region towards this source. We find that up to 70% of dust is constituted by amorphous olivine. We discuss the crystallinity of the cosmic dust found along this line of sight. Both magnesium and silicon are highly depleted into dust ($\delta_Z = 0.89$ and 0.94, respectively), while their total abundance does not depart from solar values.

3.1 Introduction

Magnesium is an essential element for life mainly because of its wide presence in the basic nucleic acid chemistry of all cells of all known living organisms (Cowan 1995). This is not surprising given the relatively high percentage of Mg in the interstellar medium (ISM). The solar photospheric abundance of magnesium is $\log A_{\rm Mg} = 7.54 \pm 0.06$[1] (the ninth element in order of mass abundance; Lodders 2010) and this is consistent with the chondrite composition in the solar nebula (Anders & Grevesse 1989). Magnesium is primarily synthesised in Type Ia supernovae and in core-collapse supernovae (Heger & Woosley 2010), and it is present in quiescent stellar outflows during the asymptotic giant branch (AGB) phase of their evolution (van den Hoek & Groenewegen 1997).

Magnesium is significantly depleted into the solid phase of the ISM. The depletion is parametrised by the depletion index, which refers to the underabundance of the gas-phase element with respect to its standard abundance, resulting from its inclusion in cosmic grains. This term depends on the environment properties showing three typical patterns as a function of density, turbulence, and galactic latitude (Jones 2000; Whittet 2002): high element depletions are found in dense, quiescent regions in the Galactic plane.

The mean value of depletion index for magnesium in the diffuse clouds is $D_{Mg} = -1.10$ with fractional depletion[2] in the range $\delta_{\rm Mg} = 0.85 - 0.95$ (see e.g. Savage & Sembach 1996; Jenkins 2009). Together with silicon, magnesium is almost completely included in silicate grains. Silicate dust is of great interest to astronomers because of its prevalence in many different astrophysical environments, including the diffuse ISM, protoplanetary discs around young stars, evolved and/or massive stars (e.g. AGB stars, red supergiant stars, and supergiant Be stars; see Henning 2010, and references therein), and even in the immediate environments of active galactic nuclei (i.e. Markwick-Kemper et al. 2007; Mehdipour & Costantini 2018).

The physical and chemical properties of silicates in the ISM have traditionally been studied through infrared spectroscopy. The broad and smooth infrared features at 10 and 18 μm are attributed to Si-O stretching and O-Si-O bending modes of cosmic silicates in amorphous state (Henning 2010). However, it is still not known exactly what composition or structure (i.e. dust size and crystallinity) characterise these dust grains, or how these properties change as a function of the Galactic environment (Speck et al. 2015). The shape, position, and width of the two bands depend on multiple factors, which are often difficult to disentangle, such as the level of SiO_4 polymerisation (Jäger et al. 2003), the Fe content (Ossenkopf et al. 1992), crystallinity (Fabian et al. 2000), particle size (Li & Draine 2001a), and particle shape and size of the interstellar dust grains (Voshchinnikov & Henning 2008; Mutschke et al. 2009).

---

[1] The abundances are given in logarithmic scale relative to a hydrogen column density $N_{\rm H} = 10^{12}$. Explicitly for magnesium we have

$$\log A_{\rm Mg} = 12 + \log(N_{\rm Mg}/N_{\rm H}) \ ,$$

where $N_{\rm Mg}$ is the indicate the magnesium column density.

[2] The fractional depletion, often expressed as a percentage, is defined as $\delta_{\rm X} = 1 - 10^{D_{\rm X}}$, where the depletion index $D_{\rm X}$ is evaluated comparing the abundance of the gas-phase element X with respect to its standard solar reference abundance: $D_{\rm X} = \log\left\{\frac{N_{\rm X}}{N_{\rm H}}\right\} - \log\left\{\frac{N_{\rm X}}{N_{\rm H}}\right\}_{\odot}$.

X-ray observations provide a powerful and direct probe of cosmic silicates and interstellar dust in general (Draine 2003). The cosmic grains interact with the X-ray radiation by absorbing and scattering the light. In particular the X-ray energy band contains the absorption edges of the most abundant metals. Several works (Lee et al. 2009; Costantini et al. 2012; Pinto et al. 2013; Valencic & Smith 2013; Corrales & Paerels 2015; Zeegers et al. 2017; Bilalbegović et al. 2018; Rogantini et al. 2018) have already shown how these absorption edges allow us to study in detail the chemical and physical properties of the dust grains. In contrast to the gas phase, the interaction between X-rays and solid matter modulates the post-edge region and imprints characteristic features. These features, named X-ray absorption fine structures (XAFS; see Bunker 2010, for a detail theoretical explanation) are characteristic of the chemical species present in the absorber. They are unique fingerprints of dust. Moreover, these features are sensitive to the crystalline order of the grains. The peak on the pre-edge is due to the scattering interference between the X-rays and the grains. Zeegers et al. (2017) and Rogantini et al. (2018) have shown how this scattering peak is sensitive to the grain size and how it allows us to investigate the dust geometry in various environments for the Si and Fe absorption edges, respectively. The XAFS are often divided into two regimes: the X-ray absorption near-edge structure (XANES), which extends from about 5 to 10 eV below the K- or L- edge threshold energy to about 30 eV above the edges; and the extended X-ray absorption fine structure (EXAFS), which extends from $\sim$ 5 eV above the K- or L- edge energy to some hundred electron volts (Newville 2004).

To determine the nature of dust grains in space, we first carry out laboratory measurements of dust analogue minerals whose chemical compositions are well characterised to derive optical functions of minerals predicted to occur in space. Afterwards, we match the positions, widths, and strengths of observed spectral absorption features with those seen in the laboratory spectra.

We use low mass X-ray binaries (LMXBs) as background sources to illuminate the interstellar dust along the line of sight. The standard spectrum of this X-ray source class does not usually present emission lines, which may confuse the absorption spectrum, and it is characterised by a high continuum flux. As they are distributed along the Galactic plane, the X-ray emission of LMXBs allows us to investigate a large range of column densities including those crossing dense interstellar dust environments of the Galaxy.

In this paper we simultaneously characterise the extinction by Mg- and/or Si-bearing cosmic grains along the line of sight of a bright LMXB. We use multiple-edge extinction models that we build from synchrotron measurements. In this work, we focus on the Mg K-edge. In Section 3.2 we present the relative extinction cross sections of a set of physically motivated compounds. The Si K-edge profiles are taken from the works of Zeegers et al. (2017, 2019). In Section 3.3 we present the bright LMXB, GX 3+1. For the analysis of the spectrum of this LMXB, we use SPEX version 3.04.00 (Kaastra et al. 1996; Kaastra et al. 2017). The source presents a line-of-sight hydrogen column density ($N_{\mathrm{H}} \sim 1.6 \times 10^{22}\,\mathrm{cm}^{-2}$; Oosterbroek et al. 2001) and a flux ($F_{2-10\,\mathrm{keV}} \sim 4 \times 10^{-9}$ erg s^{-1} cm^{-2}, Oosterbroek et al. 2001) which are ideal to study the cold absorbing medium through the two extinction edges of interest. Although the spectrum of GX 3+1 is well known in the literature, the absorption by cold interstellar dust has never been studied in detail for this source. The results of the Mg and Si edges analysis are discussed and summarised in Section 3.4 and 3.5, respectively.

3.2 Laboratory data analysis

3.2.1 The sample

The laboratory sample set belongs to a larger synchrotron measurement campaign that was already presented by Costantini & de Vries (2013) and Zeegers et al. (2019). In the first part of Table 3.1 we present all the laboratory samples for which we measured the Mg K-edge. We report their chemical formulas, forms, and origins. Some of these values are already presented in previous works (Zeegers et al. 2017; Rogantini et al. 2018). In this work we refer to the models used in the spectroscopic analysis of the astronomical source using the #Mod indexes of Table 3.1.
In order to reproduce laboratory analogues of astronomical silicates, we selected our samples taking into account the two main stoichiometric classes, olivine and pyroxene. Both classes share the same building block represented by the silicate tetrahedron, SiO_4. This is a four-sided pyramid shape with an atom of oxygen at each corner and silicon in the middle. However, the spatial disposition of the tetrahedron is different (Panchuk 2017): olivine shows a structure composed of isolated tetrahedra, whereas pyroxene is an example of a single-chain silicate where adjacent tetrahedron share one oxygen atom.

In our sample set we considered pyroxenes and olivine with varying Mg-to-Fe ratios. Olivine can be pure Mg_2SiO_4 (forsterite), Fe_2SiO_4 (fayalite), or some combination of the two, written as $(Mg, Fe)_2SiO_4$. Pyroxene can be Mg-pure $MgSiO_3$ (enstatite), Fe-pure $FeSiO_3$ (ferrosilite), or a combination of the two. The nomenclature En(x)Fs(1-x) indicates the fraction of iron (or magnesium) included in the compound. "En" stands for enstatite and "Fs" for ferrosilite. These silicate compounds are present in both crystalline and amorphous forms. We completed our sample set adding spinel, which is a Mg-bearing compound which crystallises in the cubic crystal system formed by oxygens, whereas Mg and Al atoms sit in tetrahedral and octahedral sites in the lattice (Mutschke et al. 1998). Spinel has been observed in chondritic meteorite with pre-solar composition and has been produced by gas outflows of red giant stars (Zinner et al. 2005).

3.2.2 Synchrotron measurements

Similar to the Si K-edge already presented by Zeegers et al. (2017, 2019), for the Mg K-edge we made use of the laboratory data that we obtained at the beamline LUCIA (Line for Ultimate Characterization by Imaging and Absorption; Flank et al. 2006) at the SOLEIL facility in Paris. The LUCIA X-ray microprobe is capable of performing spatially resolved chemical speciation via X-ray absorption spectroscopy (XAS). The $0.8-8$ keV X-ray domain of the tunable beam gives access to the K edges of low Z elements (from sodium up to iron) with a resolving power of about 4000. The measurements of the magnesium absorption edge are part of a larger synchrotron campaign in which the absorption edges due to Al and Si

Table 3.1: List of samples in our set with their relative chemical formula, form, origin, and reference index. In the top part of the table we list the compounds for which the Mg K-edge was analysed in the present work.

Name	Chemical formula	Form	#Mod
Enstatite [a]	$MgSiO_3$	amorphous	1
Enstatite [b]	$MgSiO_3$	crystalline	2
Forsterite [c]	Mg_2SiO_4	crystalline	3
Hypersthene [d]	$Mg_{1.502}Fe_{0.498}Si_2O_6$	crystalline	-
Olivine [a]	$MgFeSiO_4$	amorphous	4
Olivine [e]	$Mg_{1.56}Fe_{0.4}Si_{0.91}O_4$	crystalline	5
En60Fs40 [a]	$Mg_{0.6}Fe_{0.4}SiO_3$	amorphous	6
En60Fs40 [a]	$Mg_{0.6}Fe_{0.4}SiO_3$	crystalline	7
En75Fs25 [a]	$Mg_{0.75}Fe_{0.25}SiO_3$	amorphous	8
En90Fs10 [a]	$Mg_{0.9}Fe_{0.1}SiO_3$	amorphous	9
En90Fs10 [a]	$Mg_{0.9}Fe_{0.1}SiO_3$	crystalline	10
Spinel [f]	$MgAl_2O_4$	crystalline	-
Quartz [g]	SiO_2	crystalline	11
Quartz [g]	SiO_2	amorphous	12
Quartz [g]	SiO_2	amorphous	13
Fayalite [g]	Fe_2SiO_4	crystalline	14
Magnesia [h]	MgO	crystalline	15

[a] Synthesised in laboratories at AIU Jena and Osaka University;
[b] Origin: Kiloza, Tanzania;
[c] Commercial product (Alfa Aesar);
[d] Origin: Paul Island, Labrador;
[e] Origin: Sri Lanka;
[f] Commercial product (Aldrich);
[g] We refer to Zeegers et al. (2019); the quartz have two different stages of amorphisation
[h] Also known as magnesium oxide, data taken from Fukushi et al. (2017).

were also measured (Costantini et al. 2019; Zeegers et al. 2019).

The spectrum around the Mg K-edge was taken in the fluorescence geometry detecting the "secondary" (fluorescent) X-ray emission from the sample that has been excited by bombarding it with the synchrotron radiation. X-rays are energetic enough to expel tightly held electrons (photoelectron) from the inner orbitals (K-shell) making the electronic structure of the atom unstable. Consequently, one electron falls from a higher orbital level to the lower orbital to fill the hole left behind by a photoelectron. As a consequence, this releases fluorescent energy. This fluorescent signal can be used to derive the amount of absorption

beyond the edge.
For each compound we took three to four measurements to average the signal and smooth out the possible small instrumental oscillations. Finally, we shifted our measurements by 2.54 eV to lower energies since the undulator radiation of the synchrotron introduced a systematic shift in the monochromator. In Appendix A.1 we describe how we determined the exact value of this energy shift.

3.2.3 Extinction cross sections

To study the attenuation of X-rays by the interstellar dust, it is necessary to calculate the extinction cross section of each sample. We followed the same method already presented in Zeegers et al. (2017) and Rogantini et al. (2018). In this section, we summarise the procedure highlighting the most relevant steps. The main results are shown in the multiple panels of Figure 3.1.

Pile-up and self-absorption correction - Ideally, the samples should be either sufficiently thin or sufficiently diluted for the data to be unaffected by self-absorption effects. Practically, this may not be possible and the consequence would be an incorrect peak size in the XAFS. This is due to the variations in penetration depth into the sample as the energy is scanned through the edge and the fine structure (Tröger et al. 1992).
Therefore, we corrected the spectrum using the standard FLUO algorithm[3], which is part of the UWXAFS analysis package (Stern et al. 1995). For comparison, we also used the tool ATHENA[4] for the self-absorption correction, obtaining the same corrected signal (Ravel & Newville 2005). Finally, we also corrected the beamline data for any pile-up effect. For the Mg K-edge, this effect slightly distorts the region extending beyond the edge. In Figure 3.1*a* we compare the raw data (solid red line) and the corrected data (dashed blue line). It is necessary to ignore part of the pre-edge since the beamline was not yet stable during the measurement in this energy range.

Transmission - With the goal of determining the attenuation coefficient (μ) in μm^{-1} necessary to calculate the refractive index of the material, we transformed the absorption in arbitrary units obtained from the fluorescent measurements into transmittance. We used tabulated values of the X-ray transmission of solids provided by the Centre for X-ray Optics at Lawrence Berkeley National laboratory[5] (CXRO). In order to simulate the optically thin ISM condition, we chose a thickness of 0.5 μm; this value is far below the attenuation length of each sample. Knowing the transmittance (shown in Figure 3.1*b*) it is possible to acquire the optical constants.

Optical constants - To obtain the extinction cross section of a specific material, it is fundamental to derive the refractive index. It is a complex and dimensionless quantity generally defined as $m = n + ik$. The imaginary absorptive part k is derived directly

---

[3] https://www3.aps.anl.gov/~haskel/fluo.html

[4] ATHENA is an interactive graphical utility for XAFS data inside the comprehensive data analysis system DEMETER (see https://bruceravel.github.io/demeter/documents/Athena/index.html). This tool is not to be confused with the future X-ray observatory *Athena*.

[5] http://www.cxro.lbl.gov/

from the laboratory data, specifically from the transmittance signal. The real dispersive part n, on the other hand, can be calculated using the Kramers-Kronig relation (de L. Kronig 1926; Kramers 1927). For this calculation we used the algorithm introduced by Watts (2014). The final results are shown in Figure 3.1*c*. For further details on the calculation of the optical constants we refer to the dedicated paragraph in Rogantini et al. (2018).

Cross sections - To obtain the cross section from the optical constants, n and k, we employed the anomalous diffraction theory (ADT; van de Hulst 1957). This method allowed us to compute the absorption and scattering by dust grains of arbitrary geometry. In this step it is important to define the grain size range of interest. We calculated the scattering, absorption, and extinction cross sections (shown in Figure 3.1*d*) for each compound via the standard Mathis-Rumpl-Nordsieck (MRN) grain size distribution (Mathis et al. 1977). See also Section 3.2.4.

Model in SPEX - Finally, we implemented the extinction profiles into the SPEX fitting code adding these to the library of `amol` (Pinto et al. 2010). Currently this model uses the Verner absorption curves (Verner et al. 1996). We adjusted the slopes of the pre- and post-edge of our extinction profiles avoiding any discontinuities between the XAFS data and the predefined curve in SPEX (Zeegers et al. 2017).

In Figure 3.2 we compare, for illustrative purpose, the extinction cross sections of three representative compounds in our sample set: an amorphous Mg-pure pyroxene (blue dashed line), a crystalline Mg-pure olivine (red solid line), and the magnesium aluminium spinel (black solid line). The extinction cross sections of all the compounds are shown in Appendix A.2.

The chemical properties of the grains, in particular the length of the atom boundaries, determine the shape of the extinction profiles. Both olivine and pyroxene minerals, which share the same silicate tetrahedron, show similar patterns. Spinel, which instead presents an aluminium cubic structure, shows a distinct extinction shape and the main peak of the cross section is shifted at higher energy. The extinction cross section is also sensitive to the crystalline order of the mineral. Pure crystalline compounds shows multiple, distinct, and narrow peaks, whereas the extinction profiles of amorphous compounds are smoother and do not show any secondary peaks.

3.2.4 Large grain size distribution

In order to investigate the grain size, in particular focussing on the presence of particles larger than 0.25 μm, we calculate and implement in `amol` the extinction cross sections adopting a modified MRN grain size distribution. Specifically, we adopt the distribution already presented by Zeegers et al. (2017) with $(0.05 \leq a \leq 0.5)$ μm. In Figure 3.3 we show the effect of this change in the grain size distribution. The forsterite Mg K-edge with a MRN distribution with particle size of $0.005 - 0.25$ μm is shown in black and in red the same edge but now with a LMRN size distribution that has a particle size in the range $0.05 - 0.5$ μm. The feature before the edge ($\sim 1305\,\mathrm{eV}$), namely the scattering peak, is sensitive to the dust grain size and it is due to an enhanced scattering efficiency for larger grain size (Zeegers et al. 2017; Rogantini et al. 2018).

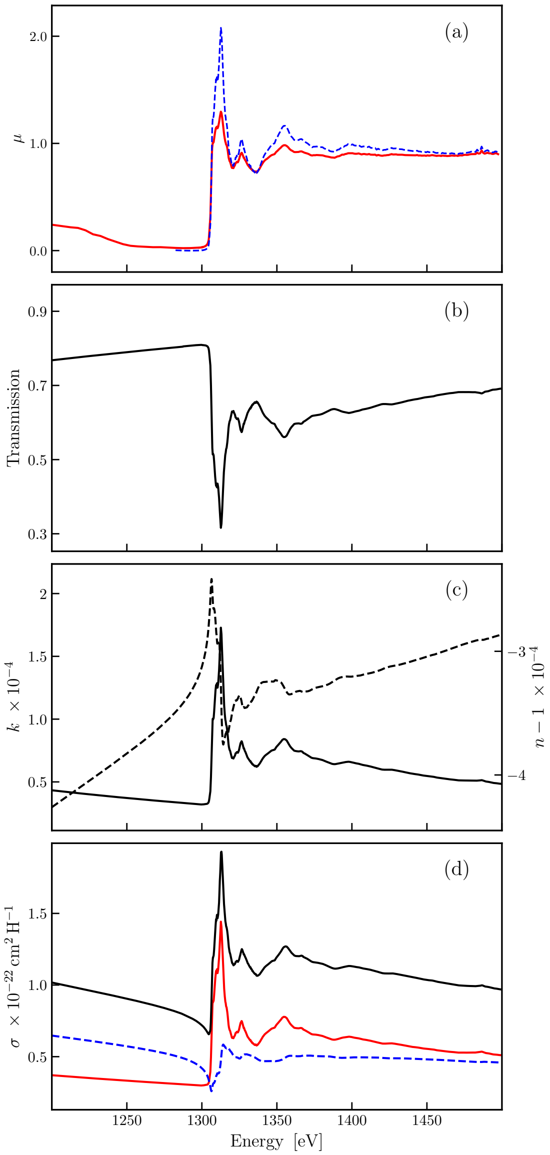

Figure 3.1: Representation of data analysis for the forsterite Mg_2SiO_4. From top to bottom: (*a*) Self-absorption correction: the synchrotron raw data (red solid line) and the signal corrected with the FLUO tool (blue dashed line). (*b*) Transmission for a thin layer ($\tau = 0.5\,\mu$m): the measured edge with XAFS (in black) are normalised using the tabulates values from Henke et al. (1993). (*c*) Optical constants: k is represented with the solid line while $n - 1$ with the dashed line (in units of 10^{-4}). (*d*) The extinction (black solid), absorption (red solid), and scattering (blue dashed) cross sections per hydrogen nucleus for the Mathis, Rumpl, & Nordsieck (1977) dust model.

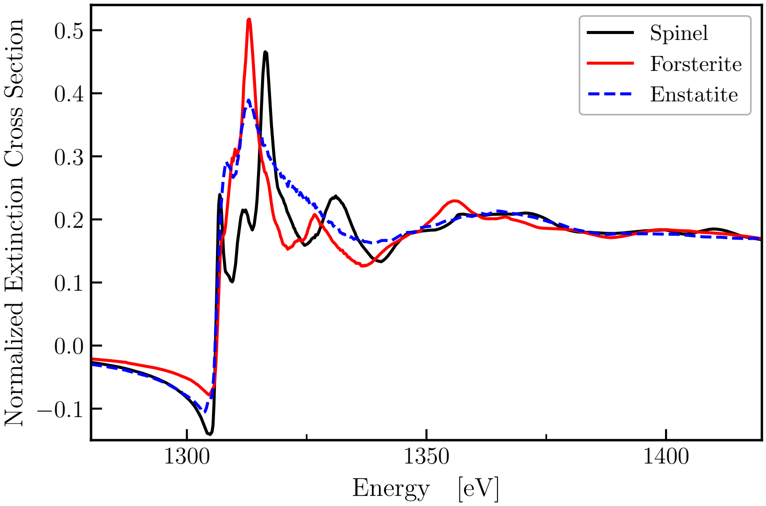

Figure 3.2: Mg K-edge model implemented in SPEX for three different chemical compounds: crystalline spinel ($MgAl_2O_4$), crystalline forsterite (Mg_2SiO_4), and amorphous enstatite ($MgSiO_3$). The major peak of spinel in the post-edge is shifted at higher energy with respect to the silicates. This is due to a different configuration of the atoms in the single unit cell.

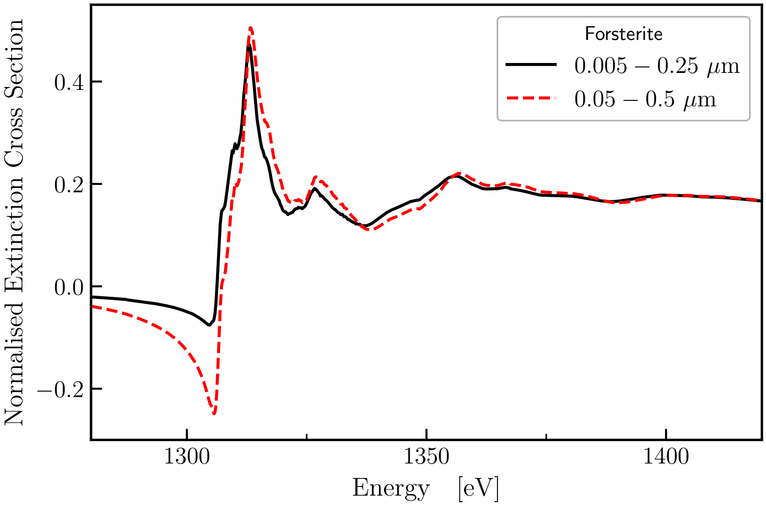

Figure 3.3: Normalised extinction cross section for forsterite using two different grain size distributions. The solid black line represents the standard MRN grain size in the range $0.005 - 0.25\,\mu$m. The dashed red line delineates the larger grain size spanning $0.05 - 0.5\,\mu$m.

3.2.5 Magnesium and silicon models

In this paper, for the first time, we simultaneously analyse the magnesium and silicon K-edges of a bright LMXB. We built our extinction model joining the laboratory cross sections of the Mg K-edge, from the present work, together with the Si K-edge cross sections taken from Zeegers et al. (2017, 2019). The extinction models with both Mg and Si K-edges were implemented in the `amol` model. Moreover, we included in our models the Si-bearing compounds that do not contain magnesium in molecules such as quartz and fayalite. We also added magnesium oxide (also known as magnesia), which contains only magnesium (Fukushi et al. 2017). Since the Si K-edge model of hypersthene is not available (Zeegers et al. 2019), we did not use this compound during the analysis and we just present its Mg K-edge cross-section. Moreover, we did not include spinel in the fitting of the astronomical data. This is because the aluminium in the compound could be misquantified as a consequence of possible calibration residuals in the Al edge[6] of the source spectrum. We report, in Table 3.1 (with the index #Mod), the complete list of the extinction profiles used to analyse the Mg and Si K-edges ISM absorption observations.

3.3 Astronomical observation

3.3.1 GX 3+1

We used the bright X-ray binary GX 3+1 as a test source. This source has a persistent bolometric luminosity of $\sim 6 \times 10^{37}\,\mathrm{erg\,s^{-1}}$ (den Hartog et al. 2003) and the spectrum shows deep Mg and Si absorption edges at 1.308 and 1.840 keV (9.50 and 6.74 Å), respectively. GX 3+1 (also known as Sgr X-1 and 4U 1744-26) is one of the first discovered cosmic X-ray sources. This X-ray binary was detected during an *Aerobee*-rocket flight on June 16, 1964 (Bowyer et al. 1965). Ever since this initial observation, this source has been intensely observed with multiple satellites: i.e. Hakucho (Makishima et al. 1983), Granat (Lutovinov et al. 2003), Ginga (Asai et al. 1993), Rossi X-ray Timing Explorer (RXTE, Kuulkers & van der Klis 2000), *Beppo*-SAX (Oosterbroek et al. 2001; den Hartog et al. 2003; Seifina & Titarchuk 2012), *Integral* (Chenevez et al. 2006), XMM-*Newton* (Piraino et al. 2012; Pintore et al. 2015), and *Chandra* (Schulz et al. 2016). The detection of multiple thermonuclear bursts (Makishima et al. 1983; Kuulkers 2002) suggests that the compact object hosted in GX 3+1 was an accreting neutron star. Thanks to the detection of these X-ray bursts with radius expansion the distance to the source was estimated to be in the range $4.2 - 6.4$ kpc with a best estimate of ~ 6.1 kpc (Kuulkers & van der Klis 2000; den Hartog et al. 2003). Spectral analysis of the source showed that its X-ray spectrum can be described by a model comprised of a black-body component, which is most likely associated with the accretion disc; and a Comptonised component, which is produced by an optically thick electron population located close to the neutron star corona (Oosterbroek et al. 2001; Mainardi et al. 2010; Seifina & Titarchuk 2012).

---

[6] See Figure 1.3 of *"The Chandra Proposers' Observatory Guide"* version 20.0 (http://cxc.harvard.edu/proposer/POG/).

3.3.2 Data reduction

We used seven datasets from *Chandra* (see Table 3.2), taken in timed exposure (TE) mode between July 2014 and May 2017, for a total exposure of $\sim 213\,\mathrm{ks}$. The spectrum has been observed by the High Energy Transmission Grating (HETG) instrument of *Chandra* (Canizares et al. 2005). Each dataset contains both High Energy Grating (HEG) and Medium Energy Grating (MEG) grating spectra which have been downloaded from the *Chandra* Grating-Data Archive and Catalogue (TGCat; Huenemoerder et al. 2011). Using the *Chandra* Interactive Analysis of Observations (CIAO; Fruscione et al. 2006) we combined the +/- first order for each HEG and MEG observation. The HEG and MEG spectra of a single observation are fitted together with the same model, correcting their instrumental normalisations when necessary. In total, we fit 14 spectra simultaneously.
The average count rate is $\sim$ 100 counts per second, which translates to a flux of $\sim 4.7 \times 10^{-9}$ erg s^{-1} cm^{-2} in the range $2-10$ keV (Oosterbroek et al. 2001). The observations are affected by pile-up because of this high flux. The bulk of the pile-up photons come from the MEG first order where the Si K edge resides on a back-illuminated CCD. The High Energy Transmission Grating Spectrometer (HETGS) has a high effective area between 1 and 3 keV, and we excluded some of the data ($E > 1.55\,\mathrm{keV}$). For HEG we consider the broad energy band in the range $1.1 - 5.2\,\mathrm{keV}$ ($\sim 2.4 - 10.8$ Å, respectively).

3.3.3 Continuum

We assumed the presence of both thermal and non-thermal emission to represent the continuum of GX 3+1 (Mitsuda et al. 1984). Among the thermal components present in SPEX we tested a black body (`bb`; Kirchhoff & Bunsen 1860), a disc-black body (`dbb`; Shakura & Sunyaev 1973; Shakura 1973), and a black body modified by Compton emission (`mbb`; Rybicki et al. 1986; Kaastra & Barr 1989). We tested non-thermal components of the power law (`pow`) and the Comptonisation model (`comt`, Titarchuk 1994). The best-fit model for GX 3+1 shows a black body plus a power law absorbed by a cold absorbing neutral gas model, simulated by the `hot` model in SPEX (de Plaa et al. 2004; Steenbrugge et al. 2005).

For the cold absorption model, we fixed the electron temperature at the lower limit of the `hot` model, that is $T_e = 0.5\,\mathrm{eV}$. We updated the photo-absorption cross section of neutral magnesium in SPEX, adding the resonance transitions, $1s \rightarrow np$, calculated using the Flexible Atomic Code[7] (A. Raassen, private communication). Our neutral Mg K-shell cross section is consistent with the Mg I profile obtained by Hasoğlu et al. (2014) applying the $R-$matrix method.

We simultaneously fitted the multiple datasets by coupling the absorption by neutral gas in the interstellar matter that we assume to be constant. The model was fitted to the data using the C-statistic (Cash 1979). Using the abundances tabulated by Lodders (2010), we obtained a hydrogen column density $N_{\mathrm{H}} = (1.91 \pm 0.05) \times 10^{22}\,\mathrm{cm}^{-2}$ that is consistent with the values of previous works. The average best fit of the continuum is represented in Figure

---

[7] Flexible Atomic Core, or FAC, is a software package used to calculate various various atomic radiative and collisional processes, including photo-ionisation and auto-ionisation (Gu 2008).

3.4 and the parameter values for each observation are reported in Table 3.2. The residuals in the Mg and Si K-edge region hint that we are overestimating the content of these two elements in the gas phase. Thus, it is necessary to add the dust model to fit the residuals present.

Furthermore, we tested the presence of collisionally ionised gas along the line of sight and the gas outflow from the source in its environments. Thus, we added an extra `hot` component plus the photo-ionised absorption model (`xabs` in SPEX, Steenbrugge et al. 2003) to our model. We did not find any evidence of ionised gas along the line of sight.

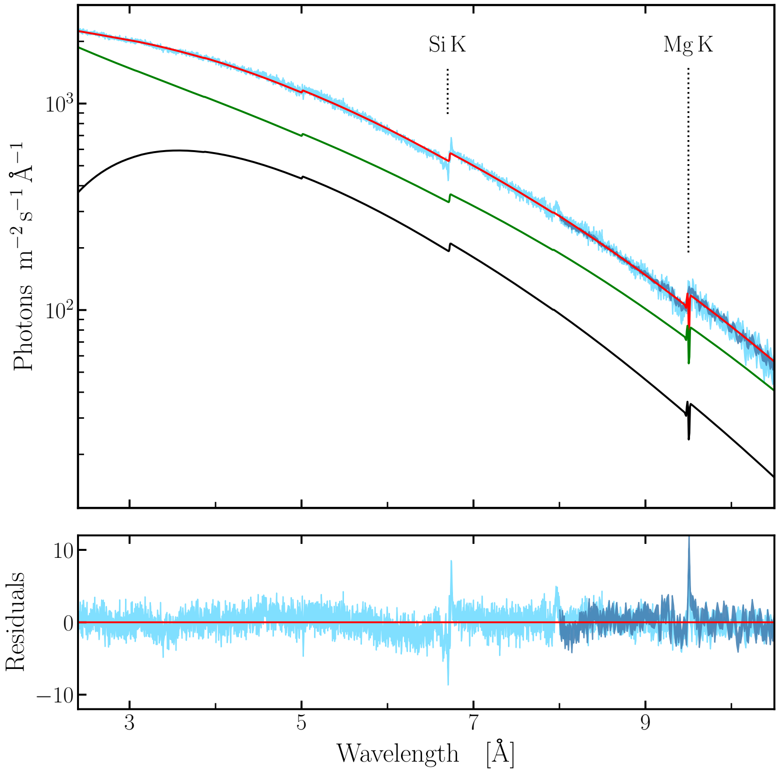

Figure 3.4: Continuum of GX 3+1. HEG (light blue) and MEG (dark blue) data from seven datasets were used to fit the continuum. We stacked and binned the observations for display purpose only. The average fit of the seven data sets is shown with a red solid line. The model consists of a black body (in black) and a power law (green) with a photoelectric absorption component with $N_{\mathrm{H}} \simeq 1.9 \times 10^{22}\,\mathrm{cm}^{-2}$. In the bottom panel we show the relative residuals defined as $(observed - model)/error$. The residual around 8 Å is due to the uncertainty on calibration for the aluminium K-edge.

Table 3.2: Broadband modelling of GX 3+1 using HEG and MEG data of seven observations.

#	Obsid	Date mm/yyyy	$t_{\rm exp}$ ks	$N_{\rm H}$ 10^{22} cm^{-2}	N$_{\rm pow}$ 10^{44} ph s^{-1} keV^{-1}	γ -	N$_{\rm bb}$ 10^{13} cm^2	$T_{\rm bb}$ keV	$F_{2-10\,\rm keV}$ 10^{-9} erg cm^{-2} s^{-1}	Cstat/dof
1	16307	07/2014	43.59	1.91 ± 0.02	29 ± 2	1.12 ± 0.04	2.7 ± 0.1	0.8 ± 0.1	7.5 ± 0.5	4198/3885
2	16492	08/2014	43.59		28 ± 2	1.09 ± 0.04	2.7 ± 0.2	0.8 ± 0.1	7.4 ± 0.5	4206/3885
3	18615	10/2016	12.16		25 ± 2	1.25 ± 0.04	1.8 ± 0.2	0.7 ± 0.2	4.8 ± 0.3	4132/3885
4	19890	05/2017	29.08		29 ± 2	1.23 ± 0.03	2.1 ± 0.1	0.8 ± 0.2	6.1 ± 0.4	4089/3885
5	19907	11/2016	26.01		22 ± 1	1.21 ± 0.04	2.4 ± 0.2	0.7 ± 0.1	4.8 ± 0.3	4058/3985
6	19957	04/2017	29.08		31 ± 2	1.20 ± 0.03	2.0 ± 0.1	0.8 ± 0.2	6.9 ± 0.4	4115/3885
7	19958	05/2017	29.08		29 ± 2	1.22 ± 0.03	2.1 ± 0.1	0.8 ± 0.1	6.2 ± 0.4	4104/3885
	Average			1.91 ± 0.02	28 ± 2	1.19 ± 0.04	2.3 ± 0.1	0.8 ± 0.1	6.2 ± 0.4	28906/27201

Notes. A part of the $N_{\rm H}$, the parameters are expressed using the default unit of SPEX. Errors given on parameters are 1σ errors.

3.3.4 Fit of the magnesium and silicon edges

After studying the continuum we fitted our dust models to *Chandra*-HETG data to study the solid phase of the ISM along the line of sight. In the fit we kept the temperature and the power-law index of the continuum model, leaving the respective normalisations free to vary. The dust models necessary to characterise the near-edge features of the Si and Mg K-edges were implemented in the multiplicative component `amol`. This SPEX model can fit a dust mixture consisting of four different types of dust at the same time. We followed the same method as described in Costantini et al. (2012), in which they tested all the possible configurations of the dust species and compared all the outcomes using a criterion based on the C-statistics value (see Section 3.3.5). The number of compound combinations is given by

$$C_{n,k} = \frac{n!}{k!(n-k)!} \quad , \tag{3.1}$$

where n is the number of compounds and k the combination class. Since each combination describes a single extinction model, $C_{n,k}$ represent the number of models utilised to fit the data.

Initially, only the extinction models obtained assuming the MRN size distribution ($n = 15$) were selected to study the XANES profiles at the Mg and Si K-edges. In Figure 3.5 we show the best fit of the two X-ray edges with the green solid line. The C-statistic (Cstat) value is 28199 with 27207 degrees of freedom (dof). The mixture that fits the data best consists mainly of amorphous olivine ($\sim 85\%$) and a smaller contribution of magnesium oxide.

Furthermore, we tested a different size distribution fitting the data using exclusively extinction cross sections obtained adopting the LMRN size distribution ($n = 15$), presented in Section 3.2.3. The relative best fit, with a Cstat/dof equivalent to 28182/27207, is shown in Figure 3.5 with the blue solid line. The C-stat improves with LMRN. However this fit requires a large amount of gas, for both Mg and Si, in order to fit the data (30% and 40%, respectively). This is difficult to reconcile with literature values (Jenkins 2009).

In the final analysis we considered both dust size distributions for all our measurements ($n = 30$). The best fit, with a Cstat value of 28129/27207, is represented with the red solid line. The relative residuals (for both HEG and MEG) are shown in the bottom panel. The dust that best represents the data is a mixture of amorphous olivine ($\sim 71\%$), crystalline fayalite ($\sim 16\%$), and amorphous quartz ($\sim 13\%$). The contribution of MRN and LMRN size distribution models is comparable at $\sim 57\%$ and $\sim 43\%$, respectively. The Si K-edge shows further residuals around the energy threshold. We discuss these residuals further in Section 3.4.1.

The mixture of standard and large MRN grains gives the best representation of the Mg and Si K-edges. The parameter values for the LMRN+MRN, MRN, and LMRN models with their statistical errors are summarised in Table 3.3. For clarity we divided the table into blocks. In the upper block of the table N_{1-4} indicate the column density of each dust species present in the model in units of 10^{17} cm^{-2}. In the second block we list the gaseous phase column density of each element of interest (N_{X}).

We summarise, in Table 3.4, the depletion values and total abundances for oxygen, magnesium, silicon, and iron. The abundances are calculated considering the total amount of atoms in both the gas and solid phases and these are compared with the solar abundances from Lodders (2010).

3.3.5 Evaluating the goodness of fit

Considering all the models calculated using both MRN and *L*MRN size distributions, we obtained 27405 models (from Equation 3.1). The *C*-statistics values representative of different dust mixtures can be similar. Since our candidate models are not-nested and with same number of free parameters, the standard model comparison tests (e.g. the χ^2 goodness-of-fit test, the maximum likelihood ratio test, and the F-test) cannot be used to evaluate the significance of the models (Protassov et al. 2002). The *Aikake Information Criterion* (AIC)[8] represents an elegant estimator of the relative quality of not-nested models without relying on time-consuming Monte Carlo simulations (Akaike 1974, 1998). The AIC value of a model is defined as

$$AIC = 2k - 2\ln(\mathcal{L}_{\max})\,, \tag{3.2}$$

where k is the number of fitted parameters of the model and $\mathcal{L}_{max}$ maximum likelihood value. Recalling the relation $Cstat = -2\ln\mathcal{L}$ (Cash 1979) the relation between C-statistic and AIC is clear.

In our work it is not the absolute size of the AIC value, but rather the difference between AIC values (ΔAIC), that is important. The AIC difference, defined as

$$\Delta AIC_i = AIC_i - AIC_{\min}\,,$$

allows for a comparison and ranking of the candidates models. For the model estimated to be best, $\Delta AIC_i \equiv \Delta AIC_{\min} \equiv 0$. Following the criteria presented in Burnham & Anderson (2002), we considered competitive with the selected best model the models with $\Delta AIC_i < 10$.

From the AIC-selected models, we obtained the relative contribution of each dust compound over the total dust obscuration. In Figure 3.6 we show the relative fraction of the dust species for both MRN (lighter colour) and *L*MRN (darker colour) dust size distributions. The red-highlighted bar indicates the compounds for which we are able to constrain their relative contribution. The amorphous olivine is the most representative compound among the selected models and has a relative value of 0.70 ± 0.09 (0.43 ± 0.04 and 0.27 ± 0.08 for the MRN and *L*MRN size distributions, respectively). In particular, the amorphous olivine ($a-$olivine) is the major contributor for every AIC-selected model. Models without any important contribution from $a-$olivine show $\Delta AIC_i > 35$.

A secondary contribution is given by the crystalline fayalite, which has a *L*MRN size distribution, which represents a relative value of 0.091 ± 0.088. For the remaining compounds we obtained the upper limits (grey bars in Figure 3.6) of their contributions, which are always lower than 0.07. Regarding the compounds listed in Table 3.1 and missing in Figure 3.6 (i.e. *a*-enstatite, *c*-En60Fs40, *c*-En90Fs10, *a*-forsterite, and *c*-olivine), they do not occur in any of the selected models and we consider their contributions negligible in this fit.The models selected with the AIC method agree not surprisingly with the best fit obtained with the *C*stat.

---

[8] AIC is founded in information theory. We refer to (Liddle 2007) and (Ranalli et al. 2017) for a extensive introduction to the informative criteria from an astrophysics viewpoint.

Table 3.3: Dust and gas column densities obtained by fitting the Mg and Si K-edges.

	MRN	***L*MRN**	**MRN+*L*MRN**	Units
N_1	*c*-quartz	*a*-enstatite	*a*-quartz^{mrn}	$10^{17}\,\mathrm{cm}^{-2}$
	< 0.4	1.9 ± 0.8	1.1 ± 0.2	
N_2	*a*-quartz	*c*-fayalite	*a*-olivine^{mrn}	
	$2.7^{+0.6}_{-0.2}$	1.7 ± 0.5	3.6 ± 0.3	
N_3	magnesia	*a*-olivine	*c*-fayalite^{lmrn}	
	$1.4^{+0.8}_{-0.3}$	$2.7^{+0.6}_{-0.1}$	1.3 ± 0.3	
N_4	*a*-olivine	*c*-en60fs40	*a*-olivine^{lmrn}	
	$5.7^{+0.1}_{-0.2}$	< 0.2	2.3 ± 0.3	
N_{O}	0.9 ± 0.2	1.2 ± 0.5	0.8 ± 0.1	$10^{19}\,\mathrm{cm}^{-2}$
N_{Mg}	< 0.2	2.4 ± 0.3	0.7 ± 0.3	$10^{17}\,\mathrm{cm}^{-2}$
N_{Si}	< 0.9	3.7 ± 0.3	0.6 ± 0.5	$10^{17}\,\mathrm{cm}^{-2}$
N_{Fe}	< 2.8	< 2.0	$0.2^{+2.0}_{-0.1}$	$10^{16}\,\mathrm{cm}^{-2}$
$Cstat$	28199	28182	28129	
dof	27207	27207	27207	

Notes. We use the abbreviations *c*− for crystalline and *a*− for amorphous.

3.4 Discussion

3.4.1 Silicon edge residuals

The HETG/*Chandra* data in GX 3+1 exhibit a peculiar shape of the pre-edge region of silicon K transition. In Figure 3.7 we show a zoom-in of the silicon K-edge. The complexity of this edge was already observed by Schulz et al. (2016). With our larger set of observations (approximately a double exposure time) we observed this complex structure with a significance $\gtrsim 5\sigma$. Schulz et al. (2016) inferred that the peak centred at 6.740 Å is due to X-ray scattering. However, its wavelength does not correspond to the scattering peak of our dust extinction model, which is instead centred at 6.728 Å. It is possible that the peak is contaminated by an unresolved and unknown instrumental artefact (Miller et al. 2002). Regarding the absorption present right before the onset of the edge, we speculate that its origin is attribute to ISM present along the line of sight and we tested different possibilities.

Neutral silicon

The K-shell X-ray absorption for a single, isolated silicon atom presents multiple resonance transitions $1s \rightarrow 3p$. We updated the Verner et al. (1996) silicon cross section present in Spex with these transitions, calculated using both the FAC and COWAN codes (Cowan

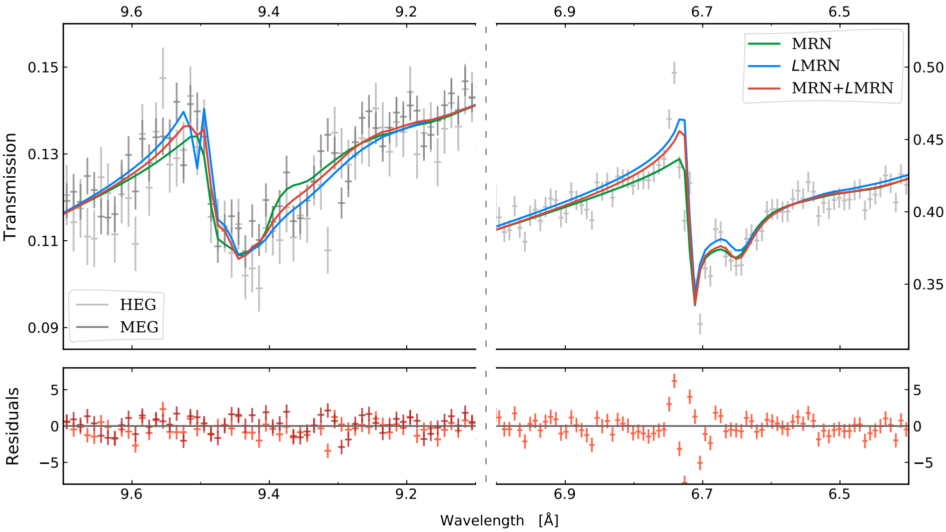

Figure 3.5: *Top panel*: Magnesium and silicon K-edges of GX 3+1. The HEG and MEG data are shown in light and dark grey, respectively. We do not consider MEG data for the Si K-edge because of the pile-up contamination. We fit the two edges using models with different grain size distributions: MRN models only in green, LMRN models only in blue, and both MRN and LMRN models in red. *Bottom panel*: We show the residuals defined as $(observed - model)/error$ of the best fit obtained using MRN and LMRN models. The HEG and MEG data are shown in light and dark red, respectively. The data are stacked and binned for display purposes.

1981, A. Raassen, private communication). Assuming the silicon depletion value found in the best fit ($\delta_{\rm Si} = 0.94$), with the update cross section we obtained an absorption feature with a strength similar to the absorption feature observed right before the onset of the Si K-edge. However, none of these absorption features correspond exactly to the energy measured by HETG: the absorption line calculated with the two different codes are shifted to lower energies (higher wavelengths) of $\Delta E \sim 1.5 - 4.5$ eV ($\Delta\lambda \sim 0.006 - 0.017$ Å). These shifts are noticeable since the differences are close to the energy resolution of HEG in the silicon region ($\Delta\lambda = 0.012$ Å). In Figure 3.7 the green dashed line shows the absorption line due to the resonance transitions calculated with the COWAN code, which presents the less divergent shift. Moreover, Hasoglu & Gorczyca (2018) calculated the K-shell photoabsorption of neutral silicon using a modified version of the R-Matrix method (Berrington et al. 1995). Their final result is somewhat consistent to our calculation using the COWAN code.

Ionised gas

We tested if a photo-ionised gas is able to reproduce the absorption feature right before the onset of the edge. Thus, we added a photo-ionised component (`xabs` in SPEX) with a systematic velocity that is free to vary to our model. This results in a modest column density

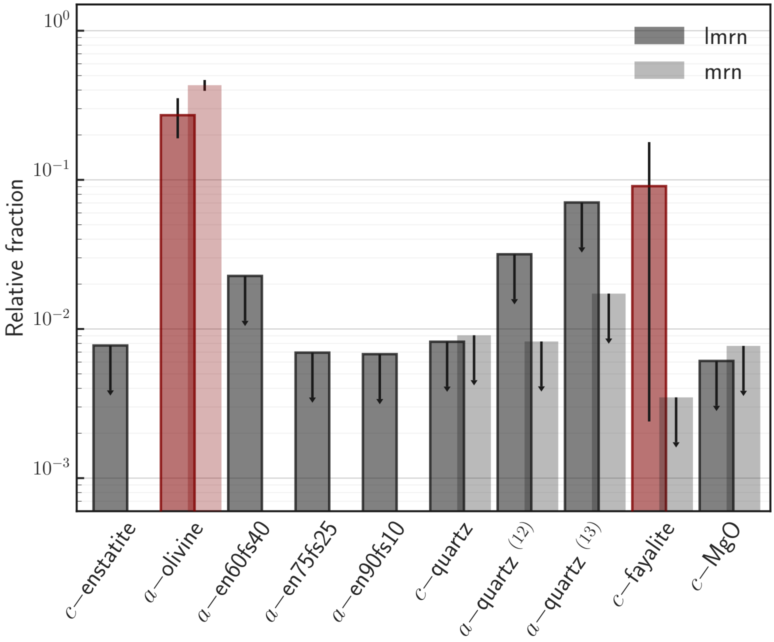

Figure 3.6: Bar plot of the relative abundance for each dust species calculated considering *AIC*−selected models. Darker bars represent models with a *L*MRN size distribution; lighter bars refer to MRN models. We highlight the dust species with a constrained relative fraction with red filled bars.

($N_{\rm H} = 3^{+7}_{-2} \times 10^{19}$ cm^{-2}) for an ionisation parameter of $\log \xi = 1.7^{+0.2}_{-0.4}$.
We also tested collisional ionised plasma (component `hot` in SPEX), with a temperature constrained between 0.3 and 2 keV, to ensure absorption by SiXIII in the Si K-edge region, obtaining an upper limit for the column density ($N_{\rm H} < 1.5 \times 10^{20}$ cm^{-2}).

Si-bearing dust

In the interstellar dust, silicon is potentially able to create a chemical bound with different elements than oxygen, the standard characteristic bond of silica and silicates. Therefore, we included in our Si K-edge model set cosmic dust candidates such as crystalline silicon (Witt et al. 1998; Li & Draine 2002), crystalline silicon carbide (SiC; Whittet et al. 1990; Min et al. 2007), and silicon nitride (Si_3N_4; Jones 2007)[9]. The Si-Si, Si-C, and Si-N bonds are characterised by lower energy thresholds and consequently, their Si K-edges are wavelength-shifted with respect to those of the silicate. We added magnesia (MgO) to our model to compensate for any silicate-poor (and therefore magnesium poor) fitting that we tested.

---

[9] The XANES profiles of crystalline Si, SiC, and Si_3N_4were taken from Chang et al. (1999) and analysed with the method presented in Section 3.2.3. We created the extinction model, adopting the MRN and *L*MRN size distributions.

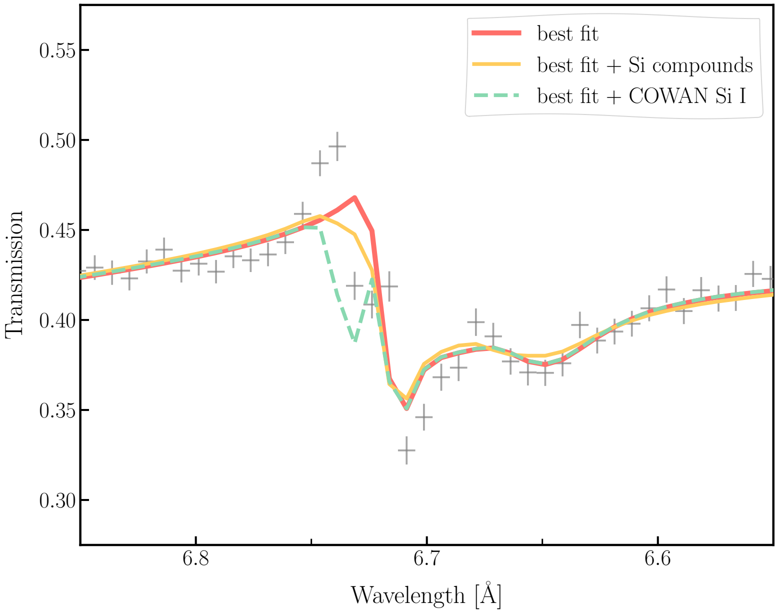

Figure 3.7: Zoom-in of the silicon K-edge. We represent the best fit with a red solid line. We show, in orange, the model obtained by adding secondary Si-bearing dust candidates presented in the text to the best fit. The green dashed line represents the best fit adding the neutral silicon cross section calculated with the COWAN code. We use a data bin size of $\sim 0.04\,\text{Å}$, approximately one-third full width half maximum (in other words the energy resolution of the detector).

The resulting model is presented in Figure 3.7 with a orange solid line. The fit has a better $C-$statistic value but a lower AIC value owing to the penalty term $2k$ in Equation 3.2.

Double silicate edge

We naively added a supplementary silicate component with systematic velocity free to vary to our best model and this resulted in a relative large amount of cold material ($N_{\mathrm{H}} \sim 3 \times 10^{17}\,\mathrm{cm}^{-2}$) with a receding velocity $\gtrsim 500\,\mathrm{km/s}$ along the line of sight. This scenario is hard to justify since such motion of matter is not observed the literature (e.g. van den Berg et al. 2014; Pintore et al. 2015) and furthermore the magnesium K-edge does not show an evident additional, redshifted feature.
We can also discarded porosity and different grain geometries as possible cause of the residuals since Hoffman & Draine (2016) showed that their effects on the silicon edge profile is negligible. Presently, we are not able to characterise the features located next to the onset of the Si K-edge between 6.72 and 6.75 Å. The comparison of the Mg and Si K-edges detected in different lines of sight will be crucial to understand the nature of it in forthcoming works.

Table 3.4: Abundances and fractional depletions.

Element	δ_Z	$A_Z/A_\odot$
Oxygen	$0.27^{+0.02}_{-0.02}$	$1.01^{+0.03}_{-0.02}$
Magnesium	$0.89^{+0.10}_{-0.10}$	$0.88^{+0.07}_{-0.08}$
Silicon	$0.94^{+0.06}_{-0.08}$	$1.21^{+0.08}_{-0.10}$
Iron	$0.99^{+0.01}_{-0.17}$	$1.13^{+0.17}_{-0.09}$

Notes. We indicate with δ_Z the fractional depletion of the elements. The term A_Z represents the total (dust plus gas) element abundance found analysing the spectrum of GX 3+1. The solar abundances used to calculate the ratio $A_Z/A_\odot$ are taken from Lodders (2010).

3.4.2 Depletions & Abundances

By fitting the low energy curvature of the X-ray spectrum of GX 3+1 and adopting the proto-solar abundances of Lodders (2010), we find a hydrogen column density of $N_{\rm H} = (1.91 \pm 0.02) \times 10^{22}\,{\rm cm}^{-2}$. Using the solar abundances of Anders & Grevesse (1989), adopted by previous authors, this value corresponds to $\sim 1.61 \times 10^{22}\,{\rm cm}^{-2}$ and is consistent with the neutral column density obtained by Oosterbroek et al. (2001), where $N_{\rm H} = (1.59 \pm 0.12) \times 10^{22}\,{\rm cm}^{-2}$. From the residuals of the continuum analysis in Figure 3.4, it is clear that the silicon and magnesium edges cannot be represented only by pure gas absorption and it is necessary to introduce the dust component by adding `amol` to the fitting model. The dust models used in the analysis (see Table 3.1) contain oxygen, magnesium, silicon, and iron. The content of these elements in the solid phase is expressed by the depletion values shown in Table 3.4.

Silicon is highly depleted along the line of sight of the source: more than 90% is found in the solid phase. Similarly, a high percentage of magnesium (more than 80%) is included in dust grains. The two elements share the similar depletion values, which is in agreement with the fractional depletion observed by Dwek (2016) and Jenkins (2009). The depletions of oxygen and iron in dust are derived indirectly from the model since the absorption edges of these elements fall outside the spectral band. Therefore, no strong conclusions can be drawn regarding these two elements. However, oxygen shows a moderate fractional depletion value ($\delta_{\rm O} = 0.27 \pm 0.02$). This value would be consistent with the depletion observed for lines of sight with different neutral column densities (e.g. Costantini et al. 2012; Pinto et al. 2013), confirming the weak correlation between the depletion of oxygen and the physical conditions of the environment (e.g. density and temperature; Whittet 2002). Instead, iron seems highly depleted consistently with the values shown by Whittet (2002) and Jenkins (2009).

The total abundances were evaluated by summing the column densities of the gas and solid phases for each element. Our values do not depart significantly from the solar values (see Table 3.4).

3.4.3 Dust chemistry

The simultaneous analysis of the silicon and magnesium edges is in principle able to constrain the typical cations-to-silica ratio (Mg+Fe)/Si of interstellar silicate grains. For the best fit of the data we find that $(\text{Mg} + \text{Fe})/\text{Si} \sim 2$, considering only pyroxene and olivine compounds. This gives $\text{O}/\text{Si} = 4$, implying that silicates along the line of sight present an olivine-type stoichiometry. Indeed, the amorphous and crystalline olivine, together with the fayalite, are characterised by the orthosilicate anion $[\text{SiO}_4^{4-}]$ and represent $\sim 91\%$ of the dust in our fit. Moreover, the best fit is characterised by $\text{Mg}/(\text{Mg} + \text{Fe}) = 0.41 \pm 0.02$ (and therefore by $\text{Mg} : \text{Fe} = 0.69 \pm 0.05$). Fayalite gives the major contribution of iron for the dust component and it is preferred over the magnesium-rich forsterite. We found a larger presence of iron in silicates with respect to the values observed for different lines of sight (e.g. Costantini et al. 2012), wavelengths (e.g. Tielens et al. 1998; Min et al. 2007; Blommaert et al. 2014), and/or environments (e.g. the interplanetary medium; Altobelli et al. 2016), where Mg-rich silicates are detected. However, we cannot constrain the iron depletion value since we cannot characterise the iron absorption edges directly and simultaneously. The analysis of the *AIC*-selected models shows similar ratios (namely, $(\text{Mg} + \text{Fe})/\text{Si} \approx 1.9$; $\text{Mg}/(\text{Mg} + \text{Fe}) \approx 0.45$; $\text{Mg}/\text{Fe} \sim 0.8$), which agrees with the nominal best-fitting model.

3.4.4 Dust crystallinity

The best fit suggests the presence of a relatively large amount of crystalline grains along the line of sight of GX 3+1. Defining the crystalline-to-amorphous ratio as ζ_1 = crystalline dust / (crystalline dust + amorphous dust) (Zeegers et al. 2019), we find a value of $\zeta_1 = 0.15 \pm 0.03$. This is consistent to the range of values found by Zeegers et al. (2019), $\zeta_1 = 0.04 - 0.12$, using several several LMXBs. Comparing our results with the literature, we find higher percentages of crystalline dust with respect to the fractions observed by the infrared spectroscopy. For example, Li et al. (2007), Kemper et al. (2004), analysing the 9.7 μm and 18 μm features, set the possible maximum crystalline fraction of the total silicate mass in the ISM to a maximum of 5% and 1.1%, respectively.

The crystalline ratio that we find may be partially biased by the limitation of our measured set of compounds. Previous works already showed and discussed the presence of this bias (Zeegers et al. 2017). Indeed, our laboratory model set does not include the amorphous counterpart for all the compounds (see Table 3.1) and consequently, the estimation of the crystallinity may be overestimated. Indeed, in our case, the crystalline ratio is led by the crystalline fayalite, for which the amorphous counterpart, which might contribute to the total fit, is not available.

However, if this observed amount of crystalline dust is real, the differences with the infrared observations might be explained in two possible ways. The first is that cold and dense regions, accessible only by X-rays, host cosmic dust with a different crystalline order with respect to the grains which populate the diffuse medium. These differences could be explained by the theoretical model presented by Tanaka et al. (2010) and Yamamoto et al. (2010), which predict a low-temperature crystallisation of amorphous silicate grains induced by exothermic chemical reactions. An alternative explanation is that we might be detecting poly-mineralic silicates, which are expected to be agglomerated particles, possibly containing both crystalline and glassy constituents. In this case, because X-rays are sensitive to a short-range order, XAFS would show crystalline features, whereas there might not be sharp crystalline features in the infrared spectrum Speck et al. (2011).

3.4.5 Dust size

The best fit of the magnesium and silicon K edges is obtained assuming the existence of two dust populations with different size distributions: MRN and *L*MRN presented in Section 3.2.3. From the results of analysing the two X-ray edges, the two distributions show similar weights with $\mathrm{MRN}/(L\mathrm{MRN} + \mathrm{MRN}) \sim 0.57$.
This approach was motivated by the known complexity of the line of sight towards GX 3+1, which is at a distance of about 6.1 kpc (Kuulkers & van der Klis 2000) and at longitude $l = 2.29$ and latitude $b = 0.79$ in galactic coordinates (Ebisawa et al. 2003). Therefore, assuming a distance towards the Galactic centre of 8.5 kpc, the source is located in the outskirts of the Galactic bulge. In particular, this source is situated just behind the "near 3 kiloparsec arm", which is expanding at a speed of $\sim 57\,\mathrm{km/s}$ (van Woerden et al. 1957; Dame & Thaddeus 2008), and the molecular ring (Clemens et al. 1988; Jackson et al. 2006), located at a distance of 5.5 and 5 kpc from the Sun, respectively. The CO emission in these latter two regions is clumped (Bania 1980). In particular, the molecular ring contains about 70% of all the molecular gas inside the solar circle (Clemens et al. 1988). The ring is thus an enormous reservoir of material in gaseous and solid form. Moreover, GX 3+1 is aligned with the known Bania's Clump 2, a molecular cloud complex near the Galactic centre (Bania 1977; Stark & Bania 1986). Several dust lanes in the Galactic bar seem to be connected with this feature (Liszt 2008). However, because of the uncertainties on the distance estimate, it is unclear if our source is embedded in these structures or if it is in front of them (Marshall et al. 2008).
Within 5 kpc from the Sun the line of sight crosses several spiral arms (located at different solar distances; Benjamin 2008; Urquhart et al. 2014): i.e., Sagittarius-Carina ($\sim 1.5\,\mathrm{kpc}$), Scutum-Centaurus ($\sim 3.5\,\mathrm{kpc}$), and Norma arms ($\sim 4.5\,\mathrm{kpc}$).

In this scenario, diffuse dust with a MRN distribution would be naturally located within the spiral arms. The large dust population, containing mainly amorphous olivine and fayalite, would instead probably belong to the molecular regions close to the Galactic centre. Here, shielded from dissociating interstellar radiation, the dust grains can easily grow (e.g. Chapman et al. 2009; Hirashita 2012). The presence of large grains in these regions is thought to be supported by the "core shine" effect seen in mid- and near-infrared observations of dark clouds (e.g. Pagani et al. 2010; Lefèvre et al. 2014).
Moreover, at these particular coordinates, the 3D polarisation model, developed by Martínez-Solaeche et al. (2018) taking into account observed dust emission and observed intensity and polarisation power spectra, shows an enhanced polarisation vector P at distance $\gtrsim 3.8\,\mathrm{kpc}$. As found by Kim & Martin (1995) the astronomical silicates of $a > 0.1\,\mu\mathrm{m}$ n size can reproduce the observed polarisation of the starlight.
Finally, previous works have already observed the presence of different dust populations distributed along the line of sight. Recently, Vasilopoulos & Petropoulou (2016) analysed

the X-ray dust-scattered rings from the LMXB V404 Cyg. These authors found that the dust grains are concentrated in different dust layers each characterised by a different size distribution. However, future works, using different grain size distributions such as Weingartner & Draine (2001), Zubko et al. (2004), and The Heterogeneous dust Evolution Model for Interstellar Solid (THEMIS, Jones et al. 2013; Köhler et al. 2014) as well as an in-depth understanding of the instrument around crucial edges, will be necessary to study the dust distribution in detail.

3.5 Conclusion

In this paper we present the first attempt to build an X-ray broadband extinction model with multiple edges. In particular, in this work we focus on the simultaneous modelling of the magnesium and silicon extinction profiles both based on synchrotron measurements. This approach allows us to better constrain the cosmic dust properties and to avoid degeneracies that can occur using a single edge fit.

We introduce the Mg K-edge extinction cross sections of 12 different dust species focussing on their XANES profiles. We analyse the X-ray spectrum of the bright LMXB GX 3+1, whose hydrogen column density is optimized for the simultaneous detection of the magnesium and silicon edges, and we characterise the gas and dust along the line of sight. Below we summarise the main results.

- The absorption spectrum shows the presence of both gas and dust along the line of sight. We find standard solar abundances of magnesium and silicon ($A_{\rm Mg}/A_{\odot} = 0.88 \pm 0.08$ and $A_{\rm Si}/A_{\odot} = 1.21 \pm 0.10$) and their relative depletion values are in agreement with the results obtained by Jenkins (2009) ($\delta_{\rm Mg} = 0.89 \pm 0.10$ and $\delta_{\rm Si} = 0.94 \pm 0.6$).
- We find that amorphous olivine is the most representative dust species along the line of sight of GX 3+1. The olivine orthosilicates characterised by the anion SiO_4 are highly preferred over silica (SiO_2) and pyroxene (SiO_3). For the best fit we find a cations-to-anion ratio of $(\rm Mg + Fe)/Si \sim 2$.

To fully characterise the silicon and magnesium K-edges and in view of future X-ray missions with better resolving power (XRISM and Athena) it is necessary to develop accurate and detailed cross sections of neutral gas. Those can indeed explain the residuals that we still find in our analysis in the Si K-edge region and they will help to determine the depletion values of the respective elements. Moreover it is also crucial to understand if the pre-edge of the silicon K-edge is contaminated by possible instrumental artefacts and how these affect the modelling of dust extinction.

ACKNOWLEDGEMENTS

DR, EC, IP, and MM are supported by the Netherlands Organisation for Scientific Research (NWO) through The Innovational Research Incentives Scheme Vidi *grant 639.042.525. The Space Research Organization of the Netherlands is supported financially by NWO. We acknowledge SOLEIL for provision of synchrotron radiation facilities and we thank Delphine*

Vantelon for assistance in using the beamline LUCIA. This research has made use of data obtained from the Chandra *Data Archive and the* Chandra *Source Catalog, and software provided by the* Chandra *X-ray Center (CXC) in the application package CIAO. We are grateful to the referee for valuable comments that lead to improvements of the paper. We thank A.J.J. Raassen for providing the photo-absorption cross section of neutral magnesium and silicon. We are grateful to P. Ranalli for useful discussions. We also thank A. Dekker and D. Lena for reading an early draft of the manuscript and for providing valuable comments and suggestions.*

4

Magnesium and silicon in interstellar dust: an X-ray overview

D. Rogantini, E. Costantini, S.T. Zeegers, M. Mehdipour, I. Psaradaki, A.J.J. Raassen, C.P. de Vries, L.B.F.M. Waters

Submitted to Astronomy & Astrophysics

Abstract

The dense Galactic environment is a large reservoir of interstellar dust. Therefore, this region represents a perfect laboratory to study the properties of the cosmic dust grains. X-rays are the most direct way to detect the interaction of light with dust present in these dense environments. The interaction between the radiation and the interstellar matter imprints specific absorption features in the X-ray spectrum. We study them with the aim of defining the chemical composition, the crystallinity and structure of the dust grains which populate the inner regions of the Galaxy. We investigate the magnesium and the silicon K-edges detected in the *Chandra*/HETG spectra of eight bright X-ray binaries, distributed in the neighbourhood of the Galactic centre. We model the two spectral features using accurate extinction cross sections of silicates, that we have measured at the synchrotron facility Soleil, France. Near the Galactic centre magnesium and silicon show abundances similar to the solar ones and they are highly depleted from the gas phase ($\delta_{\rm Mg} > 0.90$ and $\delta_{\rm Si} > 0.96$). We find that amorphous olivine with a composition of $\rm MgFeSiO_4$ is the most representative compound along all lines of sight according to our fits. The contribution of Mg-rich silicates and quartz is low (less than 10%). The amount of crystalline dust is constrained to be less than 11% by our model. For the extragalactic source LMC X-1, we find a preference for forsterite, a magnesium-rich olivine. Along this line of sight we also observe an underabundance of silicon $A_{\rm Si}/A_{\rm LMC} = 0.5 \pm 0.2$.

4.1 Introduction

Over the last 20 years, X-ray absorption spectroscopy demonstrated to be a successful tool to study the chemical and physical properties of interstellar dust. Pioneering works (e.g. Lee et al. 2002; Takei et al. 2003; Costantini et al. 2005) already detected dust signatures in the X-ray spectra taken with the high-resolution spectrometers aboard XMM-*Newton* and *Chandra*, at that time newly launched (both in 1999). These dust features generically known as X-ray Absorption Fine Structures (XAFS, Newville 2004), appear as a modulation of the region beyond the energy of photoelectric absorption edge. They are produced by the interaction between a photoelectron wave and all the other waves backscattered by neighbouring atoms in the solid lattice. XAFS are sensitive to the composition and structure of the absorber and, therefore, they represent a unique probe for investigating the chemistry, crystallinity and size distribution of the interstellar dust.

Most of the common metals included in the cosmic dust show a photoelectric edge in the X-ray band $0.2 - 8$ keV. This allows us to investigate the nature of different dust species like silicates, carbonaceous material, sulphides and oxides. Nowadays, accurate extinction cross-sections of several interstellar dust analogues are available. It is possible to characterise the XAFS for multiple photoelectric K-shells: in particular the K edges of carbon (Bilalbegović et al. 2018; Costantini et al. 2019), oxygen (Costantini et al. 2012, Psaradaki et al., in prep.), magnesium (Rogantini et al. 2019), silicon (Zeegers et al. 2017, 2019), iron (Lee & Ravel 2005; Rogantini et al. 2018), aluminium, sulfur and other low abundant elements (Costantini et al. 2019) plus the L-edges of iron (Lee et al. 2009; Westphal et al. 2019). The extinction cross-sections are calculated from the optical constants specific to the material. These are mainly measured using synchrotron radiation or through electron energy loss spectroscopy (e.g. with the electron microscope, Egerton 2009). An alternative is to use the density functional theory (DFT, Jones 2015), a computational quantum mechanical modelling which allows the prediction and calculation of material behaviour based on the relative electron density.

The spectra of bright low-mass X-ray binaries, lying in the plane of our Galaxy, are perfect laboratories to investigate the dust fine structures. Indeed, relative large column densities guarantee an optimal optical depth of the edge and high fluxes are necessary to ensure a sufficient signal-to-noise ratio to distinguish the dust features. Zeegers et al. (2019) analysed the line of sight of 9 bright X-ray sources nearby the Galactic centre. They found that most of the spectra can be fit well by amorphous olivine ($MgFeSiO_4$). Nonetheless, interstellar silicates are expected to exist in various forms in the interstellar medium. For example, Kemper et al. (2004), Chiar & Tielens (2006), and Min et al. (2007) compared laboratory spectra with mid-infrared observations and found, in fact, that a mixture of olivine and pyroxene dust models fit the $\sim 9\,\mu$m feature.

The broad, smooth and featureless infrared bands around 9.7 and 18 μm also suggest that most of the interstellar silicates are amorphous (Li & Draine 2001b; Li et al. 2007; Molster et al. 2010). From a direct comparison of the Sgr A* spectrum with theoretical spectra for pure silicates, Kemper et al. (2004) found that only 1.1% of the dust should have a crystalline order. Li et al. (2007) concluded that the allowed degree of crystallinity would be $\sim 5\%$ considering the effect of the ice mantle coating the silicates cores on the determination of the crystallinity degree of silicates. Recent X-ray observations found a higher amount of crystalline dust, between 3-20%, in the region near the centre of the Galaxy (Rogantini et al. 2019; Zeegers et al. 2019). Moreover, crystalline dust has been observed in a variety of environments, from proplanetary disks (Honda et al. 2003; Natta et al. 2007) to diffuse interstellar medium (Westphal et al. 2014). The precise amount of crystalline dust and its survival in the interstellar medium are still widely debated in the scientific community.

X-ray absorption spectroscopy provides the possibility to study the composition of the dust grains in different environments (Lee et al. 2002; Draine 2003; Ueda et al. 2005; Valencic et al. 2009; Costantini et al. 2012; Pinto et al. 2013; Corrales et al. 2016; Hoffman & Draine 2016; Schulz et al. 2016; Zeegers et al. 2019). Dust grains undergo a cyclic process of production, growth and destruction which may change their properties. Dust particles mainly condense in the vicinity of late-type stars, in nova and supernova ejecta. In harsh and turbulent regions, the grains are exposed to radiation which may reprocess and destroy them. Only refractory cores survive in these environments (Whittet 2002). Differently, in the dark and cold molecular clouds of the Galaxy, grains are shielded from the radiation. Consequently, we expect to observe larger grains in these environments with a more complex structure. In these low temperature environments ices may accrete onto these pre-existing refractory cores. The ice mantle is the chemical laboratory for the production of more elaborate molecules.
Due to their high penetration capability, X-rays can be used to probe the dust grain properties in Galactic regions characterised by different densities.

From studying the metallicity of the B-type stars, Cepheids and open clusters, the abundances of the common elements show, in general, a gradient as a function of the distance from the Galactic centre (Rolleston et al. 2000; Pedicelli et al. 2009; Genovali et al. 2014). These variations would be a consequence of the successive generations of stars having enriched the interstellar matter. Thus, abundance investigation can provide a key to understanding the formation and chemical evolution of galaxies. However, only a few measurements are available within 5 kpc from the Galactic centre (Rich et al. 2017; Schultheis et al. 2019). With X-rays, we can investigate directly the abundances and depletions of several metals in the inner part of the Galaxy and therefore extend the characterisation of the metallicity gradient observed in the Galactic plane.

In this study, we focus on the magnesium and silicon K-edges (located at 1.3 and 1.84 keV, respectively) through which we study the denser region in the central part of the Galaxy. Currently, *Chandra*/HETG represents the best instrument for studying simultaneously the two absorption K-edges because of the high effective area and energy resolution of its devices, MEG and HEG, in the $1-2\,\mathrm{keV}$ energy range.
Magnesium and silicon are two abundant metals in the interstellar matter: respectively, they are the eight and the ninth most abundant element in the Universe with $\log A_{\mathrm{Mg}} = 7.599$

and $\log A_{\rm Si} = 7.586$[1] (Lodders 2010). Magnesium is mostly the product of carbon and neon burning in core-collapse supernovae, whereas silicon is produced by oxygen shell burning (Arnett & Thielemann 1985; Thielemann & Arnett 1985). In the interstellar matter, they are both highly depleted from the gas phase: in dense environments, more than 90% of their mass is thought to have been locked in dust particles (Jenkins 2009; Palme et al. 2014; Zhukovska et al. 2018). The depletion[2] of magnesium and silicon is adequately explained by the formation of a mixture of both iron-rich and iron-poor silicates (Jones & Williams 1987; Jones 2000; Kimura et al. 2003; Mattsson et al. 2019). Other silicon- and magnesium-bearing species, such as silicon carbide (SiC), spinel ($MgAl_2O_4$), gehlenite ($Al_2Ca_2SiO_7$) and diopside ($MgCa(SiO_3)_2$) are too rare to make a significant contribution (Jones 2007). Thus, magnesium and silicon share the same depletion trend as a function of the environment. This is also observed in the interstellar medium of galaxies with different metallicity (De Cia et al. 2016).

In our pilot work we showed the analysis of Mg and Si K-edges of the bright X-ray binary GX 3+1 (Rogantini et al. 2019, henceforth, Paper I). Here, we expand the number of sources to characterise the cosmic dust properties and quantify the abundances and depletion of silicon and magnesium in the dense neighbourhood of the Galactic centre. The source sample is presented in Section 4.2 together with the data reduction and the analysis of the *Chandra* observations. The analysis of the simultaneous fits of the silicon and magnesium K-edges is described in Section 4.4.5. We discuss the results and the properties of the interstellar dust in Section 4.4. Finally, in Section 4.5, we give our conclusions and a summary of our results. Throughout the paper, for the fitting process we use the C-statistics (Cash 1979; Kaastra 2017) unless otherwise stated. The errors quoted are for the 68% confidence level.

4.2 Sample and analysis

4.2.1 Source sample selection

We select our sources from the *Chandra* Data Archive[3] following a criterion to optimise the detections of the two edges. The primary selection is based on the hydrogen column density ($N_{\rm H}$). The column density towards the source is closely related to the optical depths of the edges. The range $0.5 - 5 \times 10^{22}\,{\rm cm}^{-2}$ allows an adequate level of X-ray transmittance for our analysis. Second, we select the sources with a flux larger than $1 \times 10^{-11}\,{\rm erg\,cm^{-2}\,cm^{-1}}$ in the soft X-ray energy band $0.5 - 2\,{\rm keV}$ and enough exposure time, in order to ensure a high signal-to-noise ratio to observe the fine structures of the edges.

---

[1] The abundances are given in logarithmic scale relative to $N_{\rm H} = 10^{12}$ In other words for element X,

$$\log A_{\rm X} = 12 + \log(N_{\rm X}/N_{\rm H})\ .$$

It is often more convenient to express the abundances of the common metals on a linear scale relative to $N_{\rm H} = 10^6$, i.e. in parts per million (ppm) relative to hydrogen: $A_{\rm Mg} = 39$ ppm and $A_{\rm Si} = 35$ ppm.

[2] We define depletion as the ratio of the dust abundance to the total abundance of a given element, i.e. both gas and dust.

[3] See http://cxc.harvard.edu/cda/

In this study, we use bright low mass X-ray binaries (LMXBs). They obey the two conditions above and their spectrum, generally, does not host emission lines in the soft energy band. Moreover, we verify that the sources in our sample are persistently bright, in order to make the best use of the satellite exposure times.

Finally, we select only the observations taken in timed exposure (TE) mode. The continuous clocking (CC) mode is not suitable for analysing the magnesium and silicon K-edge. Absorbed CC-mode spectra are affected by the contribution of the two-dimensional scattering halo around the source collapse in a one-dimensional image. Its contribution is hard to disentangle from the dispersed spectrum, particularly in the absorption edge regions (we refer to the *Chandra* Proposers' Observatory Guide[4], version 21.0). In total, we select seven Galactic X-ray binaries plus the brightest X-ray source in the Large Magellanic Cloud, LMC X-1. These sources are summarised in Table 4.1 where we indicate the obsID, exposure time, and average count rate for each observation, plus the Galactic coordinates and distance of the sources, as reported in the literature.

4.2.2 Data reduction

We obtain the observations for our analysis from the *Chandra* Transmission Gratings Catalog and Archive (TGCAT[5], Huenemoerder et al. 2011). For each observation, we select both HEG and MEG spectra and we combine separately the positive and negative first orders using the tool `combine_grating_spectra` included in the Chandra's data analysis system CIAO (version 4.11, Fruscione et al. 2006). For the brighter sources, the grating spectra taken in TE mode are affected by photon pile-up. The bulk of pileup events comes from the MEG 1st orders and affects, in particular, the harder part of the spectra. Both magnesium and silicon edge regions are relatively less affected, as in these regions the spectrum is depressed due to the interstellar medium column density (see also Appendix B.1).

All spectra show an apparent 1-resolution-element-bin-wide excess at 6.741 Å. This excess has been previously observed also in other sources, with different interpretations: an emission line from Si XIII (e.g. Iaria et al. 2005), dust scattering peak (Schulz et al. 2016, and Paper I) or instrumental effect (Miller et al. 2002, 2005). Here, we adopt the latter interpretation (justified in Appendix B.3). Therefore, we add to the continuum a delta line model centred at 6.741 ± 0.001 Å. This value has been estimated using the spectrum of three bright and well-known low mass X-ray binaries, namely GX 9+9, Cyg X-2, and 4U 1820-30, plus the blazar Mrk 421 (see Appendix B.3).

4.2.3 Continuum and absorption

In order to study the dust absorption, first we characterise the broadband spectrum and then we focus on the fit of the magnesium and silicon K-edges with our dust extinction models. To fit the underlying continuum of each source we use the spectral analysis code SPEX[6] version 3.05 (Kaastra et al. 1996; Kaastra et al. 2018). We use a two-component spectral

---

[4] http://cxc.harvard.edu/proposer/POG/pdf/MPOG.pdf

[5] See http://tgcat.mit.edu/

[6] 10.5281/zenodo.1924563

Table 4.1: X-ray binaries

Obsid	Date	Exp.	Rate	Galactic coordinates		Distance
				l	b	
	UT	ks	c/s	deg	deg	kpc
GRS 1758-258						
2429	2001-03-24	29.6	17.2	4.508	−1.361	$8^{(a)}$
2750	2002-03-18	27.5	30.3			
GRS 1915+105						
660	2000-04-24	30.6	127.2	45.366	+0.219	$8.6 \pm 2.0^{(b)}$
7485	2007-08-14	48.6	150.3			
GX 3+1						
16492	2014-08-17	43.6	100.4	2.294	+0.794	$6.1^{(c)}$
16307	2014-08-22	43.6	102.2			
18615	2016-10-27	12.2	67.6			
19890	2017-05-23	29.1	86.2			
19907	2016-11-02	26.0	70.0			
19957	2017-04-30	29.1	93.1			
19958	2017-05-21	29.1	86.4			
GX 9+1						
717	2000-07-18	9.0	165.2	9.077	+1.154	$5^{(d)}$
GX 17+2						
11088	2010-07-25	29.1	176.5	16.432	+1.277	$9.1 \pm 0.5^{(e)}$
H 1742-322						
16738	2015-06-11	9.2	16.8	357.255	−1.833	$8.5^{(f)}$
17679	2015-06-12	9.2	17.4			
17680	2015-06-13	9.2	18.0			
16739	2015-07-03	26.8	10.7			
IGR J17091-3624						
12406	2011-10-06	27.3	46.8	349.525	+2.213	$12^{(g)}$
17787	2016-03-30	39.5	29.9			
17788	2016-04-30	38.8	28.5			
LMC X-1						
93	2000-01-16	18.9	26.5	280.203	−31.516	$48^{(h)}$
11074	2010-01-02	17.2	24.2			
11986	2010-01-07	8.2	25.5			
11987	2010-01-18	18.6	22.3			
12068	2010-01-04	13.1	23.5			
12071	2010-01-09	4.3	25.7			
12069	2010-01-08	18.1	26.0			
12070	2010-01-10	17.4	25.7			
12089	2010-01-21	14.7	23.3			
12090	2010-02-26	14.0	23.4			
12072	2010-01-05	18.1	23.9			

References. (a) Soria et al. (2011): assumed distance; (b) Reid et al. (2014); (c) den Hartog et al. (2003); (d) Iaria et al. (2005); (e) Galloway et al. (2008); (f) Steiner et al. (2012); (g) Court et al. (2017): assumed distance; (h) Orosz et al. (2009).

model consisting of a thermal component in the soft end and non-thermal component in the hard end of the spectral bandpass. In order to obtain the best fit of the continuum we test different combinations of several SPEX emission models: blackbody (`bb`, Kirchhoff & Bunsen 1860), disk blackbody (`dbb`, Shakura & Sunyaev 1973; Mitsuda et al. 1984), modified blackbody (`mbb`, Rybicki et al. 1986; Kaastra & Barr 1989) as thermal models and power-law (`pow`) and Comptonisation (`comt`, Titarchuk 1994) as non-thermal models.

The absorption by cold gas is given by the multiplicative model `hot` (de Plaa et al. 2004; Steenbrugge et al. 2005) fixing the electron temperature at the lower limit, that is $kT_{\rm e} = 0.5\,{\rm eV}$. By default, SPEX adopts protosolar abundances for the gas phase (Lodders 2010). For LMC X-1 we apply the typical element abundances found in the Large Magellanic Cloud, listed with the relative references in Table B.2.

In this study we update the neutral magnesium and silicon cross-sections with respect to the official release of SPEX adding the resonance transitions, $1s \rightarrow np$, calculated using both the Flexible Atomic Code (Gu 2008) and COWAN code (Cowan 1995), respectively. We present them in Appendix B.2.

For sources with multiple data sets, we fit simultaneously the continuum of the different observations by coupling the absorption by neutral gas in the interstellar matter that we assume to be constant. In Table B.1 we summarise the parameter values of best model for each source.

Also, we test whether there is ionised gas along the line of sight towards the sources. In particular, we investigate the presence of collisionally ionised gas, by adding to the model an extra `hot` component, and photo-ionised gas, by applying the `xabs` model (Steenbrugge et al. 2003) to the continuum. For an accurate modelling, it is essential to distinguish absorption lines due to ionised gas, especially if they appear near the edges, where they can be confused with absorption features by neutral gas or cosmic dust. We find the presence of photo-ionised gas in outflow in GRS 1915+105 with an outflow velocity of $v \sim 145 \pm 9\,{\rm km/s}$ and logarithmic ionisation parameter[7] $\log \xi = 3.72 \pm 0.02$ and $N_{\rm H} = (5.9 \pm 0.7) \times 10^{20}\ {\rm cm}^{-2}$. These values are consistent, within the uncertainties, with the results obtained by Ueda et al. (2009).

Along the line of the sight of the remaining sources, we do not find significant evidence of either photo-ionised and collisional-ionised gas.

4.3 The magnesium and silicon edge models

In Paper I, we show how the simultaneous fit of multiple edges of different elements allows us to better constrain, with respect to a single-edge modelling, the chemical properties and size of the interstellar grains limiting the possible degeneracies of the fit. These edges are the result of the absorption by cold gas together with the interstellar dust present along a relatively dense line of sight. In the case of magnesium and silicon, we expect a large contribution by cosmic dust since a large fraction of these elements is included in dust grains.

---

[7] Here, the ionisation index is defined as $\xi = L/(nr^2)$ where L is the luminosity of the source, n the density and r the distance between the ionising source and the absorbing gas.

Whereas gaseous contribution is already modelled by the `hot` component, it is necessary to add to the broadband model the `AMOL` model (Pinto et al. 2010) for shaping the cosmic dust scattering and absorption. In order to evaluate the dust-to-gas ratio, we set these two models free to compete for the fitting of the edges.

In our analysis, we use dust extinction models based on accurate laboratory measurements and they include both the scattering and absorption cross-sections. We summarise them in Table 4.2, where we specify their chemical formula and crystallinity. The laboratory measurements and post-processing are explained in Zeegers et al. (2017, 2019) and Paper I. Here, we assume the Mathis-Rumpl-Nordsieck (MRN, Mathis et al. 1977) dust grain size distribution, which follows a power-law distribution, $dn/da \propto a^{-3.5}$ where a is the grain size, with minimum and maximum cut-offs of 0.005 and 0.25 μm, respectively.

The `AMOL` model allows for four dust compounds to be tested in a given fitting run. Four is the maximum for different compounds that can be constrained in the modelling. Thus, we test all the possible combinations of the 14 dust models following the method of Costantini et al. (2012) and obtaining 1001 different models to fit for each source.

We select as best fit the dust mixture which presents the minimum C-statistic value among all the models. We list in Table 4.3 the dust mixture of the best fits with the relative column densities. In Figures 4.1 and 4.2 we show, for all the sources, the *Chandra* data and their best fit around the magnesium and silicon edges and residuals to the best fit. Following the procedure presented in Paper I, we select the models statistically similar to the best fit through the *Aikake Information Criterion* (AIC, Akaike 1974, 1998). In particular, the $\Delta\mathrm{AIC_i}$, namely the difference between the i-model and the selected best model, allows a quick comparison and ranking of the candidate's models. Based on the criteria presented in Burnham & Anderson (2002) we consider the i-models with $\mathrm{AIC_i} < 4$ competitive with respect to the selected best model. The overall analysis of these selected models permits to understand and define the characteristics of the most representative dust compounds and at the same time to rule out the dust species which fail in shaping the magnesium and silicon edges.

In Figure 4.3 we show the relative fractions of the dust compounds. For clarity, we cluster the compounds with similar crystallinity and structure. In particular, compounds number (1, 2, 4) are grouped as crystalline olivine (c-olivine); compound number 3 as amorphous olivine (a-olivine); (6, 8, 11) as c-pyroxene; (5, 7, 9, 10) as a-pyroxene; 12 as c-quartz; (13, 14) as a-quartz. In the bar chart, we show the models with $\Delta\mathrm{AIC} < 4$ in light blue together with the models with $\Delta\mathrm{AIC} < 10$, in black, which include fits with has a less significance compared to the best fit.

4.4 Discussion

4.4.1 Mineralogy of the dust toward the Galactic center

The properties of the cosmic dust derived through the fits of the eight X-ray binaries are listed in Table 4.3. The analysis of the sample shows a clear preference for amorphous olivine (compound number 4) in the best fit and all the fits with $\Delta\mathrm{AIC} < 4$. In every source, the

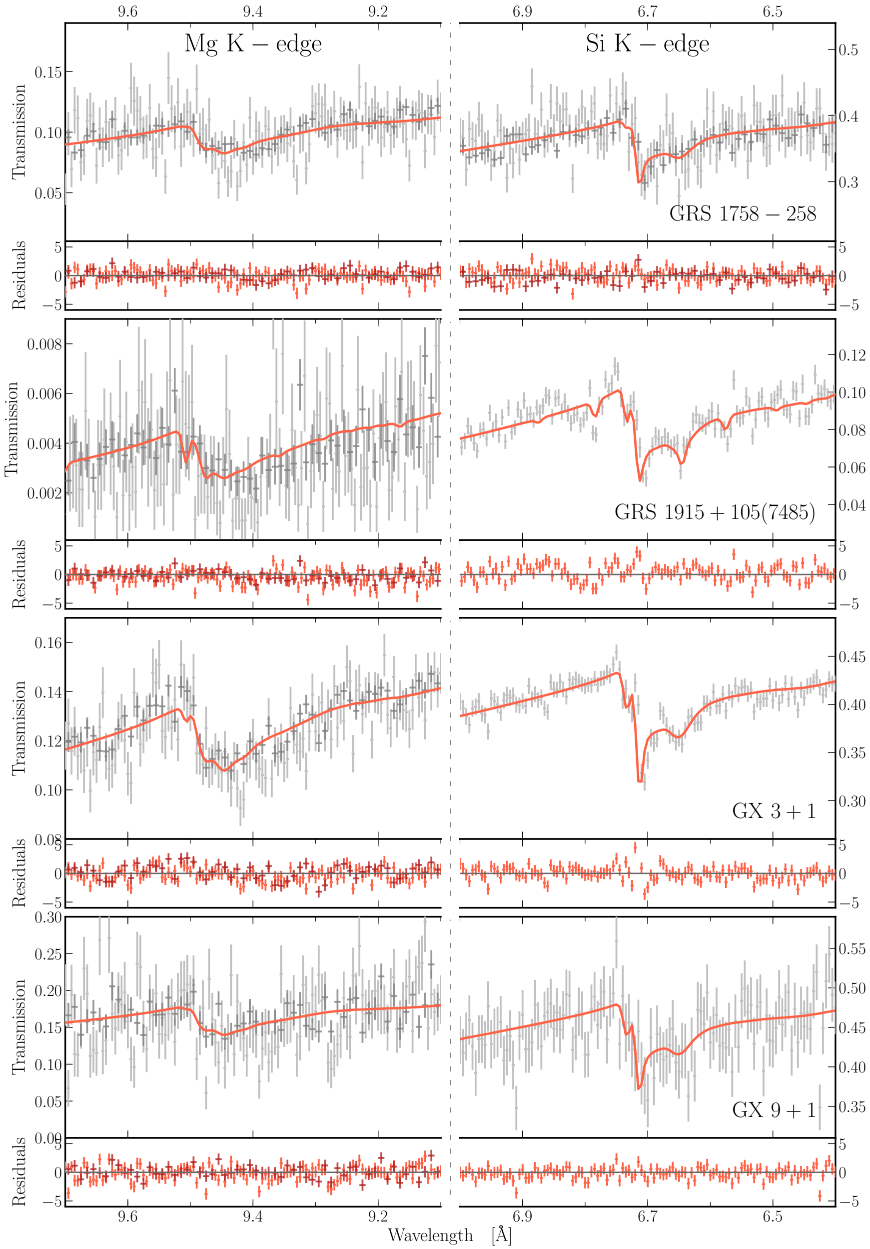

Figure 4.1: Zoom in on the magnesium (on the left column) and silicon K-edge (on the right column). The HEG and MEG data are respectively shown in light and dark grey. The solid red line represents the best fit. In bottom panels we show the residuals defined as (observation−model)/error. The data are stacked and binned for display purpose.

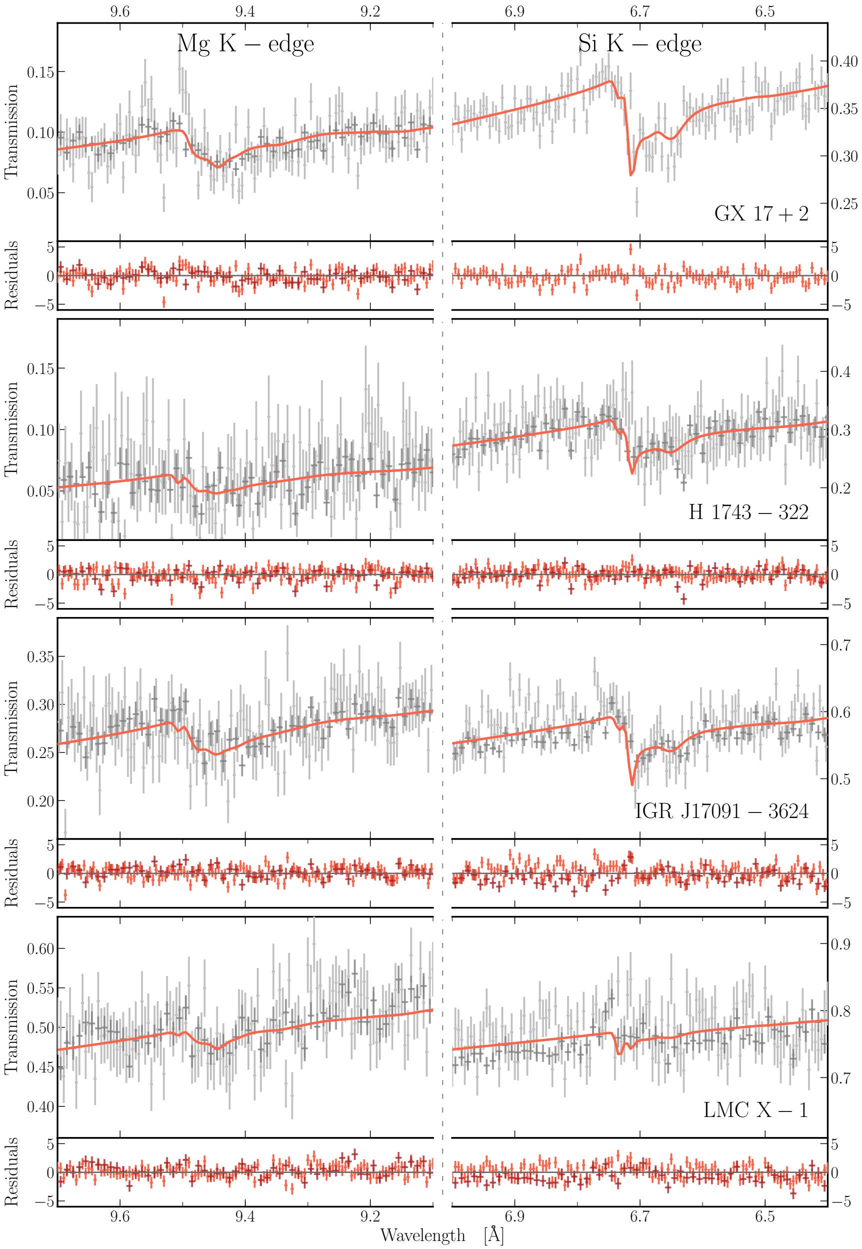

Figure 4.2: Zoom in on the magnesium (on the left column) and silicon K-edge (on the right column). The HEG and MEG data are respectively shown in light and dark grey. The solid red line represents the best fit. In bottom panels we show the residuals defined as (observation−model)/error. The data are stacked and binned for display purpose.

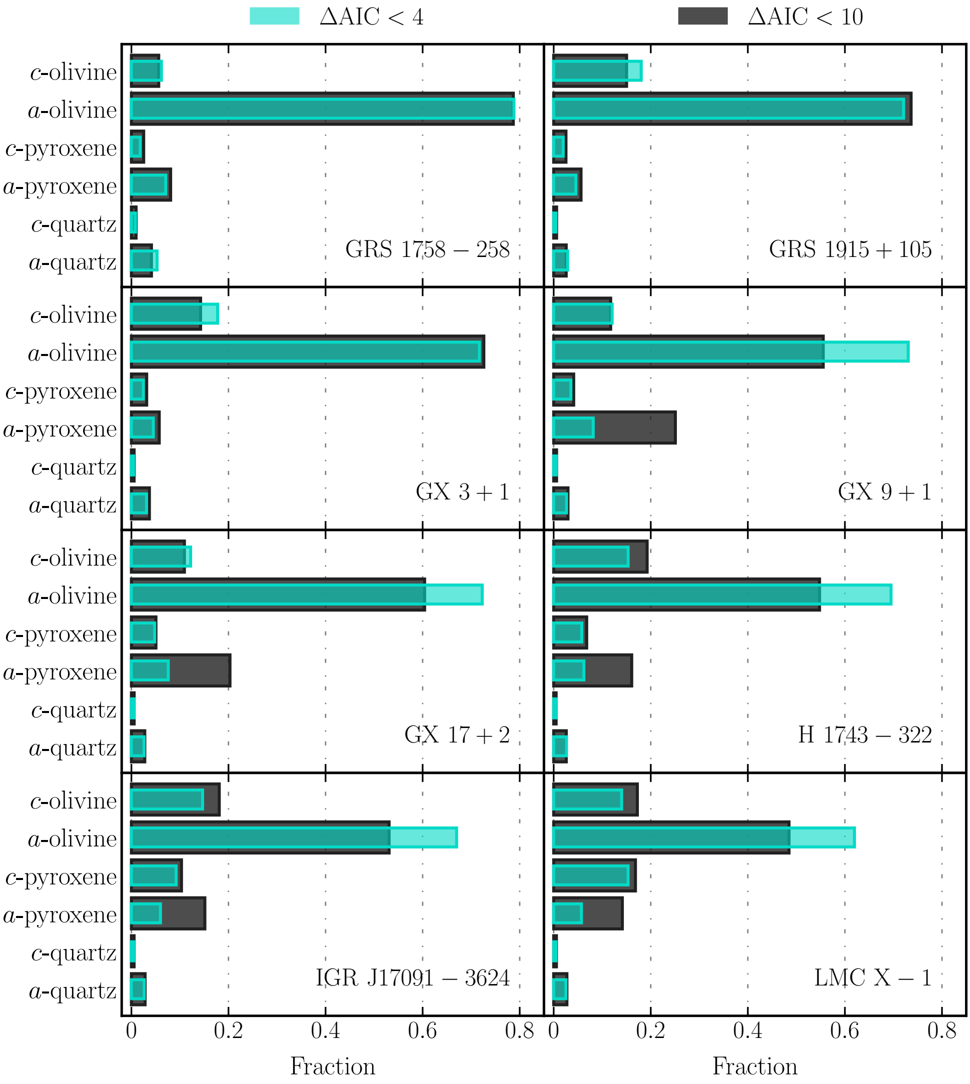

Figure 4.3: Relative fraction for the different dust species calculated considering models with $\Delta\mathrm{AIC} < 4$ in light blue and $\Delta\mathrm{AIC} < 10$ in dark gray. We gather the compounds by their structure and crystallinity (see Section 4.4.5 for details). We use the abbreviations $c-$ for crystalline and $a-$ for amorphous.

Table 4.2: List of interstellar dust extinction models.

#	Name	Chemical formula	Form
1	Forsterite	Mg_2SiO_4	crystalline
2	Fayalite	Fe_2SiO_4	crystalline
3	Olivine	$MgFeSiO_4$	amorphous
4	Olivine	$Mg_{1.56}Fe_{0.4}Si_{0.91}O_4$	crystalline
5	Enstatite	$MgSiO_3$	amorphous
6	Enstatite	$MgSiO_3$	crystalline
7	En60Fs40	$Mg_{0.6}Fe_{0.4}SiO_3$	amorphous
8	En60Fs40	$Mg_{0.6}Fe_{0.4}SiO_3$	crystalline
9	En75Fs25	$Mg_{0.75}Fe_{0.25}SiO_3$	amorphous
10	En90Fs10	$Mg_{0.9}Fe_{0.1}SiO_3$	amorphous
11	En90Fs10	$Mg_{0.9}Fe_{0.1}SiO_3$	crystalline
12	Quartz	SiO_2	crystalline
13	Quartz	SiO_2	amorphous
14	Quartz	SiO_2	amorphous

Notes. The nomenclature En(x)Fs(1-x) indicates the fraction of magnesium (or iron) included in the compound. "En" stands for enstatite (the Mg-pure pyroxene, $MgSiO_3$) and "Fs" for ferrosilite (the Fe-pure pyroxene, $FeSiO_3$). The two amorphous quartz present two different level glassiness: compound number 13 has an intermediate amorphous form whereas compound 14 has a full amorphous structure.

amorphous olivine represents more than 60% of the total amount of the dust reaching $\sim 95\%$ of the total for GRS 1758-258. In the bottom part of Table 4.3 we report the quantities ζ_1, ζ_2, and ζ_3, which, respectively, give information about the crystallinity, structure and chemistry of the cosmic dust. Following the notation used by Zeegers et al. (2019), they are defined as:

$$\begin{aligned}
\zeta_1 &= \text{crystalline dust}/(\text{crystalline dust} + \text{amorphous dust}) \ , \\
\zeta_2 &= \text{olivine}/(\text{olivine} + \text{pyroxene}) \ , \\
\zeta_3 &= \text{Mg}_{\text{dust}}/(\text{Mg}_{\text{dust}} + \text{Fe}_{\text{dust}}) \ .
\end{aligned} \tag{4.1}$$

These quantities together with the chemical composition represent the dust properties accessible by X-ray absorption spectroscopy and we discuss them separately below. The extragalactic source LMC X-1 will be discussed in Section 4.4.4.

Crystallinity

In our analysis the best fits show a crystallinity ζ_1 between $0 - 0.3$. Among all the sources, the microquasar GRS 1915+105 shows the largest amount of crystalline dust with $\zeta_1 = 0.27 \pm 0.05$. On the other hand, selecting the fits of X-rays sources with higher quality data, GX 3+1, GX 9+1, GX 17+2, and considering the uncertainties on the values, we observe crystallinity below 0.2. In particular for GX 3+1 we obtain a crystallinity upper limit of 0.01.

Table 4.3: Best fitting dust compounds for each source and their derived properties.

Dust compound	GRS1758-258	GRS1915+105	GX 3+1	GX 9+1	GX 17+2	H1743-322	IGRJ17091-3624	LMC X-1
	Dust column densities [$10^{17}\,\mathrm{cm}^{-2}$]							
(1) *c*-Forsterite	–	–	–	–	0.6 ± 0.3	–	–	0.45 ± 0.08
(2) *c*-Fayalite	–	6 ± 1	–	< 0.3	< 0.8	2 ± 1	–	–
(3) *a*-Olivine	7.7 ± 0.4	15 ± 1	7.0 ± 0.1	6 ± 2	7.8 ± 0.7	8 ± 2	4.1 ± 0.1	0.33 ± 0.09
(4) *c*-Olivine	–	–	–	–	–	–	–	< 0.23
(5) *a*-Enstatite	–	–	–	< 2.9	–	–	–	–
(6) *c*-Enstatite	–	–	–	–	–	–	–	< 0.05
(7) *a*-En60Fs40	–	–	–	–	–	–	–	–
(8) *c*-En60Fs40	–	–	–	–	–	–	–	–
(9) *a*-En75Fs25	< 0.9	< 0.2	–	–	< 0.6	–	< 0.4	–
(10) *a*-En90Fs10	–	–	–	–	–	–	–	–
(11) *c*-En90Fs10	–	–	–	–	–	–	–	–
(12) *c*-Quartz	0.6 ± 0.4	–	< 0.08	< 0.4	–	< 0.7	< 0.09	–
(13) *a*-Quartz	–	–	1.4 ± 0.2	–	–	< 0.1	0.4 ± 0.3	–
(14) *a*-Quartz	< 0.3	< 0.1	< 0.06	–	–	–	–	–
Total	8^{+2}_{-1}	21 ± 2	8.4 ± 0.3	6^{+5}_{-2}	8^{+2}_{-1}	10 ± 3	$4.5^{+0.8}_{-0.4}$	$0.8^{+0.4}_{-0.2}$
ζ_1	0.07 ± 0.04	0.27 ± 0.05	< 0.01	< 0.07	0.11 ± 0.07	0.21 ± 0.18	< 0.02	> 0.73
ζ_2	> 0.94	> 0.98	1	> 69	0.96 ± 0.03	1	0.95 ± 0.04	> 0.92
ζ_3	0.50 ± 0.03	0.36 ± 0.02	0.50 ± 0.01	0.58 ± 0.14	0.52 ± 0.08	0.39 ± 0.08	0.51 ± 0.02	> 0.76

Notes. In the upper part of the table we report the column density for each dust species and we calculate the total dust column density. In the bottom we show the value of ζ_1, ζ_2, and ζ_3 as defined in the text. Errors given on parameters are 1σ errors.

Therefore, ζ_1 may vary depending on the line of sight. The other sources in the analysis, show similar results, although for some of them, the ζ_1 value is affected by large uncertainties because of the quality of the data.

Even considering the uncertainties on the parameters ζ_1, the average crystallinity fraction, $< \zeta_1 > \sim 0.11$, is larger than the ones observed at longer wavelengths, in particular in the infrared. The smooth shape of the ~ 9 μm and ~ 18 μm absorption features suggests that 1.1% of the dust in the interstellar medium appears to be crystalline (Kemper et al. 2004). One explanation might be that bias could affects our estimation of the amount of crystallinity along the line of sight of the X-ray binaries. Indeed, our laboratory model set does not include the amorphous counterpart of all the compounds (see Table 4.2). Consequently, the fit of the magnesium and silicon edges may overestimate the fraction of crystalline dust. In particular, this seems the case for GRS 1915+105 where the crystalline percentage is driven by the fayalite, for which the amorphous cross-section is not available (see also Zeegers et al. 2017, and Paper I).

However, if we are observing a real overabundance of crystalline grains, this apparent discrepancy with the infrared results might be attributed to the presence of poly-mineralic silicates which are expected to be agglomerated particles, possibly containing both glassy and crystalline constituents (Marra et al. 2011; Speck et al. 2011). In this case, because X-rays are sensitive to a short range order (Mastelaro & Zanotto 2018), XAFS would show crystalline features, whereas there might not be sharp crystalline features in the infrared spectrum (see Zeegers et al. 2019, Paper I and reference therein). Infrared vibrational spectroscopy is indeed sensitive to a long-range order of the particles which is missing for poly-mineralic grains (Oberti et al. 2007).

Another argument is the number of studied sight lines in the infrared. This is limited and it is therefore hard to conclude from these infrared sight lines that the whole interstellar medium is build up op 1.1% crystalline dust.

Olivine, pyroxene, quartz

The dust observed along the line of sight of our sources shows overall an olivine structure characterised by the anion $[SiO_4]^{-4}$. Indeed, we find values of ζ_2 very close to unity (meaning that the dust is olivine dominated) except for GX 9+1 for which we find a lower limit of 0.7 due to the large uncertainties on the column densities of the dust compounds. For all the fits with ΔAIC < 4 and ΔAIC < 10 pyroxene is not important.

Our results are consistent with Zeegers et al. (2019); they observe similarly a large fraction of olivine dust along the lines of sight of their sample of X-ray binaries near the Galactic centre. In the infrared, the broad silicate features are typically modelled with a mixture of olivines and pyroxenes (Molster et al. 2002; Chiar & Tielens 2006; Henning 2010). However, Kemper et al. (2004) found that cosmic silicates are composed of $\sim 85\%$ of olivine and $\sim 15\%$ of pyroxene, values similar to our observations.

Differently, Fogerty et al. (2016) studying the line of sight of heavily reddened stars observed with *Spitzer* found the presence of polivene, an amorphous silicate with intermediate stoichiometry ($Mg_{1.5}SiO_{3.5}$, Jäger et al. 2003). This compound is not present in our sample set and we plan to include the relative XAFS cross-section in future X-ray studies.

Finally, the overall contribution of quartz in the fits of the sources is modest. Even in the fits with ΔAIC < 10, its fraction is always less than 10%. This is consistent with the infrared spectroscopy results, where a strong absorption band by quartz particles in the interstellar medium has never been observed (Sargent et al. 2009).

4.4.2 Silicate cations

Analysing the silicate features in the infrared spectrum of an evolved star, Kemper et al. (2002) found that $\sim 80\%$ of the silicate is characterised by a comparable amount of magnesium and iron cations and less than 10% is represented by magnesium-pure pyroxene ($MgSiO_3$) and olivine (Mg_2SiO_4). Similar results were found by Kemper et al. (2004), where they concluded that the cation composition of the dust in the interstellar medium is most likely $\zeta_3 \approx 0.5 - 0.6$, where ζ_3 expresses the magnesium percentage overall cations (see Equation 4.1). As shown in Table 4.3, the dust that we observed along the line of sight of the X-ray binaries shows similar properties. In general, the cation ratio ζ_3 has values very close to 0.5. Only two sources, H 1743-322 and GRS 1915+105, diverge from the average trend showing a preference for iron-rich olivine, namely fayalite. Whereas for the former source ζ_3 is affected by large uncertainties because of the quality of the data, for the latter it shows a consistent deviation from the average value found in the other sources. The predominance of the fayalite is also observed in the fits with ΔAIC < 4 (see Figure 4.3). In future studies, it would be interesting to investigate the iron content of silicates including in the fit the iron K-edge located at ~ 7.1 keV. Iron is highly depleted in gas form but little is known about its form and occurrence in cosmic dust (Dwek 2016). Unfortunately, the relative low resolving power in the hard band of the current X-ray mission limits the detection of the iron K-edge. This will be possible with the micro-calorimeters aboard the coming X-ray Imaging and Spectroscopy Mission (XRISM, Tashiro et al. 2018) and the future Athena X-ray mission (Nandra et al. 2013; Barret et al. 2016). From the simulation of these detectors, the hydrogen column density and the flux of GRS 1915+105 ($N_{\rm H} \sim 5\ \times 10^{22}$ cm^{-2} and $F_{2-10\ \rm keV} \sim 1$ Crab) will allow studying simultaneously the K edges of Mg, Si and Fe (Rogantini et al. 2018).

4.4.3 Abundances and depletions

In Table 4.4 we report the depletion and abundance values of magnesium and silicon that we observed along the lines of sight of the X-ray binaries. We find that both elements are significantly depleted from the gas phase of the interstellar medium near the Galactic centre. Silicon, in particular, shows depletion values consistently higher than 0.95. Since the signal-to-noise in the magnesium edge is usually lower than the silicon region, the uncertainties on the estimates are consequently larger, and we often find lower limits. These depletion values are consistent with Whittet (2002) and Jenkins (2009).

Absolute abundances, calculated summing the gas and the dust contribution, show that in the environment near the Galactic centre, sampled by these sources, values are consistent with solar.

The abundances and depletion do not show any trend with the hydrogen column density. This is not surprising as our sources show a limited interval of line-of-sight column densities, ranging between $(1-5)\ \times 10^{22}$cm^{-2}, which we can extend to $(1-10) \times 10^{22}$ cm^{-2} for

Table 4.4: Abundances and depletions.

Source	$N_{\rm X}^{\rm tot}$ $10^{17}\,{\rm cm}^{-2}$	$\delta_{\rm X}$	$A_{\rm X}$ $10^{-5}\,{\rm H}^{-1}$	$A_{\rm X}^{\rm dust}$ $10^{-5}\,{\rm H}^{-1}$	$A_{\rm X}/A_{\odot}$
Magnesium					
GRS 1758-258	7.7 ± 0.5	> 0.97	3.6 ± 0.3	3.6 ± 0.3	0.9 ± 0.1
GRS 1915+105	20 ± 3	0.8 ± 0.1	4.0 ± 0.5	3.0 ± 0.2	1.0 ± 0.1
GX 17+2	9.4 ± 2.2	> 0.97	4.3 ± 0.9	4.3 ± 0.9	1.0 ± 0.3
GX 3+1	7.0 ± 0.1	> 0.99	3.7 ± 0.1	3.7 ± 0.1	0.9 ± 0.1
GX 9+1	8.5 ± 3.5	> 0.90	5 ± 2	5 ± 2	1.3 ± 0.5
H1743-322	9.6 ± 2.8	> 0.74	4 ± 1	3.0 ± 0.7	0.9 ± 0.3
IGR J17091-3624	4.4 ± 0.2	> 0.96	3.6 ± 0.2	3.6 ± 0.2	0.9 ± 0.1
LMC X-1	1.4 ± 0.3	> 0.99	0.8 ± 0.2	0.7 ± 0.2	0.20 ± 0.05
Silicon					
GRS 1758-258	8.4 ± 0.8	0.98 ± 0.01	3.9 ± 0.4	3.8 ± 0.4	1.0 ± 0.1
GRS 1915+105	22 ± 2	0.98 ± 0.01	4.2 ± 0.3	4.2 ± 0.3	1.1 ± 0.1
GX 17+2	9.3 ± 2.0	0.98 ± 0.01	4.3 ± 0.9	4.2 ± 0.9	1.1 ± 0.2
GX 3+1	8.7 ± 0.2	0.96 ± 0.01	4.5 ± 0.1	4.4 ± 0.1	1.2 ± 0.1
GX 9+1	7.7 ± 2.3	0.96 ± 0.03	5 ± 1	5 ± 1	1.2 ± 0.4
H1743-322	11 ± 3	0.97 ± 0.02	4 ± 1	4 ± 1	1.0 ± 0.3
IGR J17091-3624	4.8 ± 0.3	0.98 ± 0.01	4.0 ± 0.3	3.9 ± 0.3	1.0 ± 0.1
LMC X-1	0.9 ± 0.3	> 0.98	0.5 ± 0.1	0.5 ± 0.1	0.13 ± 0.04

Notes. $N_X^{\rm tot}$ represent the total column density of the X element, $\delta_{\rm X}$ its depletion from the gas phase, A_X the total abundance, $A_X^{\rm dust}$ the abundance of the X element in dust.The solar abundances used to calculate the ratio $A_X/A_{\odot}$ are taken from Lodders (2010).

Si considering the sources studied by Zeegers et al. (2019). Moreover, our sources are all located within 5 kpc from the Galactic centre. In this view our results on the abundances are in agreement with the results obtained by previous works (Davies et al. 2009; Genovali et al. 2015; Martin et al. 2015) which advance the idea that the abundance gradient of the magnesium and silicon flatten close to solar abundances in the inner part of the Galaxy.

4.4.4 LMC X-1

LMC X-1 is the only extragalactic source in our sample. It is the brightest X-ray source of the Large Magellanic Cloud, located at a distance of 48 kpc. Despite the long exposure time ($\sim$ 160 ks, see Table 4.1), the flux is not high enough to guarantee an optimal signal-to-noise ratio. Therefore, the best value of the fits are affected by larger uncertainties compared to the fits of the spectra of the Galactic sources.
Less than 12% of the hydrogen column density towards the Large Magellanic Cloud, 4×10^{21} cm^{-2} (Kalberla et al. 2005), is of Galactic origin (Hanke et al. 2010). Thus, to model

the absorption, we use the typical Large Magellanic Cloud abundances found in the literature and given in Table B.2. Similar to the Galactic lines of sight, magnesium and silicon are highly depleted from the gas phase. In particular, we observe depletion values for magnesium and silicon of $\delta_{\mathrm{Mg}} > 0.98$ and $\delta_{\mathrm{Si}} > 0.99$, respectively. These results are consistent with the work by Tchernyshyov et al. (2015).

Comparing the abundances of the two elements with the abundances tabulated in Table B.2 we find $A_{\mathrm{Mg}}/A_{\mathrm{LMC}} = 1.0 \pm 0.3$ and $A_{\mathrm{Si}}/A_{\mathrm{LMC}} = 0.5 \pm 0.2$. Moreover, our fit show the presence of magnesium-rich silicate, in particular, the presence of forsterite which is the most representative compound in the dust mixture. We obtain a cation ratio ζ_3 with an upper limit of 0.76. Since our set of compounds does not include the amorphous counterpart of the forsterite, the crystallinity ratio, ζ_1, could be biased (see the discussion over GRS 1915+105 in Section 4.4.1 and in Paper I). A possible presence of forsterite in its amorphous state would, therefore, decrease the crystalline ratio.

Our results hint at a possible under-abundance of silicon along the line of sight of LMC X-1. However, the quality of the data in the silicon region (see Figure 4.2) affect our estimation. The values obtained studying the supernova remnants are also affected by large uncertainties (Maggi et al. 2016; Schenck et al. 2016) due to the poor statistics in the Si line feature. Moreover, the interstellar matter abundances vary over the entire Magellanic Cloud. Indeed, an abundance lower than the average is also found by Schenck et al. (2016) in the two supernova remnants (0540-69.3 and DEM L316B) close to LMC X-1.

4.4.5 Two edges fit

In this work we made use of the simultaneous fit of two edges (magnesium and silicon) in order to derive the dust properties. This is important to remove some of the degeneracies in the model. For example, Zeegers et al. (2019) only studied the Si K-edge of the GRS 1758-258 and GX 17+2 with the same technique and dust models used in the present work. Whereas for GX 17+2, which benefited from a high quality data, we find similar results when we include the magnesium K-edge, for GRS 1758-258 the joint fit of the two dust edges improves significantly the modelling of the absorption. Using a single edge, a global fit would not provide a definitive answer on the dust chemistry (Zeegers et al. 2019). However, thanks to the magnesium K-edge we can constrain the dust composition. The fit shows a striking preference for the amorphous olivine; a preference that persists even for the fits with $\Delta\mathrm{AIC} < 10$. Also the estimates of the abundances and depletion benefit from the addition of the Mg K-edge, decreasing the uncertainties on the relative best values by a factor of 4. Fitting multiple edges together help to reduce the degeneracies of the fit and to better constrain the properties of the dust. This has been done, previously, by Costantini et al. (2012) and Pinto et al. (2013) where they fit simultaneously iron L-edges with the oxygen K-edge both located below 1 keV.

4.5 Conclusion

In this paper, we characterise the absorption by the material present in the dense environments towards and near the Galactic centre. We study the X-ray spectrum of seven bright X-ray binaries which lie in the Galactic plane. In particular, we inspect the magnesium and silicon K-edges at 1.3 and 1.84 keV, respectively. We evaluate the abundances of the two elements considering both dust and gas contributions. For every line of sight, we observe Mg and Si abundances consistent with the solar ones. Moreover, magnesium and silicon are highly depleted from the gas phase: we find that more than 90% and 95% of Mg and Si, respectively, are locked in dust grains.
Therefore, the interstellar dust largely contributes to shape the magnesium and silicon edges, making these two features a good probe to investigate the properties of the cosmic grains. We model them using accurate extinction models of silicates based on our laboratory measurements performed at the Soleil-LUCIA beamline. From the best fit and the fits with ΔAIC < 4 we can conclude that:

- *dust composition*: for every line of sight, a high percentage of dust $(65 - 85)\%$ is represented by $MgFeSiO_4$, an olivine with cation ratio $\zeta_3 = 0.5$. Magnesium-rich silicates are not preferred in the fits. On the other hand, the microquasar GRS 1915+105 shows a preference for Fe-rich olivine, mainly fayalite. To confirm this evidence it is necessary to include the iron K-edge in the fit. Observations of the Fe K-edge in the hard X-ray band will be possible with the micro-calorimeters aboard on the future X-ray missions, XRISM and Athena.
- *dust crystallinity*: although the dust features are fitted mostly by dust with an amorphous structure, for some lines of sight the crystalline ratio (with a distribution between $\zeta_1 = 0 - 0.30$) is larger than found in the infrared. However, for some sources, our estimation of the percentage of crystalline dust may be affected by bias due to the incompleteness of our dust model set.
- *dust structure*: in almost all the sources the olivine dust type $[SiO_4]^{-2}$ is the dust mixture that best fit both Mg and Si K-edges. We do not find any significant presence of pyroxene along the studied lines of sight. Moreover, the contribution of the quartz is always below 10%.

In addition to the Galactic X-ray binaries, we explore the absorbed spectrum of the brightest source in the Large Magellanic Cloud, LMC X-1. Similarly, Mg and Si are highly depleted. Comparing the abundances with the tabulated values for the Large Magellanic Cloud we find that Si may be underabundant. Moreover, we observe a large amount ($\sim 50\%$) of forsterite along this line of sight. However, the results are affected by large uncertainties due to the poor photon statistics. With the higher effective area of the future X-ray missions, we will able to characterise the interstellar dust in the Magellanic Clouds.

ACKNOWLEDGEMENTS

DR, EC, IP and MM are supported by the Netherlands Organisation for Scientific Research (NWO) through The Innovational Research Incentives Scheme Vidi *grant 639.042.525. The*

Space Research Organization of the Netherlands is supported financially by NWO. This research has made use of data obtained from the Chandra Data Archive and the Chandra Source Catalog, and software provided by the Chandra X-ray Center (CXC) in the application package CIAO. This research made use of the Chandra Transmission Grating Catalog and archive (`http://tgcat.mit.edu`). We are grateful to H. Marshall for useful discussion regarding the excess found in the silicon K-edge. We thank M. Sasaki for discussion on the LMC X-1. We also thank A. Dekker and D. Lena for commenting on this manuscript.

5

Investigating the interstellar dust through the Fe K-edge

D. Rogantini, E. Costantini, S.T. Zeegers, C.P. de Vries, W. Bras, F. de Groot, H. Mutschke, and L.B.F.M. Waters

Published in Astronomy & Astrophysics, Volume 609, A22 (2018)

Abstract

The chemical and physical properties of interstellar dust in the densest regions of the Galaxy are still not well understood. X-rays provide a powerful probe since they can penetrate gas and dust over a wide range of column densities (up to 10^{24} cm^{-2}). The interaction (scattering and absorption) with the medium imprints spectral signatures that reflect the individual atoms which constitute the gas, molecule, or solid. In this work we investigate the ability of high resolution X-ray spectroscopy to probe the properties of cosmic grains containing iron. Although iron is heavily depleted into interstellar dust, the nature of the Fe-bearing grains is still largely uncertain. In our analysis we use iron K-edge synchrotron data of minerals likely present in the ISM dust taken at the European Synchrotron Radiation Facility. We explore the prospects of determining the chemical composition and the size of astrophysical dust in the Galactic centre and in molecular clouds with future X-ray missions. The energy resolution and the effective area of the present X-ray telescopes are not sufficient to detect and study the Fe K-edge, even for bright X-ray sources. From the analysis of the extinction cross sections of our dust models implemented in the spectral fitting program SPEX, the Fe K-edge is promising for investigating both the chemistry and the size distribution of the interstellar dust. We find that the chemical composition regulates the X-ray absorption fine structures in the post edge region, whereas the scattering feature in the pre-edge is sensitive to the mean grain size. Finally, we note that the Fe K-edge is insensitive to other dust properties, such as the porosity and the geometry of the dust.

5.1 Introduction

Iron plays a crucial role in biology and in human life. It is an abundant chemical element on Earth and in the Galaxy. The solar photospheric abundance[1] of iron is $\log A_{\mathrm{Fe}} = 7.50 \pm 0.05$ or 32 ppm (Lodders 2010) and is consistent with the value derived from meteorites (Anders & Grevesse 1989). Iron is by far one of the most dominant species in the solar visible spectrum. This is also true for a large number of stellar spectra. When comparing solar abundances with those measured in other stars, the iron abundance shows a spatial trend along the Galactic plane: it decreases with increasing galactocentric distance (R_{G}). Genovali et al. (2014) found a logarithmic iron abundance[2] gradient of $[\mathrm{Fe/H}] = 0.57 \pm 0.02 - 0.060 \pm 0.002\ R_{\mathrm{G}}/\mathrm{kpc}$, studying the optical spectra of a large number of Galactic Cepheids.

The abundance of iron in diffuse or molecular clouds determined from spectral lines shows a dramatic shortfall compared with the standard reference value. This apparent shortage, or depletion, of iron and metals (in general) in the gas-phase is interpreted as evidence for their inclusion in interstellar dust grains. In particular, Fe is heavily depleted and the value changes just slightly with the density of the environment. Indeed iron depletion remains high: 89 and 99% depletions respectively in the warm and the cool phases of the interstellar medium (ISM, Savage & Sembach 1996; Jenkins 2009).

Iron is known to be primarily produced in Type I Supernovae (SN Ia) or at the endpoint of the evolution of massive stars that end their life as core collapse supernovae (SNCC). Asymptotic giant branch (AGB) stars are another important source of dust with metal inclusion. Only SNCC and AGB stars are observed to be sources of interstellar dust, since searches for dust in SN Ia have shown that these events are not major providers of fresh dust (Gomez et al. 2012). Dwek (2016) infers that more than 65% of the total iron is injected into the ISM in gaseous form by SN Ia. Thus, to explain its depletion, most iron growth needs to occur outside the sources of stellar condensation. Iron must have accreted from the ISM gas by cold accretion onto pre-existing silicate, carbon, or other composite grains (Draine 2009).

Although iron is predominantly included in solid grains, the composition of the Fe-bearing grains is largely uncertain. The elements Mg and Si are also highly depleted, and together with Fe, they are the main constituents of cosmic silicates (Henning 2010). In the Galactic plane there is growing evidence that silicates are Mg-rich, rather than Fe-rich (Costantini et al. 2005, 2012; Min et al. 2007; Altobelli et al. 2016). Poteet et al. (2015) investigated the composition of interstellar dust along the line of sight toward ζ Ophiuchi. They infer that $\lesssim 40\%$ of the available elemental Fe abundance is locked up in silicate grains. Iron is expected to be present in other solid-state species. It could exist in pure metallic nanoparticles or Fe oxides (e.g. Kemper et al. 2002; Lee et al. 2009; Draine & Hensley 2013; Poteet et al. 2015, and reference therein) or as metallic inclusions in glass with embedded metal and sulphides (GEMS, e.g. Bradley 1994; Xiang et al. 2011; Keller & Messenger 2013) of interstellar origin.

---

[1] Abundance is given in logarithmic scale $\log A_{\mathrm{Fe}} = \log N_{\mathrm{Fe}}/N_{\mathrm{H}} + 12.0$, where N_{Fe} is the column density of iron. By definition the solar abundance of hydrogen is exactly $\log A_{\mathrm{H}} = 12.0$ or 10^6 ppm.

[2] The logarithmic abundance of Fe relative to its solar abundance is defined as $[\mathrm{Fe/H}] = \log(N_{\mathrm{Fe}}/N_{\mathrm{H}}) - \log(N_{\mathrm{Fe}}/N_{\mathrm{H}})_{\odot}$.

Iron is highly elusive at longer wavelengths, even at ultraviolet (UV) and infrared (IR) frequencies which are broadly used to investigate interstellar dust. Iron does not show any vibrational modes in the mid-infrared wavelength regions and contributes only to the continuum opacity of dust. However, Fe-bearing oxides exhibit single or multiple vibrational resonances within the $17-28$ μm spectral region, depending on the precise composition of these species. Because their spectral features are blended with the strong blending mode of cosmic silicates, Fe-bearing oxides are not detected in the diffuse ISM, and thus are not usually considered to be a significant component of interstellar dust (e.g. Chiar & Tielens 2006).

In addition to the study of the gas phase, X-ray high resolution spectroscopy allows us to study the presence and the abundances of the depleted elements along the line of sight. The following photoelectric K-edges of cosmic elements are located in the X-ray energy range ($0.2-10$ keV): C, N, O, Mg, Al, Si, S, Ca, Fe. In particular, iron shows two different absorption edges: the Fe K-edge (when a photon has the same energy of the K shell electron of an atom) at 7.112 keV (Bearden & Burr 1967) and three Fe L-edges (excitation of a 2s or 2p electron) located in the soft X-rays at 0.846, 0.721, and 0.708 keV ($L_{\rm I}$, $L_{\rm II}$, and $L_{\rm III}$, respectively, Bradley 1994).

In the post-edge region are located characteristic features which can be up to few electronvolt in width and are known as X-ray absorption fine structures (XAFS, see Bunker (2010) for a theoretical explanation). When a photon excites a core electron ($n = 1$) to the continuum, the wave function of the outward-propagating photoelectron scatters off surrounding atoms. This interference produces an oscillatory fine structure which is characteristic of the chemical species of the absorber. Thus the oscillatory modulations of the cross section near the photoelectric absorption edge are unique fingerprints of the dust. Using high resolution X-ray spectra it is possible, in principle, to determine the properties of dust and complex molecules.

In the X-rays we can observe absorption due to gas and dust in cold ($< 10^3$ K) and in hot ($\geq 10^7$ K) environments over a wide range of column densities ($N_{\rm H} \sim 10^{20-24}$ cm^{-2}). Thus, using the X-ray spectra we can also determine abundances in different ISM environments, thereby opening a window on the study of grain evolution and the cycle between diffuse and dense or dark clouds. Dust in diffuse regions along the Galactic plane has been modelled in the X-rays by Lee et al. (2009); Costantini et al. (2012); Pinto et al. (2013); Valencic & Smith (2015) and Zeegers et al. (2017) for several lines of sight. The best targets for this kind of study are low mass X-ray binaries (LMXB), which generally emit a featureless continuum X-ray spectrum. Therefore, only absorption features (lines and edges) from dust and from both neutral and possibly ionised gas are visible.

In this article, we present the K-edge XAFS laboratory data of various iron compounds measured at the European Synchrotron Radiation Facility (ESRF). These measurements are part of a large laboratory measurement campaign aimed at the characterisation of interstellar dust analogues (Costantini & de Vries 2013). The investigated mineral set contains both crystalline and amorphous silicates, as well as iron sulfides, and is presented in detail in Section 5.2.1. Finally, for the analysis of synchrotron radiation based X-ray absorption spectroscopy, we discuss the prospect of studying the composition of iron grains in the ISM with the microcalorimeters onboard the future missions XARM (the successor of Hitomi) and Athena.

The paper is organised as follows. In Section 5.2 we describe the synchrotron measurement campaign and the data analysis. Section 5.3 illustrates the entire procedure to calculate the final extinction cross sections taking into account both the absorption and the scattering phenomena. In Section 5.4 we discuss the properties and the potential of the Fe K-edge to investigate the silicate dust grains. The iron K-edge will be studied in detail with the future X-ray missions presented in Section 5.5. Section 5.6 summarises the points discussed in this paper.

5.2 Laboratory data analysis

5.2.1 Sample

According to infrared observations of 9.7 and 19 μm features, the silicate interstellar dust mixture consists of an olivine ($Mg_{2-x}Fe_xSiO_4$) and pyroxene ($Mg_{1-x}Fe_xSiO_3$) stoichiometry (Kemper et al. 2004; Min et al. 2007). In order to reproduce laboratory analogues of astronomical silicates, our sample set contains both pyroxene and olivine silicate with variation in the Mg:Fe ratio. The values of Mg/(Fe + Mg) of our compounds range between 0.6 for iron-rich silicates and 0.9 for iron-poor silicates. Our choice of this variation depends on previous studies about the astronomical silicate composition, see e.g. Jaeger et al. (1998); Kemper et al. (2004); Min et al. (2007); Olofsson et al. (2009); Zeegers et al. (2017).

Iron is not only found in silicate structures. A likely possibility is that Fe exists in metallic form included in larger particles (Costantini et al. 2012; Jones et al. 2013). Köhler et al. (2014) also infer a FeS inclusion in silicate grains. The bulk of the iron sulphide is formed either in the collapse phase of the molecular cloud or in the protoplanetary disc (Keller et al. 2002). There is also evidence for FeS in a few planetary nebulae, see Hony et al. (2002). In order to investigate the Fe-bearing grains in the interstellar dust we included iron sulfide compounds ($Fe_{1-x}S$ with $x = 0 - 0.2$) in our sample set.

In summary, we analysed a sample of six silicates and two iron sulfides (see Table 5.1). The sample set contains both amorphous and crystalline structures for two pyroxene compositions with different Mg:Fe ratios (samples 2, 3, 6, and 7). The amorphous samples were synthesised in the laboratory following the procedure described by Dorschner et al. (1995). The crystalline counterparts of these compounds were also artificially produced by slowly cooling the silicate mixture. The Si-bearing compounds present in the sample set correspond to the silicates already presented in detail by Zeegers et al. (2017). The two iron sulfides have different origins. The pyrrhotite was synthesised in the laboratory at Astrophysikalisches Institut und Universitäts-Sternwarte (AIU), whereas the troilite has a meteoritic origin.

The absorbance of metallic Fe is well documented in the literature. Since the metallic iron was missing from our synchrotron sample set, we selected the data from the handbook of Exafs

Table 5.1: List of samples in our set with their relative chemical formulae. The nomenclature En(x)Fs(x-1) reveals the fraction of iron (or magnesium) included in the compound; 'En' stands for enstatite (the magnesium end-member of the pyroxene silicate mineral series, $MgSiO_3$) and 'Fs' for ferrosilite (the respective iron end-member, $FeSiO_3$).

#	Name	Chemical formula	State
1	Olivine [a]	$Mg_{1.56}Fe_{0.4}Si_{0.91}O_4$	crystalline
2	En60Fs40 [b]	$Mg_{0.6}Fe_{0.4}SiO_3$	amorphous
3	En60Fs40 [b]	$Mg_{0.6}Fe_{0.4}SiO_3$	crystalline
4	Troilite [c]	FeS	crystalline
5	Hypersthene [d]	$Mg_{1.502}Fe_{0.498}Si_2O_6$	crystalline
6	En90Fs10 [b]	$Mg_{0.9}Fe_{0.1}SiO_3$	crystalline
7	En90Fs10 [b]	$Mg_{0.9}Fe_{0.1}SiO_3$	amorphous
8	Pyrrhotite[b]	$Fe_{0.875}S$	crystalline

(*a*) origin: Sri Lanka
(*b*) synthesised in laboratories at AIU Jena and Osaka University
(*c*) meteoritic origin
(*d*) origin: Paul Island, Labrador

Materials[3]. In this work the energy range of the tabulated spectra includes the extended X-ray fine structures up to 1 keV from the nominal edge energy. The X-ray spectrum of the metallic iron foil was recorded at synchrotron beamlines in the Stanford Synchrotron Radiation Laboratory (SSRL). The spectrum was taken in the transmission geometry with a spectrometer resolution of 0.5 eV in the region near the Fe absorption K-edge.

5.2.2 Synchrotron measurements

The data presented in this paper (except metallic iron, see above) were measured at the European Synchrotron Radiation Facility (ESRF) in Grenoble, France. We used the Dutch-Belgian beamline (DUBBLE[4]). The beamline BM26A is specialised in X-ray absorption fine structure spectroscopy (Nikitenko et al. 2008). In essence, the synchrotron radiation emitted by a bending magnet source is monochromatised using an energy tuneable monochromator able to select a narrow energy range ($\frac{\Delta\lambda}{\lambda} = 3 \times 10^{-4}$). By rotating the monochromator in discrete steps it is possible to scan the absorption spectrum around the Fe K-edge over the range $6.8 - 8.2$ keV with an accuracy of 1% and a resolution of 0.3 eV. During an energy scan the beam position systematically changes, and therefore sample homogeneity is required. For this reason the finely powdered samples were diluted uniformly in a boron nitride matrix used as a spacer and sticker. Afterwards the mixed material was pressed into pellets. The final thickness of the sample was enough to obtain a significant edge jump (> 0.1 of the absorption length). For 13 mm diameter pellet sample we used 20 mg of material and 100 mg of boron nitride. The contrast in the XAFS features increases as the amplitude of thermal vibrations of the atoms decreases, so we cooled our samples to 90 K. To reach this

---

[3] `http://exafsmaterials.com/ReferenceSpectra.html`

[4] `http://www.esrf.eu/UsersAndScience/Experiments/CRG/BM26`

temperature the pellets were placed into a cryostat. Several (4-6) X-ray absorption scans in transmission were measured on each sample to ensure the reproducibility of the spectra and to obtain a high signal-to-noise ratio. In addition to the sample observations, a baseline pellet of pure boron nitride without any sample inserted was measured to obtain the characteristics of the bonding material. For each measurement the incident and the transmitted beam intensities were measured using three ionisation chambers mounted in series for simultaneous measurements on the sample.

5.2.3 Analysis of the laboratory data

When an X-ray photon with energy ranging from $\sim 100\,\mathrm{eV}$ up to hundred keV interacts with material, it can be transmitted, or it can interact with the medium by photoabsorption or by coherent scattering at the electron shell of the atoms in the material. The amount of light that is transmitted depends on the original energy of the X-rays, on the optical path length, and on the properties of the material. This quantity is called transmittance T and is defined as the ratio of the transmitted I and the incident light I_0 :

$$T = I/I_0 \ . \tag{5.1}$$

Figure 5.1 shows the relative transmittance obtained from the synchrotron measurements of olivine (sample 1 in Table 5.1).

The normalisation was performed using a standard procedure (Koningsberger & Prins 1988), regressing a second-order polynomial to the region before the pre-edge. We subtracted it from the entire spectrum to eliminate any instrumental background and absorption from other edges. A third-order polynomial was regressed to a region beyond the absorption edge. The value of the post-edge polynomial extrapolated back to the edge energy was used as the normalisation constant. The attenuation of X-rays travelling through a material of thickness x (in μm) is also given by the Beer-Lambert law, which states that the intensity decreases exponentially with depth in material according to

$$I(E) = I_0 e^{-\mu(E)x} \ , \tag{5.2}$$

where $\mu(E)$ is the attenuation coefficient in $\mu\mathrm{m}^{-1}$. If we ignore reflection (at X-rays energies, the contribution of reflection becomes very small) we can equate the attenuation coefficient with the absorption coefficient. Therefore, the characteristic attenuation coefficient for a compound is approximately given by

$$\mu(E) \approx \sum_{\mathrm{i}} \rho_{\mathrm{i}} \sigma_{\mathrm{i}} = \rho_{\mathrm{M}} \sum_{\mathrm{i}} \frac{m_{\mathrm{i}}}{M} \sigma_{\mathrm{i}} \ , \tag{5.3}$$

where ρ_{M} is the mass density of the compound, m_{i}/M is the fractional mass contribution of element i, and σ_{i} is the respective mass normalised absorption cross section. In our samples we keep the total thickness x below $2-3$ absorption lengths to minimise thickness effects which may reduce the EXAFS amplitude (Parratt et al. 1957; Bunker 2010). In order to determine μ from our synchrotron measurements we use the relation with transmittance obtained by setting Equation 5.1 and 5.2 equal to each other:

$$\mu(E) = \frac{-\ln T}{x} \ . \tag{5.4}$$

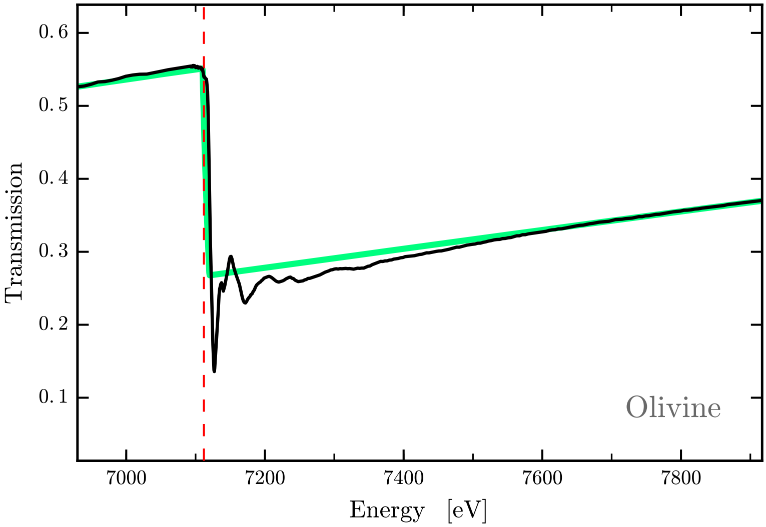

Figure 5.1: Transmission signal around the Fe K-edge measured at the Dutch-Belgian beamline (DUBBLE) at the European Synchrotron Radiation Facility (black solid line). The sample used in this measurement is olivine. The vertical dashed red line indicates the energy of the Fe K-edge (7112 eV). The green solid line represents the Henke et al. (1993) data table used to fit the laboratory measurement.

The experimental x is not known a priori since the sample is pressed in pellets and diluted. In order to evaluate the thickness we compare our laboratory transmittance signal with the tabulates values provided by the Center for X-ray Optics at Lawrence Berkeley National laboratory[5]. Using the χ^2 test we calculate the best value for the thickness, the only free parameter. To achieve this result we fit the pre- and post-edge regions. Obtaining the value of the attenuation coefficient is important in order to calculate the optical constants (n, k) of the refractive index of the material.

5.3 Extinction, scattering, and absorption cross sections

The refractive index is a complex and dimensionless number that describes how light propagates through a specific material. In the following paragraph we describe the optical constants which identify the refractive index. We summarise the different definitions present in the literature. Subsequently, we present the Kramers-Kronig (de L. Kronig 1926; Kramers 1927) relations and the anomalous diffraction theory (ADT, van de Hulst (1957)) that we use to obtain the extinction cross section.

---

[5] `http://www.cxro.lbl.gov/`

5.3.1 Optical constants

The refractive complex index is generally defined as

$$m = n + ik \;, \tag{5.5}$$

where n (or $\mathrm{Re}(m)$) describes the dispersive behaviour and k (or $\mathrm{Im}(m)$) the corresponding absorption depending on the energy of the incident light. For X-rays, the complex refractive index deviates only slightly from unity and usually the real part is smaller than 1. It is therefore commonly written as $|m-1|$. We show an example in Figure 5.2 for olivine. The refractive index has an analogue notation used in the literature (e.g. Henke et al. 1993)

$$n_{\mathrm{r}} = 1 - \delta + i\beta \;, \tag{5.6}$$

where n_{r} corresponds to m in Equation(5.5) and δ and β are the optical constants. Other notations use the complex dielectric functions, ε_1 and ε_2 (Landau & Lifshitz 1960; Draine 2003) defined as

$$\varepsilon = \varepsilon_1 + i\varepsilon_2 = m^2 \;. \tag{5.7}$$

It is sometimes useful to make explicit their relation to the optical constants n and k:

$$n = \sqrt{\frac{|\varepsilon| + \varepsilon_1}{2}} \;, \tag{5.8}$$

$$k = \sqrt{\frac{|\varepsilon| - \varepsilon_1}{2}} \;. \tag{5.9}$$

Finally, another common notation uses the atomic scattering factors, f_1 and f_2 (Henke et al. 1993)

$$f(E) = f_1(E) + if_2(E) = \frac{2\pi A}{\rho N_{\mathrm{A}} r_0} \cdot \frac{1}{\lambda^2} \cdot (m-1) \;. \tag{5.10}$$

They are related to the optical constants as

$$n(E) = 1 - \frac{\rho N_{\mathrm{A}} r_0}{2\pi A} \lambda^2 \cdot f_1(E) \;, \tag{5.11}$$

$$k(E) = \frac{\rho N_{\mathrm{A}} r_0}{2\pi A} \lambda^2 \cdot f_2(E) \;, \tag{5.12}$$

where N_{A} is the Avogadro's number, A is the atomic mass number of the compound, ρ is the density in g/cm^3, r_0 is the classical electron radius, and λ is the wavelength of the incident X-ray.

5.3.2 Kramers-Kronig relation

The imaginary, absorptive part of the refractive index (k) can be easily determined via laboratory experiments. Indeed, there is a relation between the absorptive optical constant k and the linear absorption coefficient μ:

$$k = \frac{\mu\lambda}{4\pi} \;. \tag{5.13}$$

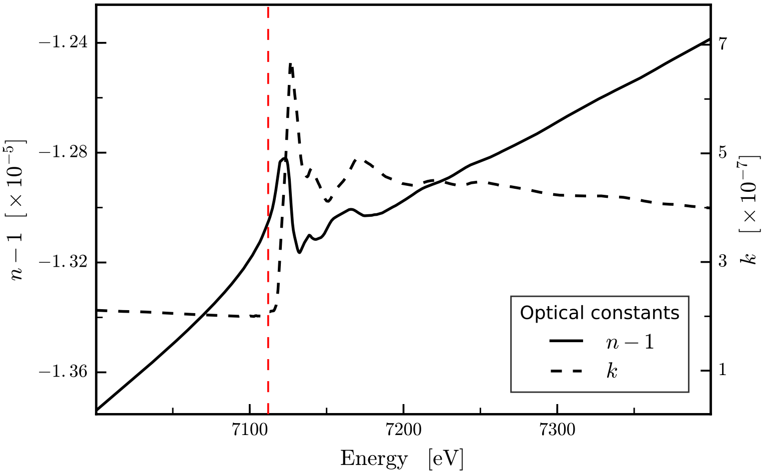

Figure 5.2: Real (solid line) and imaginary (dashed line) part of the refractive index for olivine. The optical constant k is derived from synchrotron measurement using Equation 5.13. The Kramers-Kronig relations (see Equation 5.14) were used to calculate n.

In this way we can determine k as a function of energy (or wavelength) in detail around the edge (see also Zeegers et al. 2017). The real dispersive part, on the other hand, is more difficult to measure. Fortunately, the real and imaginary parts are related to each other by the Kramers-Kronig relations and therefore the refractory index can be determined from measurements of only the imaginary part. To calculate the real part of the Henke-Gullikson scattering factor f, we use the Kramers-Kronig relation expressed in the equation (Gullikson 2001)

$$f_1(E) = Z^* - \frac{2}{\pi} P \int_0^\infty \frac{x f_2(x)}{x^2 - E^2}\, dx \ , \tag{5.14}$$

where E in this case is the photon energy at which we wish to calculate the real part of the atomic scattering factor, Z^* is the relativistic correction, and P denotes the Cauchy principal value (Landau & Lifshitz 1960). Equation (5.14) is problematic in two ways. First, the integral spans from zero to infinity, meaning that in order to calculate f_1 over a small energy range, the value of f_2 is required over a virtually infinite energy range. The second issue is that the integral contains a discontinuity at $x = E$ and therefore must be considered as a Cauchy principal value. The Cauchy principal value is central to many calculations and a number of resolving strategies have been applied to the problem, such as the fast Fourier transform (FFT, Bruzzoni et al. 2002), the Euler-MacLaurin (Cross et al. 1998), and the Chebyshev methods (Hasagawa & Torii 1991). Henke et al. (1993) demonstrated a simple method involving a manual piecewise polynomial representation of spectral data. This way of evaluating the integrals is accurate but time-consuming. Watts (2014) introduces an useful extension of the Henke et al. (1993) approach. It allows computer automation and it can provide computationally fast calculations whose accuracy is limited only by the representation of the absorption spectrum by a piecewise set of Laurent polynomials. This algorithm calculates the relativistic correction following the Henke et al. (1993) approach,

$$Z^* = \sum_q n_\mathrm{q} \left(Z_\mathrm{q} - \left(\frac{Z_\mathrm{q}}{82.5} \right)^{2.37} \right) , \tag{5.15}$$

where n_q and Z_q represent the number density of atoms and the atomic number of the qth element in the material, respectively. This method for calculating the real part of the scattering factors from the imaginary has several benefits: *i)* it does not require a homogeneous binning of data points, *ii)* a full energy range from zero to infinity is not necessary, *iii)* it can process broad sections of spectrum at once, while maintaining accuracy and precision. Thus, it is suitable for our laboratory transmission, which is measured only for a limited range of frequency around the absorption edge. The method has been implemented as a Python-based library[6] (Watts 2014).

5.3.3 Anomalous diffraction theory

To calculate the extinction cross section we used the anomalous diffraction theory[7], an algorithm for computing absorption and scattering by the dust grains. The merits of ADT are its simplicity in concept and efficiency in numerical computation. Moreover it is applicable to grains of arbitrary geometry that are larger than the incident wavelength. The approximations used in the derivation of ADT require that $|m-1| \ll 1$, and $x = 2\pi a/\lambda \gg 1$, where a is the effective radius of the grains. In other words the particle has to be optically soft (i.e. the refractive index has to be close to unity) and larger than the wavelength of incident light. Hoffman & Draine (2016) show that the ADT approximation fits well for our range of wavelengths (around the Fe K-edge at 7.112 keV) and grain radius size (up to 1 μm). Because $x \gg 1$, the concept of independent rays of light passing through the grains is valid. And, because $|m-1| \ll 1$, refraction and reflection effects are small and they can be ignored.

The ADT calculates the efficiency for absorption, scattering, and extinction efficiencies per grain size at each energy of interest. We use the following equations expressed in terms of n, k, and x (see van de Hulst (1957) for a different notation),

$$Q_\mathrm{ext} = 2 + 4 \left[\frac{\cos(2\beta) - e^{-2xk}\cos(2x(n-1) - 2\beta)}{4x^2((n-1)^2 + k^2)} + \right. \tag{5.16}$$

$$\left. + \frac{2x\sqrt{(n-1)^2 + k^2} \cdot \sin(2x(n-1) - \beta)}{4x^2((n-1)^2 + k^2)} \right] , \tag{5.17}$$

$$Q_\mathrm{abs} = 1 + \frac{e^{-4xk}}{2xk} + \frac{1}{2} \cdot \frac{e^{-4xk} - 1}{(2xk)^2} , \tag{5.18}$$

$$Q_\mathrm{sca} = Q_\mathrm{ext} - Q_\mathrm{abs} , \tag{5.19}$$

---

[6] https://bitbucket.org/benajamin/kkcalc

[7] Not to be confused with anomalous diffraction (also known in X-ray crystallography as anomalous scattering).

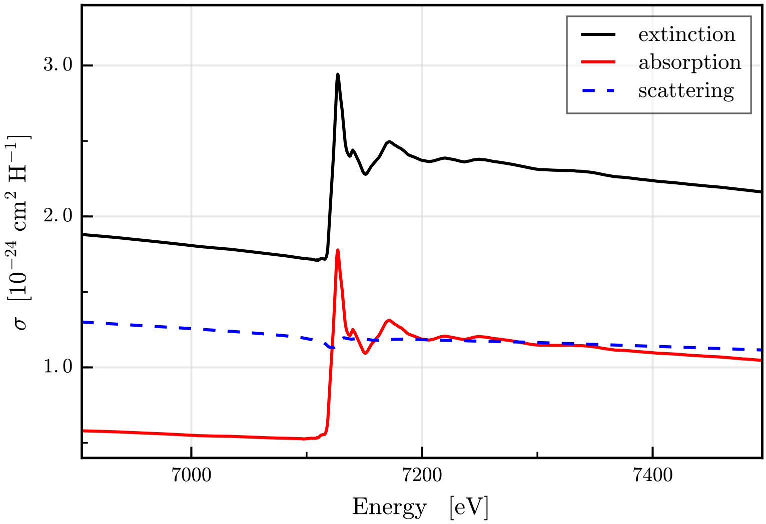

Figure 5.3: X-ray extinction (solid black line), absorption (solid red line), and scattering (dashed blue line) cross sections per H nucleon for the Mathis et al. (1977) dust model ($0.005 \leq a \leq 0.25$ μm). The scattering cross section contributes significantly to the extinction, but it does not significantly modify the absorption features in the post-edge. This plot is characteristic of olivine.

where $\beta = \arccos\left((n-1)/\sqrt{(n-1)^2+k^2}\right)$. To obtain the total cross sections per wavelength unit ($C = \pi a^2 \cdot Q$), we need to integrate over the particle size distribution. We use for the moment the Mathis-Rumpl-Nordsieck (MRN) grain size distribution (Mathis et al. 1977) with a grain size interval of ($0.005 \leq a \leq 0.25$) μm,

$$n(a)\,da = A \cdot a^{-3.5}\,da \ , \tag{5.20}$$

where a is the particle size, $n(a)$ is the number of grains, and A is the normalisation constant, which depends on the type of dust. The value of the constant for each compound can be determined following the method described by Mauche & Gorenstein (1986). In this work they use the Rayleigh-Gans approximations to calculate A. This approximation requires that $\left(\frac{4\pi a}{\lambda}\right)|m-1| \ll 1$. Consequently, we cannot use this approximation in our analysis since for the grain size distribution that we take into account the mean energy of the sources should be less than 2 keV. Therefore, we apply the ADT approximation to evaluate the normalisation constant (see Zeegers et al. 2017, in prep). In Figure 5.3 we plot the absolute cross sections for olivine, calculated with the procedure described above.

The last step, in order to compare our laboratory measurements with astronomical data, is to implement the extinction profiles in the SPEX fitting code (Kaastra et al. 1996). Our measurements were added to the already existing AMOL model. Now this model assumes Verner absorption curves for the pre- and post-edge range (Verner et al. 1996).

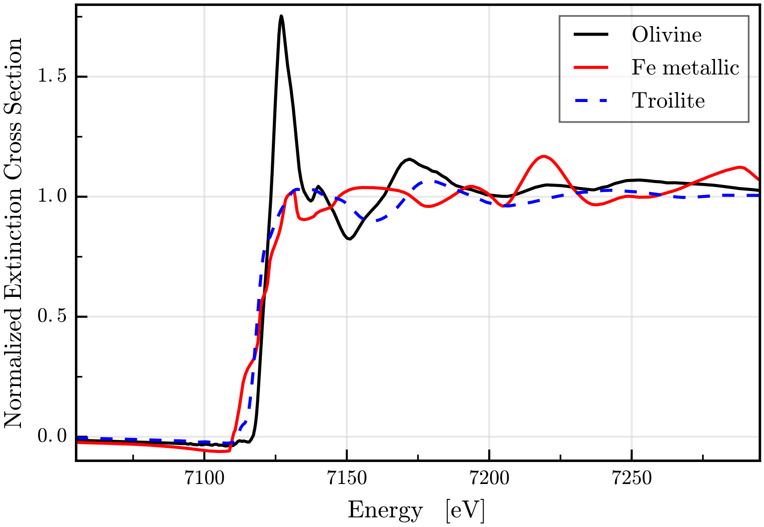

Figure 5.4: Extinction cross section in normalised units to compare the different chemical species presented here: silicate (olivine, black solid line), iron sulfide (troilite, blue dashed line), and metallic Fe (red solid line). The X-ray absorption features are different for these three compounds. In particular the silicate is characterised by the large peak just after the Fe K-edge located at E $\sim$ 7130 eV.

5.4 Fe K-edge properties

The iron K absorption edge is sensitive to particular physical and chemical characteristics of the dust grains. In this section we present the characteristics of the Fe K-edge and how the edge can help to study and investigate several properties of the grains.

Chemistry - As already shown in the introduction, the modulation of the post edge region is in principle the fingerprint for each specific compound. In Figure 5.4 we show the extinction cross section of three representative compounds in our sample set: a silicate (olivine, solid black line), an iron sulfide (troilite, blue dashed line), and Fe in the metallic form (red solid line). The silicates especially show characteristic X-ray absorption near edge structures (XANES) compared to the other compounds (see Appendix C.1). Indeed the extinction cross section of olivine displays a higher peak right after the rising edge, at $\sim$ 7130 eV. Metallic Fe and troilite do not show large features in the post-edge region. The iron sulfides are characterised by two wide peaks at $\sim$ 7135 eV and $\sim$ 7175 eV. Instead, the absorption cross section of the metallic iron presents a distinctive peak at higher energies ($\sim$ 7270 eV). All these features are useful to distinguish the compounds that contribute to the dust extinction cross section.

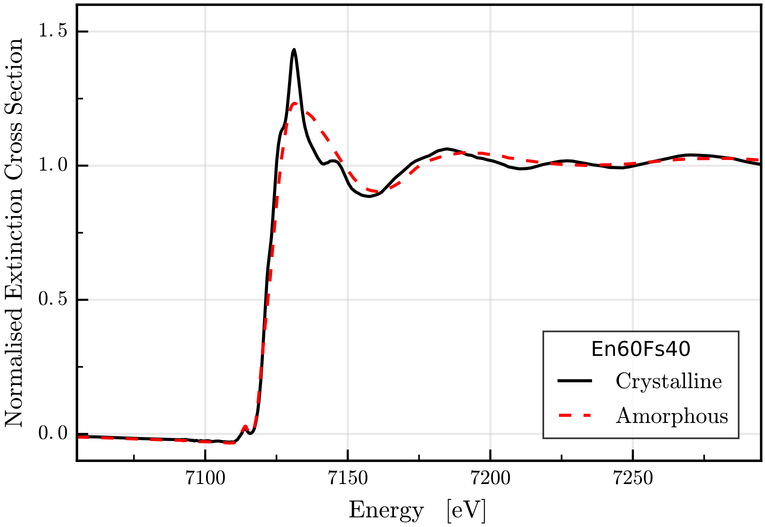

Figure 5.5: Extinction cross section in arbitrary units for pyroxene En60Fs40 in crystalline state (black and solid line) and in amorphous state (red and dashed line).

Glassiness - The absorption cross section is also sensitive to the crystalline order of the compound. In the pure crystalline form the atoms have fixed position and form a periodic arrangement. Instead, an amorphous material is a solid that lacks the long-range crystalline order and thus the absorption cross section shows a different pattern of peaks. Figure 5.5 compares the amorphous form (red dashed line) to the crystalline state (black solid line) for pyroxene En60Fs40 (see Table 5.1). The extinction cross section of the glass configuration is smoother and does not show any secondary peak near the edge. The characteristic peak of silicate at $\sim$ 7130 eV (see the previous paragraph) is smaller and wider than the feature displayed in the crystalline form.

Grain size - The scattering cross section is sensitive to the range in sizes ($a_{-} - a_{+}$) of the constituents. In general, the scattering cross section may potentially modulate the amplitude, the slope, and the features close to the absorption edges. To investigate the effect of the particle size distribution we integrate the scattering efficiency over different size ranges. We change the lower (a_{-}) and upper (a_{+}) cut-off of the MRN distribution and consequently the average grain size (Mauche & Gorenstein 1986). Draine & Fraisse (2009) investigated particles between $a_{-} = 0.02$ μm and $a_{+} = 1$ μm for a model of spherical silicates grains. In order to study the enhancement of the scattering features around the iron K-edge we introduce this large particle size range with an average grain size $\bar{a} \sim 0.6$ μm. The effect of the size distribution change is shown in Figure 5.6. The olivine Fe K-edge with the standard MRN distribution with particle sizes of $0.005 - 0.25$ μm is shown in black (solid line). In red (dashed line) the same edge is shown, but now with a MRN size distribution that has a particle range of $0.02 - 1$ μm. Here we compare the shape of the two extinction cross sections

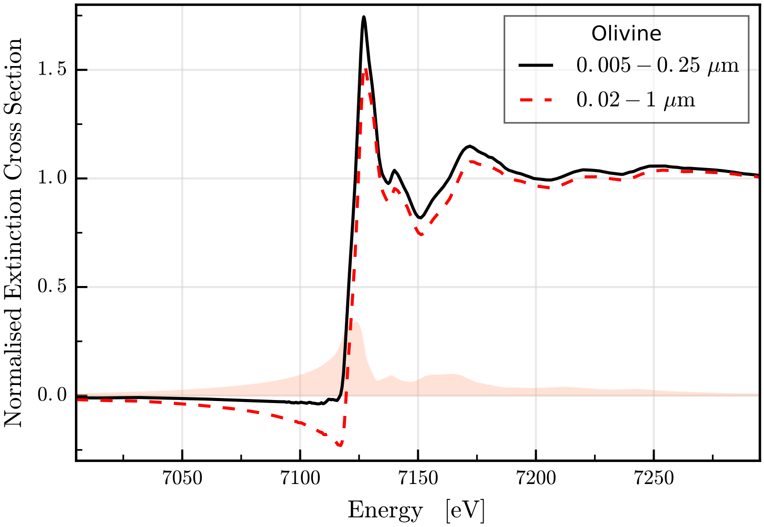

Figure 5.6: Normalised extinction cross sections for olivine calculated using two different grain size distributions. The solid black line represents the standard MRN grain size ranging between $0.005 - 0.25$ μm. The dashed red line delineates the larger grain size spanning between $0.02 - 1$ μm by Draine & Fraisse (2009). The orange shadow in the bottom highlights the shape difference between the two extinction cross sections.

(normalised for this purpose). The main difference is the peak, due to the scattering cross section, right before the edge. This scattering feature can potentially be used to investigate the mean range size of the interstellar dust.

Figure 5.7 gives a general overview on the efficiency as a function of grain size for the energies investigated in this paper. We show a comparison among the calculated absorption, scattering, and extinction efficiencies at a fixed energy ($E = 7120$ eV). In particular the scattering becomes more efficient for larger grains and dominates the extinction process for radii larger than 0.2 μm. The scattering efficiency (and thus the extinction efficiency) continues to increase up to ~ 3 μm where it reaches the maximum value, as highlighted in the right panel of Figure 5.7, which shows the Q-factors per unit radius. The scattering efficiency also depends on the energy of the incident light: for higher energies the peak of the scattering efficiency is shifted to larger grain radii (see Zeegers et al. 2017 in prep.). This peak is followed by smaller bumps due to the resonance of the diffraction (see Berg et al. 2010). From the trend of $Q_{\rm ext}$, larger grains (> 1 μm) seem more efficient at extinguishing X-rays, but at the same time they are less abundant. However, we do not expect a significant grain population with radii larger than 1 μm even in the molecular core, as near- and mid-infrared observations show (Andersen et al. 2013).

Size distribution model and porosity - Hoffman & Draine (2016) have studied in detail the X-ray extinction for astrosilicate grains (Draine 2003). They find that the Fe K-edge

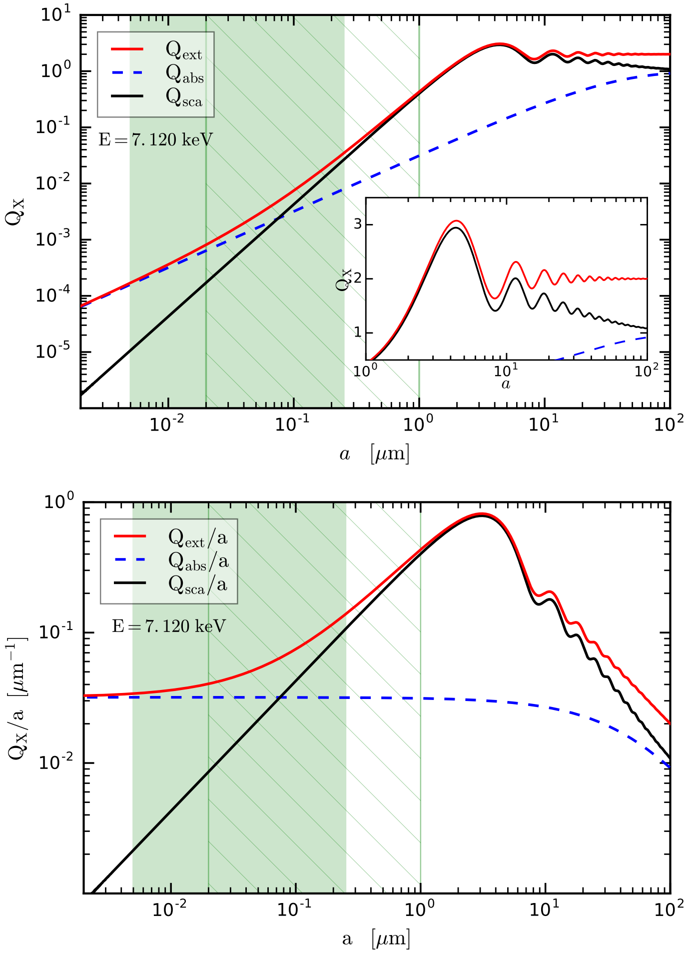

Figure 5.7: *Upper panel*: Comparison of the calculated absorption (dashed blue line), scattering (solid black line), and extinction (solid red line) efficiencies at $h\nu = 7120$ eV (near Fe K-edge) for olivine. The two green regions indicate the size range investigated in this work: in particular $(0.005 \le a \le 0.25)$ μm (filled green) and $(0.02 \le a \le 1)$ μm (hatched green). *Lower panel*: Comparison of the calculated absorption, scattering, and extinction efficiencies per unit of radii as a function of the grain size. The absorption Q-factor per grain size remains roughly constant along the two size ranges analysed in this work (the green areas). Instead, the scattering Q-factor per radii unit increases, achieving the maximum value at ~ 3 μm.

Table 5.2: Principal characteristics of the X-ray spectrometer of Chandra-HETG, XARM-SXS, and Athena-XIFU at 7 keV

Instrument	Resolving Power $E/\Delta E$	Effective Area [cm^2]
Chandra HETG	148	18
XARM SXS	1750	225
Athena X-IFU	2800	1600

References. (a) Canizares et al. (2005); (b) Mitsuda et al. (2012); (c) Barret et al. (2016).

shape is not significantly affected by the choice of the dust size distribution tested (namely MRN and Weingartner & Draine 2001). Hoffman & Draine (2016) also show that the geometry and the porosity level of the grains do not alter the fine structure of the absorption Fe K-edge. Thus, in the study of the iron K-edge porosity, both the effect of the porosity and dust size distribution can be at first order ignored.

5.5 Simulations

5.5.1 Present and future X-ray missions

The laboratory measurements cannot be applied to astronomical data from the current X-ray missions because of insufficient energy resolution at 7.1 keV. In the following, we explore the prospects of observing the Fe K-edge with the resolution provide by the X-ray Astronomy Recovery Mission[8] (XARM, successor of Hitomi) and the Athena[9] mission (see Table 5.2). The high energy resolution in the Fe K-edge will be achieved by using microcalorimeters.
With the Athena satellite it will be easier to probe the dense interstellar regions for the iron component of the dust grains. In particular, it will be possible to obtain direct measurements of the Fe abundance and inclusion in dust in dense regions only accessible through the Fe K-edge. The large effective area of the X-ray spectrometer X-IFU allows us to obtain high quality spectra not only of the brightest X-ray sources, but also of a fainter source population.

5.5.2 Simulated sources

X-rays are highly penetrating, thus it is possible to explore the dust in the denser regions of the Galaxy using low mass X-rays binaries as background sources. The presence of the absorption edges of O, Mg, Si, and Fe in the extinction profile depends on the column density (N_{H}) on the line of sight towards the source. It is difficult to detect dust in the Fe K-edge region. Extreme conditions are required to observe the iron absorption features: *i)* a very

---

[8] The recovery mission XARM will have the same technical characteristic of the previous mission ASTRO-H specially for the microcalorimeter.
http://astro-h.isas.jaxa.jp/en/

[9] see Nandra et al. (2013) for an overview.

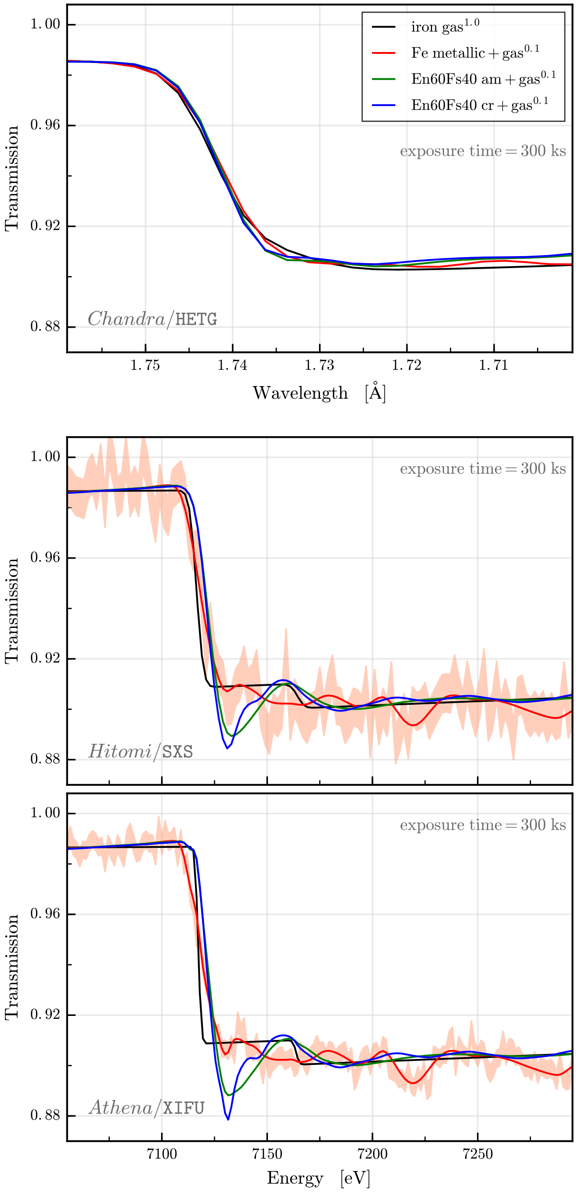

Figure 5.8: Simulated transmission for a mixture of gas (10%) plus a dominant dust component: iron gas (black), metallic iron (red), and pyroxene En60Fs40 in both amorphous (green) and crystalline (blue) form. We set a solar abundance and we also simulate the transmission of pure iron gas (black) as a reference. The red shadow represents the noise for the iron metallic model. *Top*: Simulation with Chandra-HETG. *Middle*: Simulation with the XARM-SXS microcalorimeter (see also Paerels et al. 2014). *Bottom*: Simulation with Athena-XIFU (see also Decourchelle et al. 2013).

high hydrogen column density $> 6 \times 10^{22}$ cm^{-2} and *ii)* a bright background X-ray source with a $2 - 10$ keV flux $> 1 \times 10^{-9}$ erg cm^{-2} s^{-1}.

In order to test and compare the sensitivity of the present Chandra transmission grating and the future XARM and Athena microcalorimeters we simulate the response of these instruments under optimised conditions to study the Fe K-edge for a reasonable exposure time. We simulate an outbursting X-ray source near the Galactic centre (here SAXJ1747.0-2853, in't Zand et al. 2004) with a $2 - 10$ keV flux 3×10^{-9} erg cm^{-2} s^{-1} and $N_{\rm H} = 8.5 \times 10^{22}$ cm^{-2}. In this simulation we considered a mixture of gas (15%) and one dominant dust component in amorphous or crystalline form (either $\rm Mg_{0.6}Fe_{0.4}Si_3$ or metallic Fe) with the standard MRN dust size distribution. The total Fe abundance has been set to proto-solar (Lodders 2010).

As shown in Figure 5.8, the resolving power of Chandra-HETG is not enough to detect any dust features in the Fe K region. It will be possible to distinguish the iron silicate present in the dust with XARM-SXS because the silicate peak at ~ 7130 eV can be easily detected. However, only the resolving power of Athena-XIFU is able to detect the secondary features and then identify the different compound with enough accuracy.

5.5.3 Chemistry, depletion, and abundances

Here we test the sensitivity of the X-IFU to both depletion and abundances of iron. We consider a mixture of iron silicates, sulfides, and metallic iron (50%, 40%, and 10%, respectively, of the total amount of iron included in dust). To develop the simulation we take into account the same source presented in the previous section.

Iron is heavily embedded in dust and its depletion factor ranges between 0.90 and 0.99 (Savage & Sembach 1996; Jenkins 2009). In Figure 5.9*a* we present the transmission expected for the limit values of the depletion range. The two curves do not change significantly. The data errors overlap for almost the entire the edge region and this would complicate the calculation of the percentage of iron present in the solid and gaseous phase.

The iron abundance in the innermost Galactic disc regions is well above solar ([Fe/H] ~ 0.4, Pedicelli et al. 2009), while in the outer disc it is significantly more metal-poor ([Fe/H] $\sim -0.2/-0.5$, Lemasle et al. 2008). Figure 5.9*b* compares the transmission with solar abundance to the transmission with over-solar iron abundance for a source near the Galaxy centre. We fix the depletion factor to 0.99. To calculate the abundance of iron for a region located at 7.5 kpc away from the Earth and 1 kpc away from the Galactic centre we consider the iron gradient presented by Genovali et al. (2014). The simulations show a detectable difference especially in the depth of the Fe K-edge, which is larger for over-solar metallicities.

5.5.4 Grain size

In Section 5.4 we see how the pre-edge shape is sensitive to the dust size. Here we test the capability of Athena to investigate the expected grain size in the most dense region of the Galaxy. In Figure 5.10 we present the results of the simulation for the two size ranges. The population of grains with sizes ranging between 0.02 and 1 μm shows a pronounced scattering peak in the pre-edge region. Consequently with Athena-XIFU we will be able to

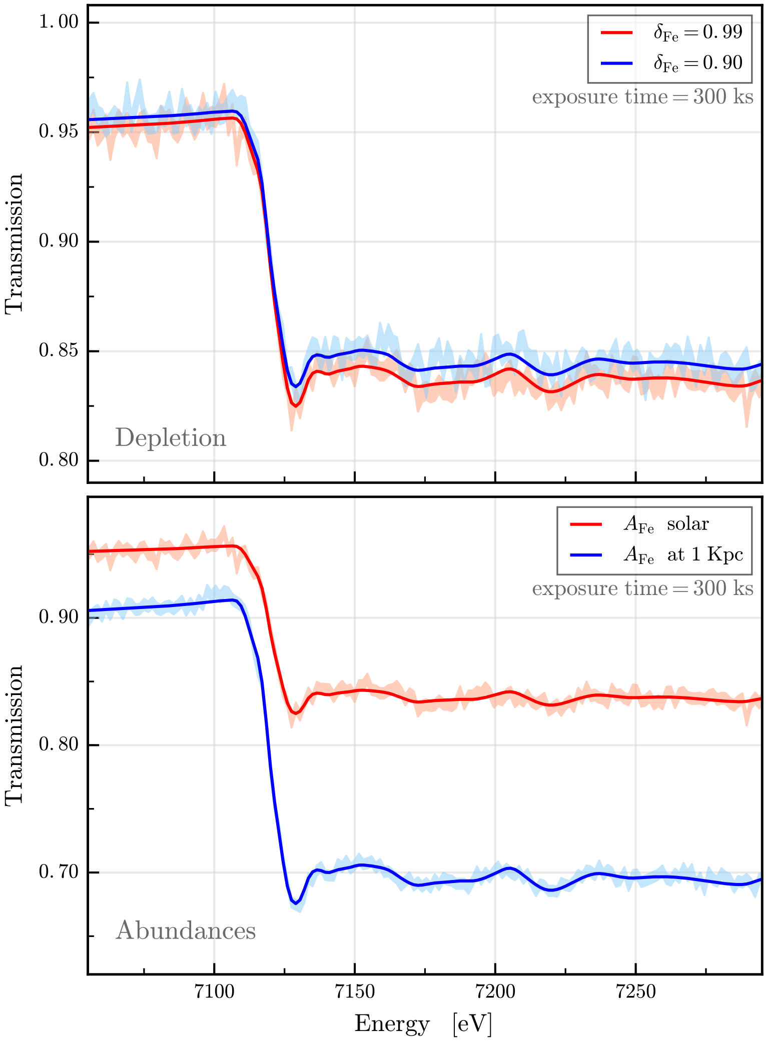

Figure 5.9: Depletion and abundances simulations with the Athena-XIFU instrument for the source and the hypothetical interstellar dust composition presented in the text. *Top*: transmittance expected for two different iron depletion values: $\delta_{Fe} = 0.9$ in blue and $\delta_{Fe} = 0.99$ in red. We assume solar abundances. *Bottom*: transmittance calculate taking into account solar abundance of iron (in red) and abundance expected in a region located at 1 kpc away from the Galactic centre (in blue). We fix the depletion at $\delta_{Fe} = 0.99$.

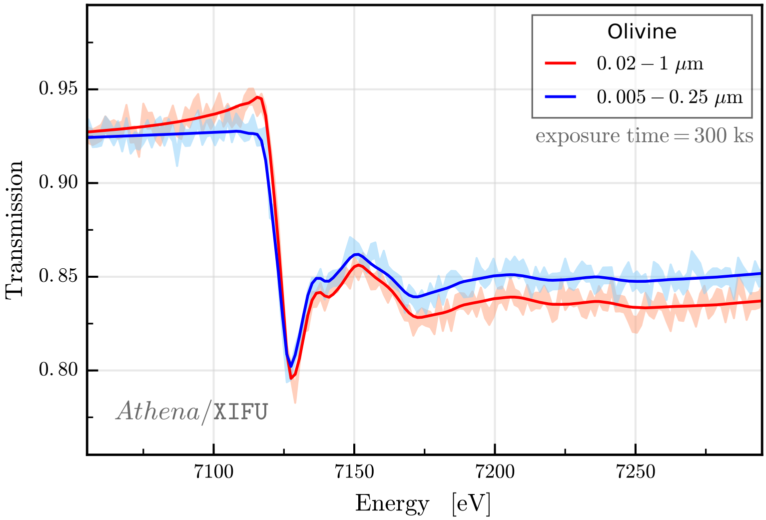

Figure 5.10: Simulated transmittance for two dust size ranges: (0.005 ≤ a ≤ 0.25) μm (blue) and (0.02 ≤ a ≤ 1) μm (red).

distinguish the peak and asses the presence a population of large grains along the line of sight.

5.6 Conclusion

In this paper we present the laboratory measurements of silicates in amorphous and crystalline forms and iron sulfides that we carried out at the synchrotron facilities in transmission geometry. In our study we include the literature value of metallic iron. Using these new data, we calculated the scattering, absorption, and extinction profiles of these samples. We implemented the absolute extinction curves in the spectral model AMOL of SPEX. We then explored the potential of the Fe K-edge probing the interstellar dust properties. The results of this analysis are as follows:

1. The absorption cross section in the Fe K-edge region is very sensitive to the chemical composition of the dust grains. The post-edge is a real fingerprint of the grain chemistry.
2. The absorption features in the Fe K post-edge region are also sensitive to the lattice order of the material. Non-crystalline solids display a smoother curve than the crystalline samples. The transition from crystalline to amorphous phase does not affect the characteristics of the main features in the spectra, although it levels out the secondary peaks. In addition, the extinction cross section near the iron K-edge is insensitive to the grain porosity and geometry and to the grain size distribution model chosen. Thus, the iron K-edge spectra is not contaminated by other grain properties.

3. The scattering cross section is significantly sensitive to the grain size range. For grains with sizes ranging between $0.005-0.25$ μm (as in the MRN distribution) the scattering cross section is flat and does not affect the shape of the extinction cross section (see Figure 5.3). If we consider grains with sizes ranging between $0.02-1$ μm, the scattering cross section becomes more intense; in particular, it shows a deep feature in the pre-edge region. The extinction cross section displays the scattering peak for large grains in the pre-edge region. By detecting this scattering feature, it will be possible to investigate directly the dust size range even in very dense regions of the Galaxy.
4. Iron is highly depleted in the Galaxy and the level of the depletion does not change enough to vary the transmittance significantly. However, the edge is suitable for investigating the iron abundance gradient, which influences considerably the attenuation of the transmission and the depth of the Fe K-edge.

The simulations with the XARM-SXS microcalorimeter and the Athena-XIFU spectrometer show the potential of using the Fe K-edge at 7.112 keV as a diagnostic tool. This edge will be a useful probe to investigate the iron abundance, the chemistry, and the grain size of the interstellar dust in the most dense environment of the Galaxy. These properties show distinctive features in the spectrum, making the modelling of different properties of dust easier.

ACKNOWLEDGEMENTS

DR and EC are supported by the Netherlands Organisation for Scientific Research (NWO) through The Innovational Research Incentives Scheme Vidi *grant 639.042.525. The NWO is acknowledged for making access to the DUBBLE beamlines possible. The Space Research Organization of the Netherlands is supported financially by the NWO. We thank Hiroki Chihara and Simon Zeidler for their contributions to the preparation of the sample. Furthermore, we made use of* KKcalc *code provided by Benjiamin Watts. We also thank A. Dekker for commenting on this manuscript.*

A

Appendices to Chapter 3

A.1 Mg K-edge shift

Comparing our synchrotron measurements with previous and independent works we notice a discrepancy in the energy of the magnesium K-edge threshold. In particular, in Figure A.1 we compare the normalised XANES spectra of crystalline forsterite. We show the result of our measurements with the XANES profiles obtained by Wu et al. (2004), Trcera et al. (2009), and Takahashi et al. (2018). Our result appears shifted to higher energies with respects to the other reference XANES spectra. We chose to evaluate the energy shift calibrating our model on the spectrum of GX 3+1 presented in this paper in Section 3.2. We set the systematic velocity of the absorber (`zv` parameter in `AMOL`) as a free parameter and we run the fit of the magnesium K-edge using a combination of all the minerals (see Equation 3.1). This approach to define the absolute energy value of a particular transition (difficult to define by experimental data and/or calculations) was already adopted by Gorczyca et al. (2013) for the atomic oxygen. We selected the models with a $\Delta AIC < 2$ (Burnham & Anderson 2002) from the best fit and we found an average speed of $zv = -585\,\mathrm{km/s}$ corresponding to an energy shift of $E = -2.54$ eV in the Mg K-edge region. This value is in agreement with previous works shown in Figure A.1.

A.2 Extinction cross sections of the Mg K edges.

In Figure A.2 we present the extinction cross section profiles around the magnesium K-edge for each sample presented in 3.1. The measurements were taken at SOLEIL (Paris). We adopt the standard MRN size distribution (Mathis et al. 1977) to obtain the extinction cross sections. These curves were implemented in the `amol` model of the spectral fitting code SPEX with a fixed energy resolution of 0.1 eV. The absorption, scattering, and extinction

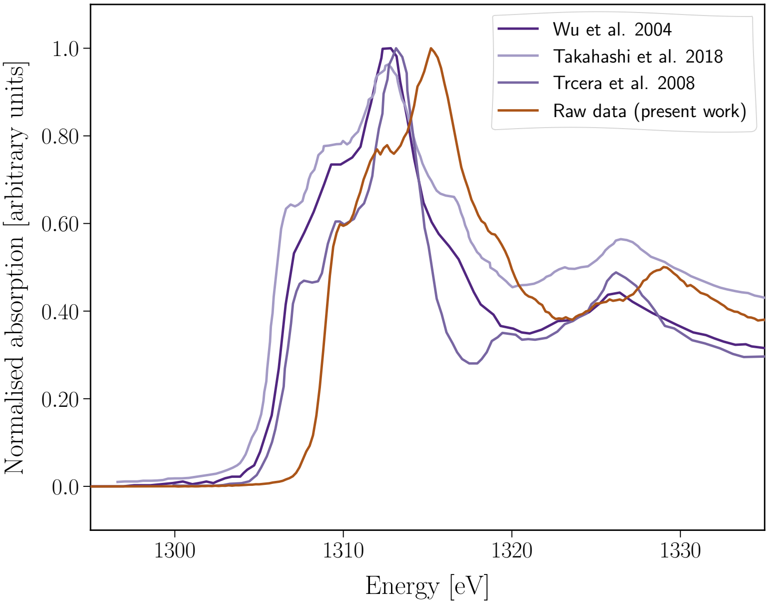

Figure A.1: XANES spectra of crystalline forsterite at the Mg K-edge. Experimental spectra from different works are listed in the panel.

cross sections of the compounds (with an energy range between 1100 eV and 1550 eV) are available in ASCII format at the following links: `www.sron.nl/~elisa/VIDI/`, `https://zenodo.org/deposit/2790329`.

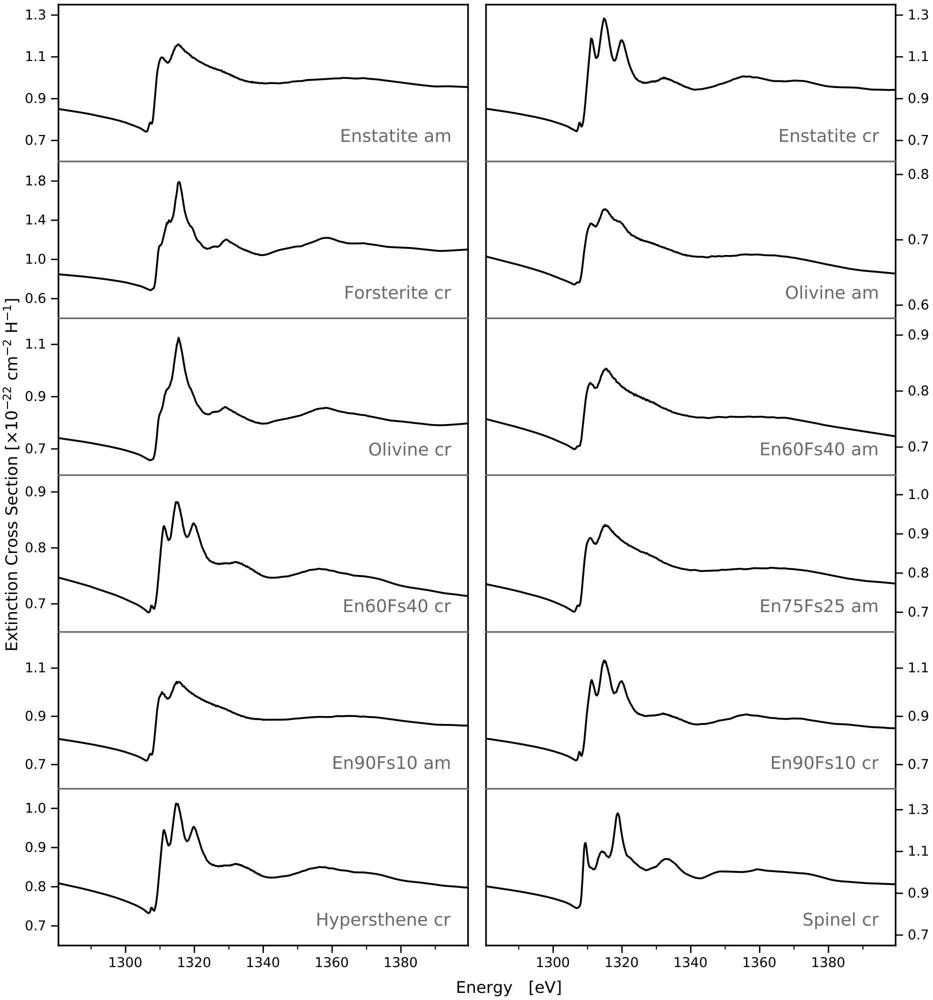

Figure A.2: Mg K-edge extinction cross sections of the mineral compounds presented in this work and listed in Table 3.1.

B

Appendices to Chapter 4

B.1 Broadband spectra

We give an overview of the parameters obtained from the best fit modelling of the X-ray binaries studied this work. As mentioned in Section 4.2.1, the sources were selected by their value of N_{H} and flux.

The effect of pileup on these bright sources can be high and distort the signal from the source. Therefore, we ignore the regions of the spectra where this effect is present. In particular, MEG, for the shape of its effective area, is affected by pile-up around 2 keV. Thus, in many observations, we exclude MEG data around the region of the silicon K-edge. GRS 1915+105 (obsid 7458) presents an extreme case where the effect of pile-up is higher than 40% around 2-3 keV because of the high 2-10 keV flux. For this specific source we only select the energy band between 1.2 and 2.4 keV of the HEG spectrum, whereas for MEG we ignore the region above 1.7 keV. In this way, we limited the spectrum into a narrow band which we fit adopting the pile-up corrected model used by Lee et al. (2002).

In general, we fit the continuum of the sources using both thermal and non-thermal components (see Section 4.2.3) absorbed by interstellar matter. In Table B.1 we list all the models and the best values of their relative parameters. For every source the hydrogen column density does not change significantly among the different observations and we assume it constant for all the observations. The Large Magellanic Cloud (LMC) has a much lower metallicity than our Galaxy (Russell & Dopita 1992). We compile both abundances sets in Table B.2.

Finally, we inspect the spectra for the presence of out-flowing ionised gas and hot gas present along the line of sight. Indeed, if absorption lines of ionised gas appear close to the edge, it is necessary to take them into account for precise modelling. We test whether if adding a `hot` model (to model collisionally ionised gas), `xabs` (to model photoionised gas), or a combination of the two improves the statistics of the broadband fit. As specified in Section 4.2.3 we find evidence of gas intrinsic to the source only in the microquasar GRS 1915+105. For ObsID 660 we find a column density of $N_{\rm H} = 3 \pm 1 \times 10^{20}{\rm cm}^{-2}$, a ionisation parameter $\log\xi = 2.7 \pm 0.2$ and outflow velocity of $v = -700 \pm 200$ km s^{-1}, whereas for obsID 7485 we obtain $N_{\rm H} = 5.9 \pm 0.7 \times 10^{20}{\rm cm}^{-2}$, $\log\xi = 3.72 \pm 0.02$ and $v = -145 \pm 9$ km s^{-1}.

Notes of Table B.1: we report the parameter values for each models used in the analysis where $k_{\rm B}T$ indicates the temperature in keV, $N_{\rm H}$ the column density, Γ the photon index of the power-law model, $F_{0.5-2\,{\rm keV}}$ and $F_{2-10\,{\rm keV}}$ the fluxes in the two different energy ranges. Errors given on parameters are 1σ errors. We also list the obsID of each observation and the C-statistic and degree of freedom (dof) for every fit.

B.2 Neutral silicon cross section

Here, we present our calculation of the photoabsorption cross-section for the neutral silicon K-shell in gas form. The inner-shell X-ray absorption for a single, isolated silicon atom implemented in SPEX is obtained by independent-particle calculation (Verner et al. 1993) which returns, a simple step function model where resonant transitions are not included. However, in order to investigate the presence of gaseous atomic silicon in the interstellar medium, in addition to the overwhelming abundance of silicon in cosmic dust, it is important to calculate and include in the model the resonance transition and relaxation effect.

In Figure B.1 we show the Si I photoabsorption cross-sections obtained from the Flexible Atomic Code (`FAC`, Gu 2008, in black) and the `COWAN` code (Cowan 1981, in blue). We overlap for comparison the cross-section calculated by Hasoglu & Gorczyca (2018) using the modified R-matrix method (Berrington et al. 1995). The cross-sections show different profiles with a shift in the energy of $1.5 - 3.5$ eV. In our analysis, we use the Si I cross-section calculated with the `COWAN` code since it can represent better the residual in the pre-edge of the Si K-shell for GX 3+1, used as test source in Paper I due to its high signal to noise ratio. In Table B.3 we list the atomic parameters of the Si I transitions, namely the line-centre wavelengths $\lambda_{\rm c}$ and the oscillator strengths $f_{\rm osc}$, necessary to evaluate the optical depth of the lines.

B.3 Instrumental feature at 6.741 Å

For all the sources in our sample, we observe a line in emission at 6.741 Å, in the vicinity of the silicon K-edge. This feature was already noticed in other sources, leading to different interpretation (see Section 4.2.2). In the present sample, we explored first the possibility of a Si XIII forbidden line emission ($\lambda = 6.7405$ Å). However, this is difficult to explain since, at the ionisation parameter that produces the Si XIII (f) line, we expect to detect also the Ne X and Mg XII lines, which are not observed. Their ionic densities peak at the same ionisation parameter (Figure 6 of Mehdipour et al. 2016).

The emission feature could be also associated with the scattering peak of Si. This possibility was explored in Paper I. However, this apparent emission feature was also observed in sources

Table B.1: Best fit parameters for all the sources.

obsID	`hot`	`pow`	`comt`		`bb`	`dbb`	$F_{0.5-2\,\mathrm{keV}}$	$F_{2-10\,\mathrm{keV}}$	Cstat/dof
	N_{H}	Γ	$k_{\mathrm{B}}T$	τ	$k_{\mathrm{B}}T$	$k_{\mathrm{B}}T$			
	10^{22} cm^{-2}		kev		kev	kev	10^{-10} erg cm^{-2} s^{-1}	10^{-9} erg cm^{-2} s^{-1}	
GRS 1758-258									
2429	2.14 ± 0.05	3.9 ± 0.2	–	–	0.90 ± 0.06	–	0.79 ± 0.08	0.12 ± 0.01	12621/11561
2750		2.8 ± 0.1	–	–	1.00 ± 0.01	–	1.2 ± 0.2	0.42 ± 0.06	
GRS 1915+105									
660	5.06 ± 0.02	–	–	–	–	3.0 ± 0.1	1.5 ± 0.1	7.8 ± 0.8	6056/5241
7485		–	–	–	–	12 ± 3	1.3 ± 0.4	23 ± 7	
GX 3+1									
16492	1.91 ± 0.05	1.12 ± 0.04	–	–	0.8 ± 0.1	–	3.7 ± 0.2	7.5 ± 0.5	28199/27207
16307		1.09 ± 0.04	–	–	0.8 ± 0.1	–	3.6 ± 0.2	7.4 ± 0.5	
18615		1.25 ± 0.04	–	–	0.7 ± 0.2	–	2.6 ± 0.1	4.8 ± 0.3	
19890		1.23 ± 0.03	–	–	0.8 ± 0.2	–	3.3 ± 0.2	6.1 ± 0.4	
19907		1.21 ± 0.04	–	–	0.7 ± 0.1	–	2.7 ± 0.1	4.8 ± 0.3	
19957		1.20 ± 0.03	–	–	0.8 ± 0.2	–	3.4 ± 0.2	6.9 ± 0.4	
19958		1.22 ± 0.03	–	–	0.8 ± 0.1	–	3.3 ± 0.2	6.2 ± 0.4	
GX 9+1									
11088	1.65 ± 0.02	–	2.4 ± 0.4	22 ± 9	0.76 ± 0.04	–	0.53 ± 0.04	10 ± 1	4815/4293
GX 17+2									
717	2.19 ± 0.01	–	2.5 ± 0.1	16 ± 4	0.79 ± 0.02	–	4.3 ± 0.2	13 ± 1	4946/4244
H 17433-322									
16738	2.67 ± 0.09	1.47 ± 0.04	–	–	–	0.38 ± 0.09	0.35 ± 0.02	0.88 ± 0.05	19169/18365
17679		1.47 ± 0.03	–	–	–	0.45 ± 0.05	0.21 ± 0.01	0.54 ± 0.03	
17680		1.48 ± 0.04	–	–	–	0.42 ± 0.06	0.35 ± 0.02	0.91 ± 0.05	
16739		1.49 ± 0.04	–	–	–	0.44 ± 0.08	0.39 ± 0.02	0.96 ± 0.05	
IGR J17091-3624									
12406	1.20 ± 0.01	1.78 ± 0.03	–	–	0.86 ± 0.01	–	2.5 ± 0.1	1.9 ± 0.1	17403/16586
17787		2.04 ± 0.02	–	–	0.55 ± 0.01	–	2.3 ± 0.2	1.1 ± 0.1	
17788		1.99 ± 0.03	–	–	0.69 ± 0.01	–	1.9 ± 0.1	1.0 ± 0.1	
LMC X-1									
93	0.79 ± 0.01	2.46 ± 0.03	–	–	0.61 ± 0.01	–	1.6 ± 0.1	0.38 ± 0.03	22659/21818
11074		2.45 ± 0.04	–	–	0.63 ± 0.01	–	1.7 ± 0.1	0.42 ± 0.04	
11986		2.65 ± 0.05	–	–	0.68 ± 0.01	–	1.4 ± 0.1	0.32 ± 0.03	
11987		2.44 ± 0.04	–	–	0.62 ± 0.01	–	1.6 ± 0.1	0.37 ± 0.03	
12068		2.40 ± 0.03	–	–	0.70 ± 0.01	–	1.7 ± 0.1	0.47 ± 0.04	
12071		2.59 ± 0.05	–	–	0.61 ± 0.01	–	1.8 ± 0.1	0.39 ± 0.04	
12069		2.51 ± 0.07	–	–	0.64 ± 0.01	–	1.7 ± 0.1	0.41 ± 0.03	
12070		2.62 ± 0.06	–	–	0.60 ± 0.01	–	1.6 ± 0.1	0.34 ± 0.03	
12089		2.58 ± 0.05	–	–	0.64 ± 0.01	–	1.6 ± 0.1	0.35 ± 0.03	
12090		2.79 ± 0.06	–	–	0.67 ± 0.01	–	1.6 ± 0.1	0.34 ± 0.03	
12072		2.59 ± 0.03	–	–	0.72 ± 0.01	–	1.5 ± 0.1	0.37 ± 0.03	

Table B.2: Comparison of element abundances in the Galactic interstellar medium (Lodders 2010) and in the Large Magellanic Cloud.

X	$A_{\mathrm{Gal}}(X)$	$A_{\mathrm{LMC}}(X)$	$10^{\Delta A(X)}$	Ref.
He	10.987	10.94	0.897	(1)
C	8.443	8.04	0.395	(1)
N	7.912	7.14	0.169	(1)
O	8.782	8.04	0.181	(2)
Ne	8.103	7.39	0.194	(2)
Na	6.347	5.50	0.142	(3)
Mg	7.599	6.88	0.191	(2)
Al	6.513	5.86	0.222	(4)
Si	7.586	6.99	0.254	(2)
S	7.210	6.70	0.309	(1)
Cl	5.299	4.76	0.289	(1)
Ar	6.553	6.29	0.546	(1)
Ca	6.367	5.89	0.333	(1)
Sc	3.123	2.64	0.329	(1)
Ti	4.949	4.81	0.678	(1)
V	4.042	4.08	1.094	(1)
Cr	5.703	5.47	0.585	(1)
Mn	5.551	5.21	0.456	(1)
Fe	7.514	6.84	0.211	(1)
Ni	6.276	6.04	0.581	(1)
Zn	4.700	4.28	0.380	(1)

References. (1) Russell & Dopita (1992); (2) Schenck et al. (2016); (3) Garnett (1999); (4) Korn et al. (2000).
Notes. The third column is the Large Magellanic Cloud abundance relative to the Galactic abundance, which is a parameter of the `hot` absorption model in Spex. For all the other not listed elements (which are low abundant and hardly contribute to the absorption in the soft X-ray band) the average value $10^{A(X)} = 0.4$ is assumed.

that should not display either an emission line, as they present a featureless spectrum, or a scattering peak, as their column density is too low to produce absorption by Si (e.g., Mrk 421).
Here, we explore the possibility of an instrumental line. We consider the Galactic X-ray binaries, GX 9+9, 4U 1820-30, CYG X-2, and the blazar MRK 421. In Figure B.2 we show the silicon K-edge region of the previous sources subtracted by the underlying continuum. We fit simultaneously the line with a delta function and we find a line-centre wavelength of $\lambda_{\mathrm{c}} = 6.741 \pm 0.001$. Moreover, we analyse separately the ± 1 order of MEG and HEG for sources (e.g. 4U 1636-53) with a relatively lower flux, to minimize the pileup effect. We notice that only +1 MEG, which does not cross the front-illuminated chip in the silicon region, does not display the emission peak. We suggest therefore that the deep calibration

Table B.3: Atomic parameter of those Si I transitions, which contribute to the line absorption of Si I.

Lower energy level	Upper energy level	FAC			COWAN		
		λ_c (Å)	E_c (eV)	$f_{\rm osc}$	λ_c (Å)	E_c (eV)	$f_{\rm osc}$
$1s^2 2s^2 2p^6 3s^2 3p^2\ ^3P_0$	$1s^1\left(^4S\right)2s^2 2p^6 3s^2 3p^3\ ^3S_1$	6.7489	1837.1	4.19×10^{-3}	6.7364	1840.5	5.36×10^{-3}
	$1s^1\left(^2D\right)2s^2 2p^6 3s^2 3p^3\ ^3D_1$	6.7445	1838.3	6.10×10^{-3}	6.7324	1841.6	6.64×10^{-3}
	$1s^1\left(^2P\right)2s^2 2p^6 3s^2 3p^3\ ^3P_1$	6.7408	1839.3	3.26×10^{-3}	6.7284	1842.7	3.58×10^{-3}
	$1s^1\left(^2P\right)2s^2 2p^6 3s^2 3p^3\ ^1P_1$	6.7393	1839.7	5.12×10^{-5}	6.7273	1843.0	2.17×10^{-7}
$1s^2 2s^2 2p^6 3s^2 3p^2\ ^3P_1$	$1s^1\left(^4S\right)2s^2 2p^6 3s^2 3p^3\ ^5S_2$	6.7514	1836.4	3.99×10^{-7}	6.7390	1839.8	4.67×10^{-7}
	$1s^1\left(^4S\right)2s^2 2p^6 3s^2 3p^3\ ^3S_1$	6.7489	1837.1	1.42×10^{-2}	6.7364	1840.5	1.60×10^{-2}
	$1s^1\left(^2D\right)2s^2 2p^6 3s^2 3p^3\ ^3D_1$	6.7448	1838.2	3.73×10^{-3}	6.7324	1841.6	4.75×10^{-3}
	$1s^1\left(^2D\right)2s^2 2p^6 3s^2 3p^3\ ^3D_2$	6.7448	1838.2	1.32×10^{-2}	6.7324	1841.6	1.50×10^{-2}
	$1s^1\left(^2D\right)2s^2 2p^6 3s^2 3p^3\ ^1D_2$	6.7434	1838.6	4.27×10^{-5}	6.7313	1841.9	2.65×10^{-6}
	$1s^1\left(^2P\right)2s^2 2p^6 3s^2 3p^3\ ^3P_0$	6.7408	1839.3	3.37×10^{-3}	6.7287	1842.6	3.81×10^{-3}
	$1s^1\left(^2P\right)2s^2 2p^6 3s^2 3p^3\ ^3P_1$	6.7408	1839.3	2.52×10^{-3}	6.7284	1842.7	2.88×10^{-3}
	$1s^1\left(^2P\right)2s^2 2p^6 3s^2 3p^3\ ^3P_2$	6.7404	1839.4	4.09×10^{-3}	6.7284	1842.7	4.39×10^{-3}
	$1s^1\left(^2P\right)2s^2 2p^6 3s^2 3p^3\ ^1P_1$	6.7393	1839.7	1.91×10^{-5}	6.7273	1843.0	3.93×10^{-8}
$1s^2 2s^2 2p^6 3s^2 3p^2\ ^3P_2$	$1s^1\left(^4S\right)2s^2 2p^6 3s^2 3p^3\ ^5S_2$	6.7514	1836.4	3.74×10^{-6}	6.7393	1839.7	1.32×10^{-6}
	$1s^1\left(^4S\right)2s^2 2p^6 3s^2 3p^3\ ^3S_1$	6.7489	1837.1	2.21×10^{-2}	6.7368	1840.4	2.63×10^{-2}
	$1s^1\left(^2D\right)2s^2 2p^6 3s^2 3p^3\ ^3D_1$	6.7448	1838.2	4.57×10^{-4}	6.7324	1841.6	2.80×10^{-4}
	$1s^1\left(^2D\right)2s^2 2p^6 3s^2 3p^3\ ^3D_2$	6.7448	1838.2	3.99×10^{-3}	6.7324	1841.6	4.49×10^{-3}
	$1s^1\left(^2D\right)2s^2 2p^6 3s^2 3p^3\ ^3D_3$	6.7448	1838.2	2.44×10^{-2}	6.7324	1841.6	2.72×10^{-2}
	$1s^1\left(^2D\right)2s^2 2p^6 3s^2 3p^3\ ^1D_2$	6.7434	1838.6	–	6.7313	1841.9	3.89×10^{-5}
	$1s^1\left(^2P\right)2s^2 2p^6 3s^2 3p^3\ ^3P_1$	6.7408	1839.3	4.29×10^{-3}	6.7284	1842.7	4.97×10^{-3}
	$1s^1\left(^2P\right)2s^2 2p^6 3s^2 3p^3\ ^3P_2$	6.7404	1839.4	1.32×10^{-2}	6.7284	1842.7	1.46×10^{-2}
	$1s^1\left(^2P\right)2s^2 2p^6 3s^2 3p^3\ ^1P_1$	6.7393	1839.7	4.53×10^{-5}	6.7273	1843.0	4.91×10^{-8}

Notes. λ_c and E_c are the line-centre wavelength and energy, respectively. The oscillator strength, indicated with $f_{\rm osc}$, is dimensionless.

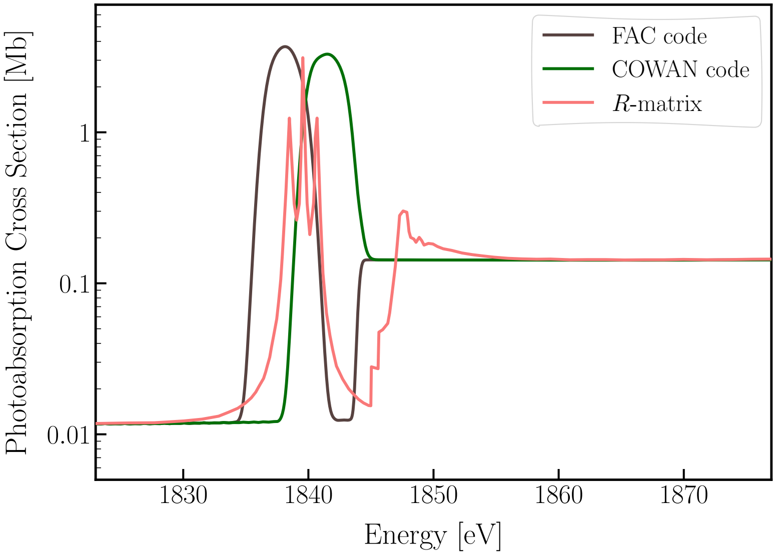

Figure B.1: Comparison of the cross-section for neutral silicon, Si I, calculated with different codes. The cross-section calculated with the R-matrix, in red, is taken from Hasoğlu et al. (2014).

silicon feature present in the effective area of −1 MEG and ±1 HEG could play a role in displaying the spike at 6.741 Å.

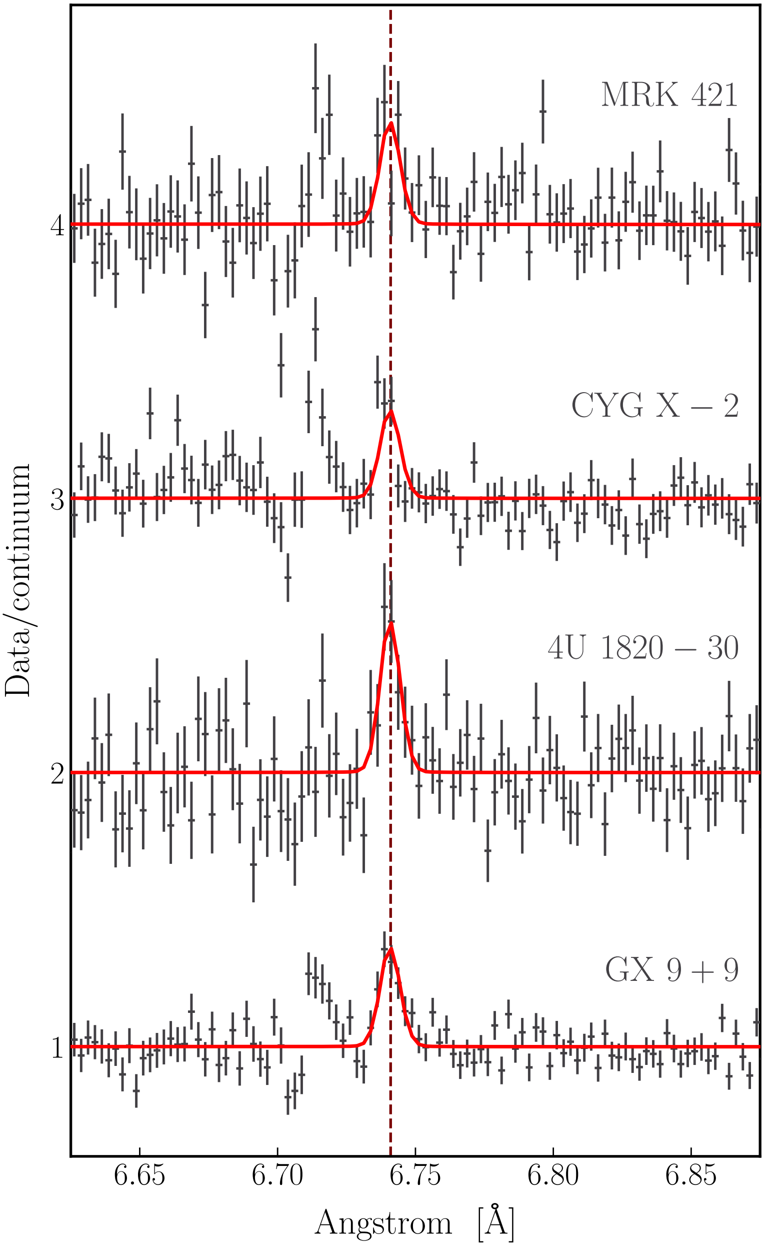

Figure B.2: Fit of the line in emission present in the silicon K-edge region. To fit the underlying continuum we use a simple power-law. The different data-sets are shifted in the interest for clarity.

C

Appendices to Chapter 5

C.1 Extinction cross sections

In Figure C.1 we present the extinction cross section profiles around the iron K-edge for each sample presented in Table 5.1. We developed these data from the synchrotron measurements taken at the European Synchrotron Radiation Facility in Grenoble, France. These curves were implemented in the AMOL model of the spectral fitting code SPEX with a fixed energy resolution of 0.1 eV. The absorption, scattering, and extinction cross sections of the compounds (with an energy range between 6.7 and 8.0 keV) are available in ASCII format at the following link: `www.sron.nl/~elisa/VIDI/`.

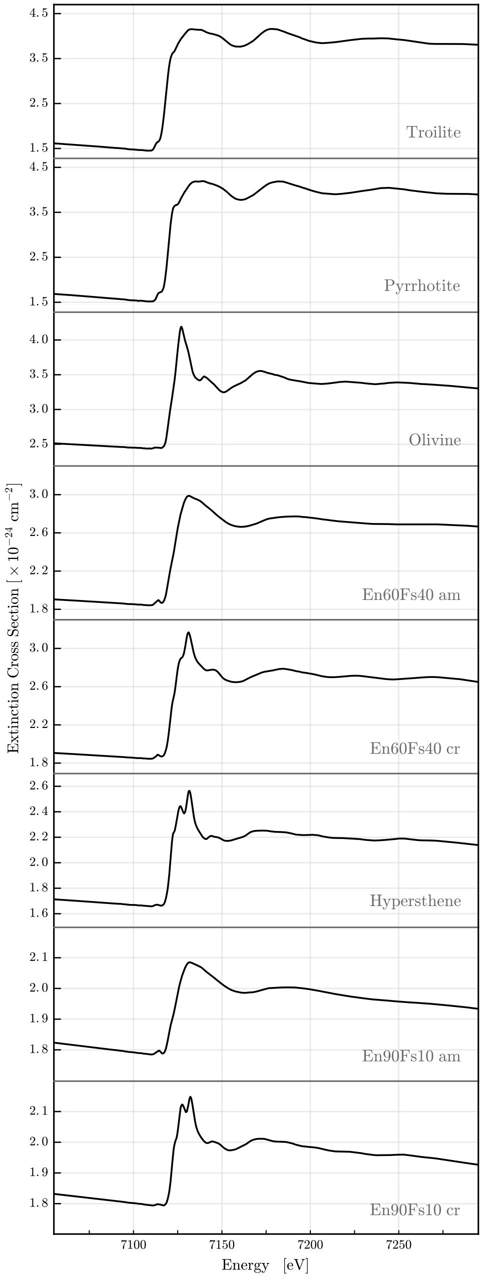

Figure C.1: Iron K-edge extinction cross sections of the samples presented in this work.

Bibliography

Akaike, H. 1974, IEEE Transactions on Automatic Control, 19, 716

Akaike, H. 1998, Prediction and Entropy, ed. E. Parzen, K. Tanabe, & G. Kitagawa (New York, NY: Springer New York), 387–410

Altobelli, N., Postberg, F., Fiege, K., et al. 2016, Science, 352, 312

Anders, E., & Grevesse, N. 1989, Geochim. Cosmochim. Acta, 53, 197

Andersen, M., Steinacker, J., Thi, W.-F., et al. 2013, A&A, 559, A60

Anderson, S. F., Margon, B., Deutsch, E. W., Downes, R. A., & Allen, R. G. 1997, ApJ, 482, L69

Arnett, W. D., & Thielemann, F. K. 1985, ApJ, 295, 589

Asai, K., Dotani, T., Nagase, F., et al. 1993, PASJ, 45, 801

Bania, T. M. 1977, ApJ, 216, 381

—. 1980, ApJ, 242, 95

Barret, D., Lam Trong, T., den Herder, J.-W., et al. 2016, in Proc. SPIE, Vol. 9905, Space Telescopes and Instrumentation 2016: Ultraviolet to Gamma Ray, 99052F

Bautista, M. A., & Kallman, T. R. 2001, The Astrophysical Journal Supplement Series, 134, 139

Bayes, T. 1763, Phil. Trans. of the Royal Soc. of London, 53, 370

Bearden, J. A., & Burr, A. F. 1967, Reviews of Modern Physics, 39, 125

Bell, K. L., & Kingston, A. E. 1967, MNRAS, 136, 241

Benjamin, R. A. 2008, in Astronomical Society of the Pacific Conference Series, Vol. 387, Massive Star Formation: Observations Confront Theory, ed. H. Beuther, H. Linz, & T. Henning, 375

Berg, M. J., Sorensen, C. M., & Chakrabarti, A. 2010, J. Quant. Spec. Radiat. Transf., 111, 782

Berrington, K. A., Eissner, W. B., & Norrington, P. H. 1995, Computer Physics Communications, 92, 290

Bilalbegović, G., Maksimović, A., & Valencic, L. A. 2018, MNRAS, 476, 5358

Blommaert, J. A. D. L., de Vries, B. L., Waters, L. B. F. M., et al. 2014, A&A, 565, A109

Bohren, C. F. 2010, European Journal of Physics, 31, 573

Boothroyd, A. I. 2006, Science, 314, 1690

Bowen, D. V., Jenkins, E. B., Tripp, T. M., et al. 2008, ApJS, 176, 59

Bowyer, S., Byram, E. T., Chubb, T. A., & Friedman, H. 1965, Science, 147, 394

Bradley, J. P. 1994, Science, 265, 925

Brinkman, A. C., Dijkstra, J. H., Geerlings, W. F. P. A. L., et al. 1980, Appl. Opt., 19, 1601

Brinkman, B. C., Gunsing, T., Kaastra, J. S., et al. 2000, Society of Photo-Optical Instrumentation Engineers (SPIE) Conference Series, Vol. 4012, Description and performance of the low-energy transmission grating spectrometer on board Chandra, ed. J. E. Truemper & B. Aschenbach, 81–90

Bruzzoni, P., Carranza, R. M., Lacoste, J. R. C., & Crespo, E. A. 2002, Electrochimica Acta, 48, 341

Buchner, J., Georgakakis, A., Nandra, K., et al. 2014, A&A, 564, A125

Bunker, G. 2010, Introduction to XAFS (Cambridge, UK: Cambridge University Press)

Burnham, K. P., & Anderson, D. R. 2002, Model selection and multimodel inference: a practical information-theoretic approach, 2nd edn. (Springer), 1–488

Cackett, E. M., Miller, J. M., Raymond, J., et al. 2008, ApJ, 677, 1233

Canizares, C. R., Davis, J. E., Dewey, D., et al. 2005, PASP, 117, 1144

Cash, W. 1979, ApJ, 228, 939

Chang, Y., Hsieh, H.-H., Pong, W.-F., et al. 1999, Journal of Applied Physics, 86, 5609

Chapman, N. L., Mundy, L. G., Lai, S.-P., & Evans, II, N. J. 2009, ApJ, 690, 496

Charles, P. A., Kahn, S. M., Bowyer, S., et al. 1979, ApJ, 230, L83

Chenevez, J., Falanga, M., Brandt, S., et al. 2006, A&A, 449, L5

Chiar, J. E., & Tielens, A. G. G. M. 2006, ApJ, 637, 774

Clemens, D. P., Sanders, D. B., & Scoville, N. Z. 1988, ApJ, 327, 139

Compiègne, M., Verstraete, L., Jones, A., et al. 2011, A&A, 525, A103

Corrales, L. R., García, J., Wilms, J., & Baganoff, F. 2016, MNRAS, 458, 1345

Corrales, L. R., & Paerels, F. 2015, MNRAS, 453, 1121

Costantini, E., & de Vries, C. P. 2013, Mem. Soc. Astron. Italiana, 84, 592

Costantini, E., Freyberg, M. J., & Predehl, P. 2005, A&A, 444, 187

Costantini, E., Zeegers, S. T., Rogantini, D., et al. 2019, A&A, 629, A78

Costantini, E., Pinto, C., Kaastra, J. S., et al. 2012, A&A, 539, A32

Court, J. M. C., Altamirano, D., Pereyra, M., et al. 2017, MNRAS, 468, 4748

Cowan, J. 1995, The Biological Chemistry of Magnesium (Wiley)

Cowan, R. D. 1981, The theory of atomic structure and spectra

Cross, J. O., Newville, M., Rehr, J. J., et al. 1998, Phys. Rev. B, 58, 11215

Cruddace, R., Paresce, F., Bowyer, S., & Lampton, M. 1974, ApJ, 187, 497

Dame, T. M., & Thaddeus, P. 2008, ApJ, 683, L143

Davies, B., Origlia, L., Kudritzki, R.-P., et al. 2009, ApJ, 694, 46

Davisson, C. M. 1965, in Alpha-, Beta- and Gamma-ray Spectroscopy, ed. K. Siegbahn, Vol. 1, 827

de Avillez, M. A., & Breitschwerdt, D. 2005, ApJ, 634, L65

De Cia, A., Ledoux, C., Mattsson, L., et al. 2016, A&A, 596, A97

de L. Kronig, R. 1926, J. Opt. Soc. Am., 12, 547

de Plaa, J., Kaastra, J. S., Tamura, T., et al. 2004, A&A, 423, 49

Decourchelle, A., Costantini, E., Badenes, C., et al. 2013, ArXiv e-prints, arXiv:1306.2335

den Hartog, P. R., in't Zand, J. J. M., Kuulkers, E., et al. 2003, A&A, 400, 633

den Herder, J. W., Brinkman, A. C., Kahn, S. M., et al. 2001, Astronomy and Astrophysics, 365, L7

Díaz Trigo, M., & Boirin, L. 2016, Astronomische Nachrichten, 337, 368

Díaz Trigo, M., Parmar, A. N., Boirin, L., Méndez, M., & Kaastra, J. S. 2006, A&A, 445, 179

Dijkstra, J. H., Lantwaard, L. J., & Timmerman, C. 1978, in New Instrumentation for Space Astronomy, ed. K. A. van der Hucht & G. Vaiana, 257–264

Dorschner, J., Begemann, B., Henning, T., Jaeger, C., & Mutschke, H. 1995, A&A, 300, 503

Draine, B. T. 2003, ApJ, 598, 1026

Draine, B. T. 2009, in Astronomical Society of the Pacific Conference Series, Vol. 414, Cosmic Dust - Near and Far, ed. T. Henning, E. Grün, & J. Steinacker, 453

—. 2011, Physics of the Interstellar and Intergalactic Medium

Draine, B. T., & Fraisse, A. A. 2009, ApJ, 696, 1

Draine, B. T., & Hensley, B. 2013, ApJ, 765, 159

Draine, B. T., & Lee, H. M. 1984, ApJ, 285, 89

Draine, B. T., & Li, A. 2007, ApJ, 657, 810

Dwek, E. 2016, ApJ, 825, 136

Dwek, E., & Cherchneff, I. 2011, ApJ, 727, 63

Dwek, E., & Scalo, J. M. 1980, ApJ, 239, 193

Dyson, J. E., & Williams, D. A. 1997, The physics of the interstellar medium, doi:10.1201/9780585368115

Ebisawa, K., Bourban, G., Bodaghee, A., Mowlavi, N., & Courvoisier, T. J.-L. 2003, A&A, 411, L59

Egerton, R. F. 2009, Reports on Progress in Physics, 72, 016502

Ehrenfreund, P., & Foing, B. 2015, Nature, 523, 296

Evans, A. 1986, MNRAS, 223, 219

Fabian, D., Jäger, C., Henning, T., Dorschne, J., & Mutschke, H. 2000, in ESA Special Publication, Vol. 456, ISO Beyond the Peaks: The 2nd ISO Workshop on Analytical Spectroscopy, ed. A. Salama, M. F. Kessler, K. Leech, & B. Schulz, 347

Feroz, F., Hobson, M. P., & Bridges, M. 2009, MNRAS, 398, 1601

Feroz, F., Hobson, M. P., Cameron, E., & Pettitt, A. N. 2013, arXiv e-prints, arXiv:1306.2144

Ferrière, K. M. 2001, Reviews of Modern Physics, 73, 1031

Fireman, E. L. 1974, ApJ, 187, 57

Flank, A.-M., Cauchon, G., Lagarde, P., et al. 2006, Nuclear Instruments and Methods in Physics Research B, 246, 269

Fogerty, S., Forrest, W., Watson, D. M., Sargent, B. A., & Koch, I. 2016, ApJ, 830, 71

Foreman-Mackey, D., Hogg, D. W., Lang, D., & Goodman, J. 2013, PASP, 125, 306

Fruscione, A., McDowell, J. C., Allen, G. E., et al. 2006, in Proc. SPIE, Vol. 6270, Society of Photo-Optical Instrumentation Engineers (SPIE) Conference Series, 62701V

Fukushi, K., Suzuki, Y., Kawano, J., et al. 2017, Geochimica et Cosmochimica Acta, 213, 457

Futamoto, K., Mitsuda, K., Takei, Y., Fujimoto, R., & Yamasaki, N. Y. 2004, ApJ, 605, 793

Galli, D., Walmsley, M., & Gonçalves, J. 2002, A&A, 394, 275

Galloway, D. K., Muno, M. P., Hartman, J. M., Psaltis, D., & Chakrabarty, D. 2008, The Astrophysical Journal Supplement Series, 179, 360

Garnett, D. R. 1999, in IAU Symposium, Vol. 190, New Views of the Magellanic Clouds, ed. Y.-H. Chu, N. Suntzeff, J. Hesser, & D. Bohlender, 266

Gaskin, J. A., Swartz, D. A., Vikhlinin, A., et al. 2019, Journal of Astronomical Telescopes, Instruments, and Systems, 5, 021001

Gatuzz, E., & Churazov, E. 2018, MNRAS, 474, 696

Gelman, A., Carlin, J., Stern, H., et al. 2013, Bayesian Data Analysis, Third Edition, Chapman & Hall/CRC Texts in Statistical Science (Taylor & Francis)

Genovali, K., Lemasle, B., Bono, G., et al. 2014, A&A, 566, A37

Genovali, K., Lemasle, B., da Silva, R., et al. 2015, A&A, 580, A17

Giacconi, R., Gursky, H., Paolini, F. R., & Rossi, B. B. 1962, Phys. Rev. Lett., 9, 439

Giacconi, R., Murray, S., Gursky, H., et al. 1972, ApJ, 178, 281

Goldsmith, P. F. 1987, Molecular Clouds: An Overview, ed. D. J. Hollenbach & J. Thronson, Harley A., Vol. 134, 51

Gomez, H. L., Clark, C. J. R., Nozawa, T., et al. 2012, MNRAS, 420, 3557

Goodman, J., & Weare, J. 2010, Communications in Applied Mathematics and Computational Science, 5, 65

Gorczyca, T. W. 2000, Phys. Rev. A, 61, 024702

Gorczyca, T. W., Bautista, M. A., Hasoglu, M. F., et al. 2013, ApJ, 779, 78

Gorenstein, P., Harris, B., Gursky, H., et al. 1971, Science, 172, 369

Gregory, P. C. 2005, Bayesian Logical Data Analysis for the Physical Sciences: A Comparative Approach with ‘Mathematica’ Support (Cambridge University Press)

Gu, M. F. 2008, Canadian Journal of Physics, 86, 675

Guainazzi, M., & Bianchi, S. 2007, MNRAS, 374, 1290

Gullikson, E. M. 2001, X-RAY DATA BOOKLET

Hagihara, T., Yamasaki, N. Y., Mitsuda, K., et al. 2011, PASJ, 63, S889

Hagihara, T., Yao, Y., Yamasaki, N. Y., et al. 2010, PASJ, 62, 723

Hanke, M., Wilms, J., Nowak, M. A., Barragán, L., & Schulz, N. S. 2010, A&A, 509, L8

Hasagawa, T., & Torii, T. 1991, Mathematics of Computation, 56, 741

Hasinger, G., & van der Klis, M. 1989, A&A, 225, 79

Hasoglu, M. F., & Gorczyca, T. W. 2018, in Astronomical Society of the Pacific Conference Series, Vol. 515, Workshop on Astrophysical Opacities, 275

Hasoğlu, M. F., Abdel-Naby, S. A., Gatuzz, E., et al. 2014, ApJS, 214, 8

Heger, A., & Woosley, S. E. 2010, ApJ, 724, 341

Henke, B. L., Gullikson, E. M., & Davis, J. C. 1993, Atomic Data and Nuclear Data Tables, 54, 181

Henning, T. 2010, ARA&A, 48, 21

Hirashita, H. 2012, MNRAS, 422, 1263

Hoffman, J., & Draine, B. T. 2016, ApJ, 817, 139

Honda, M., Kataza, H., Okamoto, Y. K., et al. 2003, ApJ, 585, L59

Hony, S., Bouwman, J., Keller, L. P., & Waters, L. B. F. M. 2002, A&A, 393, L103

Huenemoerder, D. P., Mitschang, A., Dewey, D., et al. 2011, AJ, 141, 129

Hughes, J. P., Hayashi, I., & Koyama, K. 1998, ApJ, 505, 732

Iaria, R., di Salvo, T., Robba, N. R., et al. 2005, A&A, 439, 575

in’t Zand, J., Verbunt, F., Heise, J., et al. 2004, Nuclear Physics B Proceedings Supplements, 132, 486

Jackson, J. M., Rathborne, J. M., Shah, R. Y., et al. 2006, ApJS, 163, 145

Jaeger, C., Molster, F. J., Dorschner, J., et al. 1998, A&A, 339, 904

Jäger, C., Dorschner, J., Mutschke, H., Posch, T., & Henning, T. 2003, A&A, 408, 193

Jeffreys, H. 1961, Theory of Probability, 3rd edn. (Oxford, England: Oxford)

Jenkins, E. B. 1978, ApJ, 219, 845

—. 2009, ApJ, 700, 1299

Jones, A. P. 1997, in Astronomical Society of the Pacific Conference Series, Vol. 122, From Stardust to Planetesimals, ed. Y. J. Pendleton, 97

Jones, A. P. 2000, J. Geophys. Res., 105, 10257

Jones, A. P. 2007, European Journal of Mineralogy, 19, 771

Jones, A. P., Fanciullo, L., Köhler, M., et al. 2013, A&A, 558, A62

Jones, A. P., & Nuth, J. A. 2011, A&A, 530, A44

Jones, A. P., & Williams, D. A. 1987, MNRAS, 224, 473

Jones, R. O. 2015, Rev. Mod. Phys., 87, 897

Juett, A. M., Schulz, N. S., & Chakrabarty, D. 2004, ApJ, 612, 308

Juett, A. M., Schulz, N. S., Chakrabarty, D., & Gorczyca, T. W. 2006, ApJ, 648, 1066

Kaastra, J. S. 2017, A&A, 605, A51

Kaastra, J. S., & Barr, P. 1989, A&A, 226, 59

Kaastra, J. S., Mewe, R., & Nieuwenhuijzen, H. 1996, in UV and X-ray Spectroscopy of Astrophysical and Laboratory Plasmas, ed. K. Yamashita & T. Watanabe, 411–414

Kaastra, J. S., Raassen, A. J. J., de Plaa, J., & Gu, L. 2017, SPEX X-ray spectral fitting package, doi:10.5281/zenodo.2272992

—. 2018, SPEX X-ray spectral fitting package, doi:10.5281/zenodo.2419563

Kalberla, P. M. W., Burton, W. B., Hartmann, D., et al. 2005, A&A, 440, 775

Kalberla, P. M. W., Westphalen, G., Mebold, U., Hartmann, D., & Burton, W. B. 1998, A&A, 332, L61

Kass, R. E., & Raftery, A. E. 1995, Journal of the American Statistical Association, 90, 773

Keller, L. P., & Messenger, S. 2013, Geochim. Cosmochim. Acta, 107, 341

Keller, L. P., Messenger, S., Flynn, G. J., Wirick, S., & Jacobsen, C. 2002, in Lunar and Planetary Inst. Technical Report, Vol. 33, Lunar and Planetary Science Conference

Kemper, F., de Koter, A., Waters, L. B. F. M., Bouwman, J., & Tielens, A. G. G. M. 2002, A&A, 384, 585

Kemper, F., Vriend, W. J., & Tielens, A. G. G. M. 2004, ApJ, 609, 826

Kim, S.-H., & Martin, P. G. 1995, ApJ, 444, 293

—. 1996, ApJ, 462, 296

Kimura, H., Mann, I., & Jessberger, E. K. 2003, ApJ, 583, 314

Kirchhoff, G., & Bunsen, R. 1860, Annalen der Physik, 186, 161

Knuth, K. H., Habeck, M., Malakar, N. K., Mubeen, A. M., & Placek, B. 2014, ArXiv e-prints, arXiv:1411.3013

Köhler, M., Jones, A., & Ysard, N. 2014, A&A, 565, L9

Koningsberger, D. C., & Prins, R. 1988, X-Ray Absorption: Principles, Applications, Techniques of EXAFS, SEXAFS and XANES (New York: Wiley)

Korn, A. J., Becker, S. R., Gummersbach, C. A., & Wolf, B. 2000, A&A, 353, 655

Kortright, J. B., & Kim, S.-K. 2000, Phys. Rev. B, 62, 12216

Kramers, H. A. 1927, Atti Cong. Intern. Fisica (Transactions of Volta Centenary Congress)

Como, 2, 545

Kulkarni, S. R., & Heiles, C. 1987, The Atomic Component, ed. D. J. Hollenbach & J. Thronson, Harley A., Vol. 134, 87

Kuntz, K. D., & Snowden, S. L. 2000, ApJ, 543, 195

Kuulkers, E. 2002, A&A, 383, L5

Kuulkers, E., den Hartog, P. R., in't Zand, J. J. M., et al. 2003, A&A, 399, 663

Kuulkers, E., & van der Klis, M. 2000, A&A, 356, L45

Landau, L. D., & Lifshitz, E. M. 1960, Electrodynamics of continuous media (New York: Pergamon)

Lee, J. C., & Ravel, B. 2005, ApJ, 622, 970

Lee, J. C., Reynolds, C. S., Remillard, R., et al. 2002, ApJ, 567, 1102

Lee, J. C., Xiang, J., Ravel, B., Kortright, J., & Flanagan, K. 2009, ApJ, 702, 970

Lefèvre, C., Pagani, L., Juvela, M., et al. 2014, A&A, 572, A20

Lemasle, B., François, P., Piersimoni, A., et al. 2008, A&A, 490, 613

Li, A., & Draine, B. T. 2001a, ApJ, 554, 778

—. 2001b, ApJ, 550, L213

—. 2002, ApJ, 564, 803

Li, D., Goldsmith, P. F., & Menten, K. 2003, ApJ, 587, 262

Li, M. P., Zhao, G., & Li, A. 2007, MNRAS, 382, L26

Liao, J.-Y., Zhang, S.-N., & Yao, Y. 2013, ApJ, 774, 116

Liddle, A. R. 2004, MNRAS, 351, L49

—. 2007, MNRAS, 377, L74

Liszt, H. S. 2008, A&A, 486, 467

Lodders, K. 2010, Astrophysics and Space Science Proceedings, 16, 379

Lutovinov, A., Grebenev, S., Molkov, S., & Sunyaev, R. 2003, Astronomische Nachrichten Supplement, 324, 337

Maciel, W. J. 2013, Astrophysics of the Interstellar Medium, doi:10.1007/978-1-4614-3767-3

Maggi, P., Haberl, F., Kavanagh, P. J., et al. 2016, A&A, 585, A162

Mainardi, L. I., Paizis, A., Farinelli, R., et al. 2010, A&A, 512, A57

Makishima, K., Mitsuda, K., Inoue, H., et al. 1983, ApJ, 267, 310

Markwick-Kemper, F., Gallagher, S. C., Hines, D. C., & Bouwman, J. 2007, ApJ, 668, L107

Marra, A. C., Lane, M. D., Orofino, V., Blanco, A., & Fonti, S. 2011, Icarus, 211, 839

Marshall, D. J., Fux, R., Robin, A. C., & Reylé, C. 2008, A&A, 477, L21

Martin, P. G. 1970, MNRAS, 149, 221

Martin, R. P., Andrievsky, S. M., Kovtyukh, V. V., et al. 2015, MNRAS, 449, 4071

Martínez-Solaeche, G., Karakci, A., & Delabrouille, J. 2018, Mon. Not. Roy. Astron. Soc., 476, 1310

Mastelaro, V. R., & Zanotto, E. D. 2018, Materials, 11, doi:10.3390/ma11020204

Mathis, J. S., Rumpl, W., & Nordsieck, K. H. 1977, ApJ, 217, 425

Mattsson, L., De Cia, A., Andersen, A. C., & Petitjean, P. 2019, A&A, 624, A103

Mauche, C. W., & Gorenstein, P. 1986, ApJ, 302, 371

McKee, C. F., & Ostriker, J. P. 1977, ApJ, 218, 148

Mehdipour, M., & Costantini, E. 2018, ArXiv e-prints, arXiv:1808.04628

Mehdipour, M., Kaastra, J. S., & Kallman, T. 2016, A&A, 596, A65

Micelotta, E. R., Matsuura, M., & Sarangi, A. 2018, Space Sci. Rev., 214, 53

Miller, E. D., Tsunemi Hiroshi, Bautz, M. W., et al. 2008, PASJ, 60, S95

Miller, J. M., Cackett, E. M., & Reis, R. C. 2009, ApJ, 707, L77

Miller, J. M., Wojdowski, P., Schulz, N. S., et al. 2005, ApJ, 620, 398

Miller, J. M., Fabian, A. C., Wijnands, R., et al. 2002, ApJ, 578, 348

Miller, M. J., & Bregman, J. N. 2013, The Astrophysical Journal, 770, 118

Min, M., Waters, L. B. F. M., de Koter, A., et al. 2007, A&A, 462, 667

Mitsuda, K., Inoue, H., Koyama, K., et al. 1984, PASJ, 36, 741

Mitsuda, K., Kelley, R. L., Boyce, K. R., et al. 2012, Journal of Low Temperature Physics, 167, 795

Molster, F. J., Waters, L. B. F. M., & Kemper, F. 2010, The Mineralogy of Interstellar and Circumstellar Dust in Galaxies, ed. T. Henning, Vol. 815, 143–201

Molster, F. J., Waters, L. B. F. M., & Tielens, A. G. G. M. 2002, A&A, 382, 222

Muno, M. P., Remillard, R. A., & Chakrabarty, D. 2002, ApJ, 568, L35

Mutschke, H., Begemann, B., Dorschner, J., et al. 1998, A&A, 333, 188

Mutschke, H., Min, M., & Tamanai, A. 2009, A&A, 504, 875

Nandra, K., Barret, D., Barcons, X., et al. 2013, ArXiv e-prints, arXiv:1306.2307

Natta, A., Testi, L., Calvet, N., et al. 2007, in Protostars and Planets V, ed. B. Reipurth, D. Jewitt, & K. Keil, 767

Newville, M. 2004, Consortium for Advanced Radiation Sources, University of Chicago (USA)[http://xafs. org], 78, doi:10.2138/rmg.2014.78.2

Nicastro, F., Mathur, S., Elvis, M., et al. 2005, Nature, 433, 495

Nikitenko, S., Beale, A. M., van der Eerden, A. M. J., et al. 2008, Journal of Synchrotron Radiation, 15, 632

Novick, R. 1973, in IAU Symposium, Vol. 55, X- and Gamma-Ray Astronomy, ed. H. Bradt & R. Giacconi, 118

Oberti, R., Hawthorne, F., Cannillo, E., & Cámara, F. 2007, Reviews in Mineralogy and Geochemistry, 67, 125

Olofsson, J., Augereau, J.-C., van Dishoeck, E. F., et al. 2009, A&A, 507, 327

Oosterbroek, T., Barret, D., Guainazzi, M., & Ford, E. C. 2001, A&A, 366, 138

Orosz, J. A., Steeghs, D., McClintock, J. E., et al. 2009, ApJ, 697, 573

Ossenkopf, V., Henning, T., & Mathis, J. S. 1992, A&A, 261, 567

Otte, B., & Dixon, W. V. D. 2006, ApJ, 647, 312

Paerels, F., Yamasaki, N., Anabuki, N., et al. 2014, ArXiv e-prints, arXiv:1412.1174

Pagani, L., Steinacker, J., Bacmann, A., Stutz, A., & Henning, T. 2010, Science, 329, 1622

Palme, H., Lodders, K., & Jones, A. 2014, Solar System Abundances of the Elements, ed. A. M. Davis, Vol. 2, 15–36

Panchuk, K. 2017, Physical Geology, Second Adapted Edition (CC BY 4.0 International License)

Parmar, A. N., Oosterbroek, T., Boirin, L., & Lumb, D. 2002, A&A, 386, 910

Parratt, L. G., Hempstead, C. F., & Jossem, E. L. 1957, Physical Review, 105, 1228

Pedicelli, S., Bono, G., Lemasle, B., et al. 2009, A&A, 504, 81

Pian, E., D'Avanzo, P., Benetti, S., et al. 2017, Nature, 551, 67 EP

Pinto, C., Kaastra, J. S., Costantini, E., & de Vries, C. 2013, A&A, 551, A25

Pinto, C., Kaastra, J. S., Costantini, E., & Verbunt, F. 2010, A&A, 521, A79

Pintore, F., Di Salvo, T., Bozzo, E., et al. 2015, MNRAS, 450, 2016

Piraino, S., Santangelo, A., Kaaret, P., et al. 2012, A&A, 542, L27

Pontoppidan, K. M., van Dishoeck, E. F., & Dartois, E. 2004, A&A, 426, 925

Poteet, C. A., Whittet, D. C. B., & Draine, B. T. 2015, ApJ, 801, 110

Protassov, R., van Dyk, D. A., Connors, A., Kashyap, V. L., & Siemiginowska, A. 2002, ApJ, 571, 545

Psaradaki, I., Costantini, E., Mehdipour, M., & Díaz Trigo, M. 2018, A&A, 620, A129

Ranalli, P., Hobbs, D., & Lindegren, L. 2017, ArXiv e-prints, arXiv:1704.02493

Ravel, B., & Newville, M. 2005, Journal of Synchrotron Radiation, 12, 537

Reddish, V. C. 1971, Nature, 232, 40

Reid, M. J., McClintock, J. E., Steiner, J. F., et al. 2014, ApJ, 796, 2

Reynolds, R. J. 1986, National Radio Astronomy Observatory Workshop, 12, 53

Rich, R. M., Ryde, N., Thorsbro, B., et al. 2017, AJ, 154, 239

Rogantini, D., Costantini, E., Zeegers, S. T., et al. 2018, A&A, 609, A22

—. 2019, A&A, 630, A143

Rolleston, W. R. J., Smartt, S. J., Dufton, P. L., & Ryans, R. S. I. 2000, A&A, 363, 537

Ruffio, J.-B., Mawet, D., Czekala, I., et al. 2018, AJ, 156, 196

Russell, S. C., & Dopita, M. A. 1992, ApJ, 384, 508

Rybicki, G. B., Lightman, A. P., & Paul, H. G. 1986, Astronomische Nachrichten, 307, 170

Ryter, C., Cesarsky, C. J., & Audouze, J. 1975, ApJ, 198, 103

Sargent, B. A., Forrest, W. J., Tayrien, C., et al. 2009, ApJ, 690, 1193

Savage, B. D., & Sembach, K. R. 1996, ARA&A, 34, 279

Schattenburg, M. L., & Canizares, C. R. 1986, ApJ, 301, 759

Schenck, A., Park, S., & Post, S. 2016, The Astronomical Journal, 151, 161

Schultheis, M., Rich, R. M., Origlia, L., et al. 2019, A&A, 627, A152

Schulz, N. S., Corrales, L., & Canizares, C. R. 2016, in AAS/High Energy Astrophysics Division, Vol. 15, AAS/High Energy Astrophysics Division, 402.05

Schwarz, G. 1978, Annals of Statistics, 6, 461

Seifina, E., & Titarchuk, L. 2012, ApJ, 747, 99

Sembach, K. R., Wakker, B. P., Savage, B. D., et al. 2003, ApJS, 146, 165

Shakura, N. I. 1973, Soviet Ast., 16, 756

Shakura, N. I., & Sunyaev, R. A. 1973, in IAU Symposium, Vol. 55, X- and Gamma-Ray Astronomy, ed. H. Bradt & R. Giacconi, 155

Sidoli, L., Oosterbroek, T., Parmar, A. N., Lumb, D., & Erd, C. 2001a, A&A, 379, 540

Sidoli, L., Parmar, A. N., Oosterbroek, T., et al. 2001b, A&A, 368, 451

Slavin, J. D., Dwek, E., & Jones, A. P. 2015, ApJ, 803, 7

Smith, R. K., Valencic, L. A., & Corrales, L. 2016a, ApJ, 818, 143

Smith, R. K., Abraham, M. H., Allured, R., et al. 2016b, Society of Photo-Optical Instrumentation Engineers (SPIE) Conference Series, Vol. 9905, Arcus: the x-ray grating spectrometer explorer, 99054M

Soria, R., Broderick, J. W., Hao, J., et al. 2011, MNRAS, 415, 410

Speck, A. K., Pitman, K., & Hofmeister, A. 2015, IAU General Assembly, 22, 2257874

Speck, A. K., Whittington, A. G., & Hofmeister, A. M. 2011, ApJ, 740, 93

Spitzer, L. 1998, Physical Processes in the Interstellar Medium

Stark, A. A., & Bania, T. M. 1986, ApJ, 306, L17

Steenbrugge, K. C., Kaastra, J. S., de Vries, C. P., & Edelson, R. 2003, A&A, 402, 477

Steenbrugge, K. C., Kaastra, J. S., Crenshaw, D. M., et al. 2005, A&A, 434, 569

Steiner, J. F., McClintock, J. E., & Reid, M. J. 2012, ApJ, 745, L7

Stella, L., Priedhorsky, W., & White, N. E. 1987, ApJ, 312, L17

Stern, E. A., Newville, M., Ravel, B., Yacoby, Y., & Haskel, D. 1995, Physica B Condensed Matter, 208, 117

Strom, S. E., & Strom, K. M. 1961, PASP, 73, 43

Takahashi, O., Tamenori, Y., Suenaga, T., et al. 2018, AIP Advances, 8, 025107

Takei, Y., Fujimoto, R., Mitsuda, K., Futamoto, K., & Onaka, T. 2003, in Astrophysics of Dust, 45

Takeuchi, T. T. 2000, Ap&SS, 271, 213

Tanaka, K. K., Yamamoto, T., & Kimura, H. 2010, ApJ, 717, 586

Tanaka, Y., & Bleeker, J. A. M. 1977, Space Sci. Rev., 20, 815

Tarter, C. B., Tucker, W. H., & Salpeter, E. E. 1969, ApJ, 156, 943

Tashiro, M., Maejima, H., Toda, K., et al. 2018, in Society of Photo-Optical Instrumentation Engineers (SPIE) Conference Series, Vol. 10699, Proc. SPIE, 1069922

Tchernyshyov, K., Meixner, M., Seale, J., et al. 2015, ApJ, 811, 78

The Lynx Team. 2018, arXiv e-prints, arXiv:1809.09642

Thielemann, F. K., & Arnett, W. D. 1985, ApJ, 295, 604

Tielens, A. G. G. M. 2001, in Astronomical Society of the Pacific Conference Series, Vol. 231, Tetons 4: Galactic Structure, Stars and the Interstellar Medium, ed. C. E. Woodward, M. D. Bicay, & J. M. Shull, 92

Tielens, A. G. G. M. 2005, The Physics and Chemistry of the Interstellar Medium

—. 2013, Interstellar PAHs and Dust, ed. T. D. Oswalt & G. Gilmore, Vol. 5, 499

Tielens, A. G. G. M., Seab, C. G., Hollenbach, D. J., & McKee, C. F. 1987, ApJ, 319, L109

Tielens, A. G. G. M., Waters, L. B. F. M., & Bernatowicz, T. J. 2005, in Astronomical Society of the Pacific Conference Series, Vol. 341, Chondrites and the Protoplanetary Disk, ed. A. N. Krot, E. R. D. Scott, & B. Reipurth, 605

Tielens, A. G. G. M., Waters, L. B. F. M., Molster, F. J., & Justtanont, K. 1998, Ap&SS, 255, 415

Titarchuk, L. 1994, ApJ, 434, 570

Trcera, N., Cabaret, D., Rossano, S., et al. 2009, Physics and Chemistry of Minerals, 36, 241

Treffers, R., & Cohen, M. 1974, ApJ, 188, 545

Tröger, L., Arvanitis, D., Baberschke, K., et al. 1992, Phys. Rev. B, 46, 3283

Trotta, R. 2008, Contemporary Physics, 49, 71

Trumpler, R. J. 1930, PASP, 42, 214

Ueda, Y., Mitsuda, K., Murakami, H., & Matsushita, K. 2005, ApJ, 620, 274

Ueda, Y., Murakami, H., Yamaoka, K., Dotani, T., & Ebisawa, K. 2004, ApJ, 609, 325

Ueda, Y., Yamaoka, K., & Remillard, R. 2009, ApJ, 695, 888

Urquhart, J. S., Figura, C. C., Moore, T. J. T., et al. 2014, MNRAS, 437, 1791

Valencic, L. A., & Smith, R. K. 2013, ApJ, 770, 22

—. 2015, ApJ, 809, 66

Valencic, L. A., Smith, R. K., Dwek, E., Graessle, D., & Dame, T. M. 2009, ApJ, 692, 502
van de Hulst, H. C. 1957, Light Scattering by Small Particles
van den Berg, M., Homan, J., Fridriksson, J. K., & Linares, M. 2014, ApJ, 793, 128
van den Hoek, L. B., & Groenewegen, M. A. T. 1997, A&AS, 123, 305
van Dishoeck, E. F. 2014, Faraday Discussions, 168, 9
van Dyk, D. A., Connors, A., Kashyap, V. L., & Siemiginowska, A. 2001, ApJ, 548, 224
van Peet, J. C. A., Costantini, E., Méndez, M., Paerels, F. B. S., & Cottam, J. 2009, A&A, 497, 805
van Woerden, H., Rougoor, G. W., & Oort, J. H. 1957, Academie des Sciences Paris Comptes Rendus, 244, 1691
Vasilopoulos, G., & Petropoulou, M. 2016, MNRAS, 455, 4426
Verner, D. A., Verner, E. M., & Ferland, G. J. 1996, Atomic Data and Nuclear Data Tables, 64, 1
Verner, D. A., Yakovlev, D. G., Band, I. M., & Trzhaskovskaya, M. B. 1993, Atomic Data and Nuclear Data Tables, 55, 233
Vink, J. 2011, The Astronomy and Astrophysics Review, 20, 49
Voshchinnikov, N. V., & Henning, T. 2008, A&A, 483, L9
Wang, Q. D. 2010, Proceedings of the National Academy of Science, 107, 7168
Wasserman, L. 2000, J. Math. Psychol., 44, 92
Waters, L. B. F. M., & Waelkens, C. 1998, ARA&A, 36, 233
Watson, D., Christensen, L., Knudsen, K. K., et al. 2015, Nature, 519, 327
Watts, B. 2014, Optics Express, 22, 23628
Weingartner, J. C., & Draine, B. T. 2001, ApJ, 548, 296
Westphal, A. J., Butterworth, A. L., Tomsick, J. A., & Gainsforth, Z. 2019, ApJ, 872, 66
Westphal, A. J., Stroud, R. M., Bechtel, H. A., et al. 2014, Science, 345, 786
Whittet, D. 2002, Dust in the Galactic Environment, 2nd Edition, Series in Astronomy and Astrophysics (Taylor & Francis)
Whittet, D. C. B., Duley, W. W., & Martin, P. G. 1990, MNRAS, 244, 427
Whittet, D. C. B., Boogert, A. C. A., Gerakines, P. A., et al. 1997, ApJ, 490, 729
Witt, A. N., Gordon, K. D., & Furton, D. G. 1998, ApJ, 501, L111
Woolf, N. J., & Ney, E. P. 1969, ApJ, 155, L181
Wu, Z. Y., Mottana, A., Marcelli, A., et al. 2004, Phys. Rev. B, 69, 104106
Xiang, J., Lee, J. C., Nowak, M. A., & Wilms, J. 2011, ApJ, 738, 78
Yamamoto, T., Chigai, T., Kimura, H., & Tanaka, K. K. 2010, Earth, Planets and Space, 62, 23
Yao, Y., Schulz, N., Wang, Q. D., & Nowak, M. 2006, ApJ, 653, L121
Yao, Y., & Wang, Q. D. 2005, ApJ, 624, 751
—. 2006, ApJ, 641, 930
Yao, Y., Wang, Q. D., Hagihara, T., et al. 2009, ApJ, 690, 143
Zeegers, S. T., Costantini, E., Rogantini, D., et al. 2019, A&A, 627, A16
Zeegers, S. T., Costantini, E., de Vries, C. P., et al. 2017, A&A, 599, A117
Zhukovska, S., Henning, T., & Dobbs, C. 2018, ApJ, 857, 94
Zinner, E., Nittler, L. R., Hoppe, P., et al. 2005, Geochim. Cosmochim. Acta, 69, 4149
Zubko, V., Dwek, E., & Arendt, R. G. 2004, ApJS, 152, 211

"Lime and limpid green, a second scene
Now fights between the blue you once knew
Floating down, the sound resounds
Around the icy waters underground
Jupiter and Saturn, Oberon, Miranda and Titania
Neptune, Titan, stars can frighten"

Pink Floyd - Astronomy Domine (1967)

Summary

The interstellar medium is an enormous painting consisting of strong strokes of gas and dust which fill interstellar space and shades smoothly into the surrounding intergalactic canvas. Despite the extremely low particle density, on average lower than the vacuum in laboratories, from the interstellar medium, spectacular structures can arises which can be greatly different in temperature, density, composition and size. These define the patchy structure of the Milky Way, our home-galaxy.

The interstellar gas is primarily composed of hydrogen and helium. All the other elements (like carbon, oxygen, iron, magnesium), indicated as metals in astronomy, represent less than 2% of the total mass. Despite this small fraction, the metals have an important role in the chemical and physical processes of the Galaxy.

The interstellar medium is usually divided in three phases (cold, warm and hot phases) distinguished by the temperature and density of the gas. Cool and dense regions of the interstellar medium, contain most of the interstellar matter and they occupy less than 5% of the Galactic volume. The material is principally concentrated into giant clouds, known as molecular clouds, where molecular hydrogen coexists with neutral gas and interstellar dust. This cold medium is embedded in a hot buoyant medium (known as hot coronal gas) which occupies most of the volume of interstellar space and extends to the Galactic halo. In this floating and rarefied medium, matter is primarily ionised and heated by powerful shocks from stellar winds or supernova explosions. The space between the cold and hot phases is occupied by an extended intercloud medium, consisting of neutral and low ionised gas.

In this thesis we focus on the characterisation of the hot coronal gas and the interstellar dust, which represent only 1% of the interstellar matter. The novel methods and models developed for the investigation are presented in the sections below.

The hot medium

The existence of the hot interstellar medium was first postulated by Lyman Spitzer in 1956. He argued that the presence of clouds in pressure equilibrium observed at high latitude can only be explained by the existence of a Galactic corona made of tenuous gas at high temperature, above $10^{5.5}$ K. The final establishment of this hot gas corresponded with the detection of the diffuse O VI absorption line by the *Copernicus* satellite at ultraviolet wavelengths.

This very hot gas is in collisional ionisation equilibrium which means that the ionisation by collision with electrons is balanced by electron-ion recombination. The ionisation balance in collisionally-ionised plasmas depends only on the electron temperature, and it is therefore

Figure A: The Horsehead Nebula located in the Orion constellation. It is visible as the dark indentation to the red emission nebula in the centre of the photograph. The emission nebula's red colour is caused by electrons recombining with protons to form hydrogen atoms. Also visible at the bottom left is a greenish reflection nebulae that reflects the blue light from nearby stars. Credits: John Chumack

tightly coupled to the local thermodynamic state of the gas.

The hot coronal gas is mainly studied through absorption lines (O VI, N V, and C IV) observed in the spectrum of hot stars. When the temperature of the plasma exceeds 10^6 K, higher ionisation states, such O VII, O VIII, Ne IX, and Ne X, are allowed. The absorption lines of these ions are located in the X-ray energy bandpass. Their detection has been possible with the launch the European X-ray satellite XMM-*Newton* and the American *Chandra* X-ray Observatory both launched in 1999. Bright low-mass X-ray binaries in the Milky Way are ideal sources to study the intervening gas along the line of sight, simply using them as a background lantern. These sources consist of one compact object (a neutron star or a stellar mass black hole) which accretes material from a companion star. The infalling material releases gravitational potential energy in form of X-rays.

These X-ray high-ionisation absorption lines can also be produced by a plasma in photoionisation equilibrium. This kind of gas is photoionised by the radiation emitted by a strong X-ray source. It is usually a gas intrinsic to the source such as an accretion disc wind or atmosphere. Therefore, to identify the nature of these absorption lines is not trivial and an accurate analysis is necessary. In Chapter 2, a novel technique based on the Bayesian inference is developed to assess the nature of the high-ionisation plasma detected along the line of sight towards 4U 1820-30. This source is a tiny binary system whose dimension is 0.1 times the radius of the Sun. In the joint modelling of XMM-*Newton* and *Chandra* we adopt state-of-art models of collisionally ionisation and photoionisation. The result of our fit indicates the existence of a single temperature $T \sim 10^6$ K plasma in collisional ionisation equilibrium along the line of sight towards the source. To overcome the complexity of the X-ray spectroscopy modelling we used a statistical approach based on the Bayesian data analysis.

The dusty medium

In the beginning of the last century, cosmic dust was regarded by astronomers as an annoying interstellar “fog” which impedes an accurate measurement of distances to stars. Only thirty years later the important role of interstellar dust as a catalyst in the evolution of galaxies, the formation of stars and planetary systems, and possibly, the origins of life was revealed. The advances of infrared astronomy, ultraviolet astronomy, and theoretical modelling had a tremendous impact on our understanding of the physical and chemical nature, origin and evolution of interstellar grains and their significance in the evolution of galaxies. Dust grains provide $\sim 30\%$ of the total Galactic luminosity through infrared emission and they actively participate in the life cycle of stars starting with the formation of small refractory particles in stellar atmospheres to their modification in diffuse and molecular clouds and ultimately to their contribution to star forming regions.

Dust exists mainly of carbon, silicon, iron, magnesium and oxygen and it can be roughly divided into two main groups, namely carbonaceous dust (comparable to soot) and silicates

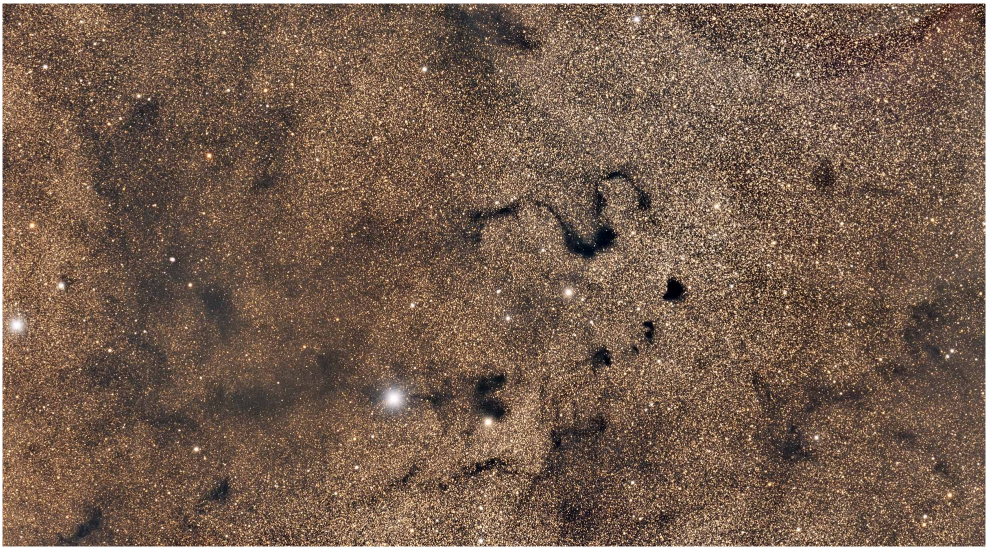

Figure B: The twisty central shape is known as Snake Nebula (or Barnard 72) and it is a dark nebula in the Ophiuchus constellation in the centre of the Milky Way. Other dark clouds are present below the Snake Nebula, in particular Barnard 68 which is the first from the right. Astronomers used to consider these dark molecular clouds as holes in the sky or "heaven" as Herschel exclaimed in 1785. Now we know that the high concentration of dust and molecular gas contained in these dark clouds absorb practically all the visible light emitted from background stars. Credits: Mario Cogo, 2014 from Tivoli Southern Sky Guest Farm, Namibia (e.g., pyroxene and olivine type, comparable to tiny sand grains). In cold and dense environment embedded in molecular clouds the refractory core of silicates can accrete an ice mantle which is dominated by water and methanol. Laboratory astrophysics showed the importance of these ices for the synthesis of complex organic molecules which possibly leads to the origins of life.

There are still many uncertainties about interstellar dust such as the precise chemical composition of the grains, or their structure (crystalline or amorphous). Furthermore, the properties of the dust grains in dense environment are difficult to assess. In this direction, X-ray absorption spectroscopy is a powerful tool and it can give some answer to some of the open questions.

XMM-*Newton* and *Chandra* enabled the detection of particular dust features known as X-ray absorption fine structure (XAFS), in the spectra of bright X-ray binaries. Through the analysis of these fine structures it is possible to probe directly the chemical composition, cristallinity and size distribution of dust grains in different Galactic environments. X-rays are sensitive to a large range of densities and their energy band hosts the edges of the main elements included in dust. In particular, the current X-ray telescopes permit the study of oxygen, iron, magnesium and silicon which are the main components of silicate grains.

The goal of this thesis is to build astronomical models based on accurate laboratory measurements in order to fit the dust fine structures and exploit the diagnostic they offer. In Chapters 3 and 5 we present, respectively, the extinction[1] models of the magnesium and iron K-edge for a large set of dust analogues. By joining all the extinction edge models, we will build the first X-ray interstellar dust extinction (XRIDE) model.

In Chapter 3 we use the spectrum of the low-mass X-ray binary GX 3+1 as a test case to study interstellar dust present along the line of sight toward the source. In particular, we investigate the magnesium and silicon K-edge using our extinction models. In Chapter 4 we expand the number of observed X-ray binaries to seven more sources located near the Galaxy centre. Amorphous olivine is the most representative dust compound along all the investigated lines of sight. We also find a significant contribution (3-15%) of crystalline dust. This is in contrast with the observational results obtained from infrared spectroscopy, where only less than 2% of crystalline dust is detected. This difference may be attributed to the sensitivity of X-rays to short range order, whereas, the infrared observations are focussed on long range order of the dust grains. To fully understand this discrepancy it is necessary to dedicate laboratory studies on the difference between the sensitivity of X-rays and infrared to the crystallinity of the solid.

The iron K-edge represents a unique feature to study the interstellar dust present in the densest region of the Galaxy. Unfortunately, both the sensitivity and the resolution of the current X-ray satellite are not high enough to enable the study of this edge. In Chapter 5 we present the potential of future X-ray missions, *XRISM* (to be launched in 2021) and *Athena* (to be launched in 2031), to observe the Fe K-edge and thanks to our extinction model, to reveal the content of iron in interstellar dust.

High-resolution X-ray spectroscopy represents a powerful method to reveal the characteristics of the interstellar dust and hot coronal gas. An accurate model and a solid statistical

---

[1] X-ray extinction is the sum of X-ray absorption and scattering.

approach are important to interpret correctly the data and obtain robust results. In this perspective, this thesis contributes in the production of a new dust extinction model and the development of a simple Bayesian inference tool suitable for fitting high-resolution X-ray spectra. These tools provide both a way for interpreting present day data and a step forward in the necessary innovation path to interpret the complex X-ray observation from upcoming X-ray missions.

Samenvatting

Het interstellair medium is een enorm schilderij dat bestaat uit krachtige stroken van stof en gas die de interstellaire ruimte vullen en kleur geven aan het omliggende intergalactische canvas. Ondanks de extreem lage deeltjes dichtheid van het interstellair medium, gemiddeld zelfs lager dan het vacuüm in laboratoria, kunnen spectaculaire structuren ontstaan die zeer verschillende temperaturen, dichtheden, compositie en grootten kunnen hebben. Deze factoren bepalen de onregelmatige structuren in de Melkweg, ons eigen sterrenstelsel.

Het interstellaire gas bestaat voornamelijk uit waterstof en helium. Alle overige elementen (zoals koolstof, zuurstof, ijzer, magnesium) worden aangegeven als metalen in astronomie, en vertegenwoordigen minder dan 2% van de totale massa. Ondanks deze kleine fractie, spelen deze metalen een belangrijke rol in chemische en fysische processen in het sterrenstelsel.

Het interstellair medium is doorgaans verdeeld in drie fases (koude, warme en hete fases) en worden onderscheiden door de temperatuur en dichtheid van het gas. Koude en compacte regio's in het interstellair medium bevatten het merendeel van de interstellaire materie en nemen minder dan 5% van het Galactisch volume in beslag. De materie is hoofdzakelijk geconcentreerd in gigantische wolken, ook wel moleculaire wolken genoemd, waar zich tegelijk zowel moleculair waterstof als neutraal gas en interstellaire stof bevindt. Dit koude medium is omsingeld door een hete drijvende medium (bekend als heet coronaal gas), en neemt het grootste deel van het interstellaire volume in dat zich uitstrekt tot het Galactische halo. In dit zwevende en ijle medium is de materie voornamelijk geïoniseerd en verwarmd door krachtige schokken van stellaire winden of supernova explosies. De ruimte tussen de koude en hete fases bestaat uit een uitgerekt medium te midden van wolken, die op hun beurt weer bestaan uit neutraal en laag geïoniseerd gas.

In dit proefschrift focussen we op de karakteristieken van het heet coronaal gas en het interstellair stof, dat echter maar 1% van de interstellaire materie weergeven. De nieuwe methoden en modellen die zijn ontwikkeld voor het onderzoek worden in de volgende secties gepresenteerd.

Het hete medium

Het bestaan van het hete interstellair medium was voor het eerst gepostuleerd door Lyman Spitzer in 1956. Hij beargumenteerde dat wolken die worden geobserveerd op hoge breedtegraad terwijl ze in evenwicht zijn met de druk, enkel kan worden verklaard door de aanwezigheid van een Galactische corona, bestaand uit dun gas met hoge temperaturen boven $10^{5.5}$ K. De definitieve samenstelling van dit hete gas kwam overeen met de *Copernicus*

Figuur A: De paardenkopnevel is gelegen in de Orion. Het is zichtbaar als de donkere plek in de rode emissie nevel in het midden van de foto. De rode emissie kleur van de nevel wordt veroorzaakt door elektronen die recombineren met protonen om waterstof atomen te vormen. Daarnaast is er linksonder ook een groenig reflectienevel zichtbaar, die het blauwe licht van nabijgelegen sterren reflecteert. Afbeelding: John Chumack

satelliet detectie van de diffuse O VI absorptielijn op ultraviolette golflengte.

Dit extreem hete gas is in collisie-geïoniseerd evenwicht, dat betekent dat de ionisatie van botsingen met elektronen in balans is met elektron-ionen recombinatie. De ionisatie balans in collisie-geïoniseerde plasma hangt enkel af van de elektron temperatuur, en is daarom sterk gekoppeld aan het lokale thermodynamische toestand van het gas.

Het hete coronale gas is voornamelijk bestudeerd door absorptielijnen (O VI, N V, and C IV), die zijn geobserveerd in het spectrum van hete sterren. Als het plasma een temperatuur van 10^6 K overschrijdt, zijn hoge geïoniseerde toestanden toegestaan zoals O VII, O VIII, Ne IX en Ne X. De absorptielijnen van deze ionen zitten in de energieband van röntgenstraling. Deze observaties zijn mogelijk gemaakt dankzij de lancering van de Europese röntgenstraling satelliet XMM-*Newton* en de Amerikaanse *Chandra* X-ray Observatory, beide gelanceerd in 1999. Heldere lage-massa röntgenstraling dubbelsterren in de Melkweg zijn ideale bronnen om het tussenliggende gas te bestuderen, eenvoudigweg door ze als een achtergrond lantaarn te gebruiken. Deze bronnen bestaan uit een compact object (een neutronenster of een stellair zwart gat) dat materiaal aantrekt van de omliggende tweede ster door middel van accretie. Het invallend materiaal laat gravitatie energie vrij in de vorm van röntgenstraling.

Deze hoog-geïoniseerde röntgenstraling-absorptielijnen kunnen ook worden geproduceerd door plasma in fotoïonisatie evenwicht. Dit soort gas is gefotoïoniseerd door straling dat is uitgezonden door een sterke röntgenstralingsbron. Het is doorgaans een gas intrinsiek aan de bron, zoals de wind van een accretie schijf of de atmosfeer. Het identificeren van de aard van deze absorptielijnen is daarom niet triviaal, en een nauwkeurige analyse is noodzakelijk.

In Hoofdstuk 2 presenteren we een nieuwe techniek die gebaseerd is op het theorema van Bayes, ontwikkeld om de aard van de hoog-geïoniseerde plasma vast te stellen in de richting van 4U 1820-30. Deze bron is een klein tweedelig systeem met een dimensie van 0.1 maal de radius van de zon. Bij het gezamenlijk modelleren van XMM-*Newton* en *Chandra*, gebruiken we de meest actuele modellen van collisie-ionisatie en fotoïonisatie. De resultaten van onze fit tonen het bestaan aan van plasma, met een enkele temperatuur van $T \sim 10^6$ K, in collisie-ionisatie evenwicht in de gezichtslijn van de bron. Om de complexiteit van het spectroscopisch modelleren van röntgenstraling te overwinnen, gebruiken we een statistische methode gebaseerd op de Bayesiaanse data analyse.

Het stoffig medium

In het begin van de vorige eeuw werd kosmische stof door astronomen gezien als hinderlijke interstellaire mist, die accurate observaties van verre sterren belemmert. Enkel dertig jaar later werd de belangrijke rol van het interstellaire stof ontdekt als katalysator voor de evolutie van sterrenstelsels, formatie van sterren en planetaire systemen, en mogelijk ook het ontstaan van leven.

De vooruitgang van infrarood astronomie, ultraviolet astronomie, en theoretische modellen hebben enorm bijgedragen aan ons begrip van zowel de fysische en chemische aard, als de herkomst en evolutie van interstellaire korrels en hun rol in de evolutie van sterrenstelsels. Stofdeeltjes voorzien $\sim 30\%$ van de totale Galactische lichtkracht via infrarode emissie, en ze spelen een actieve rol in het levenscyclus van sterren: bij de formatie van kleine weerbarstig deeltjes in de stellaire atmosfeer tot de veranderingen in diffuse en moleculaire wolken, en uiteindelijk ook als contributie in stervorming regio 's.

Stof bestaat voornamelijk uit koolstof, silicium, ijzer, magnesium en zuurstof. Het kan ruwweg worden verdeeld in twee categorieën, namelijk koolstofhoudend stof (vergelijkbaar met roet) en silicaten (bijvoorbeeld pyrogeen en olivijn typen, vergelijkbaar met kleine zandkorrels). In koude en compacte omgevingen in moleculaire wolken kan de hardnekkige kern van silicaten een ijsmantel aanhechten via accretie, waarbij de ijsmantel voornamelijk bestaat uit water en methanol. Sterrenkundig laboratoriumonderzoek toonde het belang van dit ijs aan voor de synthese van complexe organische moleculen, dat mogelijk tot het ontstaan van het leven leidt.

Er zijn nog altijd veel onzekerheden over interstellair stof, zoals de precieze chemische compositie, of de structuur (kristallijn of amorf) van de korrels. Bovendien zijn de eigenschappen van stofkorrels in compacte omgevingen moeilijk te bepalen. Hierom is röntgenstraling absorptie spectroscopie een krachtig hulpmiddel en kan het antwoorden bieden op huidige open vragen.

Dankzij XMM-*Newton* en *Chandra* kunnen we bepaalde kenmerken van deeltjes detecteren in het spectrum van heldere röntgendubbelsteren, namelijk met de röntgenstraling absorptie fijnstructuur (XAFS). Door het analyseren van deze fijnstructuren is het mogelijk om de chemische compositie, kristalliniteit en de grootte verdeling in verschillende Galactische omgevingen direct te onderzoeken. Omdat röntgenstraling gevoelig is voor een groot scala aan dichtheden, omvat het ook het energie gebied waar de kenmerken van de hoofdelementen in

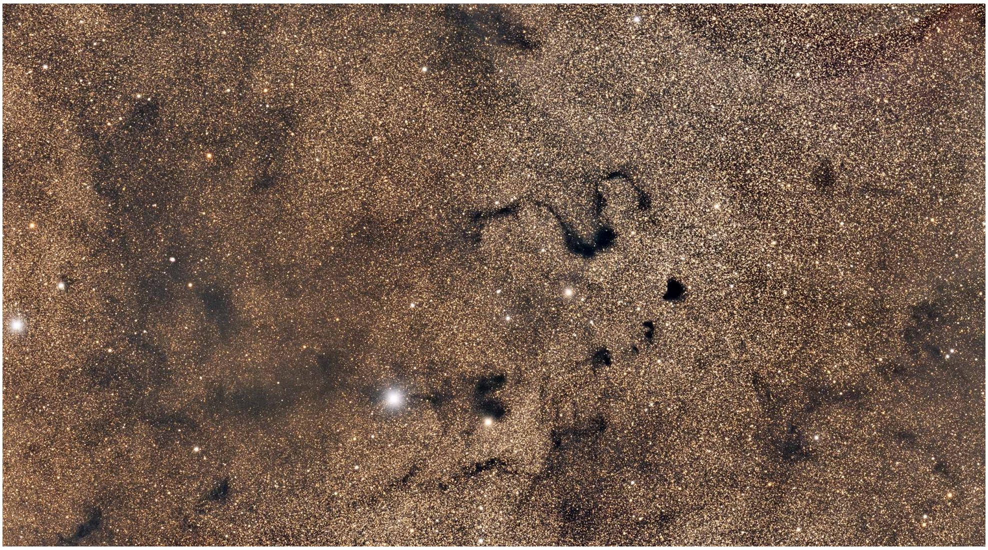

Figuur B: De kronkelende centrale vorm is bekend als Snake Nebula (of Barnard 72) en is een donkere nevel in de Slangendrager in het centrum van de Melkweg. Ook andere donkere wolken zijn te zien, zoals de Barnard 68 die rechts onder de Snake Nebula ligt. Astronomen dachten aanvankelijk dat deze donkere moleculaire wolken gaten waren in de lucht, of "hemel"zoals Herschel riep in 1785. Nu weten we dat de hoge concentratie van stof en moleculair gas in deze donkere wolken zo goed als al het zichtbaar licht absorbeert afkomstig van achtergrond sterren. Afbeelding: Mario Cogo, 2014 Tivoli Southern Sky Guest Farm, Namibia

stof liggen. In het bijzonder, met de huidige röntgentelescopen kunnen we onderzoek doen naar zuurstof, ijzer, magnesium en silicium, die de hoofdbestanddelen van silicaat korrels vormen.

Het doel van deze thesis is om astronomische modellen te bouwen, gebaseerd op accurate laboratoriummetingen, om de fijnstructuur van stof te testen en de diagnose te exploiteren. In Hoofdstuk 3 en 5 presenteren we, respectievelijk, de extinctie [1] modellen van de magnesium en ijzer k-edge voor een grote reeks aan stof anologen. Door alle extinctie edge-modellen bij elkaar te voegen, creëren we de eerste röntgenstraling interstellair stof extinctiemodel (XRIDE).

In Hoofdstuk 3 gebruiken we het spectrum van de lage-massa röntgendubbelster GX 3+1 als test om het interstellair stof te bestuderen die langs de gezichtslijn van de bron ligt. In het bijzonder onderzoeken we met behulp van onze extinctiemodellen de magnesium en silicium k-edge. In Hoofdstuk 4 breiden we het aantal geobserveerde röntgendubbelsteren uit naar zeven bronnen die dichtbij het Galactisch centrum liggen. Amorfe olivijn is de meest representatieve stof samenstelling langs alle onderzochte gezichtslijnen. Ook vinden we een significante contributie (3-15%) van kristallijn stof. Dit is in tegenstelling tot de geobserveerde resultaten verkregen met infrarood spectroscopie, waar minder dan 2% kristallijn stof werd gedetecteerd. Dit verschil zou kunnen worden toegeschreven aan de sensitiviteit van

---

[1] Extinctie is de som van absorptie en verstrooiing.

röntgenstraling voor kleine orde schaal, terwijl de infrarode observaties focussen op grote orde schaal van de stofkorrels. Om deze discrepantie volledig te begrijpen, is het belangrijk om laboratorium onderzoek toe te wijden aan het verschil in sensitiviteit tussen röntgenstraling en infrarood observaties van de kristalliniteit van de vaste stof.
De k-edge van ijzer representeert een uniek kenmerk om het interstellaire stof te bestuderen in de compactste omgevingen van het sterrenstelsel. Helaas zijn zowel de sensitiviteit als de resolutie van de huidige röntgensatellieten niet goed genoeg om de k-edge te onderzoeken. In Hoofdstuk 5 presenteren we de potentiële toekomstige röntgenstraling missies *XRISM* (geplande lancering in 2021) en *Athena* (geplande lancering in 2031), die de Fe k-edge kunnen observeren en dankzij onze extinctie modellen, de ijzergehalte in het interstellaire stof zullen openbaren.

Hoge-resolutie röntgenstraling spectroscopie vertegenwoordigt een krachtige methode om de karakteristieken van interstellair stof en heet coronaal gas aan te tonen. Een accuraat model en een solide statistische methode zijn belangrijk om de data correct te interpreteren en een robuust resultaat te verkrijgen. In dit perspectief, draagt deze thesis mee aan de realisatie van een nieuw extinctie model en aan de ontwikkeling van een simpele Bayesiaanse inferentie hulpmiddel die geschikt is voor het fitten van hoge-resolutie röntgenstraling spectra. Dit hulpmiddel voorziet zowel een manier om de huidige data te interpreteren als een stap vooruit in de noodzakelijke innovatie om de complexe röntgenstraling observaties van toekomstige röntgenstraling missies te interpreteren.

Sommario

Enorme dipinto di gas e polvere, il mezzo interstellare riempie il vuoto tra le stelle della nostra galassia e sfuma sulla circostante tela intergalattica. Nonostante la sua densità di particelle sia notevolmente bassa (in media più bassa del vuoto riprodotto in laboratorio), dal mezzo interstellare si ergono strutture spettacolari con diverse temperature, densità, composizione e dimensione. In particolare queste regioni definiscono la struttura irregolare della Via Lattea, la nostra galassia natale.

Il gas interstellare è principalmente composto da idrogeno ed elio. Tutti gli altri elementi più pesanti (come il carbonio, l'ossigeno, il ferro, e il magnesio), sono indicati per semplicità in astronomia come metalli, e rappresentano circa il 2% della massa totale della galassia. Nonostante questa piccola frazione, l'impatto dei metalli nei processi chimici e fisici della Galassia è fondamentale.

Il mezzo interstellare viene comunemente diviso in tre fasi (fase fredda, tiepida e calda) in base alla temperatura e densità del gas. Le regioni fredde e dense del mezzo interstellare contengono la maggior parte della materia occupando meno del 5% del volume galattico. La materia è concentrata in nubi gigantesche, note come nubi molecolari, nelle quali l'idrogeno molecolare coesiste con il gas neutro e la polvere interstellare. Questa fase fredda è generalmente incorporata in un mezzo caldo e tenue, conosciuto come gas coronale caldo, il quale occupa la maggior parte dello spazio interstellare estendendosi fino all'alone galattico. La materia presente in questo mezzo rarefatto è principalmente riscaldata e ionizzata da potenti collisioni provocate da venti stellari o esplosioni di supernova. Lo spazio tra il gas freddo e caldo è occupato da estese nubi di gas tiepido neutro o leggermente ionizzato.

Lo scopo di questa tesi è la caratterizzazione chimica e fisica del gas coronale caldo e della polvere interstellare, la quale rappresenta soltanto l'1% del mezzo interstellare. I metodi e i modelli sviluppati per questa ricerca sono presentati nelle seguenti sezioni.

Il mezzo caldo

L'esistenza del mezzo interstellare caldo fu per la prima volta postulata da Lyman Spitzer nel 1956. Egli argomentò che soltanto l'esistenza di una corona galattica composta da gas rarefatto con una temperatura elevata, al di sopra di $10^{5.5}$ K, fosse in grado di spiegare la presenza di nubi in equilibrio di pressione ad alte latitudini. La conferma dell'esistenza di questa componente calda giunse con la rivelazione della riga di assorbimento dell'O VI, da parte del satellite Copernicus, nella banda dell'ultravioletto.

Questo gas caldo è in equilibrio di ionizzazione collisionale; ciò significa che la ionizzazione

Figura A: La Nebulosa Testa di Cavallo nella costellazione di Orione. La nebulosa è riconoscibile dalla sagoma scura al centro della fotografia che si staglia sull'emissione rossa dello sfondo. L'emissione rossa della nebulosa è dovuta ai processi di ricombinazione tra elettroni e protoni e alla conseguente formazione di atomi di idrogeno. In basso a sinistra è visibile, in verde, una nebulosa a riflessione la quale riflette la luce blu delle stelle vicine. Crediti: John Chumack

collisionale da parte di elettroni è bilanciata dal fenomeno di ricombinazione elettrone-ione. In un gas ionizzato collisionale, l'equilibrio di ionizzazione dipende unicamente dalla temperatura degli elettroni ed è conseguentemente connesso allo stato termodinamico del gas.

Il gas caldo coronale è generalmente studiato attraverso le righe di assorbimento (O VI, N V, and C IV) osservate nello spettro di stelle calde. Quando la temperatura del plasma supera 10^6 K, è possibile raggiungere stati di ionizzazione più elevati come ad esempio O VII, O VIII, Ne IX, and Ne X. Le righe di assorbimento di questi ioni sono localizzate nella banda energetica X. Il rivelamento di queste righe fu possibile attraverso il telescopio spaziale europeo XMM-*Newton* e quello americano *Chandra*, entrambi messi in orbita nel 1999. Le binarie X rappresentano sorgenti ideali per illuminare il gas, permettendone lo studio. Queste sorgenti sono formate da un oggetto compatto (per esempio una stella di neutroni o un buco nero di massa stellare) che accresce materiale da una stella compagnia. Il materiale in accrescimento rilascia energia elettromagnetica, sotto forma di raggi X.

Le righe di assorbimento corrispondenti a stati di ionizzazione elevati possono essere prodotte anche da plasmi in equilibrio di fotoionizzazione. Tali gas sono fotoionizzati dalla radiazione emessa da potenti sorgenti X. Solitamente corrispondono a gas appartenenti alla sorgente come ad esempio un vento o atmosfera caratteristici del disco di accrescimento. Nel Capitolo 2 di questa tesi viene presentata una nuova tecnica, basata sull'inferenza Bayesiana, sviluppata per definire la natura del plasma presente lungo la linea di vista verso la sorgente 4U 1820-30. Questo oggetto rappresenta una minuscola binaria X con un raggio dieci volte più piccolo del raggio solare. Per analizzare le righe di ionizzazione osservati negli spettri ottenuti sia con XMM-*Newton* che con *Chandra* sono stati utilizzati i modelli più recenti e più accurati di fotoionizzazione e ionizzazione collisionale. I risultati mostrano l'esistenza di un plasma con una singola temperatura di $T \sim 10^6$ K in equilibrio di ionizzazione collisionale lungo la linea di vista della sorgente. L'approccio statistico Bayesiano è stato utilizzato per gestire la complessità dell'analisi degli spettri X e ottenere nello stesso tempo risultati più robusti.

Il mezzo polveroso

All'inizio del secolo scorso, la polvere cosmica fu spesso additata come un'irritante "nebbia" interstellare che ostacolava una misura accurata della distanza delle stelle. Solamente trent'anni dopo si cominciò a scoprire il ruolo fondamentale di catalizzatore ricoperto dalla polvere interstellare nell'evoluzione delle galassie, nella formazione delle stelle e dei sistemi planetari e possibilmente nell'origine della vita.
Il progresso dell'astronomia nella banda infrarossa e ultravioletta insieme ai nuovi modelli teorici ebbero un impatto significativo sulla conoscenza generale riguardante la natura fisica e chimica della polvere, insieme alla sua evoluzione e a al suo contributo all'interno delle galassie. In particolare, i grani interstellari forniscono circa il 30% della luminosità galattica totale attraverso una consistente emissione negli infrarossi. Partecipano oltretutto attivamente al ciclo di vita delle stelle: piccole particelle refrattarie si formano, infatti, nell'atmosfera delle stelle evolute; successivamente queste particelle vengono riprocessate nel mezzo interstellare e incluse in dense nubi che a loro volta costituiscono la culla di nuova formazione stellare.

La polvere interstellare è costituita principalmente da carbonio, silicio, ferro, magnesio e ossigeno e può essere divisa in due gruppi principali: carbonacei (simili alla fuliggine) e silicati (ad esempio pirosseni e olivine, simili a minuscoli granelli di sabbia). Nelle regioni fredde e dense all'interno di nebulose molecolari, il nucleo refrattario dei silicati è in grado di sviluppare un mantello ghiacciato composto principalmente da acqua e metanolo. L'astrofisica di laboratorio ha mostrato come questi mantelli ghiacciati siano fondamentali per la sintesi di molecole organiche complesse nella galassia.
Nonostante la mole di informazione accumulata negli ultimi decenni, rimangono ancora molte incertezze sulla polvere interstellare come per esempio la precisa composizione chimica dei grani cosmici e la loro struttura interna (cristallina o amorfa). Inoltre, le proprietà dei grani di polvere presenti nelle regioni più dense della galassia sono difficili da valutare. In questa direzione, la spettroscopia XAS (dall'inglese X-ray Absorption Spectroscopy) costituisce un importante strumento capace di dare una risposta ad alcune delle domande ancora aperte.
XMM-*Newton* e *Chandra* hanno permesso la rivelazione di particolari strutture spettrali dovute alla polvere, note come X-ray absorption fine structure (XAFS), negli spettri di binarie X particolarmente luminose. L'analisi di tali strutture fini permette di studiare direttamente la composizione chimica, la cristallinità e la distribuzione delle dimensioni dei grani di polvere. Infatti, i raggi X sono sensibili a un ampio intervallo di densità e la rispettiva banda di energia ospita le "*edges* di assorbimento" degli elementi chimici principali inclusi nella polvere. Nel dettaglio, gli odierni telescopi per raggi X permettono lo studio della *edge* dell'ossigeno, ferro, magnesio e silicio i quali rappresentano le componenti base dei silicati.

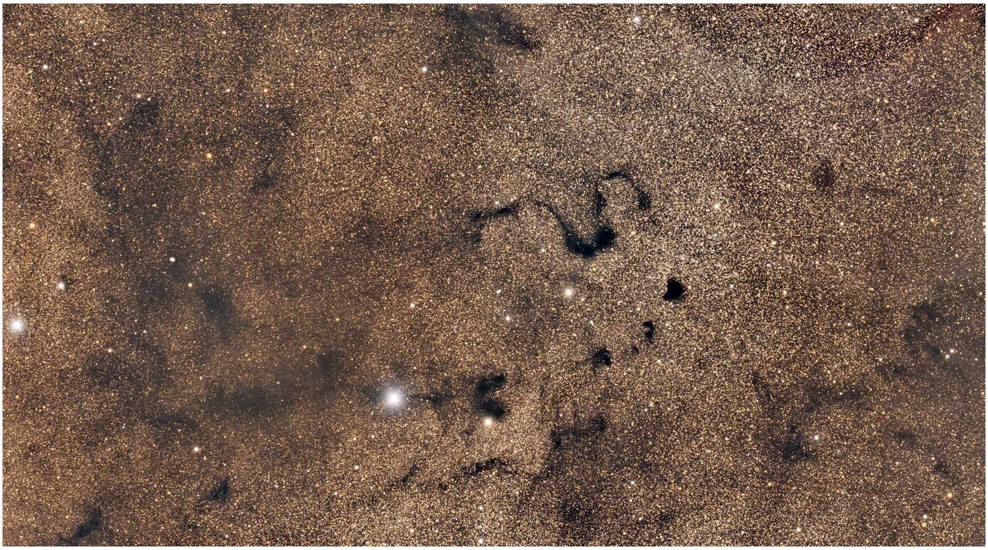

Figura B: La forma serpeggiante al centro è denominata Nebulosa Serpente (o Barnard 72). Si tratta di una nebulosa oscura nella costellazione dell'Ofiuco al centro della Via Lattea. Altre nebulose oscure sono presenti al di sotto della Nebulosa Serpente, in particolare Barnard 68, la prima a partire dalla destra. In principio, gli astronomi considerarono queste nebulose molecolari oscure come buchi nel cielo o nel "paradiso" attenendosi alle parole di Herschel nel 1785. Ora è ben risaputo che queste nebulose oscure sono dovute all'alta concentrazione di polveri e gas molecolare contenuti al loro interno, i quali assorbono completamente l'emissione ottica prodotta dalle stelle sullo sfondo. Crediti: Mario Cogo, 2014 dalla Tivoli Southern Sky Guest Farm, in Namibia

Lo scopo di questa tesi è lo sviluppo di nuovi modelli astronomici al fine di caratterizzare le strutture spettrali della polvere, e sfruttare la diagnostica collegata (derivare la composizione chimica, il livello di cristallinità e le dimensioni dei grani). Tali modelli si basano su accurate misurazioni tramite radiazione di sincrotrone. Nei Capitoli 3 e 5 sono presentati i modelli di estinzione[1] della *edge* del magnesio e del ferro per un campione di analoghi di polvere interstellare. Unendo i modelli di estinzione di tutte le *edges*, sarà possibile realizzare il primo modello di estinzione X della polvere interstellare (XRIDE, dall'inglese X-ray Interstellar Dust Extinction).
Nel Capitolo 3 lo spettro della binaria X di massa piccola, GX 3+1, viene utilizzato come banco di prova per lo studio della polvere interstellare presente lungo la linea di vista. In particolare, sono analizzate le *edges* del magnesio e del silicio usando i nuovi modelli di estinzione costruiti. Nel Capitolo 4 vengono analizzati gli spettri di altre sette binarie X, tutte localizzate vicino al centro galattico. In tutte le linee di vista studiate l'olivina amorfa è il composto chimico più rappresentativo. Inoltre si è osservato un contributo significativo (3-15%) di polvere in forma cristallina. Ciò è in apparente contrasto con i risultati ottenuti dall'astronomia in infrarosso, dove viene osservato meno del 2% di polvere con una configu-

---

[1] L'estinzione dei raggi X corrisponde alla somma dei fenomeni di assorbimento e di *scattering* dei raggi X.

razione cristallina. Ciò potrebbe essere dovuto al diverso potere diagnostico delle due bande energetiche: i raggi X sono infatti sensibili a scale più piccole della struttura dei grani rispetto all'infrarosso. Per comprendere pienamente questa discrepanza sono necessari studi di laboratorio dedicati al potere diagnostico dei raggi X e infrarossi in funzione della strutture cristallina.
La *edge* del ferro rappresenta un'eccezionale caratteristica spettrale per studiare la polvere stellare presente nelle regioni più dense della Galassia. Sfortunatamente, sia la sensitività che la risoluzione dei telescopi X odierni non sono sufficienti per osservare questa *edge* nel dettaglio. Nel Capitolo 5 viene presentato il potenziale delle future missioni per raggi X, *XRISM* (lancio previsto nel 2021) e *Athena* (lancio previsto nel 2031) nel rivelare la *edge* di assorbimento del ferro e, grazie ai nuovi modelli sviluppati, nel definire il contenuto di ferro della polvere interstellare.

La spettroscopia X ad alta risoluzione rappresenta un metodo efficiente e unico nello studio delle caratteristiche della polvere interstellare e del gas caldo coronale. Modelli accurati e approcci statistici solidi sono importanti per interpretare correttamente i dati e ottenere risultati significativi. In tale prospettiva, questa tesi contribuisce alla realizzazione di nuovi modelli di estinzione per la polvere interstellare e allo sviluppo di un semplice programma che impiega l'inferenza Bayesiana per l'analisi di spettri X ad alta risoluzione. Questi strumenti provvedono allo stesso tempo un metodo utile per analizzare i dati odierni e un passo in avanti nel percorso innovativo necessario per interpretare le complesse osservazioni X dei futuri satelliti.

Contribution from co-authors

The bibliography information for the chapters contained in this thesis is presented below. The position in the author list reflects the importance of the contribution of each co-author.

Chapter 2: The hot interstellar medium towards 4U 1820-30: a Bayesian analysis
The hot interstellar medium towards 4U 1820-30: a Bayesian analysis
Rogantini, D.; Costantini, E.; Mehdipour, M.; Ranalli, P.; & Waters, L. B. F. M.
To be submitted to *Astronomy & Astrophysics*

Chapter 3: Interstellar dust along the line of sight of GX 3+1
Interstellar dust along the line of sight of GX 3+1
Rogantini, D.; Costantini, E.; Zeegers, S. T.; de Vries, C. P.; Mehdipour, M.; de Groot, F.; Mutschke, H.; Psaradaki, I.; & Waters, L. B. F. M., 2019.
Astronomy & Astrophysics, 630, A143

Chapter 4: Magnesium and silicon in interstellar dust: an X-ray overview
Magnesium and silicon in interstellar dust: an X-ray overview
Rogantini, D.; Costantini, E.; Zeegers, S. T.; Mehdipour, M.; Raassen, A.J.J.; de Vries, C. P.; & Waters, L. B. F. M.
Submitted to *Astronomy & Astrophysics*

Chapter 5: Investigating the interstellar dust through the Fe K-edge
Investigating the interstellar dust through the Fe K-edge
Rogantini, D.; Costantini, E.; Zeegers, S. T.; de Vries, C. P.; Mehdipour, M.; de Groot, F.; Mutschke, H.; Psaradaki, I.; & Waters, L. B. F. M., 2019
Astronomy & Astrophysics, 609, A22

Publications

First-author articles

1. **Rogantini, D.**; Costantini, E.; Zeegers, S. T.; de Vries, C. P.; Mehdipour, M.; de Groot, F.; Mutschke, H.; Psaradaki, I.; & Waters, L. B. F. M., 2019.
   Astronomy & Astrophysics, 630, A143 (**Chapter 3**)
   Interstellar dust along the line of sight of GX 3+1
2. **Rogantini, D.**; Costantini, E.; Zeegers, S. T.; de Vries, C. P.; Bras, W.; de Groot, F.; Mutschke, H.; Waters, L. B. F. M., 2018.
   Astronomy & Astrophysics, 609, A22 (**Chapter 5**)
   Investigating the interstellar dust through the Fe K-edge
3. **Rogantini, D.**; Costantini, E.; Zeegers, S. T.; Mehdipour, M.; Raassen, A.J.J.; de Vries, C. P.; & Waters, L. B. F. M.
   Submitted to *Astronomy & Astrophysics* (**Chapter 4**)
   Magnesium and silicon in interstellar dust: an X-ray overview
4. **Rogantini, D.**; Costantini, E.; Mehdipour, M.; Ranalli, P.; & Waters, L. B. F. M.
   To be submitted to *Astronomy & Astrophysics* (**Chapter 2**)
   The hot interstellar medium towards 4U 1820-30: a Bayesian analysis

Co-authored articles

1. Costantini, E.; Zeegers, S. T.; **Rogantini, D.**; de Vries, C. P.; Tielens, A. G. G. M.; Waters, L. B. F. M., 2019.
   Astronomy & Astrophysics, 629, A78
   X-ray extinction from interstellar dust. Prospects of observing carbon, sulfur, and other trace elements
2. Zeegers, S. T.; Costantini, E.; **Rogantini, D.**; de Vries, C. P.; Mutschke, H.; Mohr, P.; de Groot, F.; Tielens, A. G. G. M., 2019
   Astronomy & Astrophysics, 627, A16
   Dust absorption and scattering in the silicon K-edge
3. Melandri, A.; Covino, S.; **Rogantini, D.**; Salvaterra, R.; Sbarufatti, B.; Bernardini, M. G.; Campana, S.; D'Avanzo, P.; D'Elia, V.; Fugazza, D.;

Ghirlanda, G.; Ghisellini, G.; Nava, L.; Vergani, S. D.; Tagliaferri, G., 2014
Astronomy & Astrophysics, 565, A72
Optical and X-ray rest-frame light curves of the BAT6 sample

Acknowledgements

What to say.. It was one of the most intense, maybe the longest, trip I ever did. When you ask for a ride with your thumb, you never really know what to expect and, above all, you never know which part of the Galaxy you are getting to. You don't even know if the driver can speak one of your languages.
I still remember perfectly the moment when the SRON PhD express, license plate 3584CA, stopped to give me a ride. I was euphoric and shy at the same time, like a baby kangaroo jumping inside the pouch of the mommy. It was my first time on a spacecraft equipped with the almost infinite improbability drive. It is an old Utrezia model, very welcoming and friendly with only some defects in the aeration system. I would strongly advise against drinking the coffee there. Soon, the SRON PhD express will retire and it will be replaced by a new LEIDA spacecraft, energy class A+^{23}.
The captain Elisa has an exceptional charisma. It is thanks to her that the stack of papers that you are holding in your hands exist. She is the one who decided to offer me a lift. Her skills to fly the spacecraft are remarkable and she really knows how to manage the crew. Even in the very worst of times, she was able to keep me calm exclaiming: *don't panic!* She knows everything about X-rays and she spent many hours trying to teach me how to perceive, control and use them. *May the X-rays be with you*, she always says. We speak the same language and use the same hand gesture vocabulary: I didn't need the *babelfish* during our long chats. The deputy captain Rens is equally a wise, deep and calm person. Through his infrared binoculars he is always able to create a *gezellige* atmosphere and it is very interesting to listen to his long anecdotes about the Galaxy. Luckily, he is a very patient person since I gave him a hard time with my confusion and disorganisation. I spent long days with them philosophizing about the beauty of the dust. Both the captain and the deputy are committed followers of the dust and they have a large collection. Don't try to tell them to dust off the flight deck.

I was lucky that the previous spacecraft, the Brera Master express, left me in the strategic Saturn-like ring system where it was very easy to come across a Phd express. Under the leadership of the captain Gianpiero and the deputy Andrea, I faced an intense and careful preparation. In a short time, I learnt how to drive through tight light curves and assimilate all the secrets of the ghostly analysis. They showed me their gamma bomb which they used to smuggle into the Orion Nebula.

The crew of the SRON Phd express is fantastic. Upon boarding, the tech geniuses Jelle dP and Frank, whose brains were enhanced with depleted iridium, fixed the software of my hitchhiker's guide to the Galaxy which got damage during the previous quick stop on Ursa Minor Beta. I was entrusted to the petty officers Davide, Margherita, and Missagh, who updated my language and vaccinated my brain against the desperate ignorance virus which can be particularly active in the first year of the trip. Davide has a strong passion for bones. He likes to collect the skeletons of animals from different stellar systems and play the evolution game combining them. At artificial-nightfall, he used to end the day telling one of his story, lexically similar to the famous Vogon poems. Then, with his formula *see you, guys!*, he vanishes into thin air. Nobody knows where he goes. Rumours say that he has a love affair with the chef of the spacecraft, Giusy. By the way, the food is extraordinary delicious on the SRON Phd express.

A few days before my arrival, the SRON Phd express took aboard the hitchhikers Kristhell. I shared with her the whole trip across the Galaxy. Kristhell is a three-times galactic Olympics champion in the movie marathon, long-organised jump and shot-plastic. She is also at the head of the green bloc, a group of violent protesters often associated with anarcho-extinctionism and anti-plastification. She is the only person in the whole Galaxy to have spotted the legendary ancestral quetzal. Descendant of Bellatrix Lagrange, she taught me a lot of differential spells, like the partial wingardium leviosah, which causes your left arm and leg to levitate.

To keep our bodies beefy, we trained a lot on the SRON Phd express. Every day, the hitchhiker Giacomo exercised his mouth and neck muscle. His goal is to win the 1000-words-per-second championship which is held every ten years on the Mimi planet. Experienced climber, Giacomo guided me on Sterk, the tallest mountain in the Virgo constellation. He is from the Equuleus constellation, the second smallest constellation of the Galaxy. He is a horse whisperer and he likes to go around the spacecraft riding Amelie, a horse with clear personality disorder.

The cabin where I was staying was really cozy. There were three beds, some plants and a couch which I won in a bet with Francesca. During my trip, I shared the cabin with other hitchhikers, in particular, my X-ray sisters Sascha and Ioanna, and the maestro Jeroen. Together with Sascha and Ioanna, I attended several conferences organised by the X-ray Order and many workshops on dust decoupage. They helped me a lot with my homework. In the evenings we had a lot of fun building a futuristic toy model with which we can feel the little perturbations of the X-ray force. Jeroen is a class H hitchhiker, the highest! Every day he taught me a new trick to level up my hitchhiker's status. He's the one who revealed me the importance of the towel. Now, he is busy designing and constructing his own spaceship full infinity improbability drive to access the most mysterious places of the Galaxy. I am sure I will meet him again.

Every morning the crew meets to talk about the latest news from the Galaxy. Many arguments are usually discussed, but they always end up speaking about the new Brexit, the withdrawal of the United Kingdom from the Orion Arm Union, or about the outbreak of the twist n' shout virus, which infects satellites making them spinning endlessly. It can be lethal for the newborn satellites. During these coffee breaks, I met the research division of the SRON Phd express composed of Cor, Jelle K, Lucien, Aurora, Peter, Jean, Jan-Willem, Hiroki, Luciano, Emanuele, Frank, Ton, Wim and Johan. Some of them are members of the secret association SPEX (the Secret Project Explaining Xilofoni). I made friends with many other hitchhikers: Francois, Catia, Igone, Anna, Francesca, Manuel, Deepak, Lydia, Xiaoyuan, Zhenlin, Junjie, Zuzanna, Kevin, Laura, Marianne, Tiziana, Patrick, Daniel and Ciro (an ex hitchhiker).

Every time before a stop on a planet for refuelling or visiting the families, it was customary to organize a *Borrel* (buffalo-drink only really really expensive liquors). This is a ritual where the youngest people of the crew (below 18 Jupiter-years) have to drink together 42 glasses of okapi milk. The meaning of this tradition is still unknown. The Hitchhiker's Guide to the Galaxy says about that: `[...] Probably the borrel was founded by two people stuck in a wormhole with a 24-pack of beer`. Obviously all the hitchhikers have to take part in the drinking and I had the chance to meet the Terrans aboard, Ralf, Thanos, Will, Alba, Friedemann, Andreas, Anshu, Tobias; the Exotians Yui and Katy; and the Engineers Alexander and Arno.
Nobody within the SRON Phd express reaches the social-life level of the ex hitchhiker Carlo, a true lover of the galactic discounts. Carlo knew practically everybody. He has the skill to know people even before to meet them. The mood changed a lot in the spacecraft when Carlo settled down on the planet Rambla, where there is the highest density of parties of the whole Galaxy.
The itinerary of the spacecraft is accurately organised by the space traffic controller Esther. When we stopped on planets, I joined the traditional parties with the locals. I spent long nights with the native Jaylesh, Terry and Chris going around with our speeder bikes and ringing people's doorbells. With the almost native Ben, I enjoyed abundant and delicious dinners, where often we lost the GPS tracker and we ended up climbing cliffs. Absolutely I have to mention to you the hitchhiker Igor. He speaks a dialect very similar to mine, and he is a class W hitchhiker. Igor and I met in all the planets where we stopped in the last 4 martian-years with a probability of 2 to the power of 600,000 to one against. He is a famous experimenter: his work is to experiment the experience through experiments. The goal of his research is to build a bio-brain more complex than the pet-rat's one. He wants to find the Ultimate Answer avoiding any experiments. Igor and I, together with Michiel, Stein and Thomas took part in the last Galactic championship of Zoneball. We lost.

With other hitchhikers, among them Camilla, Davide and Paul, I attended a long course to learn a new language, the Unpronounceable G. According to the Hitchhiker's Guide to the Galaxy, the Unpronounceable G is an ancient language which widespread on planet Earth through the sailing ships across the water ocean. The name of this language comes from the fact that it is almost impossible to pronounce correctly the G. Only one person in 10,000 can pronounce it. And one of them is our lerares Annemarie. It is said that she knows by heart all the dynasties of the existing kingdoms.

However, on the SRON Phd express I spent most of the time with the hitchhiker Ariane. I met her in the hallway of the spacecraft. I remember that with her hair she reflected the light from the Galactic Bulge on my face and I got Sagittarius A^*-tanned. She has a super specialised hitchhiker onion-suite: a 1000-layer neutrino-proof jacket. She shared with me her knowledge about windy and rainy hitchhiking and how to keep calm when someone steals your galactic passport. Moreover every time I lost my neurons, she helped me to find them back and to sew my synapses. Now she is super exited because she just found the mythological black-painted matter. If it is edible we are going to organise a massive barbecue with Catherine, Antoon, Pierre and Maria at her home planet where the gardens end.

Ora é tempo di lasciare la SRON phd express. L'autostoppista é come il bradipo depresso: puzza dopo 4 anni. Prima di partire per una nuova avventura passo a salutare Alessandra nel pianeta dei canguri piromani e poi torno a casa a salutare mamma Giovanna e papà Adriano. I due vecchietti hanno investito tempo e denaro per la mia formazione da futuro autostoppista galattico e mi hanno comprato il biglietto del mio primo viaggio spaziale. Mia mamma é una profeta. Fin da piccolo quando disobbedivo urlava sempre *"se non la smetti te le faccio vedere io le stelle"*. E alla fine di stelle ne ho viste tante. Ritornerò a casa con un bel pò di souveniers che ho collezionato in questi ultimi anni: bottiglie di varie nebulose, cartoline al magnesio, lumache salate, fagioli felici e frikandel. Ho comprato un nuovo paio di ramponi di geco per andare a scalare qualche vetta con papà. Ovviamente ci sarà l'artista di famiglia, Jessica. In questi anni mi ha spedito un sacco di dipinti e disegni che ho usato per decorare la SRON Phd express. Faremo qualche giro in bicicletta e sarò pronto a batterla al lancio di pupazzi infuocati. Come consuetidine sarò costretto a fare le flessioni a gravità 100 con il super sayan Gabriele. Ma so già che a fine allenamento mi delizierà con bresaola e liquore di cuore di liquirizia fatto da lui.

Con i vecchi warriors di Verderio organizzeremo una mega festa al campo di Ste per ricordare le lunghe avventure passate insieme. Grazie ai duri allenamenti nei fine settimana, non ho avuto problemi ad affrontare il salto nell'iperspazio. La sensazione che si prova é la stessa di quando si é ubriachi. Durante il mio viaggio sulla SRON Phd express ci siamo sentiti spesso con lunghe chiamate telepatiche. Per colmare il vuoto lasciato nella compagnia mi hanno rimpiazzato con una capra: Ricky le fornisce il fieno e il mangime, Fiz le ha comprato la stalla, Boss la tiene in forma con lunghi allenamenti, Pavel le sta insegnando a belare in cinese, Ste la porta allo stadio a vedere l'Atalanta, Woody la rade ogni giorno, Tom le legge i suoi capolavori prima di andare a dormire, Cisco le insegna a ballare e Marco le spaccia Coca-Cola. Per fortuna la milizia formata Isa, Clari, Serena, Kia, Cami, Valeria, Silvi, Ale, Ila, Laura e la mamma Vale tiene a bada la situazione.
Durante la scuola di autostoppismo é stato un piacere condividere il banco con il Bomber, Vero, Deme, Tommy, Sonia, Eli, Pollo e Dino. Gli ultimi due sono particolarmente attivi nella salvaguardia dei Waigo, una specie antichissima in via di estinzione.

Sulla Terra mi fermerò abbastanza a lungo per salutare i tantissimi parenti: zii, zie, cugini e cugine. Mi dispiace tanto non aver fatto in tempo ad informare lo zio Costanzo che ho scoperto il segreto della leggendaria sgrignàpola.
Passero' sicuramente a salutare anche gli amici di Dasile, in particolare lo scalét Oscar che fu il primo a mostrarmi il primo autostoppista con il suo van de telesfross. Riesumerò le mie scarpe con i tacchetti per fare una partitella con l'Ambrosiana. Sono curioso di vedere la

forma di Pizzul il mio ex compagno di autostop. Insieme siamo finiti su Compostiago, un pianeta lontano 785 anni luce governato da strane creature piediformi, spesso sofferenti di mal di stinco.

It is time now to leave the spacecraft. I hope that they won't get mad when they will discover that I took with me a doctoral degree. It might come in handy in future.
Is there anything more? Ah yes, `thank you all`.

"There's no dark side of the moon really.
Matter of fact it is all dark."

Pink Floyd - Eclipse (1973)

```
                                       /~\   Did you read that?
                                      |oo )
                                     _\=/_
                     ___             /  _  \
                    / ()\           //|/.\|\\
                  _|_____|_         \\ \_/  ||
                 | | === | |         \|\ /| ||
                 |_|  O  |_|         # _ _/ #
                  ||  O  ||           | | |
                  ||__*__||           | | |
                 |~ \___/ ~|          []|[]
                 /=\ /=\ /=\          | | |
_________________[_]_[_]_[_]_________/_]_[_\__________________________
```

Cover design by Jessica Rogantini
Concept by Jessica Rogantini

ISBN: 978-94-028-1957-1

Contact: d.rogantini@gmail.com